FY18 PROCEEDINGS OF THE EDGEWOOD CHEMICAL BIOLOGICAL CENTER

IN-HOUSE LABORATORY INDEPENDENT RESEARCH AND SURFACE SCIENCE INITIATIVE PROGRAMS

Message from the In-House Laboratory Independent Research Program Manager

It is my pleasure to present the tenth annual edition of the Proceedings of the Edgewood Chemical Biological Center's (ECBC) In-House Laboratory Independent Research (ILIR) and Surface Science Initiative (SSI) Programs. The ECBC ILIR program funds innovative fundamental research projects that are high-risk with high potential for fulfilling future Army capability needs. Specifically designed to foster increased innovation, the ILIR program also aims to mentor junior investigators in the art and practice of initiating technological innovations and pursuing phenomenology at the boundaries of chemistry, biology, mathematics, and physics to gain insight and advances in support of CBRNE defense missions.

As always, this report includes a description of the ILIR program's rigorous project selection and evaluation process. A critical component of our program is the peer review of project proposals by external senior scientists from across the government. These reviews ensure that we not only fund projects with the greatest potential for fulfilling future Army capability needs, but that we receive an honest and unbiased assessment of our research efforts to hone the Basic Research Portfolio year after year.

This year's edition highlights several major accomplishments of our basic research portfolio over the last decade. Since FY09, the portfolio has yielded more than 200 knowledge products in the form of peer-reviewed publications, technical reports, presentations, patents, and book chapters along with more than a dozen transitions—most to customer-funded lines of effort. Our portfolio has also served as a critical workforce development tool for junior scientists, affording them the opportunity to gain critical experience to enable their success as scientists within a DoD laboratory.

Finally, the report concludes with a technical manuscript from each of the six ILIR, six SSI, and six internally funded Seedling projects from FY18. Together, these projects covered areas of interest across the chemical, biological, and physical sciences, including: *Rational Molecular Synthesis and Novel Materials*, *Synthetic Biology*, *Nano Chemical and Biological Sensing*, *Panomics and Molecular Toxicology*, *Aerosol Sciences*, *Algorithm Design and Development*, and *Surface Science*.

If you have questions about the ILIR Program or this report, please do not hesitate to contact me or the ILIR Administrative Coordinator directly. I can be reached by telephone at (410) 436-0683, DSN 584-0683, or by email at augustus.w.fountain.civ@mail.mil. The ILIR Administrative Coordinator, Ms. Rebecca Braun, can be reached at (410) 417-4961 or by email at rebecca.m.braun.ctr@mail.mil.

Sincerely,

Augustus W. Fountain III, Ph.D.
Senior Research Scientist (ST) for Chemistry

Strategic Mission and Vision

The U.S. Army Edgewood Chemical Biological Center (ECBC) is the nation's principal research and development resource for non-medical chemical and biological (CB) defense. ECBC's mission to be the Nation's premier provider of innovative CB solutions supports the Center's vision of being a Provider of world-class solutions. For more than 100 years, ECBC has been a unique national asset, providing innovative and cost-effective CB defense technology solutions through our scientific and engineering expertise, coupled with our unique facilities and collaboration with partners.

ECBC's mission and vision are supported by the Center's three Directorates: Research and Technology (R&T), Engineering, and Program Integration. The R&T Directorate provides integrated science and technology (S&T) solutions that address CB defense knowledge gaps and vulnerabilities. Basic science research at ECBC contributes valuable information to the fundamental science knowledge base, enabling the development of technologies that directly benefit the Warfighter and further strengthen the Army's S&T mission. ECBC's unique set of core research and technology capabilities position it to be the Army's fundamental source of research in chemistry and biology.

ECBC ILIR Project Selection and Evaluation Process

The purpose of the ILIR program is to fund innovative basic research projects that are high-risk but have high potential payoff for fulfilling future Army capability needs. The Department of Defense (DoD) defines basic research as "systematic study directed toward greater knowledge or understanding of the fundamental aspects of phenomena and of observable facts without specific applications toward processes or products in mind."[1] The ILIR program is also specifically designed to foster increased innovation within ECBC, where it is viewed as a critical part of the Center's efforts to ensure a high level of quality in basic science; to foster innovation in the areas of chemistry and biology; to mentor junior investigators in the art and practice of laboratory science; and to explore new technological innovations and phenomenology at the boundaries of chemistry, biology, mathematics, or physics to expand the state-of-the-possible in support of CBRNE defense missions.

The ILIR program solicits the Center's principal investigators for innovative proposals that correspond to topics highlighted in the ECBC R&T Directorate's Strategic Roadmap. The FY18 ILIR topics were: *Rational Molecular Synthesis and Novel Materials*, *Synthetic Biology*, *Nano Chemical and Biological Sensing*, *Panomics and Molecular Toxicology*, *Aerosol Sciences*, *Algorithm Design and Development*, and *Surface Science*. The proposals are then reviewed and critiqued by a panel comprised of resident and external Department of the Army Senior Research Scientists (ST), Senior Scientists from other DoD organizations, and civilian and military faculty members at the United States Military Academy.

At right, a Soldier with the 82nd Airborne Division spits into a test tube that researchers from the U.S. Army Research, Development and Engineering Command Soldier Center tested for cortisol levels during a stress shoot test. (Photo credit: David Kamm, RDECOM Soldier Center)

[1] *DoD Financial Management Regulation, DoD 7000.14-R, Vol. 2B, Ch. 5*

PROPOSAL SCORING CRITERIA

Exceptional (4): Comprehensive and complete in all areas; meets all significant objectives; offers a comprehensive project that exceeds the ILIR vision and is supportable by the proposed approach; has few weaknesses which are easily correctable.

Acceptable (3): Meets most of the significant objectives and is responsive to the ILIR vision; offers a feasible technical solution; weaknesses are readily correctable; proposal is complete to the extent that an award could be made in present terms.

Marginal (2): Minimally meets ILIR vision and objectives (i.e., offers a project vision that is marginally supported by the proposed approach, and/or claims are not documented or substantiated); significant deficiencies exist.

Unacceptable (1): Fails to meet significant characteristics of the ILIR vision and/or objectives stated in the Solicitation; has weaknesses and/or deficiencies that are significant and of such magnitude that they cannot be corrected without extensive discussion/major revision of the proposal.

	REVIEWERS							AVERAGE
	1	2	3	4	5	6	7	
Scientific Objective	4.0	3.0	4.0	3.0	3.0	3.0	1.0	3.0
Methods and Approach	4.0	2.0	3	2.0	3.0	2.0	2.0	2.6
PI Qualifications	3.0	3.0	4.0	3.0	3.0	3.0	3.0	3.1
Budget	3.0	3.0	3.0	1.0	3.0	3.0	3.0	2.7
Overall Evaluation	**3.7**	**2.7**	**3.5**	**2.3**	**3.0**	**2.7**	**2.0**	**2.8**

The review panel evaluates each proposal on its scientific objective, the scientific methods proposed, the qualifications of the investigator, and the budget; with the scientific objective and methods weighted as the most important criteria. The proposals are then ranked according to merit. Only proposals deemed by the panel as basic research are considered for funding.

Quality comments from the reviewers are compiled and used, along with the numerical score, as a critical assessment of the proposal. This written feedback is essential for ECBC's mentoring of researchers and for justifying the elimination of research programs that are not competitive. Quarterly reviews of project performance provide guidance to the program's participants, ensuring that projects meet significant milestones and that substantive new knowledge is being produced and transferred to ECBC and the broader scientific community. In FY18, this cyclical review and assessment process was used to select and monitor the progress of six ILIR and six SSI projects. Internal funds were also used to support six "Seedling" projects, which are smaller scale projects of high-risk, high-reward basic research.

While the U.S. Army mandated that independent annual reviews of all ILIR programs be conducted by a panel from the National Academies of Sciences, Engineering, and Medicine beginning in FY18, ECBC continued to hold its external annual review in the fourth quarter of FY18 to assess year-to-date performance of the funded ILIR and SSI projects. In FY18, representatives from the Defense Threat Reduction Agency (DTRA), the Joint Program Executive Office for Chemical, Biological, Radiological, and Nuclear Defense (JPEO-CBRND), the United States Military Academy, and the United States Naval Research Laboratory served as reviewers. Comments and feedback from this review were used to support continued funding, or course corrections, of each ILIR and SSI project.

This Proceedings Report contains the technical reports from all 18 ECBC-produced ILIR/SSI/Seedling-funded projects.

Ten Years of Basic Research at ECBC

Over the last decade, ECBC has successfully leveraged the basic research portfolio to make significant contributions to the U.S. Army's fundamental knowledge base. Annually, ECBC's modest basic research portfolio contributes a significant portion of the Center's knowledge products, often between 10–25% of these products. Since FY09, ECBC has funded more than 100 basic research projects: 38 ILIR, 18 SSI, and 49 Seedlings. In this time, the basic research portfolio alone has yielded more than 200 knowledge products, including dozens of peer-reviewed publications and technical reports, scores of presentations and proceedings, 10 patents, and 2 book chapters.

Beyond these metrics, the ILIR and SSI programs have yielded more than a dozen transitions to a variety of sources including DTRA-funded programs, the Army Competitive ILIR program, or new ILIR/SSI projects.

Our annual TAB review serves as a decision gate for continuing projects. While the TAB provides guidance for continuation projects, they also evaluate whether projects should be recommended for continued funding. For example, a project may be recommended for termination if the project is not deemed sufficiently productive or if there are insurmountable barriers to executing the work. In this capacity, TAB recommendations have resulted in the termination of 12 ILIR or SSI projects.

PROJECTS

38 ILIR projects

18 SSI projects

49 Seedling projects

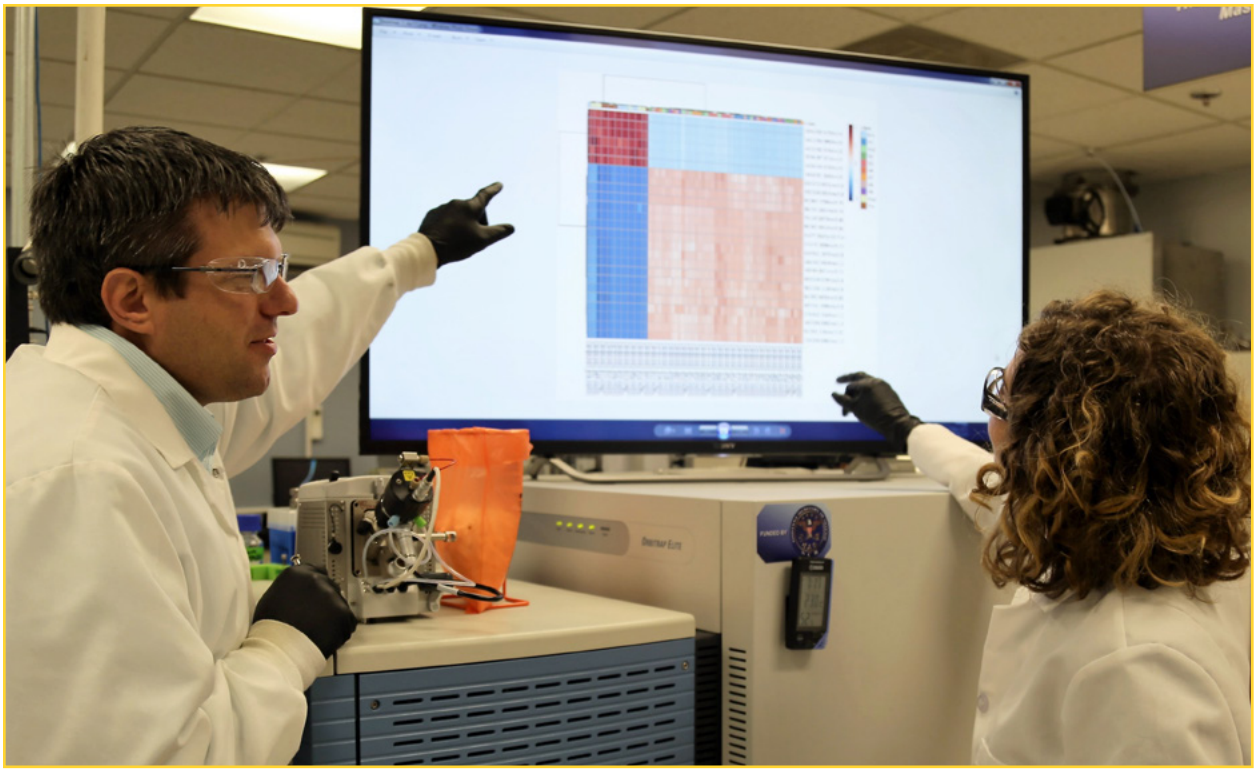

Trevor Glaros, Ph.D., and Elizabeth Dhummakupt, Ph.D., analyze data from a test of biomarkers found in blood to determine opioid exposure. (U.S. Army photo)

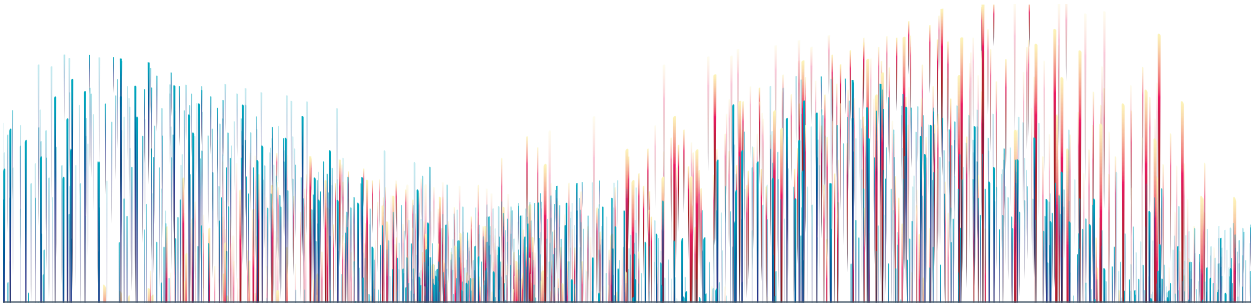

ECBC's basic research and innovation programs also serve as a critical retention and workforce development tool for our scientists. In the past ten years, nine recent hires from ECBC's post-doctoral fellowship programs through the National Research Council (NRC) and the Oak Ridge Institute for Science and Education (ORISE) have served as ILIR/SSI PIs, with dozens more contributing to the portfolio as co-PIs or contributing researchers.

The ILIR and SSI programs provide a valuable opportunity for new PIs to gain critical experience to enable their success as scientists within a DoD laboratory. PIs in our innovation programs are required to craft a proposal that is successfully peer reviewed; manage the cost, schedule, and performance of their research project; and report the findings of their research, both at internal venues and externally.

PRODUCTS

111 Presentations and proceedings

79 Peer-reviewed publications

33 Technical reports

10 Patents

2 Book chapters

A smoke grenade containing metal organic frameworks designed to block infrared light being tested in an ECBC test chamber. (U.S. Army photo)

Meet our FY18 Principal Investigators

Daniel J. Angelini, Ph.D.

Research Biologist, ***BioDefense Branch, R&T Directorate, ECBC***

Dr. Angelini received his Ph.D. in Medical Pathology from the University of Maryland, Baltimore in 2004. He worked at Johns Hopkins University as either a Post-Doctoral Fellow or a Research Associate from 2005–2011. He joined ECBC in July 2011 as an NRC post-doctoral research associate, becoming a civilian employee in 2015. His current research focuses on several different areas including cell biology, the evaluation of biological sampling devices, and the development of prototype sampling devices.

Matthew A. Browe

Chemical Engineer, ***CBR Filtration Branch, R&T Directorate, ECBC***

Mr. Browe received his bachelor's degree in Chemical Engineering from the Pennsylvania State University in 2011 and is currently pursuing his master's degree in Chemical Engineering at the University of Delaware. Mr. Browe began working at ECBC as a Chemical Engineer in 2011 focusing on permeation and micro-breakthrough testing and evaluation. His efforts include research into novel sorbents and metal-organic framework polymer hybrid films, identifying trends in performance with justification from theory, and materials characterization.

Shaun M. Debow

Chemical Engineer, ***Smoke and Target Defeat Branch, R&T Directorate, ECBC***

Mr. Debow received his master's degree in Chemical & Biochemical Engineering from the University of Iowa in 2004. In 2006, Mr. Debow joined the ECBC workforce as a Chemical Engineer managing lifecycle support for weapons systems. Mr. Debow's areas of expertise include basic and applied research of novel materials, development of novel solutions in anticipation of emerging needs, high-volume production and manufacturing, demilitarization, and systems engineering. Recent research interests include additive manufacturing, 2D materials, applications in surface science, warhead design, and gas adsorbents.

Jared B. Decoste, Ph.D.

Research Chemist, ***CBR Filtration Branch, R&T Directorate, ECBC***

Dr. DeCoste earned his Ph.D. in Materials Chemistry in 2009 from Binghamton University. He served as an NRC post-doctoral research associate in the CBR Filtration Branch at ECBC for two years, followed by several years in industry. Since accepting a position at ECBC, Dr. DeCoste has studied the fundamentals of porous materials, especially for adsorption and catalysis, to the engineering and scaling of functional nanomaterials.

Brendan G. DeLacy, Ph.D.

Research Physical Scientist, ***Smoke and Target Defeat Branch, R&T Directorate, ECBC***

Dr. DeLacy received his Ph.D. in Analytical Chemistry from Drexel University in 2006. Since joining the ECBC workforce in 2009, his research has focused on the development of obscurant materials, primarily the experimental and theoretical aspects of the optical properties of materials. Some research areas of interest include: nanoparticle synthesis of dielectric, semiconductor, and metallic nanoparticles; plasmonics, excitonics, and plasmon-exciton interactions; and applications of nanomaterials in obscuration.

Erin M. Durke, Ph.D.

Research Chemist, ***CBR Filtration Branch, R&T Directorate, ECBC***

Dr. Durke received her doctorate in Analytical Chemistry from Virginia Tech in 2011. In 2011, she accepted a position at ECBC where she studies the gas-surface interaction of chemical warfare agents and militarily relevant surfaces in ultra-high vacuum environments. Dr. Durke led the design, development, and construction of two new systems created specifically to study agent aerosols and their interactions with atmospheric components and surfaces of interest.

Erik D. Emmons, Ph.D.

Research Physicist, ***Spectroscopy Branch, R&T Directorate, ECBC***

Dr. Emmons received his Ph.D. in Physics from the University of Nevada in 2007. He began working at ECBC in 2008 as an NRC post-doctoral research associate before being hired on as a Research Scientist at ECBC in 2015. Since arriving at ECBC, Dr. Emmons has performed research on infrared spectroscopy, surface-enhanced Raman spectroscopy, Raman chemical imaging, and Raman spectroscopy of aerosols, including explosive and chemical threats.

Henry S. Gibbons, Ph.D.

Research Biologist, ***Biotechnology Branch, R&T Directorate, ECBC***

Dr. Gibbons received his Ph.D. in Biochemistry from Duke University in 2003 and conducted post-doctoral work at the University of North Carolina at Chapel Hill on protein export pathways in mycobacteria. Dr. Gibbons provides scientific and technical leadership for bacterial genetics and synthetic biology programs at ECBC. His research group combines expertise in classical bacterial genetics with modern genomic and proteomic approaches to the characterization of fundamental biological phenomena in prokaryotes.

Thomas E. Ingersoll, Ph.D.

Mathematician, ***Modeling, Simulation & Analysis Branch, R&T Directorate, ECBC***

Dr. Ingersoll received his Ph.D. in Environmental Science from the University of California, Berkley in 2010. He began working at ECBC in 2016 as a Mathematician after serving as a Computational Biologist for DTRA since 2013. Since arriving at ECBC, Dr. Ingersoll has studied various methodologies to integrate CB sensor data.

Rabih E. Jabbour, Ph.D.

Research Chemist, ***Detection Spectrometry Branch, R&T Directorate, ECBC***

Dr. Jabbour received his Ph.D. in Bioanalytical Chemistry from the University of Arizona in 1999. At ECBC, he leads the development of an automated sample processing system for the extraction and preconcentration of biomarkers for the detection and identification of biological warfare agents using mass spectrometry. He serves as a reviewer of articles with the Journal of Analytical Chemistry in the areas of microbial proteomics and genomics.

Neal D. Kline, Ph.D.

Research Chemist, ***Spectroscopy Branch, R&T Directorate, ECBC***

Dr. Kline received his Ph.D. in Physical Chemistry from the Ohio State University in 2014. He began working at ECBC in July 2014 as an ORISE post-doctoral research fellow and was hired as a government civilian in 2016. Since arriving at ECBC, Dr. Kline has been working to develop a portable device for the detection of illicit drugs in bodily fluids by combining surface-enhanced Raman spectroscopy with a microfluidic platform.

Monica L. McEntee, Ph.D.

Research Chemist, *CBR Filtration Branch, R&T Directorate, ECBC*

Dr. McEntee earned her B.S. degrees in Chemistry and Mathematics with a minor in Biology in May 2010 from Virginia Tech. She received her Ph.D. in Physical Chemistry in March 2015 from the University of Virginia. In 2015, she was awarded an ORISE post-doctoral research fellowship at ECBC studying the fundamental properties of environmental surfaces (sands and soils) as well as their interactions with chemical agent simulant vapors and aerosols and was hired as a civilian employee in 2017.

Gregory W. Peterson

Research Chemical Engineer, *CBR Filtration Branch, R&T Directorate, ECBC*

Mr. Peterson graduated from Bucknell University with a Bachelor of Science degree in Chemical Engineering in 2003 and is currently pursuing his doctoral degree from the University of Delaware. Mr. Peterson joined the ECBC workforce in 2003 where he is responsible for the design, maturation, and integration of novel sorbent technologies into military respiratory systems.

Roberto Rebeil, Ph.D.

Research Biologist, *Biosciences Division, R&T Directorate, ECBC*

Dr. Rebeil received his doctorate in Pathobiology with a minor in Biochemistry from the University of Arizona in 2001. Dr. Rebeil joined ECBC in 2013, performing basic and applied research focusing on bacteriological and biotoxin agents of concern to the biodefence community and applies recombinant DNA technologies on agents of interest. Dr. Rebeil is currently matrixed to Ft. Detrick where he is serving as an Assistant Project Manager at the Joint Project Management Office for Medical Countermeasures Systems.

Patrick C. Riley

Research Chemist, *Detection Spectrometry Branch, R&T Directorate, ECBC*

Mr. Riley received his bachelor's degree in Chemistry from Salisbury University in 2010. Shortly afterward, he began working at ECBC as a contractor before being hired on as a Research Chemist in January 2015. Mr. Riley has been evaluating the Joint Chemical Agent Detector Chemical Explosives Detector and other chemical detection technologies.

FY18 Innovation Program Highlights

ECBC Basic Research Portfolio Productivity

FY18 FUNDING

$1.1M
over **6 ILIR** projects

$2.2M
over **6 SSI** projects

$257K
over **6 Seedling** projects

FY18 PRODUCTS

11
Peer-reviewed publications

1
Technical report

13
Presentations

Teacher Joan Rome works with ECBC research biologist Daniel Angelini, Ph.D. on environmental surface sampling. (U.S. Army photo)

Peer-reviewed Publications

- Boyne, D.A.; Varady, M.J.; Lambeth, R.H.; Eikenberg, J.H.; Bringuier, S.A.; Pearl, T.P.; Mantooth, B.A., Solvent-Assisted Desorption of 2,5-Lutidine from Polyurethane Films. *J. Phys. Chem. B.* **2018**, *122* (7), pp 2155–2164.

- Debbrecht, B.; McElhiney, M.; Carey, V.; Cullen, C.; Mirotznik, M.S.; DeLacy, B.G., Cavity-based aluminum nanohole arrays with tunable infrared resonances. *Opt. Express.* **2017**, *25* (20), pp 24501–24511.

- Fang, H.; Wu, Y.; Chen, J.; Kuhn, D.L.; Zander, Z.; DeLacy, B.G.; Rao, Y.; Dai, H.L., Electron Injection from a Carboxylic Anchoring Dye to TiO_2 Nanoparticles in Aprotic Solvents. *Chem. Phys.* **2018**, *512*, pp 93–97.

- Garibay, S.J.; Iordanov, I.; Islamoglu, T.; DeCoste, J.B.; Farha, O.K., Synthesis and functionalization of phase–pure NU-901 for enhanced CO_2 adsorption: the influence of a zirconium salt and modulator on the topology and phase purity. *CrystEngComm.* **2018**, *20* (44), pp 7066–7070.

- Hudak, N.J.; Garrett, B.S.; Zablocki, M.; Creazzo, T.; Sharkawy, A.; DeLacy, B.G.; Mirotznik, M.S., In *Thin-film coating of vibro-fluidized microparticles via R. F. Magnetron sputtering*, SPIE Defense + Security, SPIE: **2018**; p 19.

- Peterson, G.W.; Lu, A.X.; Hall, M.G.; Browe, M.A.; Tovar, T.; Epps, T.H., 3rd, MOFwich: Sandwiched Metal-Organic Framework-Containing Mixed Matrix Composites for Chemical Warfare Agent Removal. *ACS Appl. Mater. Interfaces.* **2018**, *10* (8), pp 6820– 6824.

- Peurifoy, J.; Shen, Y.; Jing, L.; Yang, Y.; Cano-Renteria, F.; DeLacy, B.G.; Joannopoulos, J.D.; Tegmark, M.; Soljacic, M., Nanophotonic particle simulation and inverse design using artificial neural networks. *Sci. Adv.* **2018**, *4* (6), p eaar4206.

- Schuchman, R.; Kilianski, A.; Piper, A.; Vancini, R.; Ribeiro, J.M.C.; Sprague, T.R.; Nasar, F.; Boyd, G.; Hernandez, R.; Glaros, T., Comparative Characterization of the Sindbis Virus Proteome from Mammalian and Invertebrate Hosts Identifies nsP2 as a Component of the Virion and Sorting Nexin 5 as a Significant Host Factor for Alphavirus Replication. *J. Virol.* **2018**, *92* (14), pp e00694–00618.

- Tovar, T.M.; Iordanov, I.; Sava Gallis, D.F.; DeCoste, J.B., Enhancing Van der Waals Interactions of Functionalized UiO-66 with Non-polar Adsorbates: The Unique Effect of para Hydroxyl Groups. *Chemistry.* **2018**, *24* (8), pp 1931–1937.

- Tripathi, A.; Emmons, E.D.; Kline, N.D.; Christesen, S.D.; Fountain, A.W.; Guicheteau, J.A., Molecular Structure and Solvent Factors Influencing SERS on Planar Gold Substrates. *J. Phys. Chem. C.* **2018**, *122* (18), pp 10205–10216.

- Varady, M.J.; Knox, C.K.; Cabalo, J.B.; Bringuier, S.A.; Pearl, T.P.; Lambeth, R.H.; Mantooth, B.A., Molecular dynamics study of competing hydrogen bonding interactions in multicomponent diffusion in polyurethanes. *Polymer.* **2018**, *140*, pp 140–149.

Technical Reports

- Feasel, M.G.; Moran, T.S. *In Vitro Screening of Opioid Antagonist Effectiveness;* ECBC-TR-1509; U.S. Army Edgewood Chemical Biological Center: Aberdeen Proving Ground, MD, **2018**; UNCLASSIFIED Report.

Presentations and Posters

- DeCoste, J.B. Synergistic effects of metal-organic framework containing polymer membranes for military applications. *Presented at the International Symposium on Composites of Metal and Covalent Organic Frameworks: Fundamental Design & Applications,* Granada, Spain, **12–14 September 2017**.

- DeCoste, J.B. Modular Design of Microporous Materials for Targeting Chemical Threats. *Presented at the Home on Home Meeting of the Aberdeen Proving Ground Chemistry Networking Group,* Aberdeen Proving Ground, MD, **8 May 2018**.

- DeCoste, J.B. Modular Design of Microporous Materials for Targeting Chemical Threats. *Presented at Invited Presentation to the U.S. Army Research Laboratory,* Aberdeen Proving Ground, MD, **14 March 2018**.

- DeCoste, J.B. Modular Design of Microporous Materials for Targeting Chemical Threats. *Presented at Invited Presentation to Sandia National Laboratory,* Albuquerque, NM, **6 March 2018**.

- DeCoste, J.B. Modular Design of Microporous Materials for Targeting Chemical Threats. *Presented at the Defense Threat Reduction Agency Seminar Series,* Ft. Belvoir, VA, **6 June 2018**.

A Warfighter handles a Joint Chemical Agent Detector (JCAD) Solid Liquid Adapter (SLA) during a field test conducted by Patrick Riley, an ECBC research chemist involved in the project, in June 2018. The JCAD is undergoing concurrent modifications to detect illegal drugs and explosive compounds. (Photo credit: Jack Bunja/ECBC.)

Presentations and Posters (continued)

- DeCoste, J.B. Unexpected synergy in engineered metal-organic frameworks and polymer membranes for military protection applications. *Presented at the 256th National Meeting & Exposition of the American Chemical Society,* Boston, MA, **19–23 August 2018**.

- DeLacy, B.G.; Kuhn, D.; Zander, Z. Ag-TiO_2/TiO_x Nanocomposites for Enhanced Photocatalysis. *Presented at the 233rd Electrochemical Society National Meeting,* Seattle, WA, **13–17 May 2018**.

- Ingersoll, T. Reducing false-positives through capture/recapture modeling for early warning. *Presented at the 86th Military Operations Research Society Symposium,* Monterey, CA, **18–21 June 2018**.

- Jabbour, R.E.; Peterson, G.W.; DeCoste, J.B.; Wade, M. Advancements in MOF characterization for enhanced MALDI sensing. *Presented at SPIE Defense + Security Chemical, Biological, Radiological, Nuclear, and Explosives (CBRNE) Sensing XIX,* Orlando, FL, **17–19 April 2018**.

- Peterson, G.W. Polymer/MOF Composites for Enhanced Protection Against Chemical Warfare Agents. *Presented at the International Symposium on Composites of Metal and Covalent Organic Frameworks: Fundamental Design & Applications,* Granada, Spain, **12–14 September 2017**.

- Peterson, G.W.; Lu, A.; Hall, M.G.; Browe, M.A.; Tovar, T.; Epps, T.H. MOFwich: Sandwiched Metal-Organic Framework-Containing Mixed Matrix Composite Polymers for Chemical Warfare Agent Removal. *Presented at the 256th National Meeting & Exposition of the American Chemical Society,* Boston, MA, **19–23 August 2018**.

- Tovar, T.M.; DeCoste, J.B. Impact of MOF pore size on the diffusion of TICs and CWA simulants. *Presented at the U.S. Army Research Laboratory 3rd Annual Postdoc Research Symposium,* Aberdeen Proving Ground, MD, **18 September 2018**.

- Tovar, T.M.; Iordanov, I.; Sava Gallis, D.F.; J.B., D. Enhancing van der Waals interactions of functionalized UiO-66 with non-polar adsorbates. *Presented at CPM-8: the 8th International Workshop, Characterization of Porous Materials: From Ångströms to Millimeters,* Delray Beach, FL, **6–9 May 2018**.

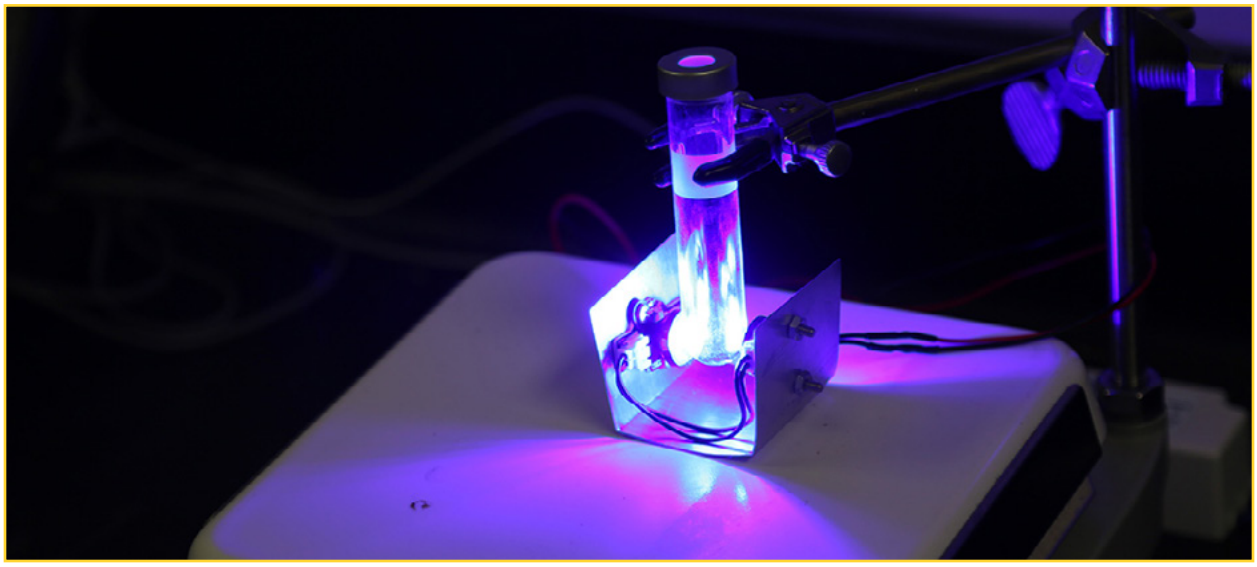

New research is exploring whether chemical weapon-neutralizing substances can be incorporated into equipment worn by Warfighters. Inside the test tube, researchers mix agent with metal-organic frameworks (MOF) and oxygen. Exposure to light starts the MOF's oxidation process, which neutralizes the agent. (U.S. Army photo)

Table of Contents

In-House Laboratory Independent Research (ILIR) Projects

Surface Science Initiative (SSI) Projects

Seedling Projects

ILIR

PROJECTS

Hierarchical systems through selective deposition and growth of metal-organic frameworks on block copolymers

Gregory W. Peterson
U.S. Army Edgewood Chemical Biological Center, Research & Technology Directorate,
8198 Blackhawk Rd, Aberdeen Proving Ground, MD 21010

ABSTRACT

The use of polymers to template arrays of metal-organic frameworks has been an under-researched area. Previously, we explored the use of block copolymers to selectively deposit metal-organic framework constituents followed by *in situ* growth. In FY18, the modification of the archetypal metal-organic frameworks HKUST-1 and UiO-66-NH_2 using acyl chloride chemistry was investigated with the objective of tuning interaction parameters between metal-organic framework and polymer. Modifications of the UiO-66-NH_2 metal-organic framework included acyl chlorides with aliphatic and cyclic hydrocarbons as well as fluorinated compounds. Polymers investigated included polystyrene, poly(styrene)-*block*-poly(isoprene)-*block*-polys(styrene), poly(ethylene oxide), poly(acrylonitrile), and poly(vinylidene fluoride). It was found that modifications of the metal-organic frameworks with the aforementioned functional groups did indeed improve compatibility with certain polymers, and also may lead to enhanced processing of polymer/metal-organic framework composites.

Keywords: metal-organic framework, block copolymer, electrospinning, mixed-matrix membrane, acyl chloride

1. INTRODUCTION

Metal-organic frameworks (MOF) are a relatively new class of highly porous materials that offer unprecedented control of porosity and chemistry.[1-3] By combining metal secondary building units with functionalized organic linkers, a wide variety of structures can be synthesized offering a wide range of properties. Over the past decade, the number of MOFs synthesized has grown, with well over 100,000 structures identified *in silico*.[4] Due to the ability to tune properties of MOFs, a wide range of potential applications have been identified, including gas storage,[5] catalysis,[6] toxic gas removal,[7] and sensing,[8] among others. However, although the chemistry of synthesis has been explored, tangible constructs other than crystalline powders have remained mostly unexplored.

Beyond simple growth of MOF crystallites, there have been some, albeit limited, investigations of hierarchical assembly of MOFs into thin films. MOFs are grown by connecting metal oxide secondary building units with organic linkers—by utilizing similar functional groups, such as oxygen centers, catechols, or carboxylic acids on polymer surfaces, nucleation and growth can occur. Layer-by-layer techniques using self-assembled monolayers have been investigated to create thin films, where MOFs are grown onto substrates, such as gold.[9] While thin films of MOFs are valuable in applications that require incorporating MOFs into devices, composite materials with MOFs on polymer substrates is far more advantageous for processability, flexibility, and reusability of the composite membrane. The two general approaches are the solution blending method (top-down approach), and *in situ* growth of MOFs in polymers (bottom-up approach). Various groups have employed the top-down approach of mixing different polymers with different MOFs. Specifically, the Cohen Group at the University of California has recently investigated using mixing of polyvinylidene fluoride (PVDF) to integrate MOFs into films.[10] The same group has also used polymerization techniques to create pure MOF films, called polyMOFs.[11] Although these techniques show promise, they do not offer the ability to deposit or grow MOFs into hierarchical or systematic patterns.

Of primary importance for incorporating either starting constituents or preformed MOFs into block copolymers (BCP) is the interaction of these chemicals with the polymers. One way of estimating these interactions, and therefore choosing the right constituents and polymer systems, is the use of Hansen Solubility Parameters, which can be used to determine solubility of polymers, solvents, and small molecules within mixtures.[12] The underlying equation is

$$\delta_t^2 = \delta_d^2 + \delta_p^2 + \delta_h^2 , \quad (1)$$

where δ_d = London dispersion parameter, δ_p = polar interaction parameter, and δ_h = hydrogen bonding parameter.

When considering the interaction of two bodies, the interaction radius is calculated according to

$$R^2 = 4 * (\delta_{d1} - \delta_{d2})^2 + \left(\delta_{p1} - \delta_{p2}\right)^2 + (\delta_{h1} - \delta_{h2})^2 \, . \quad (2)$$

Table 1. Hansen solubility radii of select functionalities and polymers.

Functionality	Interaction Radius ($MPa^{0.5}$)				
	PS	PI	PEO	PMMA	PVDF
Aniline (linker)	8.3	13.1	7.5	6.2	9.9
Decane	14.7	1.2	14.1	14.0	3.9
Benzene	5.5	10.9	8.2	5.9	8.5
Perfluoroheptane	21.8	8.3	17.1	18.5	9.2

For example, a benzene or phenyl moiety will interact preferentially with polystyrene (PS) as compared to polyisoprene (PI) within a polystyrene-*block*-polyisoprene-*block*-polystyrene (SIS) BCP. Conversely, a decane moiety will interact preferentially with PI as opposed to PS. Likewise, a polar amine will prefer PEO as opposed to PS. Thus, a MOF can hypothetically be decorated to disperse selectively in BCPs. This behavior should also carry to single polymers – functional groups that interact favorably with polymers will disperse better than those that interact unfavorably. With the appropriate chemistry, functional groups on MOFs can be tuned to take advantage of these interactions. In this work, we focused on the use of acyl chloride chemistry to modify amine linkers on UiO-66-NH_2, as shown in Figure 1.

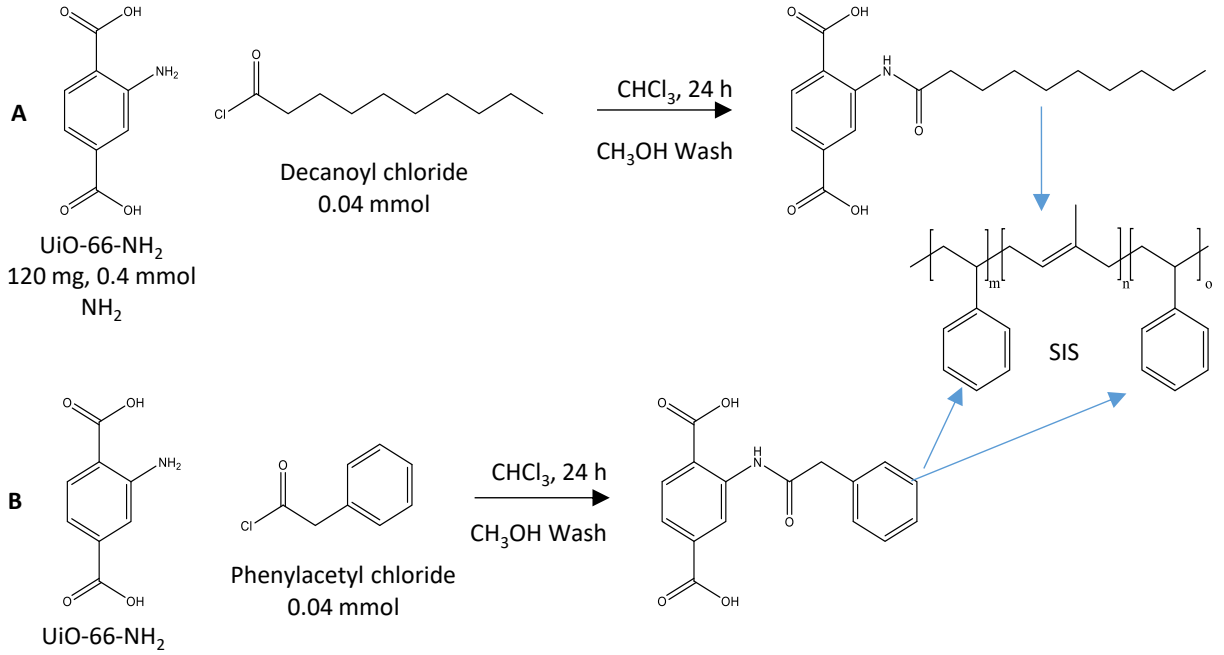

Figure 1. Schematic of the modification of amine linkers using (A) decanoyl chloride and (B) phenylacetyl chloride for preferential incorporation into BCPs.

2. METHODOLOGY

2.1 MOFs

2.1.1 Procurement and synthesis

Two MOFs were investigated in these studies: UiO-66-NH_2 and HKUST-1 (aka CuBTC), the structures of which are shown in Figure 2. The UiO-66-NH_2 was procured from TDA Research, Inc. through a Joint Science and Technology Office-sponsored Rapid Innovation Project. HKUST-1, herein referred to as CuBTC, was synthesized using a

modified procedure from Xin et al.[13] Briefly, 0.25 g (1.0 mmol) $Cu(NO_3)_2 \cdot 3H_2O$ was dissolved in 3 mL of a 1:1:1 (v/v) mixture of dimethylformamide (DMF), ethanol, and H_2O. 0.25 g (0.66 mmol) 1,3,5-benzenetricarboxylate (BTC) was dissolved separately in 3 mL of a 1:1:1 (v/v) mixture of DMF, ethanol, and H_2O. For modified samples, 5-aminoisophthalic acid (AIA) was added at increasing quantities in lieu of BTC such that the sum of AIA and BTC was ~0.66 mmol. Table 2 summarizes the conditions studied for the crystallization of CuBTC and CuBTC_AIA MOFs.

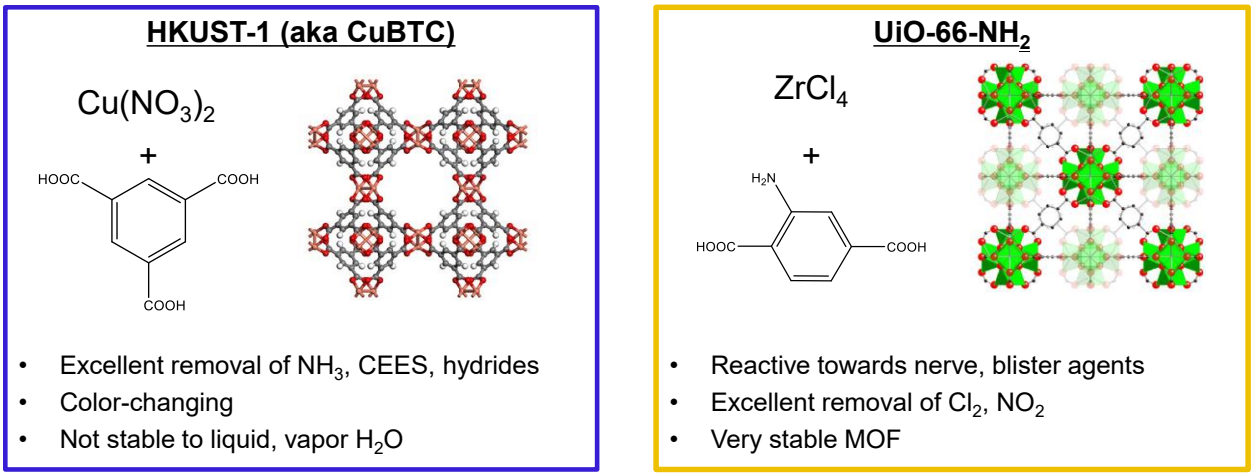

Figure 2. HKUST-1 and UiO-66-NH_2 MOFs.

Table 2. Synthesis conditions for systematic study of CuBTC/AIA growth.

Parameter	Value
mol% AIA*	0, 20, 40, 60 %
Temperature	25, 50, 85 °C
Time	24, 72 hours

*mol% refers to the molar percentage of total linker in solution

2.1.2 Post-synthetic modification

MOFs were modified using acyl chloride reactions with the amine functionality on the organic linker to form amides. This approach has been used previously with some success by Albenze and coworkers.[14] For UiO-66-NH_2, a 10 mol% conversion was targeted so as to leave some amine groups available for further reaction. For each modification, 1 g UiO-66-NH_2 (0.58 mmol based on MW = 1718 g/mol, ~3.5 mmol $–NH_2$ groups) was activated in vacuum at 150 °C for 24 hours and then was dispersed in ~10 mL $CHCl_3$ in a scintillation vial and allowed to equilibrate for 1 hour. 0.065 g (0.34 mmol) decanoyl chloride, 0.053 g (0.34 mmol) phenylacetyl chloride, and 0.08 g (0.34 mmol) perfluorobutyryl chloride were added to separate scintillation vials containing the MOF. The resulting mixture was stirred magnetically at 350 rpm for ~16 hours. For CuBTC_AIA MOFs, 100 % molar conversion was targeted with respect to the amine functionality on the organic linker.

2.2 Polymer

Several polymers were investigated in this effort, including homopolymers and BCPs. Homopolymers were investigated initially to determine appropriate conditions for synthesis and processing as they are cheaper than BCPs. PS (350,000 g/mol), PEO (300,000 g/mol), SIS, PVDF (275,000 g/mol) and PAN (150,000 g/mol) were purchased from Sigma-Aldrich® and used without purification. Table 3 summarizes the solutions that were made for casting films and electrospinning fibers.

Table 3. MOF/polymer solutions made for electrospinning fibers and casting films.

Polymer			MOF***			Solvent	
Type	**Mass (g)**	**w/v***	**Type**	**Mass (g)**	**w/w****	**Type**	**Volume (mL)**
PS	0.75	15 %	UiO-66-NH_2 UiO-66-NH_2-D	0.25	25 %	DMF	5
SIS	0.75	15 %	UiO-66-NH_2 UiO-66-NH_2-D	0.25	25 %	DMF	5
PEO	0.2	4 %	UiO-66-NH_2 UiO-66-NH_2-D	0.05	20 %	H_2O	5
PAN	0.5	10 %	UiO-66-NH_2 UiO-66-NH_2-D	0.17	25 %	DMF	5
PVDF	1.0	22 %	UiO-66-NH_2 UiO-66-NH_2-P	0.11	10 %	DMF, Acetone	4.5
PAN	0.4	10 %	CuBTC CuBTC_40AIA CuBTC_40AIA_D	0.044	10 %	DMF	4
SIS	0.3	10 %	CuBTC CuBTC_20AIA CuBTC_20AIA_D CuBTC_40AIA CuBTC_40AIA_D	0.02	6 %	THF	3

*with respect to solvent
**with respect to polymer
***See Sections 3.1 and 3.2 for nomenclature

2.3 Electrospinning

Electrospinning was conducted using a programmable floor-stand electrospinning unit (MSK NFES-4 by MTI Corporation). Solutions were loaded into 6-mL plastic syringes equipped with a 20-gauge needle. The solutions were pumped at a flow rate of 2 mL/hour onto a rotating mandrel operating at 300 rpm. The electric field was set at approximately 12 kV, but was modified, when necessary, according to perceived solution viscosity.

2.4 Materials characterization

A variety of techniques were used to characterize electrospun nanofibers and films developed. This section summarizes each technique.

2.4.1 Nitrogen isotherm

Nitrogen uptake was measured at 77 K using a Micromeritics® ASAP™ 2040. Samples were off-gassed at 60 °C overnight under vacuum. Surface area measurements were calculated using the Brunauer-Emmett-Teller method, and total pore volumes were calculated at a relative pressure of 0.975 atm.

2.4.2 Powder X-ray diffraction

Powder X-ray diffraction (PXRD) measurements were conducted using a Rigaku Miniflex 600 X-ray powder diffractometer with a D/Tex detector. Samples were scanned at 40 kV and 15 mA using Cu Kα radiation, a scan rate of 5° min^{-1}, over a 2θ range of 3° to 50°. Data were plotted relative to the highest intensity peak and offset on the *y*-axis to show differences between each sample.

2.4.3 Scanning electron microscopy

Scanning electron microscopy (SEM) images were obtained using a Phenom GSR desktop SEM. Samples were supported on double-sided carbon tape and sputter-coated with gold prior to analysis. Typical settings for the instrument used an accelerating voltage of 5 kV at a nominal working distance of 10 mm. Specific operating conditions are listed with each image for clarity.

2.4.4 Attenuated total reflectance-Fourier transform infrared spectroscopy

Attenuated total reflectance-Fourier transform infrared (ATR-FTIR) spectra of materials were collected with a Bruker Tensor 27 FTIR equipped with a Platinum ATR accessory and a single reflection diamond crystal. Sixteen scans over a range of 4000 cm^{-1} to 400 cm^{-1} were averaged with a resolution of 2 cm^{-1}.

2.4.5 Nuclear magnetic resonance spectroscopy

0.7 mL DMSO-d_6 and 50 µL hydrofluoric acid was added to approximately 5 mg of modified UiO-66-NH_2 in a 4-mL vial. The mixture was allowed to stand still until it turned into a clear solution, which indicated that the MOFs had been fully digested. Typical digestion time was approximately 10 min. The solution was then transferred to a nuclear magnetic resonance (NMR) tube and analyzed by ^{1}H NMR spectroscopy. Percent modification was calculated by integrating the aromatic protons of modified and unmodified UiO-66-NH_2 linker. ^{1}H NMR spectra were recorded on a 300 MHz Varian NMR spectrometer using the residual proton resonance of the solvent as the internal standard. DMSO-d_6 and hydrofluoric acid (48–51% solution in water) were purchased from ACROS Organics.

2.4.6 Turbidity

The turbidity of solutions were measured using a Hanna Instruments HI 88713 ISO turbidimeter in accordance with ASTM D7315-17. 10 mg of each sorbent were dispersed in 10 mL of each solvent. Solvents studied were water, dichloromethane, acetone, DMF, THF, cyclohexane, and *n*-hexane.

3. RESULTS AND DISCUSSION

3.1 Modification of UiO-66-NH_2 via acyl chloride chemistry

As described above, it was hypothesized that colloidal particles with similar functionality to polymers should interact more favorably and therefore disperse better in films and fibers. To test this hypothesis, we modified UiO-66-NH_2 with the well-known chemistry of converting amines to amides using acyl chlorides with varying functionalities, as shown in Figure 3.

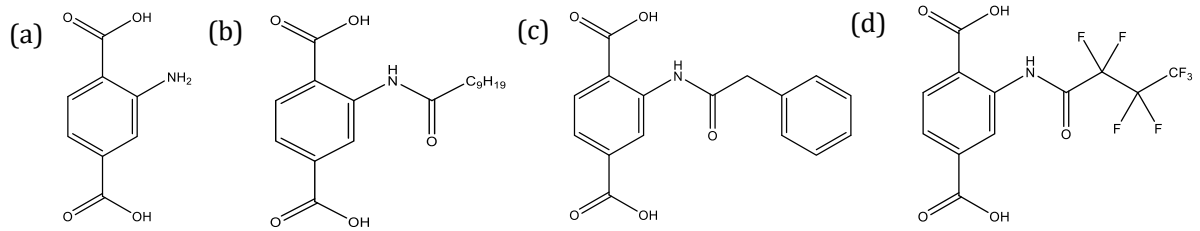

Figure 3. (a) UiO-66-NH_2 linker and modified amides formed from (b) decanoyl, (b) phenylacetyl, and (d) perfluorobutyryl chlorides.

^{1}H NMR was used to determine the conversion of amines to amides for all modified materials. An example spectrum for UiO-66-NH_2-D is shown in Figure 4. The spectrum in Figure 4 was compared to the baseline UiO-66-NH_2 spectrum, and the shift of H_C to H_Z due to amide formation was used to determine the amount of amine groups converted via

$$\%\ Conversion = \frac{Hz}{Hz+Hc}. \quad (3)$$

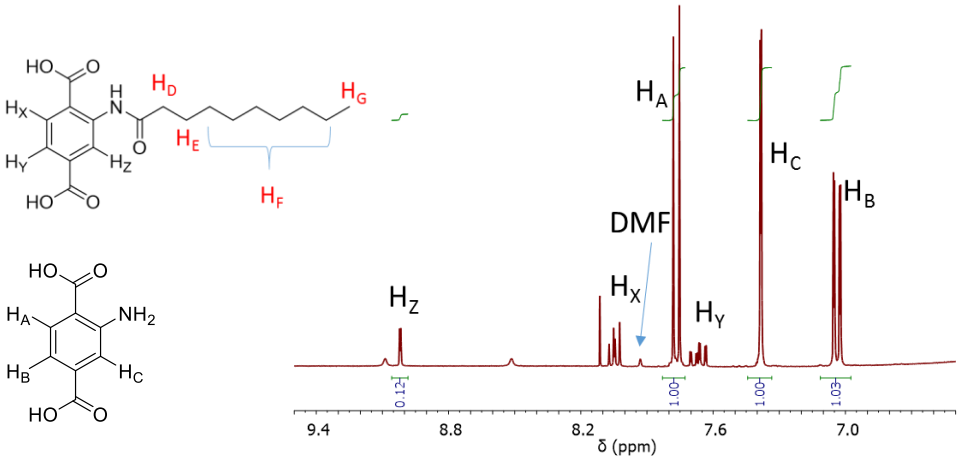

Figure 4. 1H NMR spectra for decanoyl chloride modified UiO-66-NH$_2$.

Conversions for the treatments along with PXRD, ATR-FTIR and nitrogen uptake are shown in Figure 5. PXRD patterns show that UiO-66-NH$_2$ remained intact after all treatments. ATR-FTIR spectra show the transition of a sharp peak to a broad shoulder at ~1685 cm^{-1}, indicative of an amide ν(C=O). Interestingly, the perfluorobutyryl treatment did not show conversion occurring in NMR; however, an amide shoulder appears in the FTIR spectra and C–F bonds are present at ~1210 cm^{-1}. Nitrogen uptake data show that the decanoyl and phenylacetyl chloride treatments led to reduced nitrogen uptake by ~25 % whereas the perfluorobutyryl treatment reduced nitrogen uptake by only 10 %.

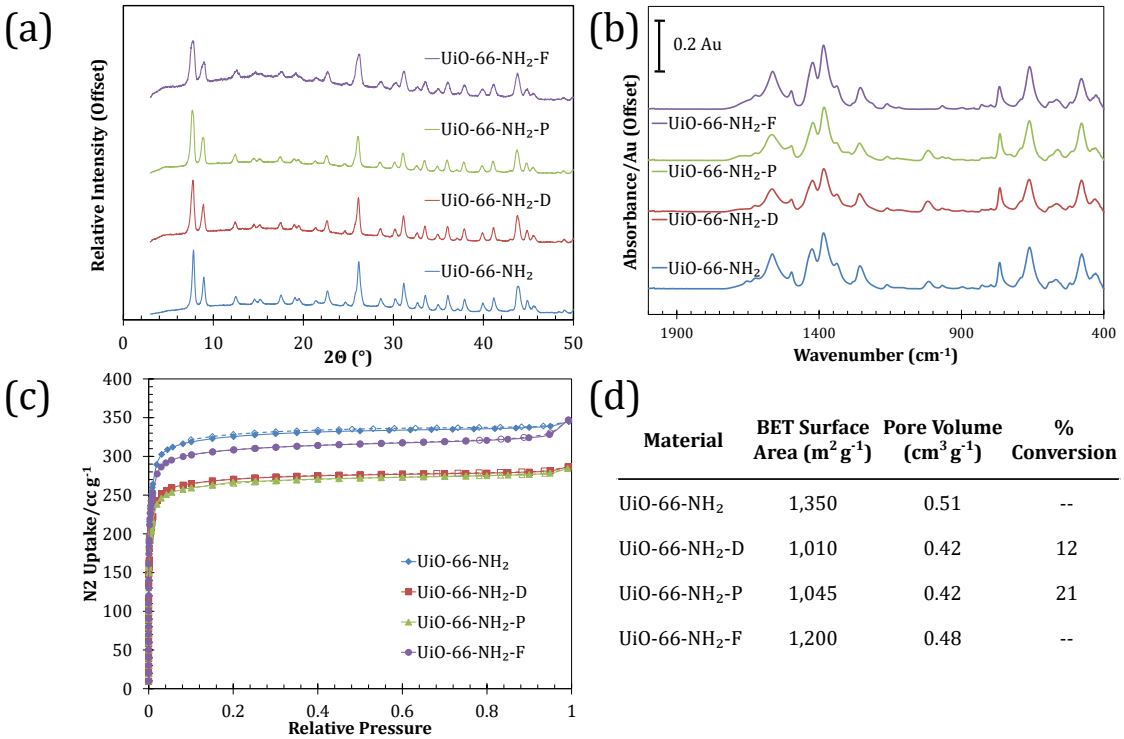

Material	BET Surface Area ($m^2 g^{-1}$)	Pore Volume ($cm^3 g^{-1}$)	% Conversion
UiO-66-NH$_2$	1,350	0.51	--
UiO-66-NH$_2$-D	1,010	0.42	12
UiO-66-NH$_2$-P	1,045	0.42	21
UiO-66-NH$_2$-F	1,200	0.48	--

Figure 5. (a) PXRD, (b) ATR-FTIR, (c) N2 isotherms, and (d) surface area, pore volume, and % conversion for baseline and treated UiO-66-NH$_2$ materials.

The turbidity of modified samples was studied in multiple solvents, including water, dichloromethane, acetone, DMF, THF, cyclohexane, and n-hexane. An example of the data collected in water is shown below in Figure 6. All modified samples result in reduced settling as compared to the baseline MOF. Of particular note is UiO-66-NH$_2$-F, which takes the most time to settle out of solution. The settling times have important implications on MOF/polymer/solvent processing properties – a longer suspension time should equate to better dispersion and processing due to less clumping of colloids in solution.

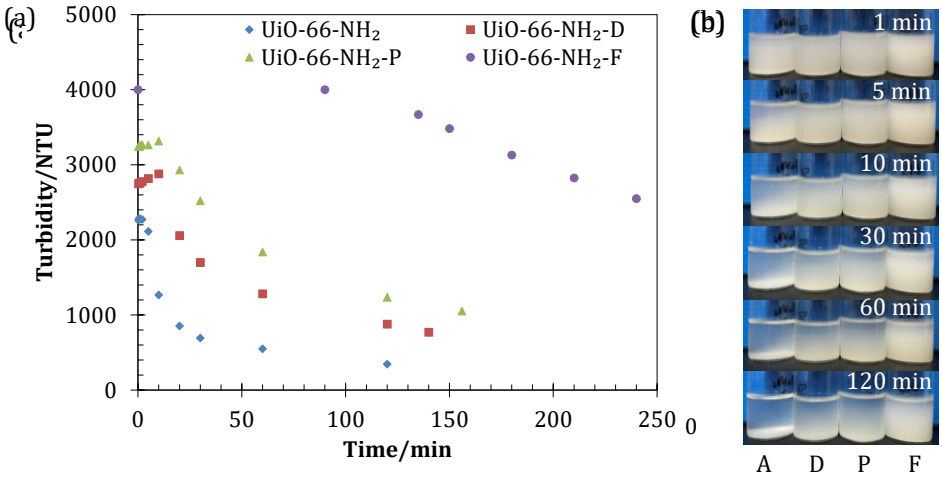

Figure 6. (a) Turbidity data for treated samples in water. (b) Pictures of particle settling as a function of time.

To test this hypothesis, we dispersed baseline and modified MOFs in a variety of films (Figure 7) and electrospun nanofibers (Figure 8). UiO-66-NH_2 shows preferential interaction with similar particles in PS and SIS but disperses much better in PEO. Conversely, UiO-66-NH_2-D disperses well in PS and SIS, but forms ball-like structures in PEO. For electrospun nanofibers, similar trends are seen. UiO-66-NH_2 clumps in both PAN and PVDF polymers during electrospinning whereas decanoyl chloride and perfluorobutyryl chloride samples disperse much more effectively along the polymer fibers.

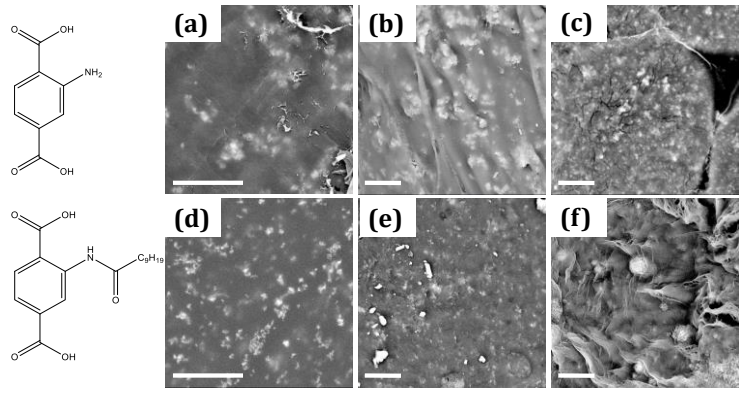

Figure 7. UiO-66-NH_2 dispersed in (a) PS, (b) SIS, and (c) PEO films. UiO-66-NH_2-D dispersed in (d) PS, (e) SIS, and (f) PEO films. Scale bars = 10 µm.

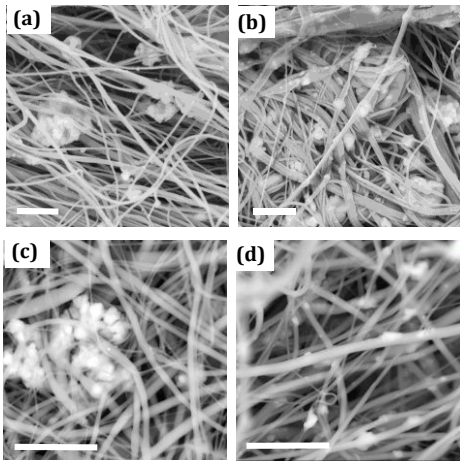

Figure 8. Electrospun PAN nanofibers with (a) UiO-66-NH_2 and (b) UiO-66-NH_2-D. Electrospun PVDF nanofibers with (c) UiO-66-NH_2 and (b) UiO-66-NH_2-P. Scale bars = 10 µm.

3.2 Synthesis of isostructural CuBTC with reactive amine handle for post-synthetic modification

Similar to UiO-66-NH_2, CuBTC is another MOF that has shown promise in a variety of applications. Unfortunately, CuBTC is not stable to moisture nor does it contain a reactive amine group for post-synthetic modification. Thus, this hydrophilic MOF is potentially incompatible with many polymers of interest. To address these shortcomings, AIA was added to the synthesis mixture such that a reactive handle could be added for post-synthetic modification.

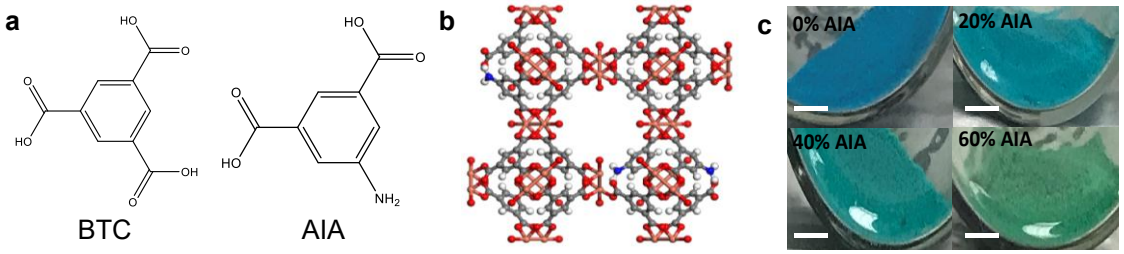

Figure 9. Mixed linkers used to make CuBTC/AIA MOF.

A variety of conditions were investigated as outlined in Section 2.1.1; MOFs synthesized at 25 °C for 72 hours were determined to give the most consistent particle size and were investigated further. As seen in SEM images (Figure 10), the typical octahedral crystal shape is consistent up until 40 mol% AIA, after which a second phase grows in noticeable quantities. Peaks at 8.4 and 10.5 2θ confirmed this new phase and was even more apparent in MOFs grown at higher temperatures. ATR-FTIR spectra lend insight into the structures. The region in blue at ~1625 cm^{-1} associated with ρ(N–H) broadened with increased amount of AIA in the MOF. As the amount of AIA was increased, a broad peak at ~1700 cm^{-1} appeared for the samples synthesized at 25 °C. This was assigned to ν(C=O) from uncoordinated carboxylate groups and indicated that part of the BTC or AIA did not crystalize into the MOF. The peak at 1410 cm^{-1} increased relative to the peak at 1442 cm^{-1} as the amount of AIA increased. As seen in the BTC and AIA spectra, BTC has two peaks from ν(C–O) whereas AIA only has one pronounced peak at ~1410 cm^{-1}. Thus, the increase in the 1410 cm^{-1} peak was consistent with incorporation of AIA into the structure at the expense of BTC. A broad peak at ~1350 cm^{-1} consistent with an aromatic ν(C–N) also appeared with increased amount of AIA. Nitrogen uptake of the MOFs indicated that incorporation of AIA reduced nitrogen uptake, but materials up to 40 % AIA still had a high surface area.

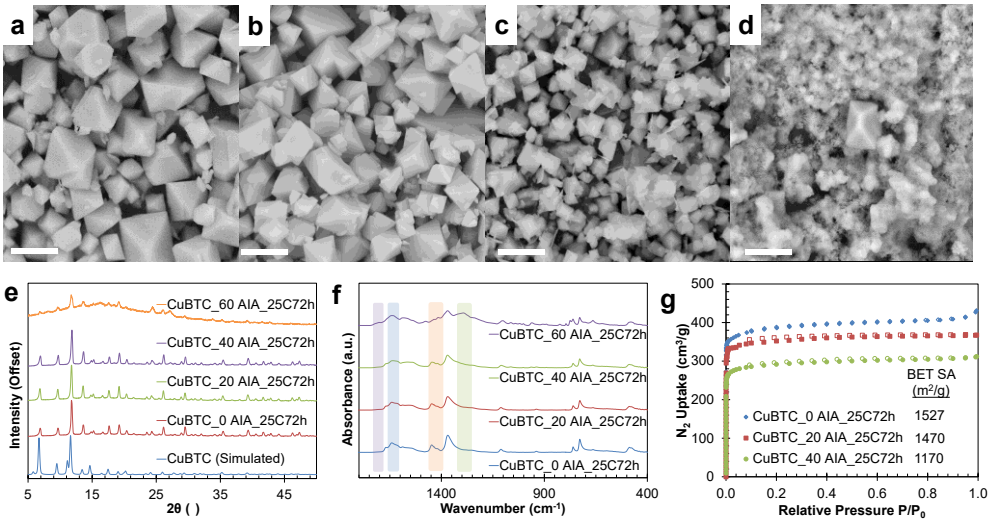

Figure 10. SEM images of CuBTC grown at 25 °C for 72 hours with (a) 0 %, (b) 20 %, (c) 40 %, and (d) 60 % AIA incorporated. Scale bar = 10 µm. (e) PXRD, (f) ATR-FTIR, and (g) N_2 isotherms for the same samples.

The successful synthesis of CuBTC containing AIA allowed for further modification with decanoyl chloride, as shown in Figure 11. The modifications were successful as seen by changes of primary amine bend (blue region) to an amide carbonyl stretch (red region). No acyl chloride is left as evidenced by a lack of carbonyl peak at 1800 cm^{-1} (green region); however, it is possible that some of the acyl chloride hydrolyzed or partially destroyed the structure with the appearance of a carboxylic carbonyl peak at ~1700 cm^{-1} (orange region).

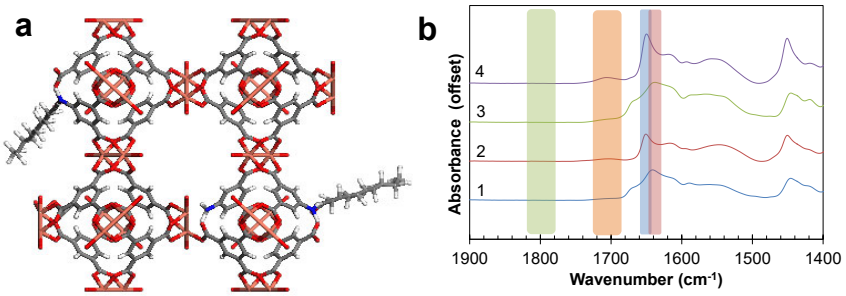

Figure 11. (a) Modification of amine group of CuBTC_AIA with decanoyl chloride. (b) ATR-FTIR spectra of (1) CuBTC_20AIA, (2) CuBTC_20AIA_D, (3) CuBTC_40AIA, and (4) CuBTC_40AIA_D. All MOFs were synthesized at 25 °C for 72 hours.

Baseline and modified CuBTC were subsequently electrospun with PAN and cast into films with SIS. SEM images are shown in Figure 12. For both form factors, the baseline CuBTC has low compatibility with the polymer as seen by large gaps/defects. Incorporation of the AIA moiety improves compatibility with PAN, but still has large defects in SIS films. The decanoyl chloride-modified CuBTC/AIA sample shows excellent compatibility with PAN and improved compatibility with SIS. It is thought that further optimization of the modification procedure (for example, selective deposition of AIA as an outer shell on CuBTC) will lead to even better compatibility.

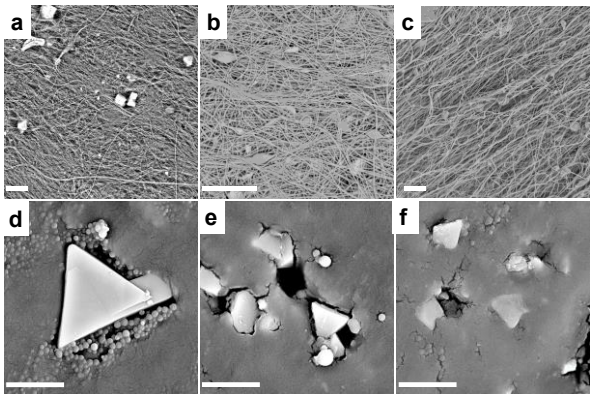

Figure 12. Electrospun PAN nanofibers in (a) CuBTC_0AIA, (b) CuBTC_40AIA, and (c) CuBTC_40AIA_D. Scale bar = 30 µm. SIS films in (d) CuBTC_0AIA, (e) CuBTC_40AIA, and (f) CuBTC_40AIA_D. Scale bar = 8 µm.

4. CONCLUSIONS

The use of acyl chloride chemistry to convert amines to functional amides on MOF linkers was taken advantage of to improve MOF-polymer compatibility. In the first case study, aliphatic, aryl, and fluorinated acyl chlorides were reacted on UiO-66-NH_2 and resulted in materials with enhanced colloidal properties in a variety of solvents as well as improved dispersion in polymers such as PS, SIS, and PVDF. In a second case study, a new MOF isostructural to CuBTC incorporating 5-aminoisophthalic acid was synthesized and subsequently modified with decanoyl chloride. The new modified MOFs showed enhanced compatibility with PAN nanofibers and SIS films. These techniques will be used in subsequent studies to selectively deposit MOFs into specific copolymer domains.

ACKNOWLEDGMENTS

Funding was provided by the U.S. Army via the In-house Laboratory Independent Research Program (PE 0601101A Project 91A) at the Edgewood Chemical Biological Center. The author thanks Dr. Hui Wang (CBR Filtration Branch), Dr. John Mahle (CBR Filtration Branch), Dr. Trent Tovar (National Research Council Post-doctoral research associate, CBR Filtration Branch) and Kathleen Au (College Qualified Leaders summer intern, University of Maryland, Baltimore County) for experimental support. The author thanks Prof. Thomas H. Epps, III from the University of Delaware for providing research guidance.

REFERENCES

[1] Eddaoudi, M.; Kim, J.; Rosi, N.; Vodak, D.; Wachter, J.; O'Keeffe, M.; Yaghi, O.M. Systematic design of pore size and functionality in isoreticular MOFs and their application in methane storage. *Science.* **2002,** *295* (5554), pp 469–472.

[2] Eddaoudi, M.; Li, H.L.; Yaghi, O.M. Highly porous and stable metal-organic frameworks: Structure design and sorption properties. *J. Am. Chem. Soc.* **2000,** *122* (7), pp 1391–1397.

[3] Cavka, J.H.; Jakobsen, S.; Olsbye, U.; Guillou, N.; Lamberti, C.; Bordiga, S.; Lillerud, K.P. A new zirconium inorganic building brick forming metal organic frameworks with exceptional stability. *J. Am. Chem. Soc.* **2008,** *130* (42), pp 13850–13851.

[4] Wilmer, C.E.; Leaf, M.; Lee, C.Y.; Farha, O.K.; Hauser, B.G.; Hupp, J.T.; Snurr, R.Q. Large-scale screening of hypothetical metal-organic frameworks. *Nat. Chem.* **2011,** *4* (2), pp 83–89.

[5] Suh, M.P.; Park, H.J.; Prasad, T.K.; Lim, D.W. Hydrogen storage in metal-organic frameworks. *Chem. Rev.* **2012,** *112* (2), pp 782–835.

[6] Corma, A.; Garcia, H.; Llabres i Xamena, F.X. Engineering metal organic frameworks for heterogeneous catalysis. *Chem. Rev.* **2010,** *110* (8), pp 4606–4655.

[7] DeCoste, J.B.; Peterson, G.W. Metal-organic frameworks for air purification of toxic chemicals. *Chem. Rev.* **2014,** *114* (11), pp 5695–5727.

[8] Kreno, L.E.; Leong, K.; Farha, O.K.; Allendorf, M.; Van Duyne, R.P.; Hupp, J.T. Metal-organic framework materials as chemical sensors. *Chem. Rev.* **2012,** *112* (2), pp 1105–1125.

[9] Shekhah, O.; Wang, H.; Kowarik, S.; Schreiber, F.; Paulus, M.; Tolan, M.; Sternemann, C.; Evers, F.; Zacher, D.; Fischer, R.A.; Woll, C. Step-by-step route for the synthesis of metal-organic frameworks. *J. Am. Chem. Soc.* **2007,** *129* (49), pp 15118–15119.

[10] Denny, M.S., Jr.; Cohen, S.M. In Situ Modification of Metal-Organic Frameworks in Mixed-Matrix Membranes. *Angew. Chem., Int. Ed. Engl.* **2015,** *54* (31), pp 9029–9032.

[11] Zhang, Z.; Nguyen, H.T.; Miller, S.A.; Cohen, S.M. polyMOFs: A Class of Interconvertible Polymer-Metal-Organic-Framework Hybrid Materials. *Angew. Chem., Int. Ed. Engl.* **2015,** *54* (21), pp 6152–6157.

[12] Hansen, C.M. Universality of Solubility Parameter. *Ind. Eng. Chem. Prod. Res. Dev.* **1969,** *8* (1), pp 2–11.

[13] Xin, C.L.; Zhan, H.J.; Huang, X.; Li, H.G.; Zhao, N.; Xiao, F.K.; Wei, W.; Sun, Y.H. Effect of various alkaline agents on the size and morphology of nano-sized HKUST-1 for CO2 adsorption. *Rsc Adv.* **2015,** *5* (35), pp 27901–27911.

[14] Venna, S.R.; Lartey, M.; Li, T.; Spore, A.; Kumar, S.; Nulwala, H.B.; Luebke, D.R.; Rosi, N.L.; Albenze, E. Fabrication of MMMs with improved gas separation properties using externally-functionalized MOF particles. *J. Mater. Chem. A.* **2015,** *3* (9), pp 5014–5022.

Epigenetic "memory" during bacterial adaptation to environmental changes

Alena M. Calm, Gabrielle M. Rizzo, Trevor G. Glaros, Henry S. Gibbons*
U.S. Army Edgewood Chemical Biological Center, Research & Technology Directorate,
8198 Blackhawk Rd, Aberdeen Proving Ground, MD 21010

ABSTRACT

Bacteria encounter numerous stresses in the environment for which they must respond rapidly and appropriately to in order to insure survival. *Salmonella typhimurium,* an enteric bacterium, survives a variety of hostile environments in the stomach, intestinal tract, and gastric-associated lymphoid tissue during infection by coordinating and modulating gene expression patterns critical for survival. We hypothesized that *S. typhimurium* retains epigenetic "memories" of prior growth conditions that influence virulence gene expression even upon transfer to a new environment, and that these heritable DNA methylation patterns, epigenetic mechanisms, or both, affect protein expression long after any triggering stimulus is removed. Using a simple *in vitro* model of adaptation to intracellular conditions, we asked whether protein expression patterns differed after bacterial populations grown in a different media were shifted to a common medium. Using high-coverage liquid chromatography-tandem mass spectrometry-based proteome analysis, we compared abundance of proteins from cultures originally grown in Luria-Bertani broth and high-Mg^{2+} minimal media and subsequently transferred to a liquid culture continuously grown in low-Mg^{2+} medium. While the majority of proteins were unaffected, a small subset of proteins including two chemotaxis receptors and portions of the phosphorelay system involved in nutrient sensing and chemotaxis were found to be more highly expressed in LB- and high-Mg^{2+}-derived cultures. Enteric pathogens represent a significant impediment to battlefield readiness,[1] understanding the effects of culture conditions prior to infection on expression of virulence factors may provide insights into the infectious process and yield new forensic biomarkers that facilitate differentiation of lab-grown from wild-acquired bacterial infections.

Keywords: epigenetics, *Salmonella typhimurium,* virulence factors, microbial forensic signatures, proteomics, DNA methylation, serial passage

1. INTRODUCTION

During the life and infection cycle of bacterial pathogens, sudden changes in the ambient environment are routine, resulting in metabolic, physical, and oxidative stresses on the organism as it transits from one environmental niche to another. The Enterobacterium *Salmonella enterica* serovar Typhimurium—commonly referred to as *S. typhimurium*—has served as a robust, well-characterized model organism for both intestinal and systemic infection modes, mimicking the symptoms and disease course of Typhoid fever in the mouse model.[2] During the course of infection, *S. typhimurium* must pass from the extremely acidic environment of the stomach to the basic, oxygen-poor, microbe-rich and hyperosmotic environment of the intestinal tract, to the hostile, acidic, magnesium (Mg^{2+})-depleted, iron-poor, and inherently antimicrobial environment of the macrophage phagolysosome.[3] In addition to its life cycle in the mammalian host, *S. typhimurium* encounters many external environmental stresses, as it can persist in soils and infect plant leaves, seeds, and fruits.[4] Throughout this cycle, the organism survives by coordinating gene and protein expression patterns to insure rapid and appropriate adaptation to new environments. The orderly progression during the mammalian infection cycle is likely to contrast dramatically with the highly variable outdoor environment, in which the passage from one condition may be seemingly random as a bacterium encounters nutrient-rich conditions, predation by amoeba, infection of alternative vertebrate hosts, dilute and ion-poor conditions, etc. Thus, it is likely that coordinated gene expression patterns during a given stage of mammalian infection might be influenced by previous conditions, thereby decreasing the likelihood of triggering a niche-inappropriate pattern of gene expression during subsequent phases of infection. We hypothesized *S. typhimurium* preserves a "memory" of previous growth conditions that can influences subsequent gene and protein expression patterns. Here, we report elevated expression

of several proteins in the *S. typhimurium* chemotaxis and motility system that is detectable over at least 10 doublings following a shift from growth in two different media into a single common medium. If confirmed during the upcoming project period, we believe that this observation would represent the first report of potential long-term hysteresis or "memory" in the chemotaxis signaling pathway.

2. MATERIALS AND METHODS

2.1 Culturing and passaging

S. typhimurium strain SL1344 was streaked out onto Luria-Bertani broth (LB) agar and incubated overnight at 37 ºC. From the plate, a single colony was selected and used to inoculate 10 mL cultures in 50 mL conical tubes (CELLTREAT®, Inc.) in triplicate. The following media was used for three different culture conditions in triplicate: LB, and two variations of N-minimal medium[5]: high-magnesium (HMg) containing 100 mM HEPES pH 7.5, 10 mM $MgCl_2$, 1X N-minimal salts, 0.1% casamino acids, 0.4 % glucose; and low-magnesium (LMg) containing 100 mM MES pH 6.0, 8 µM MgCl2, 1X N-minimal salts, 0.1 % casamino acids, 0.4 % glucose). The cultures were incubated at 300 rpm and 37 ºC. After 24 hours in culture, 10 µL of each culture was used to inoculate a fresh 10-mL culture, in the same media (1:1,000 dilution). Cultures were grown as before. After 24 hours in culture, all tubes were collected and centrifuged at 4, 000 rpm (3,320 x g) on a table-top centrifuge for 20 minutes. All pellets were suspended in 25 mL LMg media, centrifuged as before, and suspended in 10 mL of LMg media. 250 µL of the washed bacteria were then used to inoculate 250 mL of LMg media in 1 L Nalgene® (Thermo Fisher Scientific, Inc.; Waltham, MA) non-baffled plastic flasks with vent cap, in triplicate. They were cultured as before, but the agitation was adjusted to 250 rpm in a floor-model shaking incubator. After 24 hours, all cultures were collected by centrifugation and washed 3 times in sterile PBS (Thermo Fisher Scientific, Inc.; Waltham, MA). Before the last wash, cultures were split 5 ways so that for each replicate there were 5 x 50-mL tubes of washed bacteria. A 1.8-mL tube was also collected for each replicate for use in the QIAGEN® AllPrep® purification. All of the collected samples were centrifuged and the pellets were snap frozen on liquid nitrogen and stored at -80 ºC. The tubes were all labeled to capture their replicate number as well as their original culture condition and how many times they were passaged into LMg media (i.e., LB1 P_0, LB2 P_0, LB3 P_0, LMg 1 P_0, etc.). In two experiments, cultures were collected after the first transfer into LMg-minimal media (P_0). In a third experiment, cultures were passaged four times (to P_4) in the LMg media. In the latter case, cultures were diluted 1:1,000 every 24 hours by transferring 250 µL of the culture directly into the fresh medium without washing. Cultures were not washed between passages, and a 1:1,000 dilution passage was performed into fresh media. Cultures were always grown for 24 hours between passages.

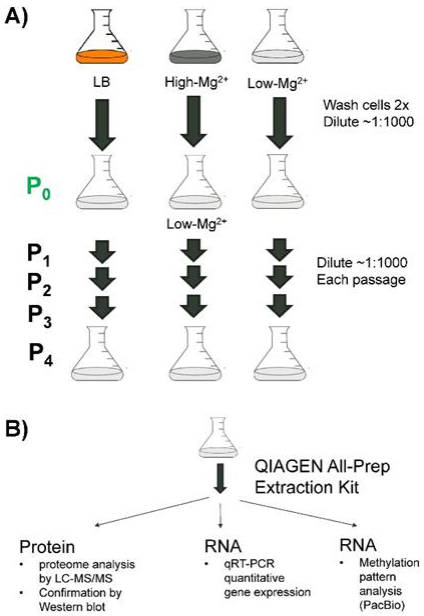

Figure 1. Experimental scheme. A) Growth and passaging scheme for *S. typhimuirium* cultures. B) Single sample utilized for extraction of nucleic acids and proteins.

2.2 Extraction of nucleic acids and protein

The AllPrep® Bacterial DNA/RNA/Protein Kit (QIAGEN®) was utilized for the extraction of protein and nucleic acids from bacterial cell cultures. A 1.8-mL sample of culture was collected, centrifuged, and pellets were snap frozen and stored at -80 °C. Tubes were thawed and re-suspended according to the manufacturer's instructions. All purified samples were collected and stored at -80 °C.

2.3 Cell lysis for proteomic analysis

Bacterial pellets were each resuspended in 500 µL lysis buffer (4 % SDS [Sigma-Aldrich®; St. Louis, MO] + 25 mM Tris HCl pH 7.6 [Bioland Scientific, LLC; Paramount, CA]), then transferred into Eppendorf® protein LoBind tubes and boiled at 95 °C for 5 minutes. Each sample was then lysed using a Branson probe sonicator set at 50 % power with a pulse setting of 5 seconds on, 5 seconds off, for a total of 25 seconds. Lysates were then clarified via centrifugation at 21,130 x g for 10 minutes, and the clarified lysates were transferred into new LoBind tubes. The protein concentration of each sample was determined using a Pierce™ BCA® protein assay kit, and 1 mg was removed from each sample for digestion.

2.4 Filter-aided sample preparation digestion

Dithiothreitol (DTT) (Sigma-Aldrich®; St. Louis, MO) was added to each sample to a final concentration of 10 mM. Samples were then boiled at 90 °C for 15 minutes, then cooled to room temperature. Amicon® 15 mL 10K molecular weight cut-off filter units were pre-washed with 4 mL UA buffer (8 M urea [Thermo Scientific™] + 100 mM Tris HCl pH 8.6 [Bioland Scientific, LLC; Paramount, CA]) and spun down at 3,220 x g for 20 minutes. The 1-mg samples were then transferred into respective filter units. 10 mL UA buffer were added to each unit, and they were spun for 30 minutes. 100 µL of 0.5 M iodoacetamide (Sigma-Aldrich®; St. Louis, MO) were added to each filter, and the samples incubated in the dark at room temperature for 30 minutes. Filter units were then centrifuged for 20 minutes, then washed two times with 4 mL UA buffer and centrifuged for 20 minutes both times, to remove iodoacetamide. Following the second rinse, 4 mL of 0.1 M triethylammonium bicarbonate (TEAB) (Sigma-Aldrich®; St. Louis, MO) was added to each filter and centrifuged for 20 minutes. This wash step was repeated 2 times. Lyophilized trypsin (Promega Corporation; Madison, WI) was resuspended to a concentration of 1 µg/µL in 50 mM TEAB and 17 µL was deposited into each 1-mg sample for a protein:enzyme ratio of ~60:1. The top of each filter unit was wrapped in Parafilm® M and incubated overnight at 37 °C.

2.5 Desalting and creating master mix sample

The next day, the filter units were cooled to room temperature and the filtrates were transferred to separate LoBind tubes. Each filter was then rinsed with 50 µL of 50 mM TEAB twice and 50 µL of 0.5 M NaCl (Sigma-Aldrich®; St. Louis, MO) once. Each rinse was pooled together with their respective sample, and then each sample was acidified with 10 % formic acid to a final concentration of 1 %. Oasis HLB 1-cc 30 mg SPE cartridges (Waters Corporation; Milford, MA) were used for desalting. The cartridges were attached to a vacuum apparatus and activated by adding 1 mL activation buffer (50 % water + 50 % acetonitrile (ACN)); the activation step was repeated once more. The columns were then washed twice each with 1 mL wash buffer (5 % ACN + 0.5 % trifluoroacetic acid in water) and each column was then loaded with their respective sample. Columns were then rinsed twice with wash buffer, followed by elution with 1 mL elution buffer (70 % ACN + 30 % water). Eluents were collected in clean LoBind tubes and 30 µL of each desalted eluent was taken and combined into a master mix tube. The master mix is intended to normalize samples across all 5 passages in order to form a vertical comparison of P_0–P_4. All samples, including the master mix, were dried down in a Savant™ SpeedVac™ (Thermo Fisher Scientific, Inc.; Waltham, MA) and resuspended in 30 % ACN + 70 % water to ~2 mg/mL (estimated concentration based on initial protein assay results). A Thermo Scientific™ Pierce™ Quantitative Colorimetric Peptide Assay kit was used to assess peptide concentration of each sample. 30 µg of each sample was transferred into LoBind Eppendorf® tubes and 30% ACN + 70% water was added to each sample to reach 45 µL total volume. An additional 5 µL of 1 M TEAB was then added to each sample for a final concentration of 30 µg in 50 µL. For the master mix sample in particular, 12 of these 30-µg aliquots were made.

2.6 Tandem Mass Tag labeling

The 30-µg aliquots were each labeled using a 5 mg Thermo Scientific™ TMT10plex™ Isobaric Label Reagent Set following the manufacturer's instructions. Briefly, each tag was resuspended in 256 µL 100 % ACN (DriSolv®), and 20 µL of each tag was mixed with its corresponding sample (see labeling scheme below). For the master mix sample,

all 12 aliquots were labeled in this fashion; 5 master mix aliquots were then paired with each of the 5 passages. After labeling samples in accordance with the manufacturer's instructions, each passage was pooled together. The 5 pools were then dried down.

2.7 Basic reverse phase fractionation

Each pool underwent basic reverse phase fractionation on an XBridge C18 5 µm, 4.6 x 250 mm column (Waters Corporation; Milford, MA). A 65-minute gradient from 100 % mobile phase A (10 % ACN + 90 % water + 20 mM ammonium formate, pH 10) to 100 % mobile phase B (90 % ACN + 10 % water + 20 mM ammonium formate, pH 10) was run, and fractions were collected. Following fractionation, the fractions were concatenated into 3 early "Start" fractions, 28 mid-phase fractions, and 5 late "End" fractions. These fractions were acidified with 100 µL of 10 % formic acid, then dried down and resuspended in 20 µL 5 % ACN + 0.1 % formic acid in water, and finally transferred into autosampler vials. The three "Start" fractions and five "End" fractions were combined into respective vials, for a total of 30 samples. This was repeated for all five passage pools.

2.8 Q Exactive™ analysis

The 30 fractions of each passage (a total of 150 fractions) were analyzed on a Thermo Scientific™ Q Exactive™ Plus mass spectrometer on a Thermo Scientific™ EASY-Spray™ column (PepMap RSLC C18, 2 µm, 100 Å, 75 µm x 50 cm). Each fraction was run on a 182-minute gradient from 95 % buffer A (0.1 % formic acid in water) to 90 % buffer B (80 % ACN + 90 % water + 0.1 % formic acid), and then back to 95 % buffer A. Full MS resolution was set at 70,000 with a scan range of 300 to 1,700 *m/z*, and data-dependent MS/MS resolution was set at 35,000.

2.9 Data analysis

The proteomics data software PEAKS® Studio 8.5 (Bioinformatics Solutions, Inc.; Waterloo, ON, Canada) was used to process the 150 raw files collected from P_0–P_4 MS analysis. The master mix sample from each passage was used to normalize data between passages to create a vertical comparison between them. The LMg sample from P_0 was used as the base sample, and the LMg channel 129C from P_0 in particular was used as the reference label, so that all expression ratios compare the HMg and LB media conditions of every passage to the LMg media condition from P_0. ANOVA-significant proteins (with false-discovery rate set to 1 %) were selected and their expression levels were monitored within each media type and through each passage.

2.10 Methods for sample prep and analysis of P_0 triplicates

Two additional sets of P_0 bacterial pellets were processed as described above. These P_0 samples were not passaged further, and so a master mix sample was not assembled for them. The two P_0 sets were labeled with two separate Thermo Scientific™ TMT10plex™ Isobaric Label Reagent Sets and were compared to the P0 pellets from the P_0–P_4 sample set. To perform this comparison, the master mix channel 131 was removed from the data analysis software, so that only the triplicates of LMg, HMg, and LB conditions were observed in each P_0. ANOVA-significant proteins (with a false-discovery rate of 1 %) that showed a 2-fold or greater expression change when comparing LB or HMg media to LMg media were selected. These proteins were further filtered to include only those that were present in all three P_0 sets, as they were presumed to be the most highly reproducible. These proteins' expression patterns were then observed in the larger P_0–P_4 data set.

3. RESULTS

To test our hypothesis, we designed a simple *in vitro* experimental scheme (Figure 1) in which bacterial populations grown in several media types were passaged into a low-Mg^{2+} medium that is designed to mimic phases of the host infection cycle.[5] Briefly, the laboratory strain of *S. typhimurium* SL1344 was grown in rich medium (LB) and in two variants of a glucose minimal medium containing either mM or µM concentrations of Mg^{2+} (HMg and LMg media, respectively). In addition to the variance in Mg^{2+} concentrations, the HMg media also is moderately alkaline (pH 7.5), whereas the LMg medium is moderately acidic (pH 6.0). The HMg medium represses genes involved in the intracellular lifecycle, whereas the LMg media condition mimics the phagolysosomal life stage of *S. typhimurium.* during its intracellular stage, the bacterium encounters an environment rich in antimicrobial compounds—including

antimicrobial peptides, reactive oxygen, and nitrogen species—and poor in divalent cations, iron, and other important nutrients. Micromolar concentrations of Mg^{2+} are known to induce expression of the major intracellular virulence regulon of *S. typhimurium*,[6] which is regulated by the PhoP/PhoQ 2-component response regulator system.[7] We passaged all three cultures by diluting 1:1,000 into LMg, grew them for several generations to optical densities (OD_{600}) of 0.3–0.5, and examined their protein profiles by LC-MS/MS-based proteomics.

We developed an isobaric tagging method based on tandem mass tagging (TMT) labeling (Figure 2). This technique allows us to quantitate simultaneously the abundance of proteins in three biological replicates in each of three experimental conditions. A "master mix" was generated by mixing equal amounts of all samples from a single experiment together. The abundance of a given protein in each individual sample was normalized to the abundance in the "master mix." We analyzed a large number of biological replicates and experimental conditions within each experiment, normalized each sample to the master mix, and repeated the entire experiment three times (to P_0) to increase our statistical confidence in the results. However, the large number of samples, fractions, and spectra generated for this forced us to work with the manufacturer of the PEAKS® Studio software (Bioinformatics Solutions, Inc.; Waterloo, ON, Canada) used to analyze the dataset to accommodate the many thousands of spectra generated per file. For example, in the four-passage experiment, a total of ~10^6 MS_1 spectra; ~10^7 MS_2 spectra; 143 GB of total data had to be analyzed.

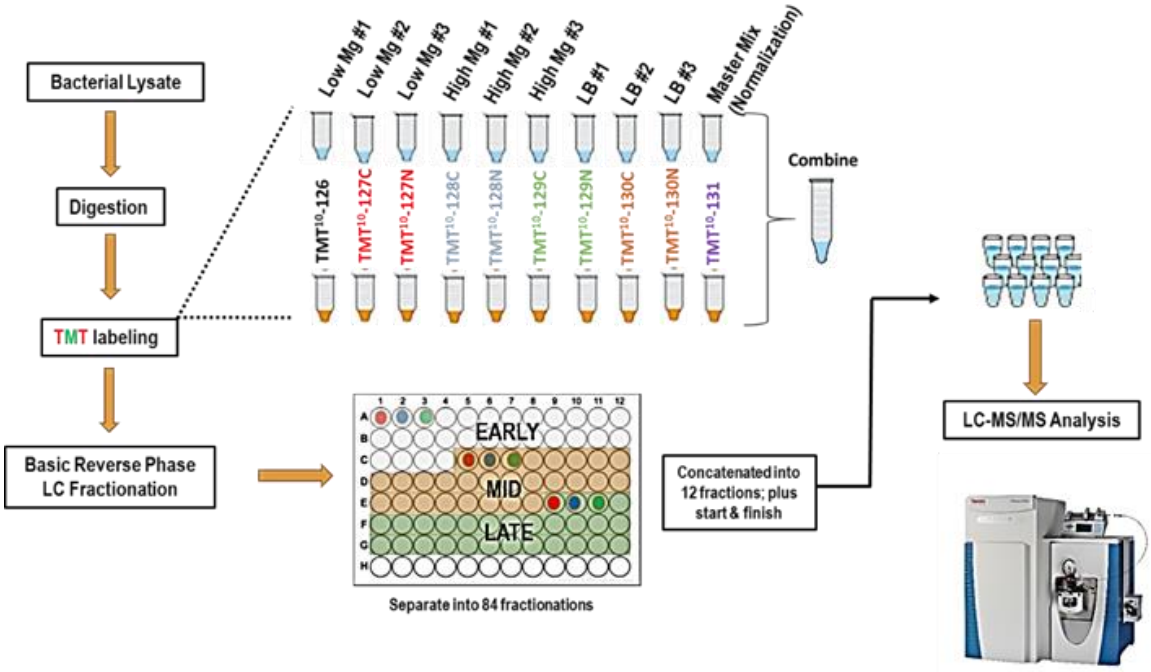

Figure 2. Proteomic extraction, labeling, and analysis pipeline.

We initially analyzed protein abundances after the first growth in minimal medium (P_0). The results of three independent experiments each performed in triplicate are summarized in Figure 3. To identify proteins whose abundance was significantly altered in each experiment, we set a threshold of > 2-fold change and set a false-discovery rate of 1 % by ANOVA. In these experiments, a small subset of proteins identified met the strict standards. We identified proteins whose abundance changed in two of the three experiments (17 proteins, or 30.9 % of identified proteins) and in all three experiments (6 proteins; 10.9 %).

Initially, we had no *a priori* reason to believe that any of these proteins would be differentially induced in LMg conditions encountered by strains grown in all three pre-transfer conditions. The observation that this was not the case pointed to the possibility that physiological or chromosomal changes occur during growth in the pre-transfer stage that influence subsequent protein expression patterns, even after multiple generations.

A)

		P0 Abundance Ratios					
		Rep 1		Rep 2		Rep 3	
UniProt ID	Gene symbol	LB/LMg	HMg/LMg	LB/LMg	HMg/LMg	LB/LMg	HMg/LMg
A0A0H3NL96	*tsr*	6.56	2.89	2.16	1.20	4.08	2.08
A0A0H3NDZ5	*cheA*	4.45	2.27	3.12	1.48	4.13	2.30
A0A0H3NAF5	*envE*	0.46	0.64	0.51	0.74	0.43	0.59
A0A0H3NMQ9	*tcp*	2.30	1.48	3.33	1.54	3.99	2.00
A0A0H3NE38	*fliG*	11.09	4.85	3.66	1.69	8.32	4.58
A0A0H3NCE6	*cheB*	6.34	3.00	3.01	1.56	3.14	1.89

B)

		Rep 2 Abundance Ratios							
		P0		P1		P2		P3	
UniProt ID	Gene symbol	LB/LMg	HMg/LMg	LB/LMg	HMg/LMg	LB/LMg	HMg/LMg	LB/LMg	HMg/LMg
A0A0H3NL96	*tsr*	2.16	1.20	0.32	0.30	0.93	0.99	1.45	1.09
A0A0H3NDZ5	*cheA*	3.12	1.48	0.19	0.20	0.93	1.07	1.63	1.15
A0A0H3NAF5	*envE*	0.51	0.74	2.05	2.00	3.20	2.87	1.88	1.37
A0A0H3NE38	*fliG*	3.66	1.69	0.22	0.23	0.77	0.93	1.26	1.16
A0A0H3NCE6	*cheB*	3.01	1.56	0.30	0.33	0.93	1.15	1.44	1.14

	≤ 0.5
	≥ 2.0

Figure 3. Proteins differentially expressed in P_0 after (A) the first transfer into low-Mg2+ media, and (B) after subsequent passages in low-Mg2+ media.

It was particularly notable that proteins involved in chemotaxis and motility (Tsr, CheA, Tcp, FliG, CheB) represented five of the six proteins identified as differentially expressed in all three experiments. We therefore examined those proteins found to be differentially expressed in two of the three experiments. Indeed, of 11 proteins found in two of three experiments, eight are in the same general functional category. The identity and function of the proteins identified are found in Table 1.

Table 1. Identity and function of differentially expressed proteins.

UniProt ID	Protein	Function	Experiments
A0A0H3NL96	Tsr	Methyl-accepting chemotaxis protein receptor component	1,2,3
A0A0H3NDZ5	CheA	Chemotaxis protein CheA	1,2,3
A0A0H3NAF5	EnvE	Envelope protein, unknown function	1,2,3
A0A0H3NMQ9	Tcp	Methyl-accepting chemotaxis citrate transducer	1,2,3
A0A0H3NE38	FliG	Flagellar motor switch protein	1,2,3
A0A0H3NCE6	CheB	Chemotaxis response regulator protein-glutamate methylesterase	1,2,3
A0A0H3NBQ0	OmpD	Outer membrane protein	1,2
A0A0H3NMF2	CheZ	Protein phosphatase	1,2
A0A0H3NYG4	SpvD	Salmonella plasmid virulence protein	1,2
A0A0H3NJ67	SlsA	Uncharacterized protein	1,2
A0A0H3NDU3	CheV	Hypothetical receptor/regulator protein	1,2
A0A0H3NXF9	SpvR	Salmonella plasmid virulence lysR family regulator	1,3
A0A0H3NS32	FolB	7 8-dihydroneopterin aldolase	1,3
A0A0H3NGY0	Trg	Methyl-accepting chemotaxis protein III	2,3
A0A0H3NG60	SL1344_3189	Methyl-accepting chemotaxis protein II	2,3
A0A0H3NMF8	CheW	Purine binding chemotaxis protein	2,3
A0A0H3NJJ9	GlpT	Glycerol-3-phosphate transporter	2,3

We hypothesized that the changes we observed in the first passage would persist over time, but that upon repeat passage the profiles will converge. We therefore re-diluted and grew cultures that had been shifted into LMg medium several more times, removing an aliquot for proteome analysis. Discrete time points of the sample were taken along the trajectory and the profiles were analyzed by LC-MS/MS, to determine whether the overall pattern converges to a common expression pattern and whether the equalization occurs with identical kinetics. Figure 3B shows the ratios in P_1–P_3 of five of the proteins identified as differentially expressed in P_0. Notably, the abundance ratios appear to invert in P_1, but as expected, the ratios converge to close to 1.0 by P_2. Notably, the convergence of the expression ratios of EnvE appear to be delayed until P_3.

4. DISCUSSION

We present evidence that, following a transfer to a single common media, abundance of a subset of proteins is affected after as many as 8–10 generations. It is unlikely that these effects would be due to simple dilution of proteins whose expression was radically different in the prior growth conditions, since 10 generations represents a 1,000-fold increase in biomass, which would render the previously existing proteins virtually undetectable by the methods employed. The differences in the abundance of the differentially detected proteins described here are therefore most likely to be due to differences in protein expression during growth in the LMg media. One caveat to this explanation is that our proteomic methods had not been tuned to detect methylated peptides. This would be particularly applicable to the methyl-accepting chemotaxis proteins (MCP) detected here. However, the methylated residues occur on only a small portion of the sequence of each of these peptides. Detailed examination of the proteome data in the upcoming project period should allow us to address this possibility.

Most of the proteins identified in this study play roles in chemotaxis or motility—processes by which cells sense gradients of nutrients in their environment and alter the direction of rotation of their flagella, which results in a transition from forward motion to a tumbling motion.[8] These gradients are sensed by the MCPs, which participate in a phosphorelay that eventually results in the phosphorylation of the CheY protein and the modulation of the flagellar motion through FliG, a component of the C-ring of the flagellar basal body.[9]

It is not clear at this time why several components of the chemosensing pathway seem to be modulated following shifts in media, but the known mechanisms of regulation of many of the genes revealed in our study suggest a possible explanation. Many of the genes encoding MCPs and the components of their downstream signaling network (e.g., *tsr, trg, cheA, cheB, cheW, cheZ*) are regulated by FliA, a flagellar σ-factor that governs transcription of late-stage flagellar subunits (e.g., the flagellar filament) and the chemosensing apparatus.[10] Assembly of the flagellar basal body must be complete for FliA to be liberated from its anti-σ-factor FlgM,[11] conferring so-called "just-in-time" expression kinetics on the FliA-regulated genes. Notably, FliG, a component of the switch complex at the base of the flagellum, is one of the proteins common to all three experiments. In this scenario, cells grown initially in LB or HMg medium and then transferred to LMg may express more FliG than the control populations, thus completing the flagellar assembly at an earlier stage, leading to elevated expression of the chemosensor system. Of particular note is that flagellar and chemotaxis system genes are strongly downregulated during intracellular growth,[12] which our LMg system mimics.

Previously, other groups have reported a "memory" or "hysteresis" response in a two-component regulatory system that bacteria use to sense environmental phosphate levels.[13] Cultures starved of phosphate express basal levels of phosphate-sensing system, and exposure to transient high-phosphate conditions triggered elevated expression of the PhoBR system that persisted following removal of phosphate, such that subsequent exposure to a high-phosphate growth condition triggered a quicker response.[14] It is possible that the chemotaxis system experiences a similar "hysteresis" in our system. It is also possible that epigenetic alterations to the loci encoding the chemotaxis/motility proteins detected in this study modulate expression of these or key regulators at a transcriptional level. Current efforts in the laboratory are directed at verifying the differences observed by proteomic methods. In the upcoming project period, we will be analyzing protein profiles of whole-cell lysates by Western blot to confirm the changes in protein expression and employing mutants in the chemotaxis system and DNA methylation pathways to discriminate between these possibilities.

ACKNOWLEDGMENTS

Funding was provided by the U.S. Army via the In-house Laboratory Independent Research Program (PE 0601101A Project 91A) at the Edgewood Chemical Biological Center.

REFERENCES

[1] Sanders, J.W.; Putnam, S.D.; Frankart, C.; Frenck, R.W.; Monteville, M.R.; Riddle, M.S.; Rockabrand, D.M.; Sharp, T.W.; Tribble, D.R. Impact of illness and non-combat injury during Operations Iraqi Freedom and Enduring Freedom (Afghanistan). *Am. J. Trop. Med. Hyg.* **2005,** *73* (4), pp 713–719.

[2] Garai, P.; Gnanadhas, D.P.; Chakravortty, D. Salmonella enterica serovars Typhimurium and Typhi as model organisms: revealing paradigm of host-pathogen interactions. *Virulence.* **2012,** *3* (4), pp 377–388.

[3] Monack, D.M.; Mueller, A.; Falkow, S. Persistent bacterial infections: the interface of the pathogen and the host immune system. *Nature reviews. Microbiology*. **2004,** *2* (9), pp 747–765.
[4] Silva, C.; Calva, E.; Maloy, S. One Health and Food-Borne Disease: Salmonella Transmission between Humans, Animals, and Plants. *Microbiol. Spectr.* **2014,** *2* (1), pp OH-0020–2013.
[5] Snavely, M.D.; Gravina, S.A.; Cheung, T.T.; Miller, C.G.; Maguire, M.E. Magnesium transport in Salmonella typhimurium. Regulation of mgtA and mgtB expression. *J. Biol. Chem.* **1991,** *266* (2), pp 824–829.
[6] Garcia Vescovi, E.; Soncini, F.C.; Groisman, E.A. Mg2+ as an extracellular signal: environmental regulation of Salmonella virulence. *Cell.* **1996,** *84* (1), pp 165–174.
[7] Kato, A.; Groisman, E.A.; Howard Hughes Medical, I. The PhoQ/PhoP regulatory network of Salmonella enterica. *Adv. Exp. Med. Biol.* **2008,** *631*, pp 7–21.
[8] Larsen, S.H.; Reader, R.W.; Kort, E.N.; Tso, W.W.; Adler, J. Change in direction of flagellar rotation is the basis of the chemotactic response in Escherichia coli. *Nature.* **1974,** *249* (452), pp 74–77.
[9] Paul, K.; Gonzalez-Bonet, G.; Bilwes, A.M.; Crane, B.R.; Blair, D. Architecture of the flagellar rotor. *EMBO J.* **2011,** *30* (14), pp 2962–2971.
[10] Fitzgerald, D.M.; Bonocora, R.P.; Wade, J.T. Comprehensive mapping of the Escherichia coli flagellar regulatory network. *PLoS Genet.* **2014,** *10* (10), p e1004649.
[11] Zaslaver, A.; Mayo, A.E.; Rosenberg, R.; Bashkin, P.; Sberro, H.; Tsalyuk, M.; Surette, M.G.; Alon, U. Just-in-time transcription program in metabolic pathways. *Nat. Genet.* **2004,** *36* (5), pp 486–491.
[12] Eriksson, S.; Lucchini, S.; Thompson, A.; Rhen, M.; Hinton, J.C. Unravelling the biology of macrophage infection by gene expression profiling of intracellular Salmonella enterica. *Mol. Microbiol.* **2003,** *47* (1), pp 103–118.
[13] Bourret, R.B. Learning from Adversity? *J. Bacteriol.* **2017,** *199* (18), p e00420-17.
[14] Hoffer, S.M.; Westerhoff, H.V.; Hellingwerf, K.J.; Postma, P.W.; Tommassen, J. Autoamplification of a two-component regulatory system results in "learning" behavior. *J. Bacteriol.* **2001,** *183* (16), pp 4914–4917.

Effect of toxicants on the regulation of endothelial barrier function

Daniel J. Angelini*, Jennifer R. Horsmon, Amber M. Prugh, Christopher S. Phillips
U.S. Army Edgewood Chemical Biological Center, Research & Technology Directorate
8198 Blackhawk Road, Aberdeen Proving Ground, MD 21010

ABSTRACT

Endothelial cells line the internal portion of the vasculature and are responsible for maintaining homeostasis within the body. This function is accomplished through tightly regulating the passage of both fluid and nutrients from the bloodstream to various tissues. When this regulation is disrupted by inflammation or exposure to specific toxic compounds, fluids, and macromolecules will accumulate in the surrounding tissues, resulting in edema. This accumulation of fluids is typically regulated through the paracellular pathway—defined as the movement of fluids and macromolecules through gaps formed at intercellular junctions. Several chemical warfare agents have been shown to disrupt the endothelium and induce edema following sub-lethal exposures in experimental animals. In the following studies, we examined the effects of four different toxicants on the immortalized dermal microvascular endothelial cell line, HMEC-1, through the measurement of cell viability and impedance. We then compared these results to those obtained from primary cultured microvascular endothelial cells from skin, lung, and heart. This assessment will demonstrate that the HMEC-1 can be suitable for assessing vascular toxicity and allow for more accurate toxicity estimates in the future. The data gathered in this study will provide fundamental knowledge regarding the regulation of endothelial barrier function.

Keywords: barrier function, edema, endothelial cells, paracellular pathway

1. INTRODUCTION

1.1 Endothelial barrier function

Endothelial cells (EC) play a crucial role in maintaining homeostasis—these cells tightly regulate the passage of fluid, nutrients, and immune cells from the intravascular compartment to tissues throughout the body.[1,2] Transenodthelial flux of molecules occurs through either the paracellular pathway (intercellular gaps) or the transcellular pathway (transcytosis or vesicular transport). Edema formation, or fluid accumulation within tissues, typically occurs through the paracellular pathway.[3] This pathway is regulated at the cell-cell level by at least two distinct junctional complexes—adherens junctions (AJ), and tight junctions (TJ).[2] The number of these specific junctions in an EC is dependent on its location within the vascular tree. For example, brain microvascular endothelial cells (MVEC) contain many more TJs than ECs from any other regional vascular bed.[2] AJs and TJs are both tethered to the actin cytoskeleton, but AJs play a prominent role in the regulation of barrier function throughout almost the entire vasculature.[4] AJs consist of the membrane-spanning vascular endothelial (VE)-cadherin, and the cytosolic proteins, α-, β-, γ-, and p120 catenins.[2] The VE-cadherin ectodomain participates in calcium-dependent, homophilic cell-cell adhesion, and is tethered to the actin cytoskeleton through the catenin proteins. Both rapidly acting (e.g., thrombin, histamine) and late acting (e.g., tumor necrosis factor-α (TNFα), endotoxin) regulators of barrier function increase tyrosine phosphorylation of VE-cadherin; these phosphorylation events induce a loss of cell-cell adhesion and actin depolymerization leading to intercellular gap formation and increased paracellular permeability.[2,5,6]

1.2 Chemical warfare agents and vascular injury

Several chemical warfare agents (CWA), including nerve agents (e.g., VX) and vesicants (e.g., HD), have been shown to disrupt the endothelium and induce edema in experimental animals.[7–10] Choking agents, such as chlorine and phosgene, have also been shown to disrupt the endothelial barrier, particularly within the lungs.[11,12] It is interesting to note that biological toxins of military importance also have been shown to disrupt the endothelial barrier, including ricin[13] and staphylococcal enterotoxin B.[14] In many of these cases, it is unknown whether these alterations in endothelial barrier function are due to necrosis/apoptosis or alterations of the EC cytoskeleton. Additional studies are

necessary to address the knowledge gap that exists concerning the mechanisms of action of these compounds/toxins on the endothelium.

2. METHODOLOGY

2.1 Human EC culture

The human MVEC line HMEC-1[15] was obtained from ATCC® (Manassas, VA) and cultured in MCDB131 culture media (ATCC®) supplemented with 10 ng/mL epidermal growth factor, 1 µg/mL hydrocortisone, 10 mM L-glutamine, 1% penicillin-streptomycin, and 10% fetal bovine serum (all supplements from Thermo Fisher Scientific™; Waltham, MA). Even though this is an immortalized cell line, we only examined these ECs within a 10-passage window. This cell line was chosen due to its EC origin and its usefulness as a generalized MVEC. HMEC-1s have been shown to express all of the typical EC markers, have EC morphology, and form consistent EC barriers.[15] Also, these ECs have been shown to be responsive to classical regulators of endothelial barrier function (e.g., histamine).[15] For comparison, we examined primary MVECs from three different areas of the body that are all major CWA targets: skin (human dermal MVEC, HMVEC-D), lung (human lung MVEC, HMVEC-L), and heart (human cardiac MVEC, HMVEC-C) (Lonza; Walkersville, MD). All primary microvascular ECs were cultured in Endothelial Cell Growth Medium MV (PromoCell GmbH; Heidelberg, Germany) supplemented with 5 % fetal calf serum, human recombinant epidermal growth factor (5 ng/mL), human recombinant basic fibroblast growth factor (10 ng/mL), insulin-like growth factor (20 ng/mL), human recombinant vascular endothelial growth factor 165 (0.5 ng/mL), ascorbic acid (1 µg/mL), and hydrocortisone (0.2 µg/mL) (all supplements from PromoCell GmbH). To prevent potential contamination, the media was also supplemented with GA-1000 (125 µg amphotericin B/5 mg gentamicin; Thermo Fisher Scientific™). Only ECs from passages 5–10 will be studied.

2.2 Preparation of experimental chemicals

Stock solutions of the organophosphate pesticide malathion (ULTRA® Scientific; N. Kingstown, RI) and its metabolite, malaoxon (Sigma-Aldrich®; St. Louis, MO), were prepared in 100 % ethanol (EtOH) and stored at 4 ºC.[16] A stock solution of bis(2-chloroethyl)amine hydrochloride (BCAH; Sigma-Aldrich®) was prepared in distilled H_2O which was stored at 4 ºC for no longer than 3 days after initial preparation. A stock solution of lipopolysaccharide (LPS) was prepared in sterile PBS, aliquoted, and stored at -20 ºC until use.[17]

2.3 Evaluation of endothelial cell viability

All MVECs were treated with increasing concentrations of the experimental compound(s) and then a MTT viability assay was performed as previously described.[16,18] This assay was used to determine the toxicity of the selected compound and indicated the optimal concentrations for examining changes in endothelial barrier function.

2.4 Evaluation of cellular impedance

Cellular impedance was measured using the ACEA xCelligence® Real-Time Cell Analyzer (RTCA).[19,20] HMEC-1, HMVEC-C, HMVEC-D, or HMVEC-L were plated on the specially designed impedance plates and grown to a post-confluent state (72 hours). Once confluent, the ECs were exposed to the selected compound with impedance readings taken every 15 minutes. Results were reported as normalized cell index (CI). Evidence of endothelial barrier dysfunction was indicated by a decrease in the CI compared to media or vehicle control.

2.5 Statistical analysis

All quantifiable results are reported as mean ± standard error of the mean. Statistical analysis was performed using GraphPad Prism 7 software (GraphPad Software, Inc.; La Jolla, CA). A one-way ANOVA was used to compare the mean responses among the experimental and control groups. The Dunnett's multiple comparisons test was used to determine whether significant differences between groups existed. A p value of < 0.05 was considered significant.

3. DATA

3.1 Effect of malathion/malaoxon on MVEC viability

ECs were plated at a density of 5.0×10^4 cells/well in 96-well tissue culture plates and allowed to attach for 24 hours. The cells were then exposed to media, vehicle (EtOH), or increasing concentrations of malathion or malaoxon (1–10,000 µM) for 24 hours at 37 ºC. The exposures were evaluated using the MTT Viability Assay (Figure 1). Following exposure to malathion, significant reductions in viability were seen at concentrations ≥ 1,000 µM in HMEC-1, HMVEC-D, and HMVEC-L. Malathion concentrations as low as 10 µM induced losses in HMVEC-C viability. Treatments with the metabolite of malathion, malaoxon, induced reductions in EC viability in concentrations ≥ 3,000 µM in HMEC-1, but ≥ 1,000 µM for HMVEC-D and HMVEC-L. HMVEC-C appeared to be the most sensitive to the effects of malaoxon, with ≥ 300 µM inducing cellular death in these cells.

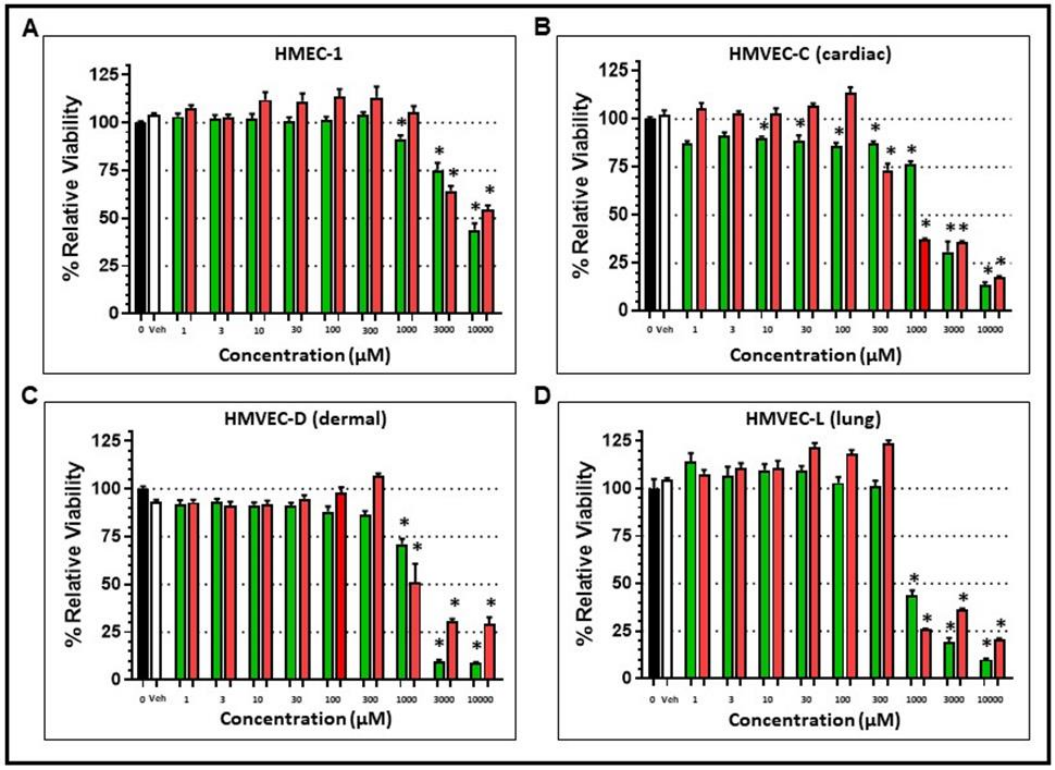

Figure 1. Effects of malathion and malaoxon on MVEC viability. (A) HMEC-1, (B) HMVEC-C, (C) HMVEC-D, and (D) HMVEC-L were exposed to increasing concentrations of malathion (1–10,000 µM; green bars), malaoxon (1–10,000 µM; red bars), media alone (closed bars), or vehicle (EtOH; open bars) for 24 hours. Following exposure, the ECs were assayed for viability using the MTT Viability Assay. The results are reported as mean ± standard error of the mean as % relative viability; $n \geq 8$ for each condition tested. *$p < 0.05$ compared to vehicle.

3.2 Effect of LPS on MVEC viability

ECs were plated at a density of 5.0×10^4 cells/well in 96-well tissue culture plates and allowed to attach for 24 hours. The cells were then exposed to media, vehicle (PBS), or increasing concentrations of LPS (0.03–10 µg/mL) for 24 hours at 37 ºC. The ECs were evaluated using the MTT Viability Assay. Following exposure to LPS, no concentration of this compound induced any visible cell death in any of the ECs examined (data not shown).

3.3 Effect of BCAH on MVEC viability

ECs were plated at a density of 5.0×10^4 cells/well in 96-well tissue culture plates and allowed to attach for 24 hours. The cells were then exposed to media, vehicle (H_2O), or increasing concentrations of BCAH (0.01–100 µg/mL) for 24 hours at 37 ºC. The ECs were evaluated using the MTT Viability Assay (Figure 2). Following exposure to BCAH, significant cell death was seen at concentrations ≥ 300 µM in HMEC-1. Significant cell death was observed in

BCAH-treated HMVEC-D at concentrations ≥ 100 µM. HMVEC-L appeared to be the most sensitive ECs to BCAH where concentrations ≥ 10 µM induced significant cell death in these cells.

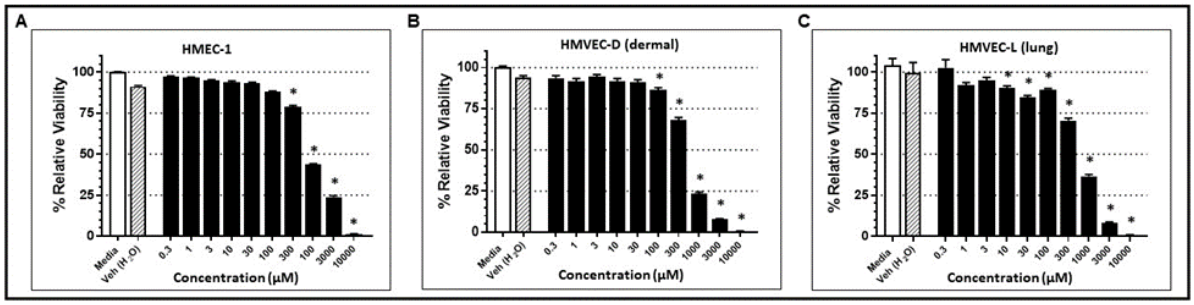

Figure 2. Effects of BCAH on MVEC viability. (A) HMEC-1, (B) HMVEC-D, and (C) HMVEC-L were exposed to increasing concentrations of BCAH (0.03–10,000 µM; closed bars), media alone (open bars), or vehicle (H_2O; cross-hatched bars) for 24 hours. Following exposure, the ECs were assayed for viability using the MTT Viability Assay. The results are reported as mean ± standard error of the mean as % relative viability; $n \geq 8$ for each condition tested. *$p < 0.05$ compared to vehicle.

3.4 Effect of selected toxicants on cellular impedance in HMEC-1

The HMEC-1 cells were grown to confluence on E-Plate® 16s for 72 hours at 37 ºC and then exposed to increasing concentrations of malathion (100–300 µM), malaoxon (100–300 µM), LPS (10–3,000 ng/mL), BCAH (0.003–3 mM), vehicle, or media alone for 16 hours. Cellular impedance was measured every 15 minutes following the exposures (Figure 3). Reductions in normalized CI were observed following malathion (100 µM) treatment at 5–6 hours post-exposure, while exposures to an increased concentration of malathion (300 µM) induced reductions at 1–3 hours post-exposure (Figure 3A). With both concentrations examined, this loss in normalized CI stabilized between 8–10 hours post-exposure remaining until the end of the experiment. A similar timeline of a reduced normalized CI was observed with both concentrations of malaoxon (Figure 3B), although the reduction was slightly more pronounced with this compound. The effects of LPS on normalized CI were also examined in these cells (Figure 3C). All of the concentrations of LPS (10–3,000 ng/mL) caused a reduction in normalized CI. Reductions were observed at approximately 1–2 hours following initial exposure and never returned to baseline during the 16-hour experiment. When examining the effect of BCAH on HMEC-1s, only concentrations of 1 mM and 3 mM induced any reductions in normalized CI (Figure 3D). Both of these concentrations of BCAH caused cellular death in these cells, suggesting that the observed reduction in normalized CI is due to cell death and not the formation of cellular gaps.

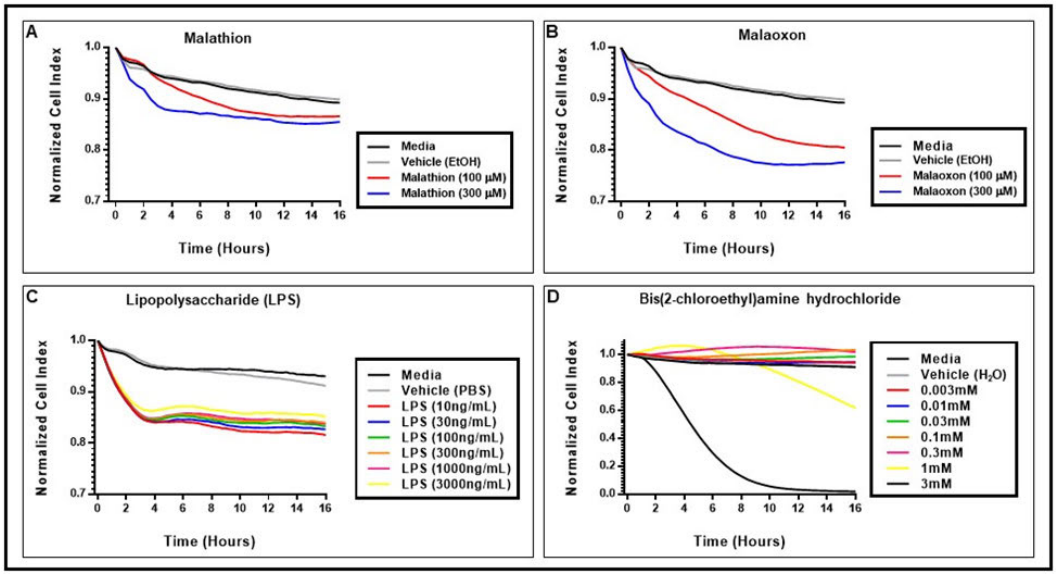

Figure 3. Cellular impedance changes in cultured HMEC-1 following treatment with selected toxicants. HMEC-1 cells were exposed to increasing concentrations of (A) malathion (100–300 µM), (B) malaoxon (100–300 µM), (C) LPS (10–3,000 ng/mL), or (D) BCAH (0.003–3 mM), media alone, or vehicle for 16 hours. The results are expressed as mean of the normalized cell index ($n \geq 5$ for each experimental condition).

3.5 Effect of selected toxicants on cellular impedance in HMVEC-D

The HMVEC-D cells were grown to confluence on E-Plate® 16s for 72 hours at 37 ºC and then exposed to increasing concentrations of malathion (100–1,000 µM), malaoxon (100–1,000 µM), LPS (10–3,000 ng/mL), BCAH (0.01–0.3 mM), vehicle, or media alone for 16 hours. Cellular impedance was measured every 15 minutes following the exposures (Figure 4). Following exposure to malathion or malaoxon, there was no observable reductions in normalized CI with the exception of the 1,000 µM malaoxon exposure (Figure 4A&B). This reduction was likely do to the induction of cellular death in response to malaoxon treatment; this concentration of malaoxon reduced cellular viability as shown in the MTT assay (Figure 2). We also examined the effects of LPS (10–3,000 ng/mL) on normalized cell index in HMVEC-D (Figure 4C). The results from these experiments were very similar to those seen with HMEC-1 cells. There was an approximate 1–2 hour time lag following initial exposure and reduction in normalized CI. This reduction lasted several hours and only slightly recovered from peak reductions. As seen with HMEC-1s, there did not appear to be a dose-dependent relationship between LPS and reductions in normalized CI. In addition to malathion, malaoxon, and LPS, we also examined the effect of BCAH (0.01–0.3 mM) on normalized CI (Figure 4D). In these treatments, we did observe a dose-dependence between BCAH concentration and reductions in normalized CI, but these concentrations seemed to correlate with BCAH concentrations that induced cellular death. These results suggest that BCAH does not induce cellular retraction and the formation of intercellular gaps but alters the endothelial barrier through cell death.

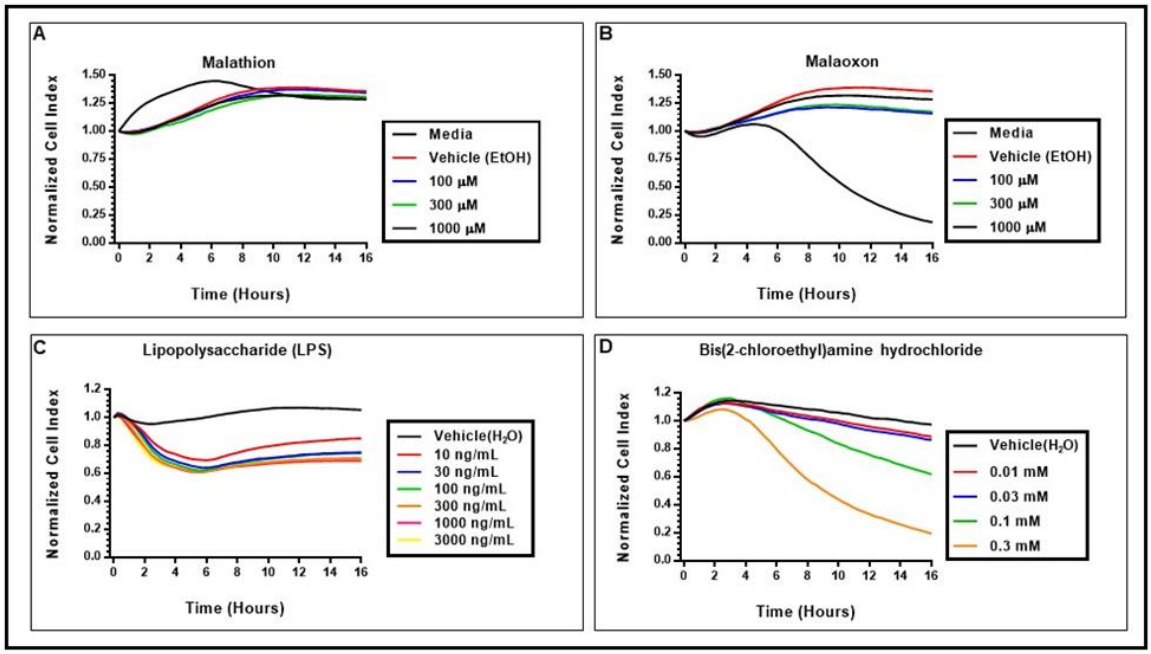

Figure 4. Cellular impedance changes in cultured HMVEC-D following treatment with selected toxicants. HMVEC-D cells were exposed to increasing concentrations of (A) malathion (100–1,000 µM), (B) malaoxon (100–1,000 µM), (C) LPS (10–3,000 ng/mL), or (D) BCAH (0.01–0.3 mM), media alone, or vehicle for 16 hours. The results are expressed as mean of the normalized cell index ($n \geq 6$ for each experimental condition).

3.6 Effect of selected toxicants on cellular impedance in HMVEC-L

The HMVEC-L cells were grown to confluence on E-Plate® 16s for 72 hours at 37 ºC and then exposed to increasing concentrations of malathion (100–1,000 µM), malaoxon (100–1,000 µM), BCAH (0.01–1 mM), vehicle, or media alone for 16 hours. Cellular impedance was measured every 15 minutes following the exposures of the selected toxicants (Figure 5). Similar to HMVEC-D, treatment with malathion or malaoxon failed to reduce the normalized CI with the exception of the 1,000 µM concentration of malaoxon (Figure 5A&B). This change appears to be related to the induction of cell death following treatment based on the results of the MTT assay on the cells. Following treatment

with BCAH (0.01–1mM), only a concentration of 1 mM induced any changes in normalized CI. As with malaoxon, this concentration is associated with the loss of cell viability as shown in the previous MTT assays.

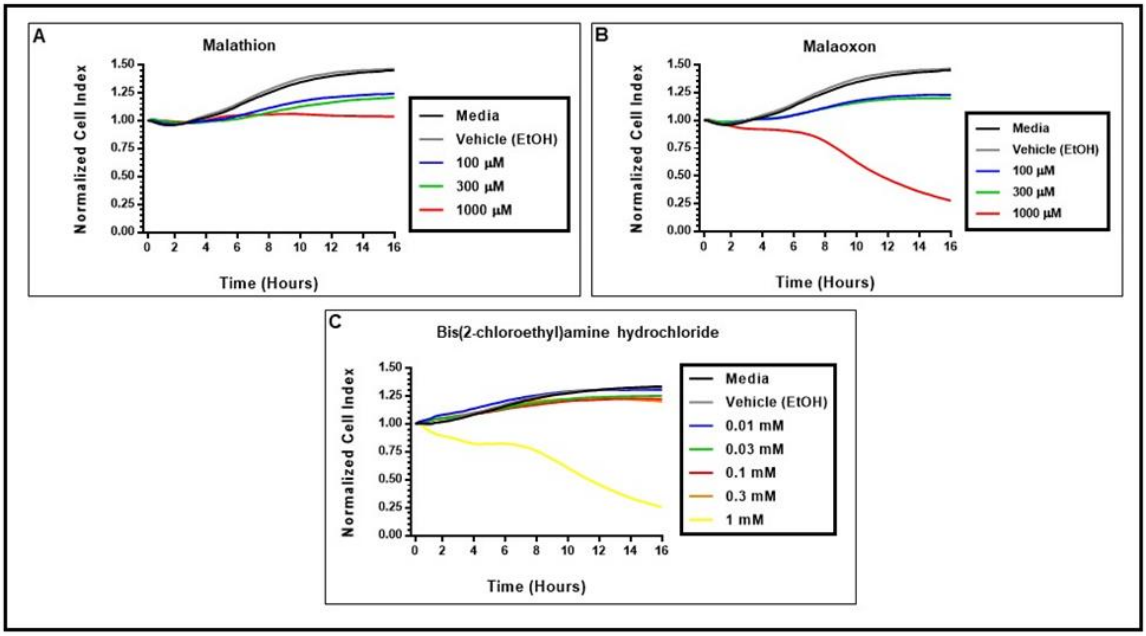

Figure 5. Cellular impedance changes in cultured HMVEC-L following treatment with selected toxicants. HMVEC-L cells were exposed to increasing concentrations of (A) malathion (100–1,000 µM), (B) malaoxon (100–1,000 µM), or (C) BCAH (0.01–0.3 mM), media alone, or vehicle for 16 hours. The results are expressed as mean of the normalized cell index ($n \geq 6$ for each experimental condition).

4. CONCLUSIONS

In the current study, we have examined the effects of four different toxicants on a MVEC line (HMEC-1) as well as primary MVECs (HMVEC-C, HMVEC-D, and HMVEC-L). Treatment with the organophosphate compounds malathion and malaoxon, as well as the chemotherapeutic compound BCAH, induced a dose-dependent reduction in cell viability in all cells examined. Treatment of the MVECs with LPS failed to produce any toxicity at concentrations as high as 10 µg/mL. Overall, it appears that the HMEC-1s are more resistant to the toxic effects of the compounds tested compared to the primary MVECs that were used in this study. In HMEC-1, malathion/malaoxon disrupted the endothelial barrier in concentrations that did not induce cell death. This was different than the primary MVECs examined, whereas only concentrations of malathion/malaoxon that were shown to be toxic caused any changes in barrier function as demonstrated by normalized CI. Our results also show that BCAH only disrupted the endothelial barrier at concentrations that caused cellular death in all cells examined. It is interesting to note that LPS disrupted the endothelial barrier in all MVECs examined in a time-dependent manner. This effect does not appear to be dose-dependent. All concentrations of LPS (10–3,000 ng/mL) examined induced similar reductions in normalized cell index regardless of concentration. Throughout this study, we have observed that HMVEC-C are very difficult to culture and have an extremely limited number of cell doublings. Due to this, we have concluded that these cells should only be used in specific circumstances when trying to answer specific questions regarding the cardiac endothelium.

ACKNOWLEDGMENTS

Funding was provided by the U.S. Army via the In-house Laboratory Independent Research Program (PE 0601101A Project 91A) at the Edgewood Chemical Biological Center. The authors would also like to thank Dr. Augustus W. Fountain, Ms. Rebecca Braun, Dr. Kelly Basi, Dr. Kyle Glover, and Mrs. Davi Kristovich for continued scientific and administrative support.

REFERENCES

[1] Garcia, J.G.; Schaphorst, K.L. Regulation of endothelial cell gap formation and paracellular permeability. *J. Investig. Med.* **1995,** *43* (2), pp 117–126.

[2] Sukriti, S.; Tauseef, M.; Yazbeck, P.; Mehta, D. Mechanisms regulating endothelial permeability. *Pulm. Circ.* **2014,** *4* (4), pp 535–551.

[3] Lucas, R.; Verin, A.D.; Black, S.M.; Catravas, J.D. Regulators of endothelial and epithelial barrier integrity and function in acute lung injury. *Biochem. Pharmacol.* **2009,** *77* (12), pp 1763–1772.

[4] Gavard, J. Endothelial permeability and VE-cadherin: a wacky comradeship. *Cell. Adh. Migr.* **2014,** *8* (2), pp 158–164.

[5] Angelini, D.J.; Hasday, J.D.; Goldblum, S.E.; Bannerman, D.D. Tumor Necrosis Factor-α-Mediated Pulmonary Endothelial Barrier Dysfunction. *Curr. Respir. Med. Rev.* **2005,** *1* (3), p 14.

[6] Angelini, D.J.; Hyun, S.W.; Grigoryev, D.N.; Garg, P.; Gong, P.; Singh, I.S.; Passaniti, A.; Hasday, J.D.; Goldblum, S.E. TNF-alpha increases tyrosine phosphorylation of vascular endothelial cadherin and opens the paracellular pathway through fyn activation in human lung endothelia. *Am. J. Physiol.: Lung Cell. Mol. Physiol.* **2006,** *291* (6), pp L1232–1245.

[7] Angelini, D.J.; Dorsey, R.M.; Willis, K.L.; Hong, C.; Moyer, R.A.; Oyler, J.; Jensen, N.S.; Salem, H. Chemical warfare agent and biological toxin-induced pulmonary toxicity: could stem cells provide potential therapies? *Inhal. Toxicol.* **2013,** *25* (1), pp 37–62.

[8] Peng, X.; Perkins, M.W.; Simons, J.; Witriol, A.M.; Rodriguez, A.M.; Benjamin, B.M.; Devorak, J.; Sciuto, A.M. Acute pulmonary toxicity following inhalation exposure to aerosolized VX in anesthetized rats. *Inhal. Toxicol.* **2014,** *26* (7), pp 371–379.

[9] Poursaleh, Z.; Ghanei, M.; Babamahmoodi, F.; Izadi, M.; Harandi, A.A.; Emadi, S.E.; Taghavi, N.O.; Sayad-Nouri, S.S.; Emadi, S.N. Pathogenesis and treatment of skin lesions caused by sulfur mustard. *Cutaneous Ocul. Toxicol.* **2012,** *31* (3), pp 241–249.

[10] Testylier, G.; Lahrech, H.; Montigon, O.; Foquin, A.; Delacour, C.; Bernabe, D.; Segebarth, C.; Dorandeu, F.; Carpentier, P. Cerebral edema induced in mice by a convulsive dose of soman. Evaluation through diffusion-weighted magnetic resonance imaging and histology. *Toxicol. Appl. Pharmacol.* **2007,** *220* (2), pp 125–137.

[11] Massa, C.B.; Scott, P.; Abramova, E.; Gardner, C.; Laskin, D.L.; Gow, A.J. Acute chlorine gas exposure produces transient inflammation and a progressive alteration in surfactant composition with accompanying mechanical dysfunction. *Toxicol. Appl. Pharmacol.* **2014,** *278* (1), pp 53–64.

[12] Werrlein, R.J.; Madren-Whalley, J.S.; Kirby, S.D. Phosgene effects on F-actin organization and concentration in cells cultured from sheep and rat lung. *Cell Biol. Toxicol.* **1994,** *10* (1), pp 45–58.

[13] Lindstrom, A.L.; Erlandsen, S.L.; Kersey, J.H.; Pennell, C.A. An in vitro model for toxin-mediated vascular leak syndrome: ricin toxin A chain increases the permeability of human endothelial cell monolayers. *Blood.* **1997,** *90* (6), pp 2323–2334.

[14] Campbell, W.N.; Fitzpatrick, M.; Ding, X.; Jett, M.; Gemski, P.; Goldblum, S.E. SEB is cytotoxic and alters EC barrier function through protein tyrosine phosphorylation in vitro. *Am. J. Physiol.* **1997,** *273* (1 Pt 1), pp L31–39.

[15] Ades, E.W.; Candal, F.J.; Swerlick, R.A.; George, V.G.; Summers, S.; Bosse, D.C.; Lawley, T.J. HMEC-1: establishment of an immortalized human microvascular endothelial cell line. *J. Invest. Dermatol.* **1992,** *99* (6), pp 683–690.

[16] Angelini, D.J.; Moyer, R.A.; Cole, S.; Willis, K.L.; Oyler, J.; Dorsey, R.M.; Salem, H. The Pesticide Metabolites Paraoxon and Malaoxon Induce Cellular Death by Different Mechanisms in Cultured Human Pulmonary Cells. *Int. J. Toxicol.* **2015,** *34* (5), pp 433–441.

[17] Gong, P.; Angelini, D.J.; Yang, S.; Xia, G.; Cross, A.S.; Mann, D.; Bannerman, D.D.; Vogel, S.N.; Goldblum, S.E. TLR4 signaling is coupled to SRC family kinase activation, tyrosine phosphorylation of zonula adherens proteins, and opening of the paracellular pathway in human lung microvascular endothelia. *J. Biol. Chem.* **2008,** *283* (19), pp 13437–13449.

[18] Prugh, A.M.; Cole, S.D.; Glaros, T.; Angelini, D.J. Effects of organophosphates on the regulation of mesenchymal stem cell proliferation and differentiation. *Chem. Biol. Interact.* **2017,** *266*, pp 38–46.

[19] Bischoff, I.; Hornburger, M.C.; Mayer, B.A.; Beyerle, A.; Wegener, J.; Furst, R. Pitfalls in assessing microvascular endothelial barrier function: impedance-based devices versus the classic macromolecular tracer assay. *Sci. Rep.* **2016,** *6*, p 23671.

[20] Ke, N.; Wang, X.; Xu, X.; Abassi, Y.A. The xCELLigence system for real-time and label-free monitoring of cell viability. *Methods Mol. Biol.* **2011,** *740*, pp 33–43.

Characterization of aerosol particle charge and the impact of a high degree of charge on the particle's physical and chemical properties

Erin M. Durke[a*], Monica L. McEntee[a], Meilu He[b], Suresh Dhaniyala[b]
[a]U.S. Army Edgewood Chemical Biological Center, Research & Technology Directorate,
8198 Blackhawk Rd, Aberdeen Proving Ground, MD 21010
[b]Clarkson University, 8 Clarkson Ave, Potsdam, NY 13699

ABSTRACT

The metal oxides, TiO_2 and SiO_2, were aerosolized expulsively and then characterized, using several different techniques, in an effort to determine the surface charge imparted upon the particles via the aerosolization process. Particle charge distribution measurements were conducted via the employment of a custom scanning mobility particle sizer. The results of the charge distribution measurements indicated that expulsive generation of 0.2 µm SiO_2 particles produced aerosols with upwards of 6+ charges on the surface of the particle. Determination of the degree of surface charging led to the use of non-traditional techniques to explore the impact of additional surface charge on the overall reactivity of the metal oxides, specifically TiO_2. TiO_2 was aerosolized, again expulsively, onto a gold-coated tungsten mesh, which was then evaluated with transmission infrared spectroscopy in an ultra-high vacuum environment. The TiO_2 aerosols were exposed to both H_2 and CO, respectively. Upon exposure to H_2, there was no observable rise in the baseline of the IR spectrum, as is typically seen for TiO_2, due to the population of electrons into the shallow trapped states and subsequent promotion of the electrons into the conduction band. This result suggests that the additional charge imparted via aerosolization fills the trapped states, therefore no rise is seen upon exposure to H_2. Dosing the TiO_2 aerosols with CO showed no adsorption of CO on the surface, even at lower temperatures (~100 K), indicative of one of two possibilities: 1) the concentration of aerosols present on the surface is not high enough to detect CO binding to the material, or 2) the additional charge on the aerosol surface prevents the CO molecules from adsorbing to the TiO_2 surface. Future testing will explore a higher concentration of TiO_2 aerosols exposed to CO at low temperatures.

Keywords: aerosol, particle, charge distribution, infrared, metal oxide, reactivity

1. INTRODUCTION

Many factors can affect the chemical reactivity of a material, such as surface area, concentration, physical state, and temperature, to name a few. When a material is aerosolized, it exists in a physical state unlike any other, one with characteristics that are still not well understood. One of the most important and intriguing features of the aerosol state is the charge present on the particles. The inherent charge can impact the particle's interactions, as well as chemical reactions taking place on its surface, ultimately affecting processes like agglomeration and atmospheric aging.[1]

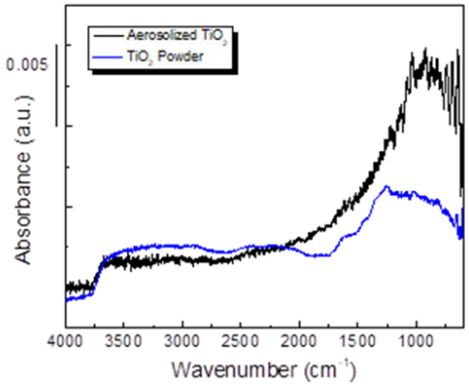

Figure 1. Transmission infrared spectrum of aerosolized TiO_2 and TiO_2 powder.

Initial studies focused on charge characteristics showed a difference in the spectral signature of TiO_2 powder and expulsively generated TiO_2 aerosols (see Figure 1). Systematic experimentation led to the conclusion that the features observed in the aerosol IR spectra were a result of the aerosolization process, as opposed to artifacts of the experimental setup.[2] With the knowledge that surface charge on the generated particles is a consequence of aerosolization, it was hypothesized that the additional charge from aerosolization can also impact the reactivity of the TiO_2. From the literature, TiO_2 is known to possess shallow trapped states within its band gap.[3–11] Depending upon the treatment of the material, the trapped states can easily be filled with excess electrons and those electrons can then be promoted to the conduction band via thermal excitation or IR illumination.[11] The detection of conduction-band electrons (CBE) is possible through the observation of a distinct background rise from 4000 cm^{-1} to ~1000 cm^{-1}.[11] For reduced TiO_2 (i.e., vacuum treatment at elevated temperatures (960 K)), exposure to O_2 will reverse the background rise associated with the CBEs, as the O_2 acts like an electron scavenger and collects the delocalized CBEs. Oxygen dosing was utilized for further confirmation of the presence of surface charge as a result of the aerosolization process. TiO_2 powder pressed into a W Mesh, with no pretreatment, showed no change in the overall background (i.e., no rise between 4000 to ~1000 cm^{-1}), indicating no occupation of the shallow trapped states just below the conduction band, see Figure 2A. However, the graph in Figure 2B, shows a distinct decrease in the baseline for the spectrum of TiO_2 aerosols exposed to ~1.2 Torr of O_2. The excess surface charge deposited during aerosol generation occupies the shallow trapped states, is then promoted to the CB during IR interrogation, and then is removed via exposure to O_2.

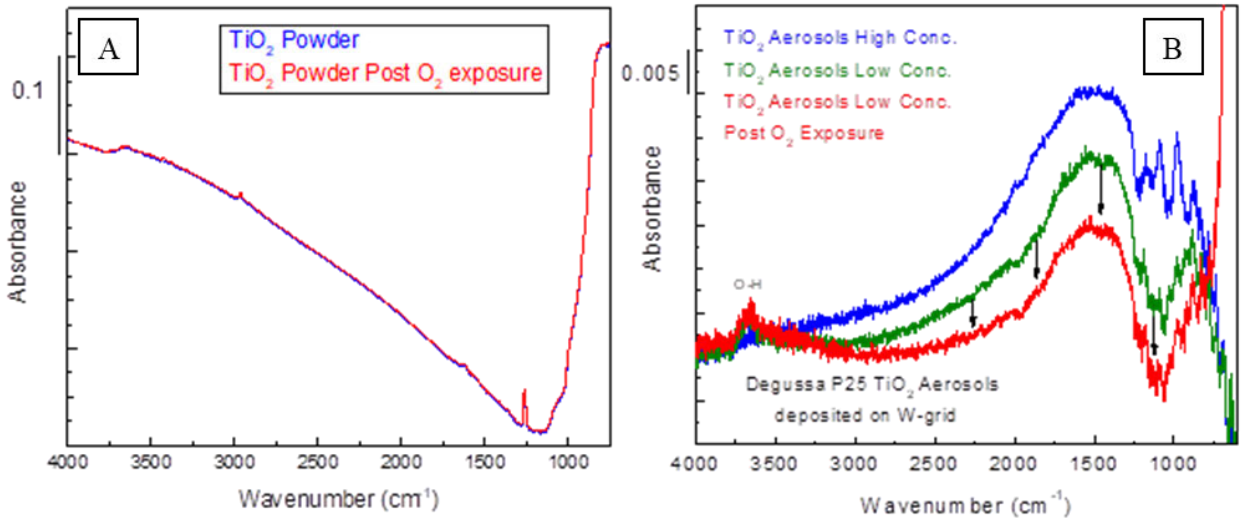

Figure 2. (A) Spectra of TiO_2 powder before and after exposure to ~1.2 Torr of O_2. No change in the baseline suggests empty shallow trapped states. (B) Spectra of TiO_2 aerosols before and after exposure to ~1.2 Torr of O_2. The decrease observed in the overall background indicates the excess charge generated during aerosolization occupies the shallow trapped states, resulting in CBEs over the sample when it is illuminated with IR light.

In this study, we used H_2 and CO to probe the impact surface charge from aerosolization has on the reactivity of the Au/TiO_2 system. Au/TiO_2 reactivity is extensively documented in the literature; therefore, it may be possible to attribute deviations observed to the presence of excess charge.

2. EXPERIMENTAL

2.1 Materials

Aeroxide® P25 TiO_2 was purchased from Sigma-Aldrich® and used without further purification. Lanthanide-tagged SiO_2 particles were used without further purification. The SiO_2 particles were custom made by Fiber Optic Center, Inc. using AngströmSphere ™ silica spheres. The SiO_2 particles characterized in these studies were 200 nm (± 10 %) in diameter.

2.2 Aerosolization

All materials were aerosolized using sonic nozzles based on the SRI annular nozzle design, shown in Figure 3.[12] The sonic nozzle is comprised of an internal tube with a high-pressure air flow passing around said tube and exiting through

an orifice. The configuration results in a Venturi Effect, which pulls material from the sample reservoir and through the nozzle, where it will experience disruptive forces causing deagglomeration and aerosolization.

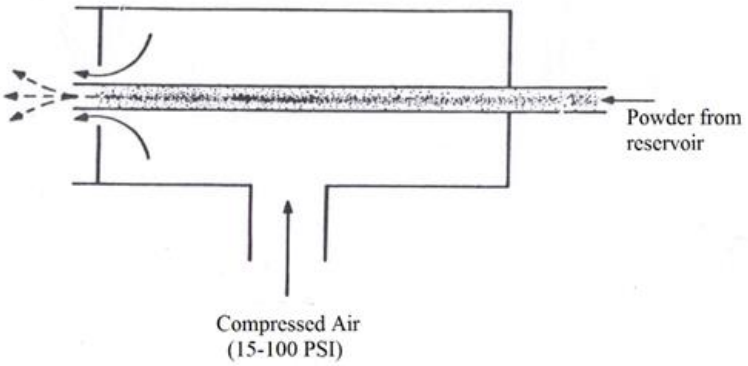

Figure 3. SRI annular nozzle design. Modified picture from Calabrese et al.[12]

For samples interrogated with transmission infrared spectroscopy (TIR), the TiO_2 powder was aerosolized inside of a Lexan™ aerosol generation box. The samples (W mesh, Au-coated W Mesh) were placed on the bottom of the box prior to aerosolization. Aerosols were generated for 10 seconds, then the particles were allowed to settle on the sample surfaces for at least one hour.

For samples generated for particle size distribution (PSD) and particle charge distribution (PCD) measurements (SiO_2 and TiO_2), the powders were contained inside sealed vials, connected to the sonic nozzle via metal tubing. The powder was aerosolized into the sample drum, see Figure 4, from which samples were pulled for characterization.

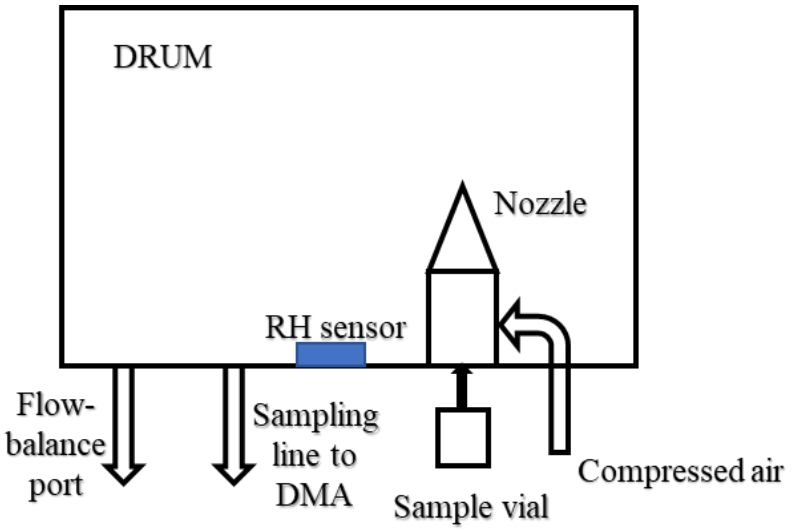

Figure 4. Sample drum utilized for PSD and PCD measurements.

2.3 Instrumentation

The aerosolized samples were interrogated with TIR spectroscopy inside of the custom mid-infrared aerosol chemistry chamber (MIRACC); sample mount schematic and picture shown in Figure 5. The TIR spectroscopy was performed using a Thermo Scientific™ Nicolet™ 6700 Fourier transform infrared spectrometer equipped with a mid-IR source and MCT Type A detector, allowing for an observable range of 4000–650 cm^{-1}. Spectra are the sum of 1,024 scans acquired at a resolution of 2 cm^{-1}.

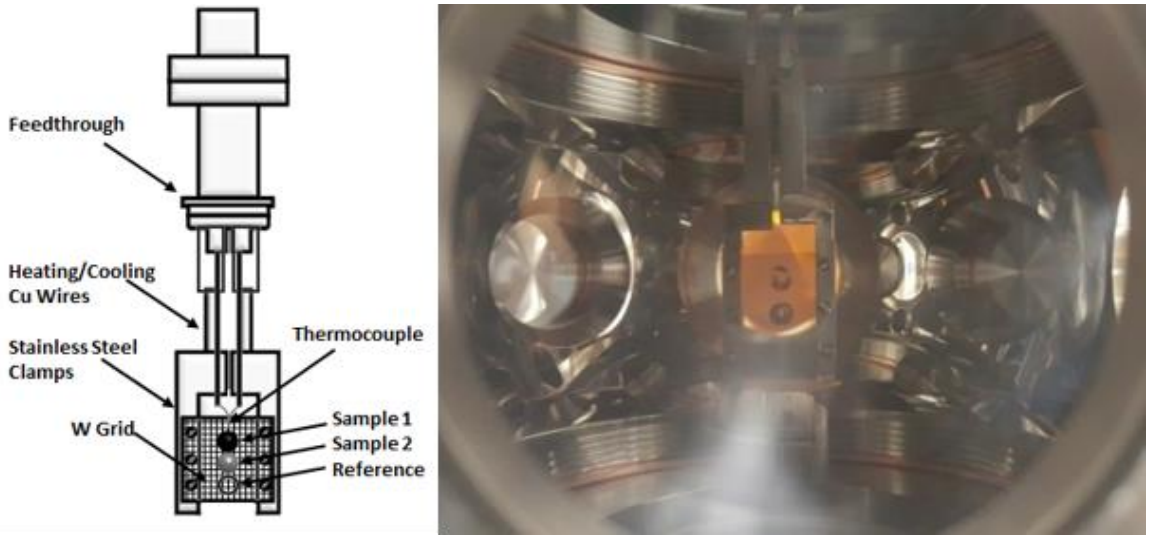

Figure 5. Schematic (left) and image (right) of the sample mount and W mesh used to perform TIR spectroscopy of the metal oxides (both powder and aerosols).

For size and charge distribution measurements, electrical mobility measurements were made using a scanning mobility particles sizer (SMPS). To determine the charge fraction of particles from the mobility measurements, the size distribution of particles must first be collected. Several instruments are utilized for PSD measurements. These instruments are based on different technologies; therefore, the PSD measurements were cross-validated. The instruments used include a customized high-flow SMPS, wide-range particle spectrometer (WPS), ultra-high sensitivity aerosol spectrometer (UHSAS), and aerodynamic particle sizer (APS). The measurement range for each instrument is shown in Table 1.

Table 2. Instruments applied for particle size distribution measurements.

	High-flow SMPS	**WPS**	**UHSAS**	**APS**
Technology	electrical mobility	electrical mobility	optical	aerodynamic
Size range (µm)	0.005–3	0.01–0.4	0.1–1	0.5–20

The schematic diagram of the experimental setup for PSD measurements is shown in Figure 6. The sonic nozzle was placed in a 20-gallon drum (Figure 4), compressed air was supplied to the nozzle at different pressures (e.g., 70 psi, 80 psi) and the aerosolized particles are dispersed into the drum. The concentrations of the dispersed particles are then measured using the four instruments listed in Table 1.

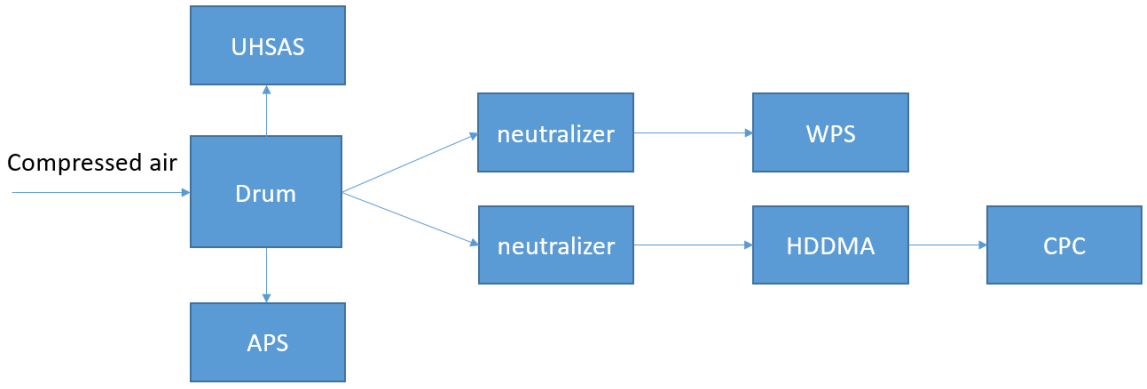

Figure 6. Schematic diagram of experimental setup for particle size distribution measurements.

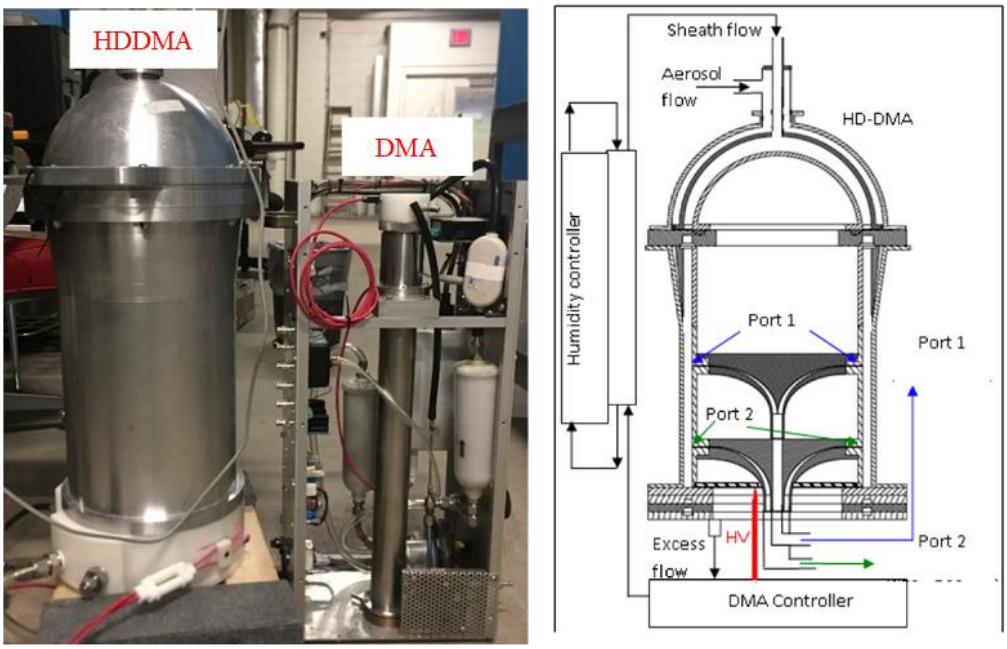

Figure 7. HDDMA (a) comparing with the conventional DMA; (b) inner diagram of HDDMA.

The high-flow SMPS is composed of a customized high-flow dual-channel differential mobility analyzer (HDDMA) for large size-range classification, and a condensation particle counter (CPC). The picture and schematic diagram of the HDDMA is shown in Figure 7. Compared with the conventional DMA, the HDDMA has a significantly larger radius which makes operation at high flow rates (sheath flow of ~100 LPM) possible. However, for the purposes of this study—to measure the size distribution of particles with a broad size range (<100 nm up to 3 µm)—the HDDMA is operated with a lower sheath flow rate (~20 LPM), much less than the sampling condition for which it was designed. The instrument was evaluated at the necessary sampling conditions for accurate data analysis.

2.4 HDDMA/multiple charge algorithm

The charge distribution is determined by first directly measuring the mobility distribution of the dispersed particles with HDDMA without the neutralizer in place, as shown in Figure 8. A CPC is used to measure total particle concentration, and the UHSAS is employed to capture any changes in the PSD as a function of the experimental setup (i.e., removal of the charge neutralizer). The charge number and corresponding fractions can be obtained from the particle size and mobility distribution according to the equation

$$Z_p = \frac{neC_c}{3\pi\mu D_p}, \tag{1}$$

where D_p is particle diameter, Z_p is electrical mobility, n is the number of elementary charges, e is the elementary charge, C_c is the Cunningham Correction factor, and μ is the air viscosity.

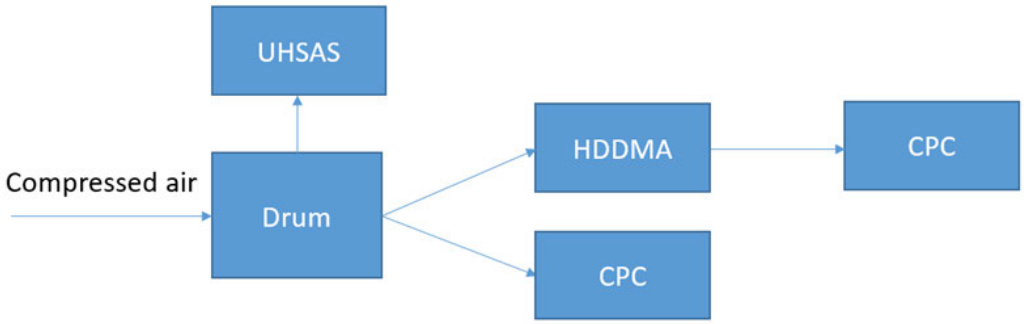

Figure 8. Schematic diagram of experimental setup for PCD measurements.

3. RESULTS AND DISCUSSION

3.1 Particle size distribution

PSDs were collected using the four instruments listed in Table 1. The PSDs of 0.2 µm SiO_2 are shown in Figure 9. Three of the four instruments (APS is out of range) capture the mode peak at 0.2 µm. In addition to the narrow peak at 0.2 µm, there is also a significant fraction of larger size particles. The fraction of larger particles implies that, 1) the commercial SMPS system cannot capture the complete particle size distribution, and 2) multiple charging plays a very import role which must be considered during data inversion. The PSD data is inverted using a newly developed multiple charging correction algorithm,[13] which allows for correction of the PSD due to contributions from multiply-charged particles to the size distribution measurements.

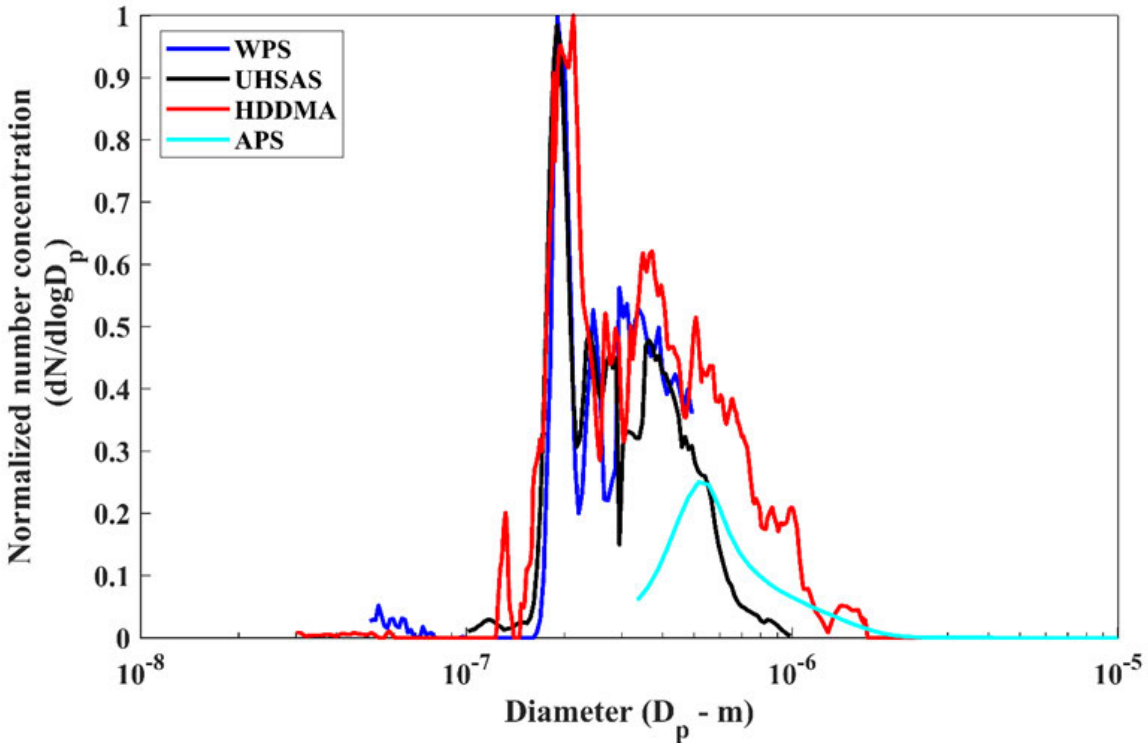

Figure 9. Measured PSD of 0.2 µm SiO_2.

3.2 Particle charge distribution

Upon removal of the charge neutralizer (see setup in Figure 8) upstream of the HDDMA, the mobility distribution is obtained. The mobility distribution for 0.2 µm SiO_2 particles is shown in Figure 10, represented by the black open circles. Using the particle size distribution measurement, the charge distribution can be predicted, depicted by the red dash line in Figure 10. The charge fractions are then obtained from inversion of the matrix

$$S = \begin{bmatrix} N_{1,1} & N_{1,2} & \cdots & N_{1,P} \\ N_{2,1} & N_{2,2} & \cdots & N_{2,P} \\ \vdots & \vdots & \vdots & \vdots \\ N_{M,1} & N_{M,2} & \cdots & N_{M,P} \end{bmatrix} \begin{bmatrix} f_1 \\ f_2 \\ \vdots \\ f_P \end{bmatrix}, \quad (2)$$

where S is the mobility distribution measured by the HDDMA. For simplicity, the size distribution ($dN/d\log D_p$) is shown as N (with a size channel up to M and charge number up to P). The fraction f_i is the then obtained from the inversion. The resultant charge fractions show individual particles with charge values of up to 6+ for 0.2 µm SiO_2.

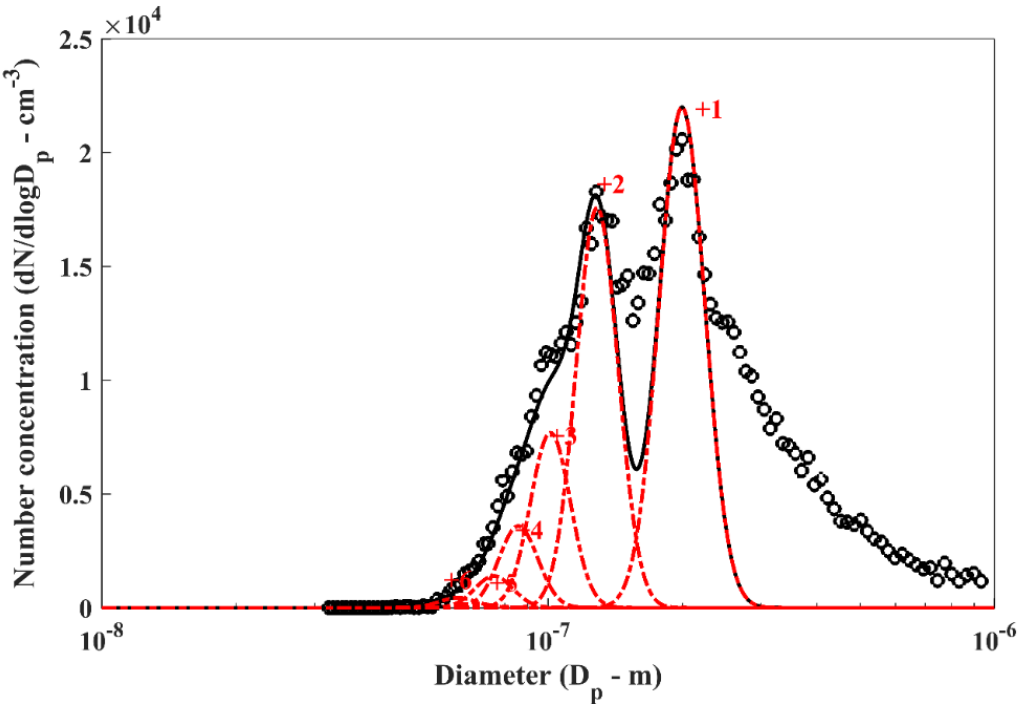

Figure 10. Mobility distribution during 0.2 µm SiO_2 powder generation. The black open circles are the measured mobility values, and the red dashed lines represent the particles with depicted corresponding charger numbers.

3.3 Chemical reactivity—H_2 exposure

In order to investigate the impact of surface charge on the chemical reactivity of the aerosolized material, several well-defined systems were studied. Based on the work of Panayotov et al., several experiments were performed on a Au/TiO_2 sample. Panayotov's research showed that upon exposure to molecular H_2, the Au particles in nanoparticulate Au/TiO_2 cause dissociation of H_2. The generated atomic H hydroxylates the Au–O–Ti linkages surrounding the boundaries of the gold particles. Subsequent to the hydroxylation, hydrogen diffuses into the bulk where it donates electrons to shallow trap states located just below the conduction band.[14] Once the sample is illuminated with IR light, the broad, featureless absorbance from 4000 cm^{-1} to ~1000 cm^{-1} is observed, similar to that seen for reduced TiO_2.[11,14]

TiO_2 powder and aerosols were exposed to ~1 Torr of H_2 in an ultra-high vacuum chamber and characterized before and after dosing using TIR. Figure 11A shows the pre- and post- H_2 exposure spectra for TiO_2 aerosols deposited on a Au-coated W mesh. The spectra are identical with no observable change in the baseline, suggesting that the aerosolized sample already possesses electrons within its shallow trapped states, potentially from the surface charge imparted via the aerosolization process. When the aerosol data is compared to the powder samples (Figure 11B), a small change is seen in the background. The powdered surface has empty trapped states (because there is no surface charge present), therefore upon dosing with H_2, atomic H is taken up, and there is a change in the overall background, along with an observable reactivity to form H_2O.

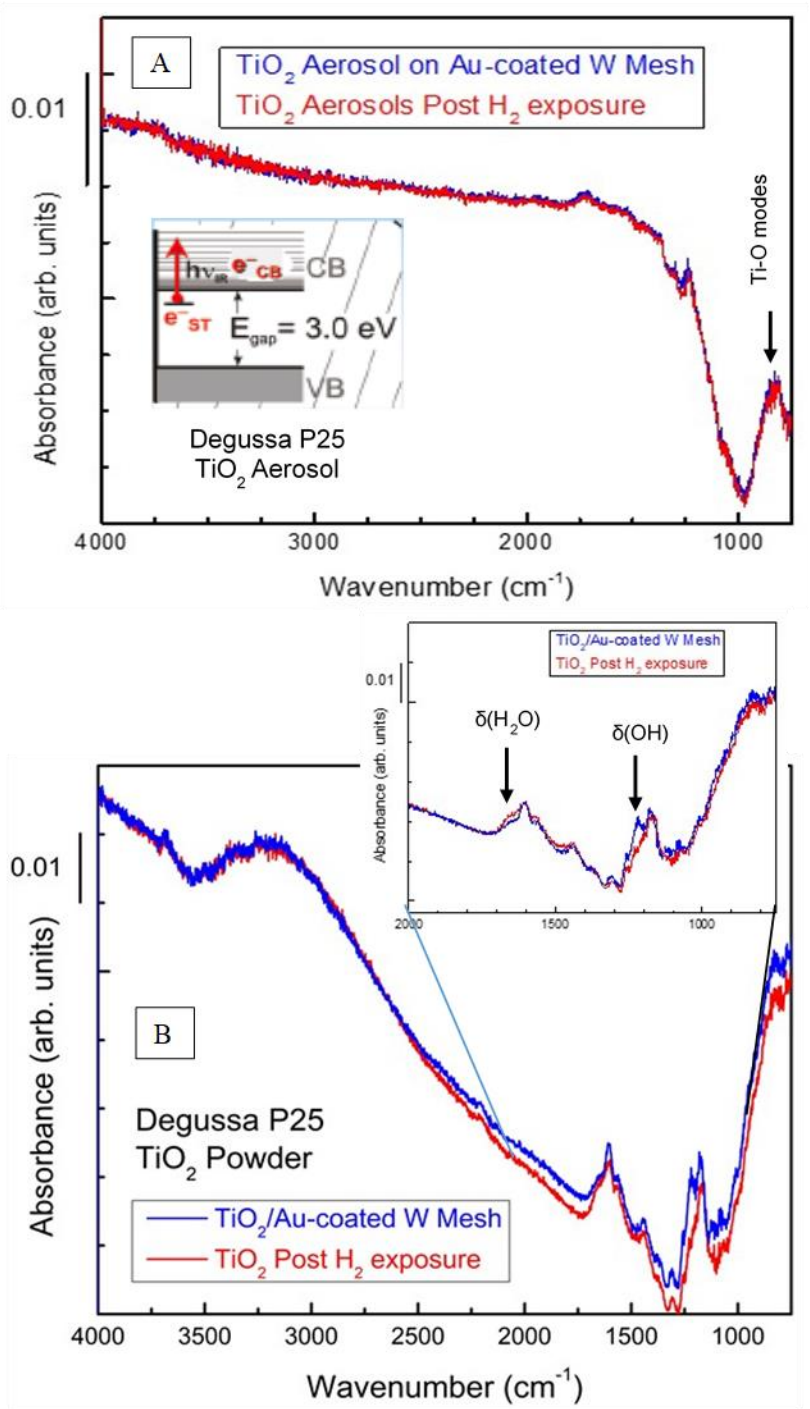

Figure 11. (A) TIR spectra before and after TiO_2 aerosols on a Au-coated mesh were exposed to H_2. (B) TIR spectra of TiO_2 powder pressed into a Au-coated W mesh, before and after exposure to H_2.

3.4 Chemical reactivity—CO exposure

The last series of reactivity studies were performed with CO, as a probe molecule.[14] Literature studies have shown that the accumulation of excess charge in TiO_2 will show a decrease in the interaction of CO.[14] TiO_2 powder pressed into a Au-coated W mesh was cooled to ~100 K, then exposed to 1 Torr of CO. The powder sample did show the uptake of CO at low temperatures—the interaction characterized by a peak at 2165 cm^{-1}. The peak position indicates

CO binding to a Ti^{4+}_{cus} site. The aerosolized TiO_2 sample, also on a Au-coated W mesh, was cooled to ~100 K and dosing with 1 Torr of CO. However, no CO was observed to interact with the aerosolized sample, see Figure 12.

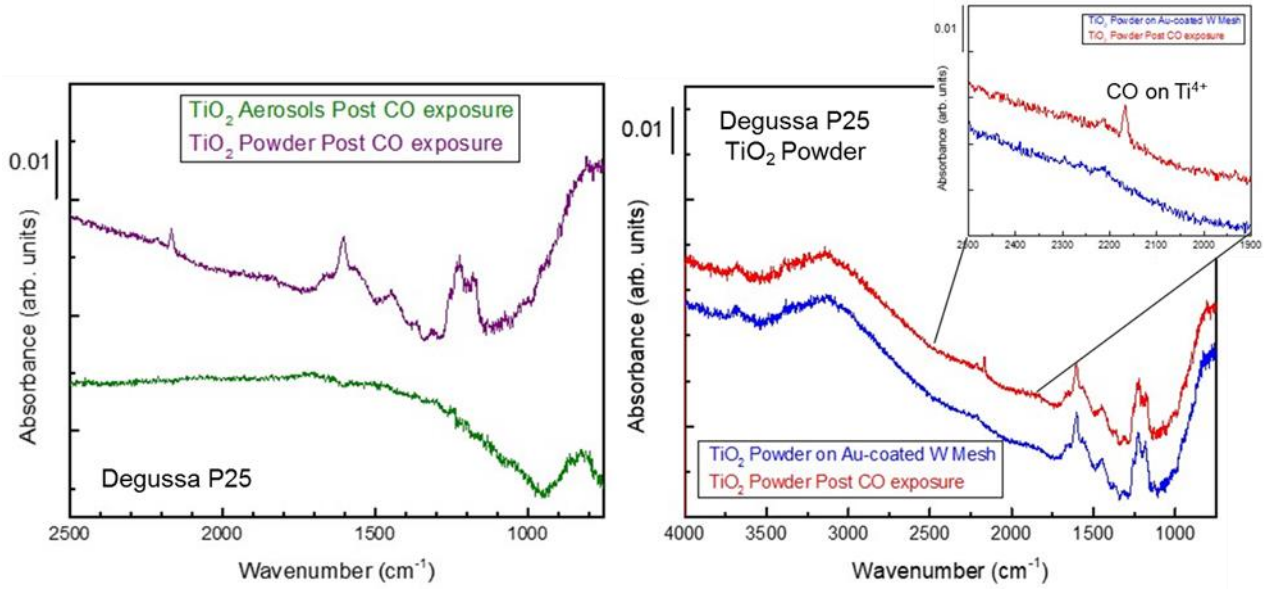

Figure 12. TiO_2 aerosols and powder, on a Au-coated W mesh, exposed to CO. Even at low temperatures, CO was only observed to interact with the powder sample.

4. CONCLUSIONS

Metal oxides, TiO_2 and SiO_2, were aerosolized and subsequently characterized to determine the inherent charge imparted during aerosolization, as well as understand the impact said charge had on the particle's reactivity. The PCD for 0.2 µm SiO_2 particles detected a notable fraction of the particles that possessed 6+ charges. The high amount of surface charge present after expulsive generation was further evaluated, with respect to how it affected the reactivity of TiO_2 with H_2 and CO. In the case of H_2, it prevented the dissociation of molecular H_2 into atomic H, and for CO, initial data suggests the additional charge may prevent the polar molecule from interacting with the surface, even at lower temperatures. Future testing will involve varying the concentration of aerosols for potential quantification of these effects, as well as exploring artificially imparted excess charge (> 10+).

ACKNOWLEDGMENTS

Funding was provided by the U.S. Army via the In-house Laboratory Independent Research Program (PE 0601101A Project 91A) at the Edgewood Chemical Biological Center. The authors would also like to thank Dr. Fountain for his support and feedback.

REFERENCES

[1] Zhang, L.; Gu, Z.; Yu, C.; Zhang, Y.; Cheng, Y. Surface charges on aerosol particles – Accelerating particle growth rate and atmospheric pollution. *Indoor Built Environ.* **2016,** *25* (3), pp 437–440.

[2] Durke, E.M.; McEntee, M.; Dhaniyala, S. Characterization of aerosol particle charge and the impact of a high degree of charge on the particle's physical and chemical properties. *FY17 Proceedings of the Edgewood Chemical Biological Center In-house Laboratory Independent Research and Surface Science Initiative Programs;* U.S. Army Edgewood Chemical Biological Center: Edgewood, MD, **2018;** pp 1–8.

[3] Göpel, W.; Anderson, J.A.; Frankel, D.; Jaehnig, M.; Phillips, K.; Schafer, J.A.; Rocker, G. Surface defects of TiO_2(110): A combined XPS, XAES and ELS study. *Surf. Sci.* **1984,** *139* (2–3), pp 333–346.
[4] Nelson, J.; Haque, S.A.; Klug, D.R.; Durrant, J.R. Trap-limited recombination in dye-sensitized nanocrystalline metal oxide electrodes. *Phys. Rev. B.* **2001,** *63* (20), p 205321.
[5] Diebold, U.; Li, M.; Dulub, O.; Hebenstreit, E.L.D.; Hebenstreit, W. The relationship between bulk and surface properties of rutile TiO2(110). *Surf. Rev. Lett.* **2000,** *7* (5–6), pp 613–617.
[6] Wang, H.; He, J.; Boschloo, G.; Lindstrom, H.; Hagfeldt, A.; Lindquist, S.-E. Electrochemical Investigation of Traps in a Nanostructured TiO_2 Film. *J. Phys. Chem. B.* **2001,** *105* (13), pp 2529–2533.
[7] Thompson, T.L.; Yates, J.T. Monitoring Hole Trapping in Photoexcited TiO_2(110) Using a Surface Photoreaction. *J. Phys. Chem. B* **2005,** *109* (39), pp 18230-18236.
[8] Ganduglia-Pirovano, M.V.; Hofmann, A.; Sauer, J. Oxygen vacancies in transition metal and rare earth oxides: Current state of understanding and remaining challenges. *Surf. Sci. Rep.* **2007,** *62* (6), pp 219–270.
[9] van de Lagemaat, J.; Frank, A.J. Nonthermalized Electron Transport in Dye-Sensitized Nanocrystalline TiO_2 Films: Transient Photocurrent and Random-Walk Modeling Studies. *J. Phys. Chem. B.* **2001,** *105* (45), pp 11194–11205.
[10] Ghosh, A.K.; Wakim, F.G.; Addiss, R.R. Photoelectronic Processes in Rutile. *Phys. Rev.* **1969,** *184* (3), p 979.
[11] Panayotov, D.A.; Morris, J.R. Thermal Decomposition of a Chemical Warfare Agent Simulant (DMMP) on TiO2: Adsorbate Reactions with Lattice Oxygen as Studied by Infrared Spectroscopy. *J. Phys. Chem. C.* **2009,** *113* (35), pp 15684–15691.
[12] Calabrese, R.V.; Ranade, M.B. Pneumatic Nozzle Dissemination of Powders into Air; TCN 91291; U.S. Army Research Office: Research Triangle Park, NC, **1993;** UNCLASSIFIED Report.
[13] He, M.L.; Dhaniyala, S. A multiple charging correction algorithm for scanning electrical mobility spectrometer data. *J. Aero. Sci.* **2013,** *61*, pp 13–26.
[14] Panayotov, D.A.; Burrows, S.P.; Yates, J.T.; Morris, J.R. Mechanistic Studies of Hydrogen Dissociation and Spillover on Au/TiO2: IR Spectroscopy of Coadsorbed CO and H-Donated Electrons. *J. Phys. Chem. C.* **2011,** *115* (45), pp 22400–22408.

Effect of quorum sensing molecules on the production of bacterial nanocellulose materials

Rabih E. Jabbour[a*], Kurt R. Kunkel[b], Erik D. Emmons[a], Ashish Tripathi[a]
[a]U.S. Army Edgewood Chemical Biological Center, Research & Technology Directorate, 8198 Blackhawk Rd, Aberdeen Proving Ground, MD 21010
[b]Univeristy of Maryland, A. James Clark School of Engineering, 8228 Paint Branch Dr, College Park, MD, 20742

ABSTRACT

Bacterial nanocellulose has been shown as a remarkably versatile nano-biomaterial with a variety applications in medicine, defense, electronics, and optics. In contrast to plant cellulose, bacterial nanocellulose has several advantages—high purity and crystallinity, large surface area, durability, and biocompatibility—making it widely used as a multifunctional material. While advantageous in many ways, bacterial nanocellulose materials can be difficult to manufacture and process into useable forms. In many instances, bacterial nanocellulose pellicles are not uniform in their composition. This is often due to a heterogeneity of cell density, often leading to large clusters of dense cellular growth. The aim of this research is to study the mechanism of quorum sensing molecules, specifically homoserine lactones, and their effect on the production of bacterial nanocellulose utilizing a synthetic biology approach. We believe that the bacterial nanocellulose morphology can be controlled through manipulation of the quorum sensing pathways of the bacterium. In this first-year effort, we investigated the fundamental factors that affect the growth of nanocellulose biofilm. The resulting data show that there is a direct correlation with the type of the quorum sensing molecules introduced during growth phase—the yield of bacterial nanocellulose is affected by the position and age of the static growth layer. Also, preliminary morphological studies showed a direct impact of the homoserine lactone molecules and the thickness of the fiber based on scanning electron microscope data. These experimental data will enhance our understanding and optimization of the quorum sensing molecule signals and expression levels, to improve bacterial nanocellulose production and customization.

Keywords: bacterial nanocellulose, biofilm, pellicles, materials, quorum sensing, homoserine lactones

1. INTRODUCTION

Nanocellulose materials can be obtained from two vastly different sources. Nanocellulose fibrils can be isolated from plant biomass or from bacterial-based sources—mainly the *Gluconacetobacter* genus. The bacterial cellulose, referred to as bacterial nanocellulose (BNC), is a remarkable material that has desired chemical and physical properties that make it very useful in various applications including tissue engineering, medicine, defense, fabrics, and electronics. However, the plant-based nanocellulose material is energetically costly and laborious to manufacture. Additionally, while the small rod-like structures can be used in the production of thin films and other materials, the physical properties of the materials are often reduced compared to those of the bacterial-based ones.

BNC is formed at the air–media interface of active *Gluconacetobacter xylinus* cultures. BNC nanofibers are synthesized from glucose units by *Acetobacter* cellulose synthase operon proteins and secreted by forming an interconnected cellulose "pellicle" around cells.[1–3] BNC pellicles are comprised of long cellulose fibrils that intertwine with each other and are highly free from other chemical compounds like lignin and pectin. BNC films often demonstrate a higher strength and flexibility than plant-based ones.[4] BNC can also be easily modified and functionalized through genetic engineering and/or synthetic biology approaches.[5–11] While advantageous in many ways, BNC materials can be difficult to manufacture and process into useable forms. In many instances, bacterial cellulose pellicles are not uniform in their composition. This is often due to a heterogeneity of cell density which often leads to large clusters of dense cellular growth. While methods have been developed to circumvent some of these during BNC production, abnormalities and irregularities in the pellicles are still encountered, no success has been achieved to date with controlling the fibril density, mechanical properties of the film, or rate of production.

Homoserine lactones (HSL) are vital quorum sensing (QS) molecules that enable bacterial cells to regulate growth and behavior of their community. HSLs consist of various acyl side chains of 4–14 carbon atoms and may also contain double bonds. The carbon chain of HSLs can be hydroxylated or oxidized to a carbonyl-carbon—resulting in quite different physicochemical properties. HSLs are the most common QS signals in Gram-negative bacteria and coordinate important temporal events—specifically, the formation of biofilms in nature and in humans.[12–13] Little has been known about the correlation between bacterial cellulose production, fibril density, pellicle thickness, and the expression of different HSL QS molecules. As such, we will address vial questions related to the proposed hypothesis, such as: 1) the kinetic impact of the QS signals of the HSLs on the synthesis of the BNC, 2) the rate of the cellulose production is affected at specific time points in the presence or absence of QS molecules, and 3) the contribution of each QS molecule to the production of cellulose and its impact on its fibril density and pellicle thickness.

Prior to utilizing BNC in various applications, it is imperative that fundamental research is performed to seek the ideal BNC composition for each individual application. There are many factors that could assist the BNC to perform to its maximum potential. For instance, morphological characterization and physical properties of the BNC (i.e., pore size, nanofiber diameter, and density) could all affect how well the BNC performs in each application. The objective of this first-year research is to grow the bacterial cellulose under different growth conditions, including the addition of different HSL signaling molecules to the growth media of each pellicle. Also, different concentration levels of the HSL molecules were added. Our initial data showed that while the type of HSL molecule does affect the morphology and physical properties of the BNC, varying the concentration of the HSLs did not affect the physical or morphological properties of the BNC. The data showed that it is possible to correlate the impact of HSLs, acting as QS molecules, with that of the morphological characteristic of the BNC.

2. MATERIALS AND METHODS

2.1 Bacterial strains

The bacterial strain used to produce the nanocellulose was *G. xylinus*. The bacterial strain was obtained from ATCC as *G. xylinus* strain 10245 (Manassas, VA). The *G. xylinus* strain was cultured in Hestrin and Schramm medium (HS medium) with 2 % glucose (wt/vol). The stock bacterial culture was added to 10 mL of HS media in 50-mL conical tubes and was grown at 27 °C over 3–7 days depending on the amount of biofilm formation. The growth was done under static culture in which no agitation of the culture broth was performed. Once the bacterial cellulose biofilm formed, it was removed for further processing and characterization.

2.2 Cellulose production and purification

The bacterial cellulose formed, on average, after 72 hours of growth time. The formation of bacterial cellulose occurred in static culture; cells were grown in 50-mL conical tubes containing 10 mL of HS medium at 27 °C for 3–7 days. The cellulose pellicles were then isolated and purified by treating them with 0.5 % NaOH at 100 °C for 1 hour, followed by extensive washing with milli-Q® H_2O to remove the excess NaOH solution and reduce the pH. The pH of the pellicle was checked periodically throughout the water washing step and was maintained at 4–5. Following the water wash, the pellicles were dried out at 30 °C for 24 hours and then weighed on an analytical balance. The mass obtained was normalized to include the culture volume used in order to compare the pellicle's yield from the addition of different HSLs. Pellicles that were cleaned but not processed were kept in 0.1 M sodium azide solution.

2.3 Solvent extraction of HSLs from the BNC pellicles

The extraction of the HSLs for MS analysis was done following the method reported by Shaw et al.[14] Briefly, after BNC pellicles were collected, the supernatant was centrifuged to remove bacterial cells and any cellular debris. Centrifugation occurred at 14,000 rpm for 15 minutes at a controlled temperature of 4 °C. Following centrifugation, the supernatant was extracted with either 100 % or 50 % cold MeOH solutions. The latter step was repeated three times for each of the methanol solutions. The extract was allowed to evaporate at room temperature and then resuspended in 2 mL milli-Q® H_2O and 2 mL of 3X ethyl acetate. The ethyl acetate partition was then evaporated and the residue was resuspended in hexane-ethyl acetate (90/10) prior to solid phase extraction. The solid phase extraction method selected was a silica hydrophilic phase. The column was washed with ethyl acetate then equilibrated with the hexane/ethyl acetate solution (90/10). The elution solvent was a mixture of hexane/ethyl acetate (95/5) ratio. The eluted samples were transferred to the MS vials for analysis.

2.4 Characterization of the bacterial proteins of the BNC pellicles

The extracted bacterial suspension from the BNC pellicles were vortexed followed by 2 minutes of lysis using bead beating process. The lysed supernatant was decanted into a new 2-mL tube and centrifuged at 6,600 x g (15,000 rpm) for 20 minutes to pellet the bacterial cells. The subsequent protocol for the denaturing and trypsin digestion of the extracted proteins from the BNC pellicles was followed. The resulting tryptic peptides were analyzed using LC-MS/MS.

2.5 LC-MS/MS analysis of the extracted BNC supernatants

The extracted HSLs were separated using a capillary Hypersil C18 column (300 Å, 5 µm, 0.1 mm i.d. x 100 mm) by using the Thermo Scientific™ EASY-nLC™ system. The elution was performed using a linear gradient from 98 % A (0.1 % formic acid in water) and 2 % B (0.1 % formic acid in ACN) to 60 % B over 60 minutes at a flow rate of 200 µL/min, followed by 20 minutes of isocratic elution. The resolved analytes were electrosprayed into a Thermo Scientific™ Q Exactive™ Orbitrap mass analyzer (at a flow rate of 0.2 µL/min. Product ion mass spectra were obtained in the data dependent acquisition mode consisting of a survey scan over the *m/z* range of 400–2,000 followed by a single scan on the most intense precursor ions activated for 30 milliseconds by an excitation energy level of 35 %. A dynamic exclusion was activated for 3 minutes after the first MS/MS spectrum acquisition for a given ion.

2.6 Protein database and database search engine

A protein database was constructed in a FASTA format using the annotated bacterial proteome sequences derived from fully sequenced chromosomes of all available bacterial strains and more than 120 common laboratory contaminant proteins. The program PERL (http://www.activestate.com/Products/ActivePerl; accessed April 2018) was used to download these sequences automatically from the National Institutes of Health National Center for Biotechnology site (http://www.ncbi.nlm.nih.gov; accessed April 2018). Each database entry for a given protein sequence has information about a source organism and about a genomic position of the respective open reading frame (ORF) embedded into a header line. The constructed bacterial proteome database resulted from translating putative protein-coding genes and consists of the corresponding amino acid sequences of potential tryptic peptides from the included bacteria and the common laboratory's contaminants. COMET[15] (open source) was used to generate the *in silico* tryptic peptides; two missed cleavages were allowed during this process.

The experimental MS/MS spectral database of bacterial peptides was searched using the COMET algorithm against the constructed proteome database of microorganisms. The COMET thresholds for searching the product ion mass spectra of peptides were correlation score (Xcorr), relative correlation score (ΔCn), specificity (Sp), relative specificity (RSp), and change in the mass of the peptide (ΔMpep). The top peptide hits generated by COMET were filtered with a $\Delta Cn > 0.1$ and the filtered hits were accepted as peptide identifications when their correlation scores (Xcorr) were higher than the thresholds that allowed generating a desired false discovery rate (FDR) value.[15] A protein is identified as present when it is matched with at least two or more validated peptides in an analyzed sample. The ABOid algorithm infers identification of the analyzed sample using assignments of organisms to taxonomic groups (phylogenetic classification) based on an organized scheme that begins at the phylum level and follows through classes, orders, families, and genus down to the strain level.

2.7 Raman chemical imaging spectroscopy measurements

The Raman chemical imaging analysis of the BNC samples were taken in Stokes vibrational spectra. The Raman spectroscopy experiments were performed using a WITec alpha300 R confocal Raman microscopy system. A 100X microscope objective in the Raman microscopy was used. A Rayshield™ notch filter was used to provide low-frequency Raman spectral features (from a wavenumber of 10 cm^{-1}). The laser used was a solid-state laser with a wavelength of 532.1 nm. A wavelength of 532 nm was used for excitation, with a power of ~2 mW incident on the substrate. The Raman-scattered light was collected in the backscattering configuration and transmitted through a 100-µm slit to a 600 grooves/mm grating, which dispersed the light onto a thermoelectrically cooled charged-coupled device camera (WITec DV401 A). A spectral resolution of approximately 5 cm^{-1} was obtained. Spectra were acquired with 5-second to 10-second acquisition times. At a lower Raman shift, spurious contributions from the elastic line can be detected by measuring the scattering from a metal surface. In the anti-Stokes side, our spectrometer instrument response is better, which allowed us to measure the Raman spectrum down to 5 cm^{-1} of the Raman shift. The sample image in the entrance spectrometer plane was selected in such a way that the contribution from the glassy slide did not come into the spectrometer. No polarization selection was used.

2.8 SEM measurement of BNC pellicles

Measurements were performed with a Phenom ProX desktop SEM. A beam energy of 15 keV was used to obtain the images shown. The samples were coated with ~30 nm of gold using a vacuum thermal evaporator system prior to the measurements to reduce charging and beam damage effects from the electron beam. The SEM is also equipped with energy dispersive spectroscopy capability, allowing for determination of the elemental content of the analyzed materials.

3. RESULTS AND DISCUSSIONS

3.1 MS analysis of extracted supernatant from BNC pellicles

The extracted supernatant from the BNC pellicle was analyzed using LC-MS/MS in order to determine the HSL excreted by the *G. xylinus* during the biofilm formation. Figure 1 shows the full mass spectrum of the extracts, showing that there are four major peaks that were scanned in MS/MS mode to reveal the chemical structure and infer a chemical identity. The MS/MS for two of the HSLs—decanoyl homoserine lactone (DHL) and dodecanoyl homoserine lactone (DDHL) are also shown in Figure 1; the other two HSLs identified were hexanoyl homo lactones (HXHL) and oxydodecanoyl homoserine lactones (ODDHL) (not shown). The HSL identification was achieved through the comparison of their tandem mass spectra with standard spectra for the mentioned compounds. However, it is noteworthy to mention that the tandem mass spectra for the identified HSLs, extracted from the BNC pellicle, have a lower signal-to-noise ratio than standard spectra obtained from stock solutions of the same lactone molecules. This could be due to the presence of impurities in the extraction samples which could be seen in the full mass spectra for these samples. Once these HSLs were identified, we analyzed their stock solutions using same LC-MS/MS method to establish a verification of their mass spectra. Moreover, literature showed these HSL are also identified in the same strain—with the exception of oxydodecanoyl, which is reported with near neighbor strains of the *G. xylinus* (i.e., *Pseudonomas aeruginosa* and *Pseudonomas* syringae.)[14]

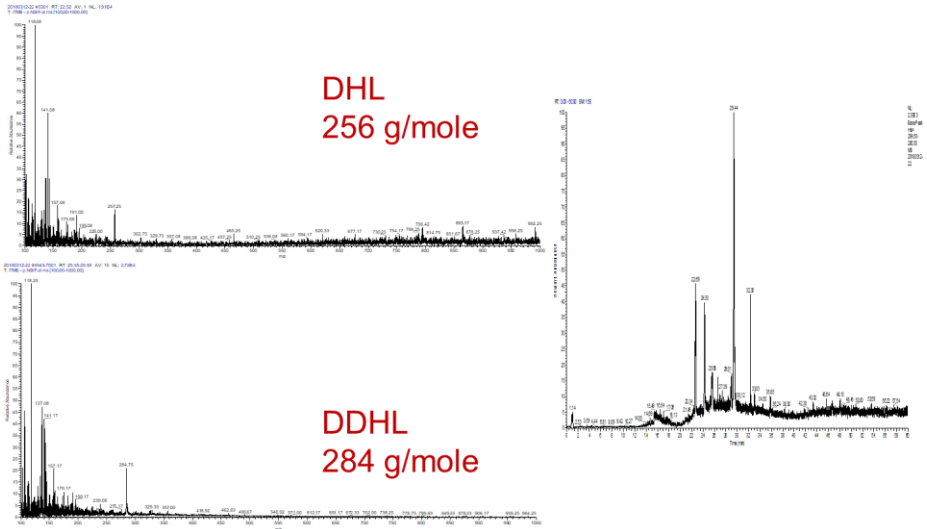

Figure 1. Mass spectral analysis of the extracted HSLs. (right) full mass spectrum for the extraction LC-MS analysis, (top left) MS/MS spectrum representing the mass spectral signature peaks for DHL, (bottom left) MS/MS spectrum representing the mass spectral signature peaks for DDHL.

The presence of ODDHL molecules in the *G. xylinus* culture implicated a verification of the strain present, resulting in the analysis of bacterial proteins obtained from processing a lysed bacterial sample of *G. xylinus*. The LC-MS/MS results showed a 95 % confidence level matching between our analyzed sample of *G. xylinus* and its public entry extracted from the NBCI depository. This was shown using our in-house algorithm, but we also utilized a public protein tool consortium to identify the experimental proteins using a non-redundant and nonrestrictive microbial database. Most of the proteins—especially those responsible for cellulose and homoserine synthesis—were strain specific with an E-value at 2×10^{-17} and a 100 % positive identification match with the experimental sequences.

Although cellulose synthase 1 operon protein is present in different BNC-forming strains, some of them are unique and have certain sequence altercation that make them strain unique[16–19] as shown in Figure 2.

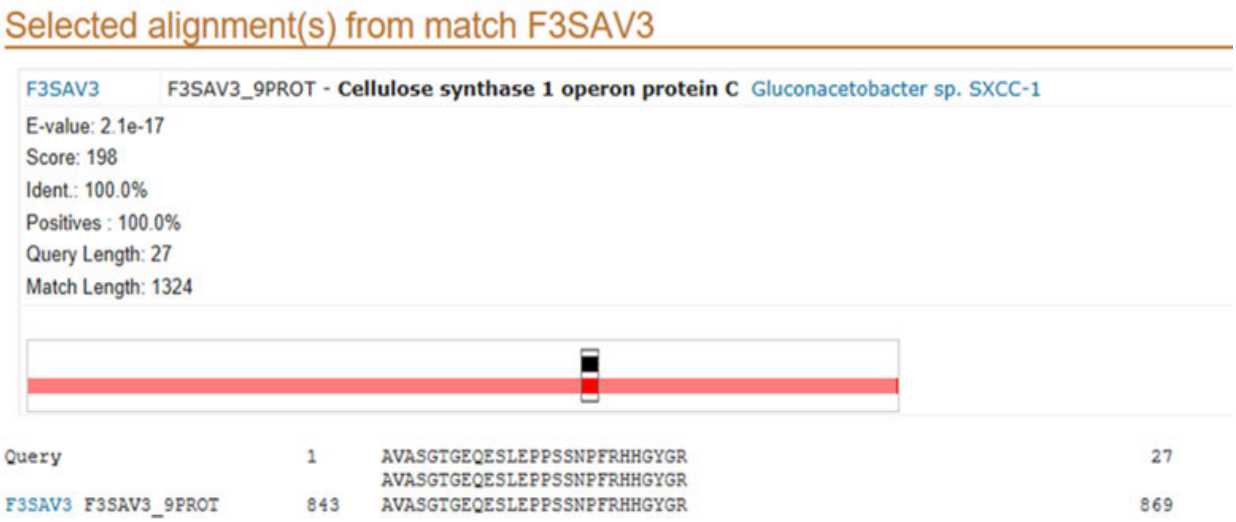

Figure 2. The output result of Uniprot® Consortium proteomic tools for the identification of experimental peptides with non-redundant microbial database containing curated Gram-positive and Gram-negative bacteria.

3.2 Effect of growth time on the yield of BNC pellicles

The *G. xylinus* strain was grown in static conditions and after 5 days a new culture media was added to the top of the same tube that had already formed a BNC pellicle. The new culture media was allowed to grow for another 5 days and, followed by the addition of another 5 mL of the culture media, and then allowed to grow for another 5 days. The resulting solution contained three distinct layers of BNC pellicles, separated by the added media. The three separated layers of BNC pellicles have the one at the bottom of the tube being the oldest (15-day), the middle layer (10-day), and the top layer (5-day). Figure 3a shows the average weight of the BNC pellicle for each layer. The layers were labelled as (T) for top layer, (M) for medium layer, and (B) for bottom layer. The higher the layer, the younger its growth age and vice versa. Figure 3b shows a picture of the growth tube that contained three different layers of BNC pellicles separated by the culture media. These results showed that the weights of the bottom and middle layers were greater than the top layer. This could be attributed to the fact that the bottom and middle layers were exposed to culture media from both below and above the BNC pellicles, thereby receiving additional nutrients with which to form more pellicles. Also, being exposed to more nutrients might produce more bacterial cells that in turn could form more pellicles. However, the top layer did not have culture media above it, thus its pellicle formation depended solely on the amount of nutrients provided by the single layer of growth media below. This data showed a drastic change in the dry weight of the BNC pellicles due to the growth period and to the position of the BNC biofilm layer in such static growth conditions. This observation is important to consider when growing BNC pellicles and could provide a guide to the growth approach of BNC biofilm, depending on the desired production amount and growth time.

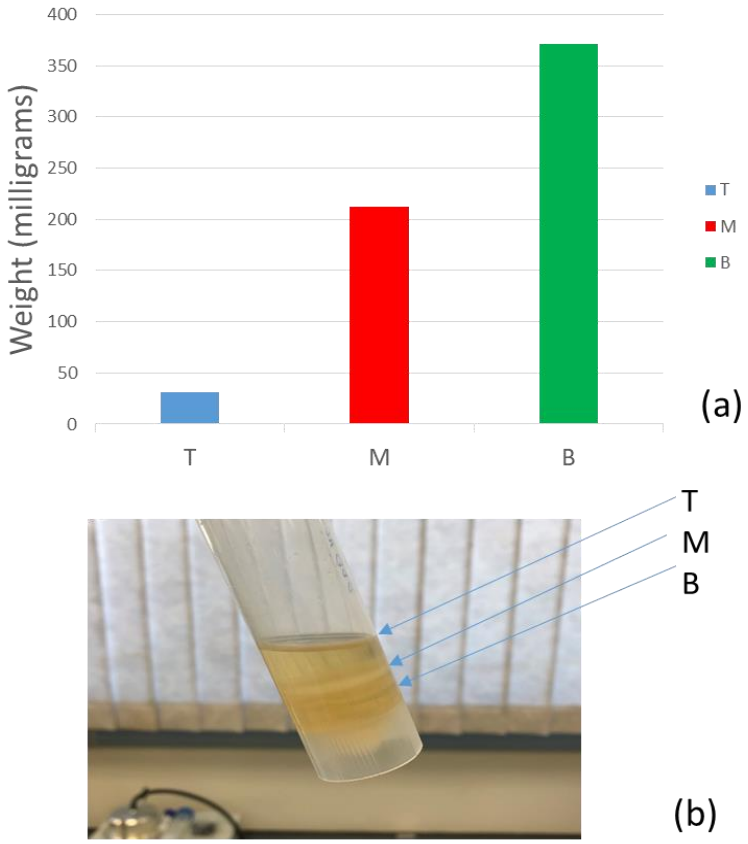

Figure 3. Effect of growth stage on the yield of BNC pellicles. (a) shows the average weight of triplicate samples, (b) depicts a pictorial view of the pellicle's static growth over a period of 15 days—three different layers of BNC pellicles can be seen. Image was cropped for clarity.

3.3 Effect of HSLs on the thickness of BNC pellicles

In order to understand how the type of HSL could potentially impact the physical properties of the BNC pellicles, different HSLs were introduced to the growth media of the BNC pellicles and effect on the thickness of the BNC pellicles was investigated. Measuring the thickness of the BNC pellicles could provide an indication on the potential impact of HSLs on BNC formation. Figure 4 shows the result of introducing five different HSLs to the growth media of *G. xylinus*. The thickness of the formed pellicles was measured at different growth times (48 hours, 72 hours, and 144 hours). The overall trend shows that there is a maximum increase in the thickness of the pellicle up to 72–96 hours, and then a plateau out pattern after such growth time. The type of HSL shows a more significant impact on thickness up to 72 hours of growth time. Within this time range, the HXHL increase the pellicle thickness the most as compared to other lactones, namely the DHL, DDHL, and ODDHL. Although the thickness of the BNC pellicles do not show any measureable increase after 96 hours of growth, there is no change in the order of HSL molecules that provides the highest thickness. Clearly, there is different impact on the BNC formation based on type of HSLs infused with the culture media during growth phase that could be attributed to change in morphology of the BNC pellicles. The potential explanation for such behavior could be due to the fact that certain signal molecules could have variable impact on signal transduction during BNC pellicle formation, or there is a more efficient route for certain HSLs to induce the cell to produce more of the pellicles. Such explanations need to be validated through genetic manipulation of the genetic factors that affect the production of specific HSLs.

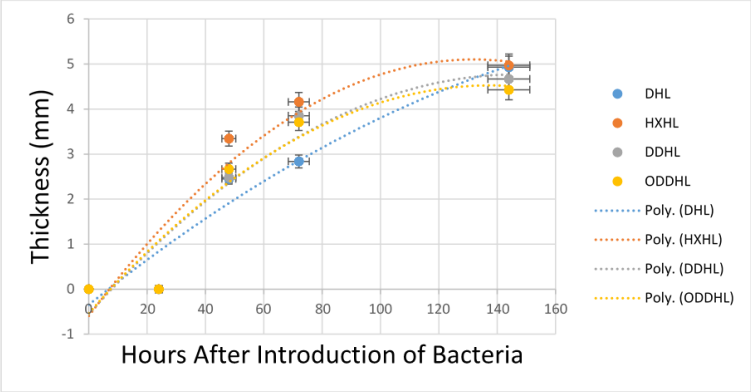

Figure 4. The effect of different HSL molecules on the thickness of the BNC pellicles.

Changing the concentration levels of the added HSLs to the growth media of *G. xylinus* was also investigated. Three different concentration levels were used (0.1 µg/mL, 0.5 µg/mL, and 1.0 µg/mL). The different concentration levels of HSLs were selected to introduce between 5–100 ng of HSL molecules into the growth media based on reported literature.[14] Figure 5 shows the effect of the concentration levels of HSL on the thickness of the BNC pellicle and the result obtained from the addition of HXHL. This HSL was selected because it showed the greatest increase of the BNC pellicle thickness when compared to other HSLs (as shown in Figure 4). However, a change in the added concentration of HSLs did not significantly affect the thickness of the BNC pellicles as shown in Figure 5. The three data sets differ in concentration of the signaling molecule. There was no growth until 48 hours and the growth period plateaued after 144 hours. There is little difference in the thickness when the pellicles are compared by concentration. This could be due to bacterial secretion of sufficient amount of HSL that is enough to initiate the signal process for the BNC pellicle, thus the added amount of HSLs were beyond the needed amount for the regulatory circuit that controls BNC pellicle formation. It should be noted that other HSLs have the same pattern as HXHL (data not shown) with no significant change in the thickness of the pellicle as compared to standard culture of *G. xylinus* with no added HSLs.

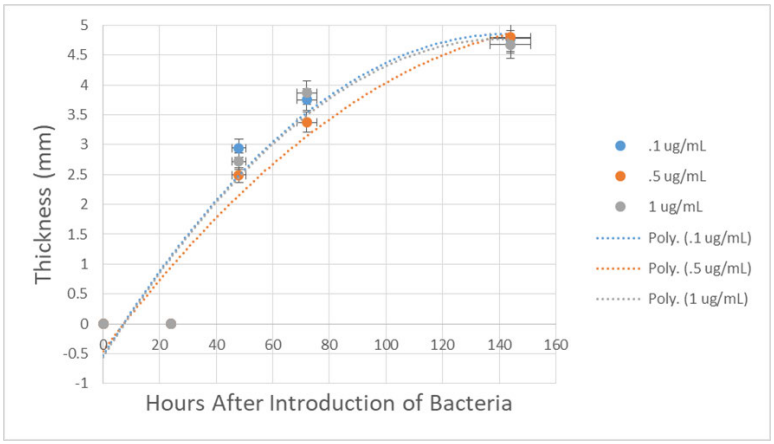

Figure 5. Effect of HSL concentrations on the thickness of the pellicles over 144 hours of growth.

3.4 Raman chemical imaging of BNC pellicles

Raman chemical imaging has been shown to be an effective technique to differentiate chemical mixtures present on a given surface. Moreover, Raman chemical imaging can provide imaging modalities by probing tissues and microorganisms at subcellular resolution, providing a visual output of the morphological and chemical details of the tested samples. Raman chemical imaging was utilized in this study to verify that the formed BNC are truly cellulose and can be distinguished from non-cellulose fibril materials. As such, an aluminum slide was spotted with 5 µL of the BNC pellicle residue and was allowed to dry at 27 °C for 2 hours. A field of view image was scanned in the xy field of view and chemical and field of view images were superimposed to provide the montage chemical image shown in Figure 6. In Figure 6a, a montage Raman chemical image reflects the different constituents deposited on the aluminum

slide. Figure 6b shows the corresponding Raman spectra for each region on the aluminum slide. Figure 6c shows the Raman signature region for cellulose material, especially the peaks at 1362 cm^{-1} and 1457 cm^{-1}, which are indicative of the presence of a CH_2 band in the cellulose polymeric materials; once the CH_2 band becomes deformed it will shift toward 1362 cm^{-1}.[20] The cellulose signature peaks are not present in either the green material located on the cellulose fibrils or in the background region that corresponds to supernatant material of the BNC pellicle.

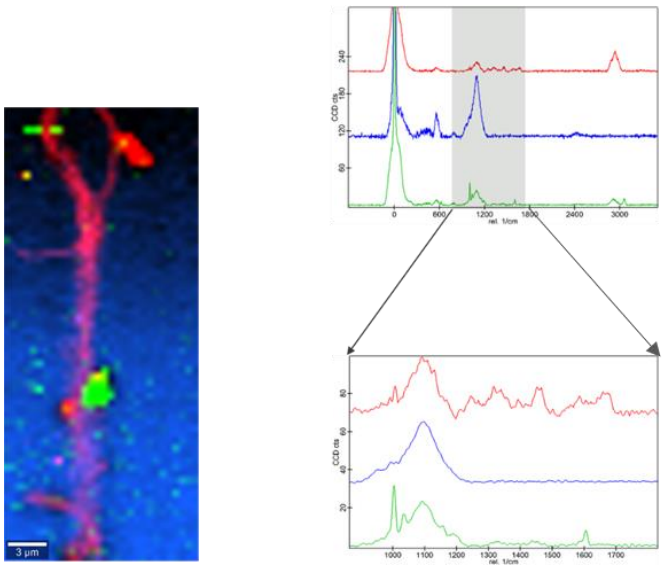

Figure 6. The Raman chemical imaging of effect of different HSL molecules on the thickness of the BNC pellicles. (a) montage Raman chemical image of the field of view, (b) normal Raman spectra for the corresponding region shown in Figure 3a, and (c) represents the Raman signature region that contains specific Raman shifts specific for cellulose polymeric material.

3.5 Effect of the HSLs on the morphology of the BNC pellicle

Morphological characterization of the BNC pellicle was investigated using SEM to determine the potential 2D-spatial variation due to the presence of different HSLs in the growth media of *G. xylinus*. The SEM analysis was focused on determining any potential changes of the BNC fiber diameter after the addition of the HSL signaling molecules. The diameter of the nanofibers was measured via the software program Fibermetric® interfaced to a bench-top SEM. SEM images for pellicles from different growth conditions were acquired. The SEM images were collected at 15 keV and 1–5 µm resolution. Six different pellicle samples were analyzed—four of which had HSL signaling molecules and two were control samples with no HSL signaling molecule. Figure 7 shows the output of the SEM measurements with the fiber diameter distribution provided by the Fibermetric® software as histograms for all the available fibers in the field of view. There is variability in the diameter size for the pellicles with signaling molecules when compared to the pellicles without. Moreover, it noteworthy to point out that when the *G. xylinus* was grown in static mode utilizing a petri dish filled with a thin layer of growth media amounting to 5 mL, the formation of thin BNC pellicles was successful. The SEM analysis of this thin film of pellicle showed a non-uniform surface with a sheet-like shape dominating the field of view as compared to the conventional fibril characteristic of the BNC pellicles, which is seen in standard static mode of growth in the 50-mL conical tubes.

Upon calculating the average diameter of the BNC fibers, it was determined that most of the pellicles produced from growth media containing HSLs had a larger average diameter as compared to that of the pellicle grown with no HSLs. However, when the SEM data are compared with the thickness measurements for the same HSLs, a direct correlation can be determined. Figure 8 shows the average diameter of the BNC fibers from different growth phase of BNC pellicles with different HSLs. Figure 8 shows that most of the added HSLs enlarged the diameter of the fibers without altering its shape or integrity. While this explanation is based on our experimental data, further experimental investigation of the factors affecting the enlargement of the pellicle in the presence of HSLs are needed. These experiments will address, on the micro level, the impact of genetic materials responsible for the secretion of HSLs and how the manipulation of these factors can impact the formation of BNC pellicles. Also, atomic force microscopy experiments have been initiated to provide specific information on the 3D-spatial variation of the pellicle morphology.

Such experiments are valuable in terms of providing a more accurate picture on morphological changes and if these changes are a direct result of the presence of HSLs in the growth media for *G. xylinus*.

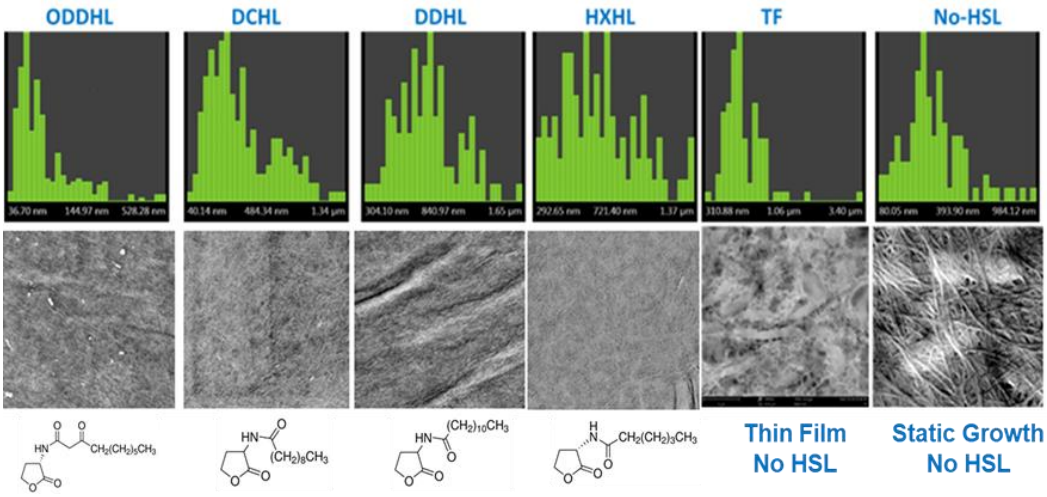

Figure 7. The SEM analysis of the different cultures containing HSLs. The top panel represents the distribution of the diameter sizes for the field of view of the detected bacterial fibers. The bottom panel represents the SEM images obtained for each BNC pellicle.

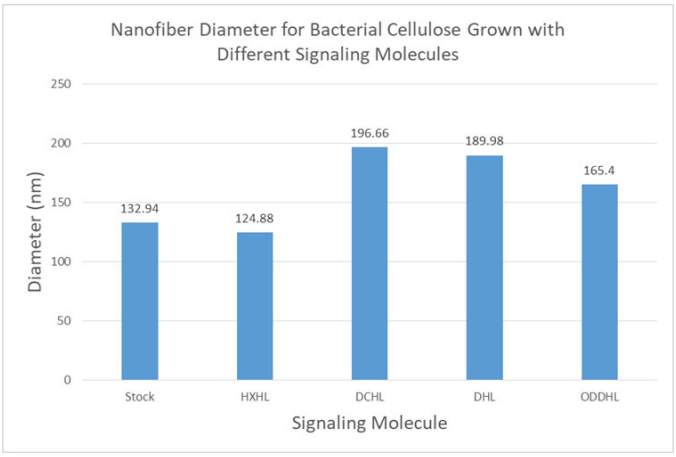

Figure 8. The average diameter of the BNC fibers obtained from the SEM data analysis for the different BNC fibers.

4. CONCLUSIONS

The experimental results showed that BNC pellicles can be manipulated using different experimental conditions and that signaling molecules seem to have direct impact on their physical properties and morphology. While there is still more work needed to confirm the present findings, they are useful for understanding BNC biofilm formation and how its physical properties are affected by QS molecules. More in-depth research into the genetic materials that control the formation and secretion of the HSL signaling molecules is needed to gain insight on the characteristics of the BNC biofilm formation. Although we were able to identify experimentally four different HSL molecules, this does not indicate that the bacterial strain is not producing different HSL molecules. Modulation of the HSL production by regulatory circuits may influence the BNC biofilm formation and provide a natural way to produce tailored BNC for certain applications. Identifying and characterizing such regulatory process may be useful in developing efficient synthetic biology approaches to produce desired BNC biofilms.

Genomic-based experiments are planned to study the physical properties of BNC pellicles and to provide better understanding of the BNC biofilm formation mechanism during the secretion of HSL signaling molecules. This genetic engineering approach will include utilizing specific enzymes, such as acyl-HSL synthase, that can be altered

by functionality to produce different types of HSLs. Measuring the expression level of such enzymes are feasible using LC-MS/MS and by comparing its expression level with different BNC-forming bacteria; results will be beneficial toward determining the optimal biological system for BNC production.

ACKNOWLEDGMENTS

Funding was provided by the U.S. Army via the In-house Laboratory Independent Research Program (PE 0601101A Project 91A) at the Edgewood Chemical Biological Center.

REFERENCES

[1] Lee, K.Y.; Buldum, G.; Mantalaris, A.; Bismarck, A. More than meets the eye in bacterial cellulose: biosynthesis, bioprocessing, and applications in advanced fiber composites. *Macromol. Biosci.* **2014,** *14* (1), pp 10–32.
[2] Rognoli, V.; Bianchini, M.; Maffei, S.; Karana, E. DIY materials. *Mater. Des.* **2015,** *86*, pp 692–702.
[3] Wong, H.C.; Fear, A.L.; Calhoon, R.D.; Eichinger, G.H.; Mayer, R.; Amikam, D.; Benziman, M.; Gelfand, D.H.; Meade, J.H.; Emerick, A.W.; et al. Genetic organization of the cellulose synthase operon in Acetobacter xylinum. *Proc. Natl. Acad. Sci. USA.* **1990,** *87* (20), pp 8130–8134.
[4] Williams, W.S.; Cannon, R.E. Alternative environmental roles for cellulose produced by Acetobacter xylinum. *Appl. Environ. Microbiol.* **1989,** *55* (10), pp 2448–2452.
[5] Zhong, C.; et al. Strong underwater adhesives made by self-assembling multiprotein nanofibres. *Nat. Nanotechnol.* **2014,** *9* (10), pp 858–866.
[6] Chen, A.Y.; Deng, Z.; Billings, A.N.; Seker, U.O.; Lu, M.Y.; Citorik, R.J.; Zakeri, B.; Lu, T.K. Synthesis and patterning of tunable multiscale materials with engineered cells. *Nat. Mater.* **2014,** *13* (5), pp 515–523.
[7] Yadav, V.; Paniliatis, B.J.; Shi, H.; Lee, K.; Cebe, P.; Kaplan, D.L. Novel in vivo-degradable cellulose-chitin copolymer from metabolically engineered Gluconacetobacter xylinus. *Appl. Environ. Microbiol.* **2010,** *76* (18), pp 6257–6265.
[8] Mohite, B.V.; Patil, S.V. Physical, structural, mechanical and thermal characterization of bacterial cellulose by G. hansenii NCIM 2529. *Carbohydr Polym.* **2014,** *106*, pp 132–141.
[9] Hsieh, Y.C.; Yano, H.; Nogi, M.; Eichhorn, S.J. An estimation of the Young's modulus of bacterial cellulose filaments. *Cellulose.* **2008,** *15* (4), pp 507–513.
[10] Rusli, R.; Eichhorn, S.J. Determination of the stiffness of cellulose nanowhiskers and the fiber-matrix interface in a nanocomposite using Raman spectroscopy. *Appl. Phys. Lett.* **2008,** *93* (3), p 033111.
[11] Gelin, K.; Bodin, A.; Gatenholm, P.; Mihranyan, A.; Edwards, K.; Stromme, M. Characterization of water in bacterial cellulose using dielectric spectroscopy and electron microscopy. *Polymer.* **2007,** *48* (26), pp 7623– 7631.
[12] Yuen, J.D.; Walper, S.A.; Melde, B.J.; Daniele, M.A.; Stenger, D.A.; Electrolyte-Sensing Transistor Decals Enabled by Ultrathin Microbial Nanocellulose. *Sci. Rep.* **2017,** *7* (1), p 40867.
[13] Rudrappa, T.; Biedrzycki, M.L.; Bais, H.P. Causes and consequences of plant-associated biofilms. *FEMS Microbiol. Ecol.* **2008,** *64* (2), pp 153–166.
[14] Shaw, P.D.; Ping, G.; Daly, S.L.; Cha, C.; Cronan, J.E., Jr.; Rinehart, K.L.; Farrand, S.K. Detecting and characterizing N-acyl-homoserine lactone signal molecules by thin-layer chromatography. *Proc. Natl. Acad. Sci. USA.* **1997,** *94* (12), pp 6036–6041.
[15] Eng, J.K.; Jahan, T.A.; Hoopmann, M.R. Comet: an open-source MS/MS sequence database search tool. *Proteomics*. **2013,** *13* (1), pp 22–24.
[16] Saxena, I.M.; Lin, F.C.; Brown, R.M., Jr. Cloning and sequencing of the cellulose synthase catalytic subunit gene of Acetobacter xylinum. *Plant. Mol. Biol.* **1990,** *15* (5), pp 673–683.
[17] Hense, B.A.; Kuttler, C.; Muller, J.; Rothballer, M.L.; Hartmann, A.; Kreft, J.U. Does efficiency sensing unify diffusion and quorum sensing? *Nat. Rev. Microbiol.* **2007,** *5* (3), pp 230–239.
[18] von Rad, U.; Klein, I.; Dobrev, P.I.; Kottova, J.; Zazimalova, E.; Fekete, A.; Hartmann, A.; Schmitt-Kopplin, P.; Durner, J. Response of Arabidopsis thaliana to N-hexanoyl-DL-homoserine-lactone, a bacterial quorum sensing molecule produced in the rhizosphere. *Planta.* **2008,** *229* (1), pp 73–85.
[19] Bauer, W.D.; Mathesius, U. Plant responses to bacterial quorum sensing signals. *Curr. Opin. Plant. Biol.* **2004,** *7* (4), pp 429–433.
[20] Adar, F. Characterizing modified celluloses using Raman spectroscopy. *Spectroscopy.* **2016,** *31* (11), pp 22–27.

Structure modeling and prediction of cystine knot miniproteins

Caitlin E. Sharpes[a,b], Katelynn M. Stafford[a,b], Alena M. Calm[a], Rabih E. Jabbour[a], Jerry B. Cabalo[a], Roberto Rebeil[a]*
[a]U.S. Army Edgewood Chemical Biological Center, Research and Technology Directorate, 8198 Blackhawk Rd, Aberdeen Proving Ground, MD 21010
[b]Excet, Inc., 6225 Brandon Ave, Suite 360, Springfield, VA 22150

ABSTRACT

Many organisms, including a diverse set of species across many genera, produce a large family of relatively short peptides collectively known as cystine knot proteins. Cystine knot proteins bind to a wide range of protein targets. These peptides, while largely divergent in primary amino acid sequence, share a similar six-cysteine residue motif which forms their characteristic structural feature termed the cystine knot. The cystine knot proteins' critical features are mainly formed and stabilized by three conserved tightly woven disulfide bonds formed by the cysteines and impart extraordinary thermal and proteolytic stability. The present study seeks to better understand how changes in primary amino acid sequence and spacing between cysteine residues can impact the ability of cystine knots to form. We hypothesize that the conserved cysteine spacing between cysteines III, IV, and V are important for generating a higher percentage of properly folded and linked peptides under oxidative conditions. Therefore, perturbations in the spacing pattern between cysteines III, IV, and V should result in slower folding dynamics or a lower percentage of properly folded peptides. Here, we leverage *in silico* protein folding and structure modeling tools with conventional protein biochemistry techniques in order to examine the impact that sequence modifications have on the ability of cystine knots to form.

Keywords: cystine knot, peptide, miniproteins, folding, *Ecballium elaterium* trypsin inhibitor-II, disulfide-rich

1. INTRODUCTION

Many chemical and biological defense applications rely heavily on chemically-selective binding. For sensing biological and some chemical threats, immunoassays depend on the high chemical specificity of immunoglobulins (Ig) to detect and identify both toxins and pathogenic organisms.[1,2] Finding acceptable alternatives to the current state-of-the-art use of proteins is highly desirable.[3] This is mainly because the chemical-specific binding of proteins, such as with Igs, suffers from a number of significant drawbacks: 1) they are large and expensive molecules to make, typically involving the use of animals for mass production, 2) Igs require precise environmental control to maintain the proper folded shape for the desired biological activity, and 3) when used as a therapeutic, Igs can trigger an immune response, especially if they were produced in an animal. DNA aptamers have been proposed to circumvent these drawbacks; however, DNA uses only four nucleotides as opposed to the 20 amino acids found in proteins, making it difficult to match the binding site diversity of the target protein when using aptamers.[4–6] Cystine knot proteins (CKP), a large family of short peptides produced by several organisms, can target a broad set of proteins, displaying a high degree of specificity and avidity to their respective targets (Figure 1).[7] Although CKPs consist of short peptides, 10–50 amino acids long, they can display remarkable variability in their 3D structure, target specificity, and affinity to various receptors.[7–10] It is reasonable to speculate that variant peptides based on CKPs may surmount the limitations known to affect conventional protein-based immunoassays and therapeutics. The objective of this project is to understand how the amino acid peptide sequence and length of the loop structures of the CKPs control the 3D structure of the molecules. While a significant amount of bioprospecting and comparisons of different structures from various CKPs are underway, few researchers are focusing on exploiting the potential use of this basic framework to target completely different ligands. The disulfide linkages between the cysteine residues are the key to their 3D structure (Figure 1). We hypothesize that the conserved cysteine spacing between cysteines III, IV, and V are important for generating a higher percentage of properly folded and linked peptides under oxidative conditions. Therefore, perturbations in the spacing pattern between cysteines III, IV, and V should result in slower folding dynamics or a lower percentage of properly folded peptides.

Of the different CKP types, the inhibitory CKPs (ICKP) have been the focus of many studies to better understand their structures and intrinsic properties.[7] For example, the 3D structure of several ICKPs has been determined using crystallography and nuclear magnetic resonance spectroscopy. This has required the generation of multiple *in vitro* reactions to help properly fold the CKPs into their native state and oxidation of all the cysteines to form the correct disulfide bonds. In the process, investigators have discovered that some ICKPs have a higher intrinsic capability to fold in the proper conformation under very simple oxidative conditions. The *Ecballium elaterium* (squirting cucumber) trypsin inhibitor II (EeTI-II) is one of the very well characterized ICKPs. The 3D structure of EeTI-II has already been elucidated, both by itself and while binding to trypsin.[11–13] Critical residues involved in binding and inhibition have also been identified via amino acid substitution and *in silico* modeling used to study these non-covalent bonds. Amino acids in loop #1 (L1) have been shown to interact directly with the trypsin proteolytic pocket. The bending of this loop is caused by the two adjacent cysteines forming the disulfide bridge, with L5 consisting of a single valine (Figure 1). At least two research groups have introduced alternative binding domains into the various loop regions of EeTI-II to generate molecular tools.[14,15] Hence, there is a wealth of background literature that can be exploited to help make progress towards testing the hypothesis.

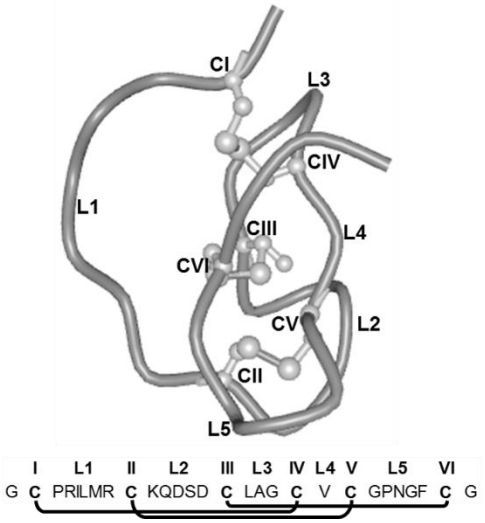

Figure 1. Primary amino acid sequence and 3D structure of EeTI-II. The diagram was obtained from the National Center of Biotechnology Information (U.S. National Library of Medicine, Bethesda, MD) structure database using the iCn3D web tool. Cysteines are designated with Latin numerals.

In order to tackle this problem, a combination of *in silico* and traditional laboratory bench research was performed in parallel to help explore how changes in loop length and primary amino acid sequence impact the intrinsic capability of the protein to fold properly. At least one research group has used this approach with significant success to help design and generate a synthetic peptide that contained alternative amino acids in place of two critical cysteines; the new peptide folded properly and showed similar physical properties to the wild-type version, even though it lacked a major covalent bond.[16] In a similar manner, this study utilizes *in silico* folding and structure analysis *in silico* tools to review or screen effects that changes in amino acid sequence may cause to the intrinsic ability of EeTI-II to form the cystine knot under oxidative conditions. Synthetic versions of the peptide will be generated to study the ability of the peptides to fold and form the cystine knot appropriately under favorable oxidative conditions. The two approaches allow comparison of results and the ability to better understand the effects observed

2. MATERIALS AND METHODS

2.1 Protein sequence collection and analysis

Primary amino acid sequences for the various ICKPs were downloaded from the National Center of Biotechnology Information protein database (Bethesda, MD, https://www.ncbi.nlm.nih.gov/protein). The sequences were manually aligned using the six conserved cysteines involved in cystine knot formation to identify conserved loop features (data not shown).

2.2 Peptide variant design

The ICKP EETI-II was chosen as the primary backbone since there already is a wealth of information in regard to function and folding information. Previous research has demonstrated that the ability of a high percentage of EETI-II to fold properly *in vivo* and *in vitro* was associated with the GPNG amino acid sequence located between cysteines V and IV. This pattern and corresponding effect in helping to initiate proper folding and oxidation introduced a variable that could mask or enhance the effect of the cysteine spacing variation. Hence, the GPNG amino acid pattern was replaced with the NEDE amino acid pattern, which has been shown to still allow proper folding (Table 1). Peptides were purchased from Creative Peptides (Shirley, NY) and New England Peptide, Inc. (Gardner, MA) and were generated using standard fluorenylmethyloxycarbonyl protecting group (Fmoc) peptide synthesis chemistry.

Table 1. Amino acid sequence alignment of various EeTI-II variants designed for this study to study the impact of the cysteine spacing on *in vitro* folding dynamics. The EeTI-II native sequence is highlighted in gray; the amino acid changes are in bold.

Variant	*I*	*L1*	*II*	*L2*	*III*	*L3*	*IV*	*L4*	*V*	*L5*	*VI*	*#*
EETI-II	**C**	PRILMR	**C**	KQDSD	**C**	LAG	**C**	V	**C**	GPNGF	**C**	**26**
EETI-N1	**C**	PRILMR	**C**	KQDSD	**C**	LAG	**C**	V	**C**	**NEDE**F	**C**	**26**
EETI-N2	**C**	PRILMR	**C**	KQDSD	**C**	LAG	**C**	**SGA**	**C**	**NEDE**F	**C**	**28**
EETI-N3	**C**	PRILMR	**C**	KQDSD	**C**	LAG	**C**	**SGQGN**	**C**	**NEDEF**	**C**	**30**
EETI-N4	**C**	PRILMR	**C**	KQDSD	**C**	LAG	**C**	V	**C**	**NEDELRIFV**	**C**	**31**
EETI-N5	**C**	PRILMR	**C**	KQDSD	**C**	-	**C**	**LAG**V	**C**	NEDEF	**C**	**26**
EETI-N6	**C**	PRILMR	**C**	KQDSD	**C**	-	**C**	**KSSNL**V	**C**	NEDEF	**C**	**28**
EETI-N7	**C**	PRILMR	**C**	KQDSD	**C**	-	**C**	**LAG**V	**C**	**NEDELRIFV**	**C**	**30**
EETI-N8	**C**	PRILMR	**C**	**DNDRGPR**	**C**	-	**C**	**LAG**V	**C**	NEDEF	**C**	**29**
EETI-N9	**C**	PRILMR	**C**	KQDSD	**C**	-	**C**	V	**C**	NEDEF	**C**	**23**

2.3 *In silico* protein sequence folding and analysis

Several *in silico* tools were installed to perform protein folding and structure analysis: 1) the Rosetta macromolecular modeling software suite; 2) PSI-blast based secondary structure prediction (PSIPRED), a program for predicting protein secondary structure; 3) Jufo 3D Server, a second/alternate program for predicting protein secondary structure; 4) the National Center for Biotechnology Information Basic Local Alignment Search Tool searches and non-redundant peptide databases to help Rosetta find 3-mer and 9-mer peptide structures of known structure; and 5) SPARKS, a program to account for solvent effects.[17,18] The PSIPRED program is used to determine the secondary structure—regions of α-helices and β-sheets. The next step was the alignment of 3-mer and 9-mer sequences to proteins of known structure using the National Center for Biotechnology Information Basic Local Alignment Search Tool database. The result was a set of structures corresponding to these fragments which were then used to build the set of output structures. Each structure was assigned an energy score and is in the protein data bank format.

For each peptide sequence, 6,000 folded structures were generated for clustering and analysis (Table 1). Based on the observation that the wild-type sequence of the CKPs forms the correct disulfide linkages at room temperature, we filtered the possible structures for configurations that displayed a short distance (~4.5 Å) between the proper cysteine residues.[19] Peptide sequences that did not produce stable structures with the correct cysteines in proximity to each other were not counted. To calculate the *in silico* probability that a given sequence would form the CKP motif, the following simple formula was used: Probability (of proper folding) = *N*-structures with close S–S pairs divided by the *N*-total structures generated. Probability numbers for the synthetic peptides tested were compared to the probability score obtained for wild-type EeTI-II. In addition to the probability score, the energy score (arbitrary units) was also compared for each structure that had the proper CKP motif.

2.4 High-performance liquid chromatography analysis of folded proteins

Analysis of the incubated peptides was performed using high-performance liquid chromatography (HPLC). The system used was an Agilent Technologies 1200 Series system (Santa Clara, CA), fitted with a Vydac C18 analytical column (4.6 mm x 250 mm, 5 µm, 300 Å) and a Vydac C18 guard column (4.6 mm x 7.5 mm, 5 µm). The mobile phase used was of 0.1 % trifluoroacetic acid (TFA) in water (solution A) and 0.1 % TFA in ACN, (solution B). Prior to starting, the column was first equilibrated by running two blank samples. For each sample, the column was first equilibrated using 20 % solution B for 3 minutes. After injection, the bound material was washed for 3 additional minutes in 20 % solution B. The toxin was eluted using a linear gradient of 20–70 % solution B, with a flow rate of 1 mL/min, for 15 minutes. Eluted peaks were detected using a photodiode UV-vis detector with a channel set to 214

nm. Peptide peaks typically eluted between 45 % and 65 % solution B; when needed, eluted peaks were manually collected and analyzed using mass spectrometry (MS). The column was then washed with 100 % solution B to clear the column of any remaining potential contaminants, before the column was reconditioned with 20 % solution B for the next sample injection.

2.5 MS analysis of CKP peptides

For structure analysis of peptides generated, a published liquid chromatography-mass spectrometry (LC-MS) approach was used since it potentially allowed a simple and more rapid analysis than other options.[20] An EeTI-II sample was custom-made by Creative Peptides (Shirley, NY) using Fmoc chemistry and the GCPRILMRCKQDSDCLAGCVCGPNGFCG primary amino acid sequence. The cysteines used in the peptide assembly process carried protective chemical groups so that the correct disulfide links could be generated in a series of deprotection and oxidation reactions. After generation, the folded peptide was purified to 95 % using HPLC. A 2.0 mg sample was dissolved in 95/5/0.1 % of water/ACN/fluoroacetic acid and allowed to dissolve for 30 minutes before MS analysis was performed. The system used for higher-energy collisional dissociation (HCD) fragmentation and MS analysis was a nanoflow liquid chromatography (nLC-1000) system and Q Exactive™ Hybrid Quadrupole-Orbitrap™ MS that is based on Fourier transformation-ion trap-MS configuration (Thermo Scientific™; Waltham, MA). The MS analyses were done in two different formats of HCD, a differential collision energy increase and a normalized collision energy approach—both were performed using direct infusion. The MS was operated in full mass scan between 100–2,000 amu, with data acquired in independent mode. The collision energy was varied after 30 seconds, and a gradual increase in collision energy from 10 % to 90 % was performed. Data was collected to show the effect of collision energy on different charge ions of the analyzed peptide chains; only ions with charge state (z) +2, +3, and +4 were observed.

3. RESULTS AND CONCLUSIONS

3.1 *In silico* analysis using Rosetta

The Rosetta suite of programs was chosen to perform structural predictions because of its performance under the critical assessment for protein structure prediction (CASP).[18] Rosetta utilizes a mixture of knowledge-based and physics-based structure search algorithms.[17] Knowledge based structure predictions rely on analogy to proteins of known structure.[21] Short sequences within the peptide of unknown structure are aligned with proteins of known structure, and the structure of the subsequences from the known proteins are assigned to the segments in the unknown peptide. A physics-based model performs a potential energy surface search given a description of the interatomic/intermolecular forces (e.g., a force field, such as AMBER or CHARMM).[22] The chief limitation of this approach is that the potential energy surface (PES) of any peptide is very large and complex. That is, the PES may contain multiple local minima, of which the native structure may only be one. Either long simulation times are necessary to sample enough of the PES to find the native structure, or the protein model may become stuck in the wrong local structure. The mixed approach utilized by Rosetta can bypass the difficulties encountered by using a single approach.

To determine its usefulness in folding prediction of CKPs, we exploited some of the numerical structure outputs of the program by generating 6,000 folded structure variants; of these, the number of structures that displayed a low relative energy score and displayed correct cysteine pairs in a distance suitable for disulfide bridge formation were extracted. The total number of structures (6,000) and the subset number were used to calculate the “probability” of proper folding. The native sequence of the EeTI-II protein was used to establish the baseline probability; this protein folds spontaneously in very simple oxidative conditions to form the appropriate disulfide bonds at a very high rate—more than 80 % properly folded/functional peptide. The various alternate sequences were likewise analyzed for comparison of their respective “probability” values (Table 2).

Table 2. Peptide variants, their respective primary amino acid sequences, and the probability calculated. Underlined amino acids are those changed compared to the native sequence.

Peptide Variant	*Sequence*	*Probability*
EeTI-II (N0)	GCPRILMRCKQDSDCLAGCVCGPNGFC	0.00136
EeTI-N1	GCPRILMRCKQDSDCLAGCVCNEDEFC	0.000643
EeTI-N2	GCPRILMRCKQDSDCLAGCSGACNEDEFC	0.0145
EeTI-N3	GCPRILMRCKQDSDCLAGCSGQGNCNEDEFC	0.164
EeTI-N4	GCPRILMRCKQDSDCLAGCVCNEDELRIFVC	0.000466
EeTI-N5	GCPRILMRCKQDSDCCLAGVCNEDEFC	0.000000
EeTI-N6	GCPRILMRCKQDSDCCKSSNLVCNEDEFC	0.0225
EeTI-N7	GCPRILMRCKQDSDCCLAGVCNEDELRIFVC	0.000000
EeTI-N8	GCPRILMRCDNDRGPRCCLAGVCNEDEFC	0.000675
EeTI-N9	GCPRILMRCKQDSDCCVCNEDEFC	0.000338

An initial survey of the structures, ignoring energy score, was performed to score the different peptides, resulting in the following ranking of likelihood for probability of generating correctly folded structures: N7∼N5<N9<N4<N1<N8<N0<N2<N6<N3. Currently, there is insufficient *in vitro* data for comparison; nevertheless, the results were surprising. The probability values supported the hypothesis that variants N2, N6, and N3 should fold and form a cystine knot structure faster or at a greater percentage than that of the peptide with the wild-type sequence. It will be important to determine the relative free-energy state of these alternate peptide folded structures to determine how those values impact probability. In addition, some sequences did not yield any structures with appropriate cysteine pairings. An effort will be made to try to "force" the proper conformation of the peptide to also determine the free-energy state of that structure, and to determine if any amino acid residues are impeding the knot formation.

3.2 *In vitro* folding reactions and analysis

Initial folding reactions followed the procedure reported in Wentzel et al.[23] Many variables (incubation time, peptide concentration, reaction quenching, etc.) were tested using the first two peptides obtained (N1 and N3). Initial analysis with HPLC indicated the presence of what appeared to be peaks consistent with the linear and folded peptide intermediates, but the peaks were very small in the case of N1. More prominent peaks were observed in reactions generated with the N3 variant. An attempt was made to inject more material and to try to increase the peptide concentration in the reactions. However, none of these approaches appeared to aid in increasing peak quality. Due to these inconsistent results, reactions were performed with all peptides available with incubation times of 0 hours (Control), 2 hours, 4 hours, 6 hours, and 24 hours. The 45 harvested reactions were analyzed using HPLC as described above; of the nine peptides, N3, N8, and N9 showed clear product peaks, but the peak patterns did not fall into the patterns expected. The 45 reactions were repeated twice with higher concentrations of peptide to determine if any consistent peaks could be observed that increased in the peptide reactions with low signal, but LC analysis did not provide the desired data. To determine if the detection problem was due to the low sensitivity of the HPLC system, a set of reactions was prepared for analysis with the LC-MS system that was to be used for fragmentation analysis. For this analysis, reactions were performed at the original peptide concentration tested (25 μg/mL) and samples were obtained after 0 hours, 6 hours, and 24 hours incubation in folding buffer. MS analysis showed that peptides in reactions prepared with the N1, N2, N4, N5, N6, and N7 variants could not be detected, consistent with the HPLC. Conversely, a strong peptide signal was detected in reactions prepared with the N3, N8, and N9 variants. This MS analysis also showed that peptide peaks at time = 0 are consistent with the linear form of the peptide—shifted during incubation time into lower molecular weight products consistent with the generation of folded-oxidized species with one, two, and three disulfide bonds. The peptide variant designated as N3 generated prominent peaks (at $z = 3$ and $z = 4$) after a six-hour incubation in folding buffer of a 2-disulfide bond intermediate. After the 24-hour incubation time, all of the peptide present showed an m/z consistent with a 3-disulfide bond form. At this time, no fragmentation analysis was performed to verify if the 3-disulfide bond form was in the correct CKP arrangement. Peptide variants N8 and N9 also generated peaks consistent with a two-disulfide bond folding intermediate(s); but unlike N3, did not produce a three-disulfide bond form even after 24 hours of incubation (data not shown).

The reason for our inability to detect peptide in the folding reactions is unknown. The peptide received was obtained with appropriate quality assurance documentation. The 10-mg lyophilized peptide was obtained in 1-mg aliquots per vial so that any portion of peptide solubilized would not have to undergo manipulations that could compromise the integrity of the peptide. In most cases, lyophilized powder was suspended in buffer the day of the reactions. In addition, no peptide fragments were observed in the MS spectra that would indicate degradation during the reactions. The possibility exists that the peptide may be precipitating and simply not entering into the LC system. While this is

unlikely given the low concentration of peptide used in the reaction, we also tested an alternate folding reaction buffer system that uses TWEEN® non-ionic detergent to help solubilize and help in the folding-oxidation of hydrophobic CKPs. The folding reaction consists of a simple buffer: 1 mM EDTA, 0.5 % TWEEN® (40 or 60), oxidized glutathione, and reduced glutathione. The detergent helps to maintain the peptide in solution and prevent unwanted peptide–peptide interactions through their hydrophobic regions. Reactions were performed in triplicate, and harvested at 0 hours, 6 hours, and 24 hours of incubation. HPLC analysis showed similar results to those observed in previous reactions (Figure 2). Peptide variants N3, N8, and N9 showed the strongest peaks, while the rest of the peptide variants displayed very weak absorbance peaks.

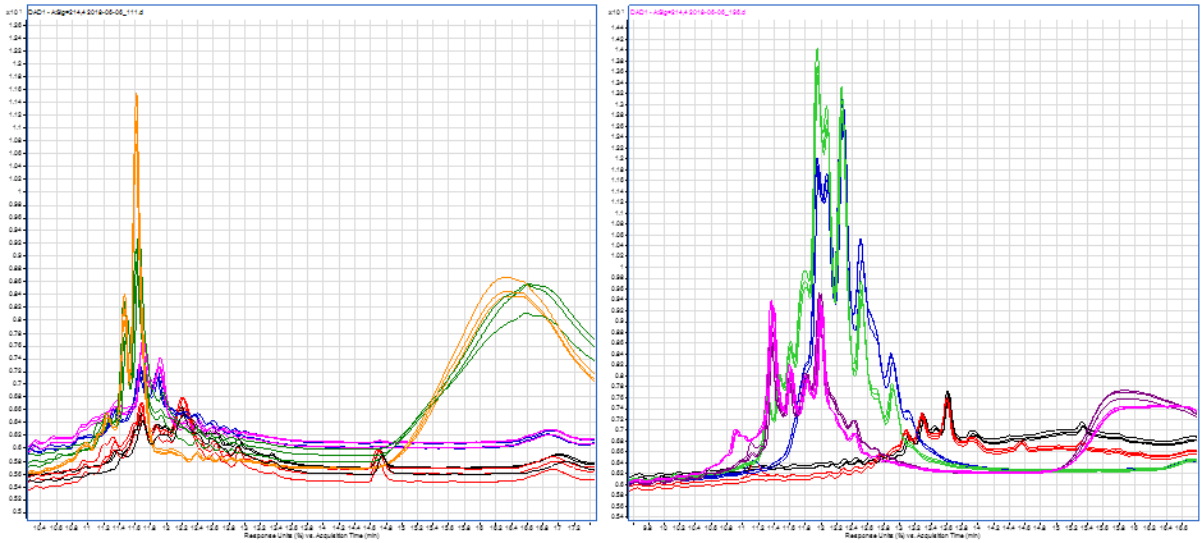

Figure 2. Comparison of the HPLC chromatograms obtained from peptide folding reactions containing TWEEN® 60. Left Graph: peptide N1 after 0 hours (Black) and 6 hours (Red) incubation, peptide N2 after 0 hours (Blue) and 6 hours (Magenta) incubation, and peptide N1 after 0 hours (Green) and 6 hours (Orange) incubation. Right Graph: peptide N7 after 0 hours (Black) and 6 hours (Red) incubation, peptide N8 after 0 hours (Blue) and 6 hours (Green) incubation, and peptide N9 after 0 hours (Purple) and 6 hours (Magenta) incubation.

3.3 MS analysis

For disulfide link status or structure determination for generated peptides, several options are available. Most commonly, the structure of this type of peptide has been determined using nuclear magnetic resonance imaging.[24–26] However, this approach requires a significant amount of peptide and is relatively difficult to perform compared to other approaches. Recently, LC-MS approaches have been used with increasing frequency to determine the state of disulfide linkage for CKPs. This analytical approach requires less peptide, and determination of essential parameters, such as percent of correctly folded peptide, occurs more rapidly. In particular, a research group generated an LC-MS approach that allows the determination of the state of disulfide connectivity in peptides or proteins.[20] The researchers showed that, instead of performing peptide cleavage using a proteolytic method before analysis, the target peptide could be fragmented using the MS directly. The fragments generated by colliding the peptide into an ion trap were reanalyzed to obtain the atomic mass of the fragments. This allowed for very rapid determination of the folding/disulfide-link state with no need for preliminary treatment/preparation.

To determine if this approach would be suitable in this study, a custom synthetic peptide was acquired using the wild-type primary amino acid sequence of EeTI-II. This peptide, 95 % pure and properly folded/linked, was used to establish the published approach in-house. The single-charge peptide was not observed due to its higher molar mass than the mass range set for the MS system. The +2 charge state parental ion appeared at m/z = 1440.10, the +3 charge state parental ion appeared at m/z = 962.40, and the +4 charge state parental ion appeared at m/z = 722.05 (Figure 3). This is consistent with the calculated molecular weight of 2885.44 Da for the synthetic peptide. The absence of any prominent peaks in the spectrogram was consistent with the highly pure state of the properly folded peptide. Initial HCD applied an increase in energy from 10–90 % over time; however, the +2 charge parental peptide was particularly resistant to dissasociation. An HCD energy strength of 95 % yielded multiple peptide fragments (z = +1) that can be used to derive the original peptide structure (Figure 3). Fragmentation performed on the +3 charge parental ion provided very different results. An HCD energy level of 45 % produced some fragmentation and a corresponding

decrease in the parental ion peak (Figure 3). An increase in energy to 50 % resulted in a marked reduction of the parental peak and most other peaks present in the 45 % energy spectrum. The information provided is potentially useful, but further tuning of the HCD energy level between 45–50 % may need to be performed in order to obtain better results.

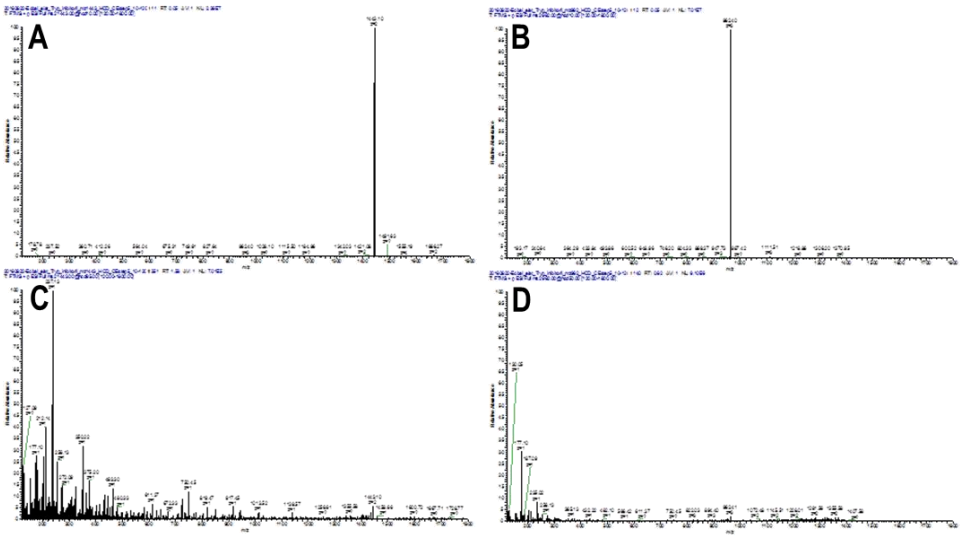

Figure 3. Sample MS spectra for the +2 charge state (A and C) and the +3 charge state (B and D) of the folded peptide ion. For the +2 charge state peptide ion at collision energy of 10 % (A) and 95 % (C), the various fragment peaks obtained from the native peptide are displayed. For the +3 charge state peptide ion at collision energy of 10 % (B) and 50 % (D), the various fragment peaks obtained from the native peptide are displayed.

Fragmentation performed on the +4 charge parental ion provided slightly different results to those shown in Figure 3. An HCD energy level of 20 % produced some fragmentation and a corresponding decrease in the parental ion peak in a similar manner to the +3 charge parental peak (data not shown). Fragment peaks possesing a +3 charge were primarily present in the spectrum with a few peaks similar to those identified earlier in the 100–300 *m/z* range possesing a +1 charge. As seen with the +3 charge parental ion, an increase in energy to 30 % resulted in a marked reduction of the parental peak and most other peaks present in the 20 % energy spectrum. As with the +3 charge parental ion, the information provided is potentially useful, but further tuning of the HCD energy level between 20–30 % may need to be performed in order to obtain better results. While further refinement is required, analysis can begin on the nature of the small ions identified in the 100–400 *m/z* range. Depending on information obtained expansion of analysis to peaks in the higher (400–800 *m/z*) range may be desirable. Now that some soluble product is being obtained, even if it is from one of the amino acid variants, an effort can start in cleaving and repurifying final product for similar MS analysis.

To perform follow-on experiments, a new set of peptides were designed and ordered from a different vendor (shown in Table 3). While experiments are ongoing with the original peptides received, the possibility exists that the detection problems observed may be due to an issue with the peptides initially purchased. These new set of peptides will help to verify or eliminate this possibility. These peptides do not include the peptide variants with the more hydrophobic Loop 5 sequence, so they should be quicker to synthesize and be more soluble in aqueous solutions.

Table 3. Amino acid sequence alignment of the second set of EeTI-II variants designed for this study. The goal was to reduce hydrophobicity and to determine if this new set would be detectable via LC and LC-MS.

Variant	*I*	*L1*	*II*	*L2*	*III*	*L3*	*IV*	*L4*	*V*	*L5*	*VI*	*#*
EETI-II (WT)	**C**	PRILMR	**C**	KQDSD	**C**	LAG	**C**	V	**C**	GPNGF	**C**	**26**
EETI-N1.1	**C**	PRILMR	**C**	KQDSD	**C**	LAG	**C**	V	**C**	**NEDE**F	**C**	**26**
EETI-N2.1	**C**	PRILMR	**C**	KQDSD	**C**	LAG	**C**	**SGA**	**C**	**NEDE**F	**C**	**28**
EETI-N3.1	**C**	PRILMR	**C**	KQDSD	**C**	LAG	**C**	**SGQGN**	**C**	**NEDEF**	**C**	**30**
EETI-N4.1	**C**	PRILMR	**C**	KQDSD	**C**	-	**C**	**SGQGN**	**C**	NEDEF	**C**	**26**
EETI-N5.1	**C**	PRILMR	**C**	KQDSD	**C**	-	**C**	**SGA**	**C**	NEDEF	**C**	**28**
EETI-N6.1	**C**	PRILMR	**C**	KQDSD	**C**	**GTSA**	**C**	V	**C**	NEDEF	**C**	**23**

ACKNOWLEDGMENTS

Funding was provided by the U.S. Army via the In-house Laboratory Independent Research Program (PE 0601101A Project 91A) at the Edgewood Chemical Biological Center.

REFERENCES

[1] Sesardic, D.; Jones, R.G.; Leung, T.; Alsop, T.; Tierney, R. Detection of Antibodies against Botulinum Toxins. *Mov. Disord.* **2004,** *19* (Suppl 8)*,* pp S85–91.
[2] Tamborrini, M.; Holzer, M.; Seeberger, P.H.; Schurch, N.; Pluschke, G. Anthrax Spore Detection by a Luminex Assay Based on Monoclonal Antibodies That Recognize Anthrose-Containing Oligosaccharides. *Clin. Vaccine Immunol.* **2010,** *17* (9)*,* pp 1446–1451.
[3] Kolmar, H. Natural and Engineered Cystine Knot Miniproteins for Diagnostic and Therapeutic Applications. *Curr. Pharm. Des.* **2011,** *17* (38)*,* pp 4329–4336.
[4] Ouyang, W.; Yu, Z.; Zhao, X.; Lu, S.; Wang, Z. Aptamers in Hematological Malignancies and Their Potential Therapeutic Implications. *Crit. Rev. Oncol. Hematol.* **2016,** *106,* pp 108–117.
[5] Hu, P.P. Recent Advances in Aptamers Targeting Immune System. *Inflammation.* **2017,** *40* (1)*,* pp 295–302.
[6] Chandola, C.; Kalme, S.; Casteleijn, M.G.; Urtti, A.; Neerathilingam, M. Application of Aptamers in Diagnostics, Drug-Delivery and Imaging. *J. Biosci.* **2016,** *41* (3)*,* pp 535–561.
[7] Daly, N.L.; Craik, D.J. Bioactive Cystine Knot Proteins. *Curr. Opin. Chem. Biol.* **2011,** *15* (3)*,* pp 362–368.
[8] Kolmar, H. Biological Diversity and Therapeutic Potential of Natural and Engineered Cystine Knot Miniproteins. *Curr. Opin. Pharmacol.* **2009,** *9* (5)*,* pp 608–614.
[9] Reinwarth, M.; Nasu, D.; Kolmar, H.; Avrutina, O. Chemical Synthesis, Backbone Cyclization and Oxidative Folding of Cystine-Knot Peptides: Promising Scaffolds for Applications in Drug Design. *Molecules.* **2012,** *17* (11)*,* pp 12533–12552.
[10] Isaacs, N.W. Cystine Knots. *Curr. Opin. Struct. Biol.* **1995,** *5* (3)*,* pp 391–395.
[11] Chiche, L.; Gaboriaud, C.; Heitz, A.; Mornon, J.P.; Castro, B.; Kollman, P.A. Use of Restrained Molecular Dynamics in Water to Determine Three-Dimensional Protein Structure: Prediction of the Three-Dimensional Structure of Ecballium Elaterium Trypsin Inhibitor II. *Proteins.* **1989,** *6,* pp 405–417.
[12] Gaboriaud, C.; Vaney, M.C.; Bachet, B.; Le-Nguyen, D.; Castro, B.; Mornon, J.P. Crystallization and Preliminary X-Ray Study of Porcine Trypsin, Free and Complexed with Ecballium Elaterium Trypsin Inhibitor, a Member of the Squash Inhibitors Family. *J. Mol. Biol.* **1989,** *210* (4)*,* pp 883–884.
[13] Heitz, A.; Chiche, L.; Le-Nguyen, D.; Castro, B. 1H 2D NMR and Distance Geometry Study of the Folding of Ecballium Elaterium Trypsin Inhibitor, a Member of the Squash Inhibitors Family. *Biochemistry.* **1989,** *28* (6)*,* pp 2392–2398.
[14] Kimura, R.H.; Jones, D.S.; Jiang, L.; Miao, Z.; Cheng, Z.; Cochran, J.R. Functional Mutation of Multiple Solvent-Exposed Loops in the Ecballium Elaterium Trypsin Inhibitor-II Cystine Knot Miniprotein. *PLoS One.* **2011,** *6* (2)*,* p e16112.
[15] Lahti, J.L.; Silverman, A.P.; Cochran, J.R. Interrogating and Predicting Tolerated Sequence Diversity in Protein Folds: Application to E. elaterium Trypsin Inhibitor-II Cystine-Knot Miniprotein. *PLoS Comput. Biol.* **2009,** *5* (9)*,* p e1000499.
[16] Yu, R.; Seymour, V.A.; Berecki, G.; Jia, X.; Akcan, M.; Adams, D.J.; Kaas, Q.; Craik, D.J. Less Is More: Design of a Highly Stable Disulfide-Deleted Mutant of Analgesic Cyclic α-Conotoxin Vc1.1. *Sci. Rep.* **2015,** *5,* p 13264.
[17] Bonneau, R.; Strauss, C.E.; Baker, D. Improving the Performance of Rosetta Using Multiple Sequence Alignment Information and Global Measures of Hydrophobic Core Formation. *Proteins.* **2001,** *43* (1)*,* pp 1–11.
[18] Bonneau, R.; Tsai, J.; Ruczinski, I.; Chivian, D.; Rohl, C.; Strauss, C.E.; Baker, D. Rosetta in Casp4: Progress in Ab Initio Protein Structure Prediction. *Proteins.* **2001,** *45* (S5)*,* pp 119–126.
[19] Le-Nguyen, D.; Mattras, H.; Coletti-Previero, M.A.; Castro, B. Design and Chemical Synthesis of a 32 Residues Chimeric Microprotein Inhibiting Both Trypsin and Carboxypeptidase A. *Biochem. Biophys. Res. Commun.* **1989,** *162* (3)*,* pp 1425–1430.
[20] Bhattacharyya, M.; Gupta, K.; Gowd, K.H.; Balaram, P. Rapid Mass Spectrometric Determination of Disulfide Connectivity in Peptides and Proteins. *Mol. BioSyst.* **2013,** *9* (6)*,* pp 1340–1350.
[21] Wu, S.; Skolnick, J.; Zhang, Y. Ab Initio Modeling of Small Proteins by Iterative Tasser Simulations. *BMC Biol.* **2007,** *5,* p 17.

[22] Lee, M.S.; Olson, M.A. Assessment of Detection and Refinement Strategies for De Novo Protein Structures Using Force Field and Statistical Potentials. *J. Chem. Theory. Comput.* **2007,** *3* (1), pp 312–324.
[23] Wentzel, A.; Christmann, A.; Krastner, R.; Kolmar, H. Sequence requirements of the GPNG beta-turn of the *Ecballium elaterium* trypsin inhibitor II explored by combinatorial library screening. *J. Biol. Chem*. **1999,** *274* (30), pp 21037–21043.
[24] Jackson, P.J.; McNulty, J.C.; Yang, Y.K.; Thompson, D.A.; Chai, B.; Gantz, I.; Barsh, G.S.; Millhauser, G.L. Design, Pharmacology, and NMR Structure of a Minimized Cystine Knot with Agouti-Related Protein Activity. *Biochemistry.* **2002,** *41* (24), pp 7565–7572.
[25] McNulty, J.C.; Thompson, D.A.; Bolin, K.A.; Wilken, J.; Barsh, G.S.; Millhauser, G.L. High-Resolution NMR Structure of the Chemically-Synthesized Melanocortin Receptor Binding Domain Agrp(87-132) of the Agouti-Related Protein. *Biochemistry.* **2001,** *40* (51), pp 15520–15527.
[26] Daly, N.L.; Koltay, A.; Gustafson, K.R.; Boyd, M.R.; Casas-Finet, J.R.; Craik, D.J. Solution Structure by NMR of Circulin A: A Macrocyclic Knotted Peptide Having Anti-HIV Activity. *J. Biol. Chem.* **1999,** *285* (1), pp 333–345.

SSI
PROJECTS

Electron transfer at an aluminum nanohole array/C_{60} interface

Xu-sheng Liu[a], Ganghua Deng[a], Yuqin Qian[a], Bryan Debbrecht[b], Mark S. Mirotznik[b], Brendan G. DeLacy[c*], Yi Rao[a]
[a]Department of Chemistry and Biochemistry, Utah State University, Logan, UT, 84322
[b]Department of Electrical & Computer Engineering, University of Delaware, Newark, DE 19716
[c]U.S. Army Edgewood Chemical Biological Center, Research & Technology Directorate, 8198 Blackhawk Rd, Aberdeen Proving Ground, MD 21010

ABSTRACT

This work details the characterization of the injection of photo-generated electrons from an aluminum-based nanohole array into a semiconductor thin film (C_{60}). A cavity-based aluminum nanohole array was first fabricated using electron-beam lithography. Next, a thin film of C_{60} was vapor deposited onto the aluminum nanohole array. The nanohole array/C_{60} interface provided a means of studying the injection of hot electrons from the aluminum into the C_{60} thin film. In order to observe and characterize the synergistic effects of charge injection at the interface, we combined a transient IR technique with transient white light techniques to explore interfacial charge injection between 2D aluminum nanohole arrays and organic semiconductors. This analysis revealed that photo-generated electrons on surfaces of aluminum nanohole array were injected into the lowest unoccupied molecular orbital for C_{60} through a Schottky barrier at a time scale of 270 ± 25 fs.

Keywords: aluminum plasmonics, hot electron injection, Schottky barrier

1. INTRODUCTION

Charge injection occurring at interfaces plays a vital role in photovoltaic and photocatalytic applications of semiconductor and metallic nanostructures. The efficiency of the charge injection process is highly dependent on 1) the structures of adsorbates at semiconductor and metallic interfaces, 2) the binding between the adsorbates and the nanostructures, which is affected by the local environment at the interfaces, 3) the density of the adsorbates at the interfaces, and 4) the electronic properties of the interfacial region, if applicable. Although the structure and density of adsorbates at interfaces have been widely investigated, interfacial charge transfer has yet to be fully explored. Since charge injection occurs on a time scale of picosecond or sub-picosecond at interfaces composed of semiconductor and metallic nanostructures, the ultrafast studies of the interfaces proposed here will improve the quantum efficiency in photovoltaic and photocatalytic conversions of semiconductor and metallic nanostructures.

Two-dimensional nanohole arrays are one of many metal-optics designs that have been explored as means of generating so-called "hot-spot," or enhanced electromagnetic near fields. These hot spots could be used as a means of enhancing detection techniques, including surface enhanced Raman spectroscopy (SERS) and surface enhanced fluorescence. While 2D nanohole arrays are traditionally made of gold and silver, the novel fabrication of aluminum nanohole arrays will not only provide an alternative approach but will also solve the problem of high cost of materials. Furthermore, the 2D aluminum nanohole arrays show broadband absorption spectra, from visible to IR.

To demonstrate synergistic effects of charge injection at interfaces, we combine transient IR technique with transient white light techniques to explore interfacial charge injection of 2D aluminum nanohole arrays on organic semiconductors.[1] Here we take C_{60} as an example of organic semiconductors. These capabilities will enable us to reveal the underlying mechanisms behind the charge injection at interfaces of metallic nanostructures and semiconductors. Ultrafast visible-pump/infrared probe will be used to probe free electron responses and explore charge separation and recombination dynamics in 2D aluminum nanohole arrays/C_{60} systems. We will further use ultrafast visible-pump/white light probe to investigate how C_{60} accepts electrons from photoexcited 2D aluminum nanohole arrays by tracking time evolutions of electronic transitions of C_{60}.

2. EXPERIMENTAL METHODS

1.1 Visible pump-transient IR absorption experimental setup

The experimental setup (see Figure 1(a)) consisted of an integrated Ti:sapphire regenerative amplifier laser system (UpteK Solutions; Bohemia, NY) operating at 1 kHz and 800 nm, producing 100-fs pulses of 4.0 mJ. 20 % of the 800 nm output was attenuated to a pulse energy of 10 µJ and used as the pump beam.

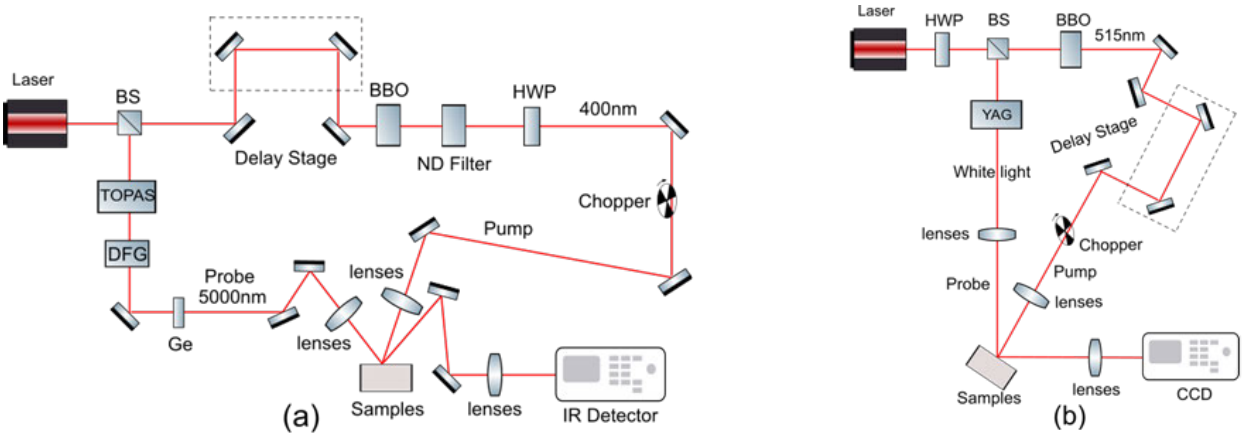

Figure 1. A schematic of experimental setup for (a) visible pump-transient IR reflection experiments, and (b) visible pump-transient white light reflection experiments.

The remaining 80 % of the output laser pulse was used to pump an optical parametric generator and amplifier with a difference frequency generator (TOPAS, DFG; Light Conversion, Lithuania) to produce an IR pulse of 5000 nm with a pulse energy of 18 µJ. The IR beam was attenuated by more than 1,000 times before the samples. The IR probe was detected by a liquid nitrogen-cooled HgCdTe detector (MCT-13-4.0; Infrared Associates, Inc.; Stuart, FL), followed by an amplifier. The pump pulse was modulated by a chopper (New Focus Model 3501) at 500 Hz. The amplified IR signal from the detector was sent to a lock-in amplifier (SR830; Stanford Research Systems, Sunnyvale, CA). The digitized outputs were processed and recorded by a home-made Labview program. The instrumentation response function for the transient IR was 300 fs.

1.2 Pump-transient absorption experiments setup

Briefly, a single-unit integrated femtosecond laser system (PHAROS; Light Conversion, Lithuania) with a seed oscillator was used in our experiments (see Figure 1(b)). The pulse duration is about 290 fs with 100 kHz repetition rate and a center wavelength at 1030 nm. The polarization of the incident light was set to be perpendicular to the optical table. The output power of the laser was 2.0 W in the experiments, and 30 % of the 1030 nm output was frequency-doubled in a BBO crystal to generate a pump pulse of 515 nm. The remaining 70 % of the output laser pulse was focused onto a YAG crystal plate to generate white light super-continuum as a probe light. The probe and pump light beams were focused and overlapped on the sample. The reflected probe light was detected by a detection system. A charge-coupled device (CCD) detection system (AvaSpec-ULS2048CL-EVO; Avantes; Apeldoorn, the Netherlands) was used to obtain the signals. The pump pulse was modulated by an optical chopper (New Focus Model 3501) at 50 kHz. The CCD sampling rate was synchronized with the chopper. The digitized outputs were processed and recorded by a home-made LabView program.

1.3 Preparation of Al nanohole array

In order to generate a nanohole array with resonances towards the mid-wavelength infrared (MWIR) regions (1.5–5 µm), electron-beam (e-beam) lithography fabrication was employed. The computational design, fabrication, and characterization of cavity-based aluminum nanohole array is detailed in our recent work.[2] The typical geometry of the cavity-based nanohole array is illustrated in Figure 2.

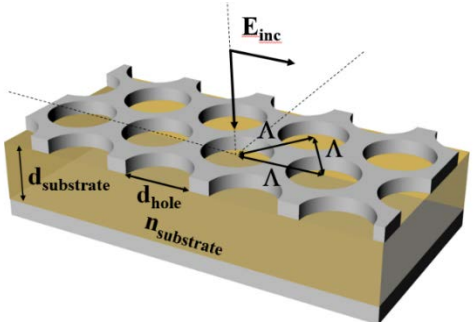

Figure 2. (Top layer) Aluminum nanohole array. (Middle layer) Transparent dielectric layer (SiO_2 of ZnSe). (Bottom layer) Aluminum base plane mirror. This "sandwiching" effect creates the necessary resonant cavity for increased use response.

Briefly, a 100-nm layer of aluminum was first evaporated onto a silicon wafer in order to create a base plane mirror, which prevented the transmission of incident radiation through the device. The SiO_2 cavity (200–600 nm) was then deposited onto the base plane mirror via plasma-enhanced chemical vapor deposition (PECVD) using SiH_4 and N_2O gases. The nanohole array was generated by e-beam lithography using a 4 % dilution of polymethyl methacrylate in anisole (PMMA A4), which was developed in a methyl isobutyl ketone/isopropanol (MIBK/IPA) mixture (1:3 v/v) after exposure. Once developed, 50 nm of aluminum was sputtered and lifted off to form the array on the surface of the device.

The choice of sputtering (versus e-beam evaporation) was justified when considering the negative effects of e-beam on the PMMA photoresist development. E-beam evaporation can heat the PMMA and potentially deform the PMMA during development. Conversely, sputtering did not introduce this risk, and therefore provided a more suitable means of depositing a layer of aluminum.

1.4 Preparation of C_{60} on Al nanohole array

The C_{60} films were grown in an organic molecular beam deposition chamber with a base pressure of 6.6×10^{-6} Torr. Commercially available C_{60} (99.5 %) molecules were used as raw material and put in the chamber. The distance between the raw C_{60} and the nanohole array is about 20 cm. The chamber temperature was heated at 673 kelvin at a speed of 0.1 kelvin /second, which corresponds to a growth rate of ~1 Å/second as determined by UV absorption spectroscopy.

3. RESULTS AND DISCUSSION

In an effort to examine charge injection of aluminum nanohole array into C_{60}, visible pump-IR probe experiments were performed. Figure 3 shows that kinetic traces of photo-induced changes in reflection at 5000 nm after photoexcitation of 800 nm for the aluminum nanohole array without (blue line) or with C_{60} (red line).

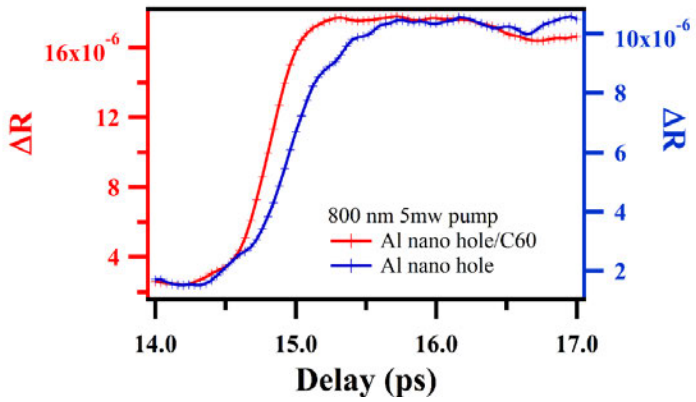

Figure 3. Kinetic traces of photo-induced changes in reflection at 5000 nm after photoexcitation of 800 nm for the aluminum nanohole array without (blue line) or with C_{60} (red line).

The IR at 5000 nm is transparent to any chemical groups, but sensitive to the change in the absorption of free carriers. Therefore, the transient IR absorption measures the absorption of free carriers of aluminum nanohole array, following the 800 nm pump excitation of hot electrons. A prominent change in the transient IR reflection was observed for the aluminum nanohole array as shown in Figure 3. A fitting of the rise signals in Figure 3 yields a time constant of 395 ± 22 fs for the aluminum nanohole array alone, suggesting that the plasmonic absorption of aluminum nanohole array generates hot electrons rapidly within the cavity of the array. With C_{60}, the kinetic process gets faster with a time constant of 270 ± 25 fs. The fast process implies that the photogenerated hot electrons relaxes in the presence of C_{60}.

To investigate if the relaxed hot electrons transfer to C_{60}, we performed the visible pump-white light probe experiments. Figure 4 presents transient white light spectra for aluminum nanoholes array with and without C_{60} under photoexcitation of 515 nm. Only one peak was observed at 772 nm for Al nanoholes array alone.

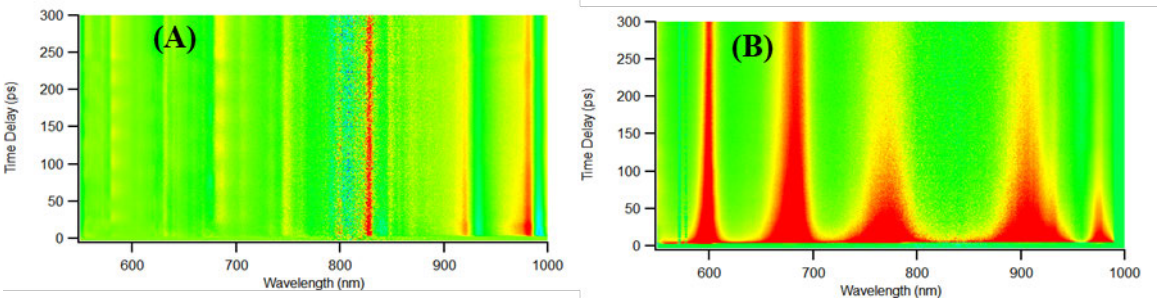

Figure 4. Transient changes in reflection of white light for aluminum nanoholes array with C_{60} (A) and without C_{60} (B).

Conversely, transient spectra of C_{60} exhibited several prominent peaks at 599 nm, 684 nm, 772 nm, 908 nm, and 982 nm for aluminum nanoholes array with C_{60}. To assign these five peaks, we plotted kinetic traces for each peak as shown in Figure 5.

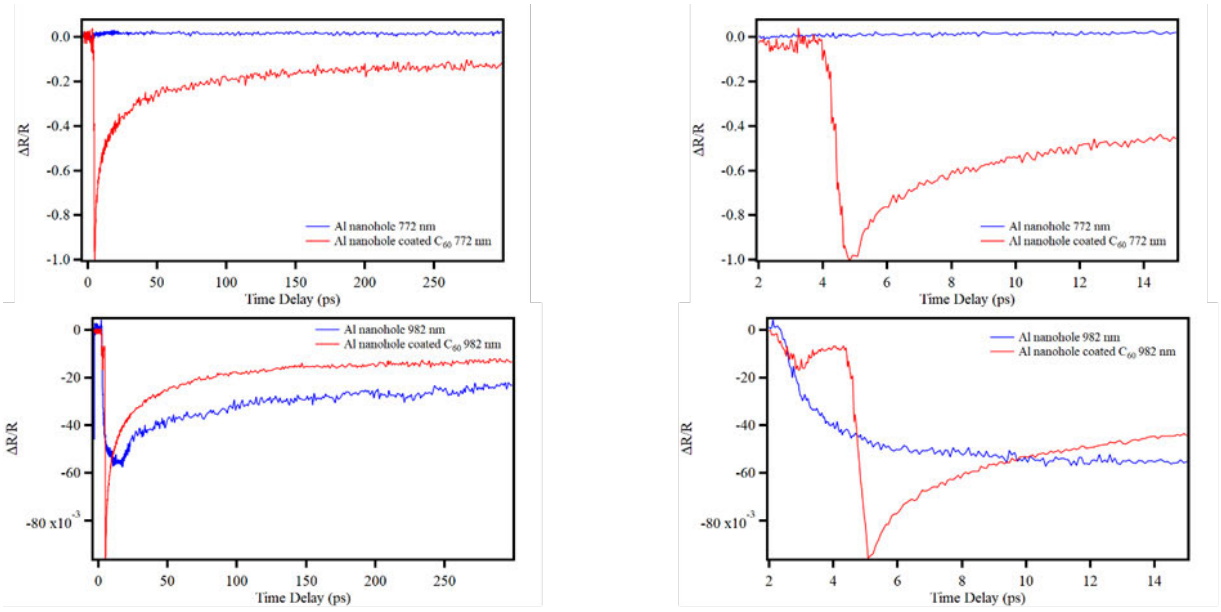

Figure 5. (left) Kinetics of Al nanoholes array without C_{60} (blue) and with C_{60} (red) at 772 nm (top) and 982 nm (bottom), at a long-time scale of 280 ps. (right) Kinetics of Al nanoholes array without C_{60} (blue) and with C_{60} (red) at 772 nm (top) and 982 nm (bottom), at a short time scale of 15 ps.

The lifetimes of the transient peaks at 772 nm and 908 nm are much shorter than those at 599 nm and 684 nm. The peaks at 772 nm and 908 nm were assigned as S_1–S_n transitions, while those at 599 nm, and 684 nm were assigned as T_1–T_n transitions. These results indicate that interfacial electron transfer definitively occurred at the Al nanoholes array/C_{60} interface. The incorporation of plasmonic nanostructures with C_{60} organic semiconductor materials facilitates the interfacial charge injection process. The relationship between the band gap of C_{60} and the Fermi level of the metallic arrays is central to the transfer of charges at the interfaces. Of particular importance in this study is that the enhancement of the aluminum nanohole array absorption and the subsequent enhancement in quantum efficiency

are caused by the near field plasmonic enhancement. These studies point to the significant potential of developing new plasmonic nanostructures to achieve more efficient photo-absorption and interfacial charge transfer.

As an organic semiconductor material, C_{60} is an excellent electron acceptor due to it has many unoccupied molecular orbitals. To further elucidate how the interfacial electron transfer takes place between Al nanoholes array and C_{60}. A schematic energy band for Al nanoholes array and C_{60} is provided in Figure 6.

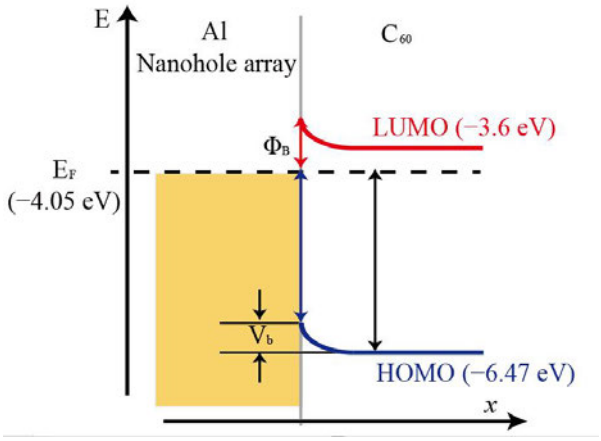

Figure 6. Energy diagram for aluminum nanohole array/C_{60} interface.

The electron on surfaces of aluminum nanohole array is excited into the lowest unoccupied molecular orbital (LUMO) for C_{60} through a Schottky barrier (ΦB). Surface plasmon resonances arise from the collective oscillation of the electrons at 2D aluminum nanohole arrays, from which hot electrons have been shown to be injected into the conduction band of the semiconductor over the Schottky barrier. When 2D aluminum nanohole arrays are in contact with C_{60}, the height of the Schottky barrier is important in that a high yield of carrier injection can be facilitated by an interfacial Schottky barrier, which drives injected electrons into the C_{60}.

4. SUMMARY AND CONCLUSIONS

We have presented the observation of hot electron transfer at an aluminum nanohole array/C_{60} interface by combining both transient IR and white light experiments. The photogenerated electrons on surfaces of aluminum nanohole array are injected into the lowest unoccupied molecular orbital for C_{60} through a Schottky barrier at a time scale of 270 ± 25 fs. When 2D aluminum nanohole arrays are in contact with C_{60}, the height of the Schottky barrier is important in that a high yield of carrier injection is facilitated by an interfacial Schottky barrier, which drives injected electrons into the C_{60}. Our research will impact both photo-absorption and charge collection for the photovoltaic and photocatalytic applications. These interfacial studies will not only provide a state-of-the-art approach to characterize ultrafast interfacial charge transfer processes but will also result in the utilization of new materials that will improve photovoltaic and photocatalytic applications of semiconductor and metallic nanostructures.

ACKNOWLEDGMENTS

Funding was provided by the U.S. Army via the Surface Science Initiative Program (PE 0601102A Project VR9) at the Edgewood Chemical Biological Center.

REFERENCES

[1] Debbrecht, B.; McElhiney, M.; Carey, V.; Cullen, C.; Mirotznik, M.S.; DeLacy, B.G. Cavity-based aluminum nanohole arrays with tunable infrared resonances. *Opt. Express.* **2017,** *25* (20), pp 24501–24511.

[2] Fang, H.; Wu, Y.; Chen, J.; Kuhn, D.L.; Zander, Z.; DeLacy, B.G.; Rao, Y.; Dai, H.-L. Electron injection from a carboxylic anchoring dye to TiO_2 nanoparticles in aprotic solvents. *Chem. Phys.* **2018,** *512*, pp 93–97.

Enhancing the uptake of oxygen and carbon dioxide in metal-organic frameworks

Trenton M. Tovar, Sergio J. Garibay, Ivan O. Iordanov, Jared B. DeCoste*
U.S. Army Edgewood Chemical Biological Center, Research & Technology Directorate,
8198 Blackhawk Rd, Aberdeen Proving Ground, MD 21010

ABSTRACT

UiO-66 is a highly stable metal-organic framework that has garnered interest for many adsorption applications. For small, nonpolar adsorbates, physisorption is dominated by weak van der Waals interactions limiting the adsorption capacity. We report here various methods for the adsorption of O_2 and CO_2. Compounding previous findings for the enhanced adsorption of O_2 by UiO-66-$(OH)_2$-*p*, other UiO-66-(X)-*p* analogs were examined and not found to have such profound effects. Furthermore, NU-901 analogs with free amine groups were synthesized for the adsorption of CO_2. As expected, most analogs exhibited an enhancement in CO_2 uptake; however, geometric and steric consideration are shown to have a profound impact through a combination of theoretical and empirical experiments.

Keywords: metal-organic frameworks, oxygen adsorption, carbon dioxide adsorption, density functional theory

1. INTRODUCTION

Metal-organic frameworks (MOF) are promising materials for use as next generation adsorbents. They consist of highly porous crystalline networks of metal nodes connected by organic linkers.[1] Due to the variability of both the metal centers and the organic linkers, the physical and chemical properties of MOFs can be tuned for specific applications such as gas storage,[2] catalysis,[3] separations,[4] and sensing.[5] Given the large number of potential MOFs,[6] it is highly desirable to develop rational design rules to guide the synthesis of MOFs with optimal properties. However, this is a complex task that requires detailed knowledge of atomistic interactions, specifically at adsorption sites.

Determining preferential adsorption sites in MOFs is complicated by the presence of multiple sites and intermolecular interactions that vary based on the desired adsorbate. Recently, experimental studies have used neutron scattering or X-ray crystallography to directly observe adsorption sites;[7–10] however, the most widely used tool to study preferential adsorption sites is molecular modeling.[11] Typical MOF adsorption sites include open-metal sites,[12–14] hydrogen bonding sites,[15,16] pore confinement sites,[17,18] and acid–base interactions.[19,20]

Physisorption of small non-polar gases, such as oxygen and carbon dioxide, lack strong intermolecular forces for adsorption. Previous studies on oxygen adsorption have primarily focused on high pressure adsorption,[21,22] which is driven by large pore volumes, or strong interactions with metals,[23–28] which typically require a hard vacuum or heating to deliver the adsorbate. The use of microporous materials, such as a MOF, has the potential to increase the adsorption capacity of the material at ambient pressure, while allowing the adsorbate to be delivered on demand without the addition of energy. We recently reported on the enhancement of weak van der Waals forces within the confined space of UiO-66 through the utilization of the 2,5-dihydroxy terephthaic acid derivative.[29] A unique effect was observed through density functional theory (DFT) calculations that the oxygen molecule lines up with the hydroxyl groups of the terephthalic acid linker to enhance adsorption.

Although many MOFs have significantly better adsorption properties than current industrial adsorbents, stability issues have limited their application. Zirconium-based MOFs are of particular interest due to their thermal, water, and acidic stability.[30–32] In UiO-66 (Figure 1) the organic ligands are amenable to functionalization for improvement of adsorption properties.[33–38] The enhanced adsorption characteristics in functionalized UiO MOFs are attributed to either the polarity of the functional group[34] or a confinement effect due to a reduction in pore size;[35] however, a specific preferential adsorption site has yet to be defined. Furthermore, the MOF NU-901 allows for the post-synthetic modification through solvent-assisted linker incorporation (SALI).[39] In SALI, ligands with carboxylic acid groups react with open zirconium sites sticking into the open channels of the MOF (Figure 2).

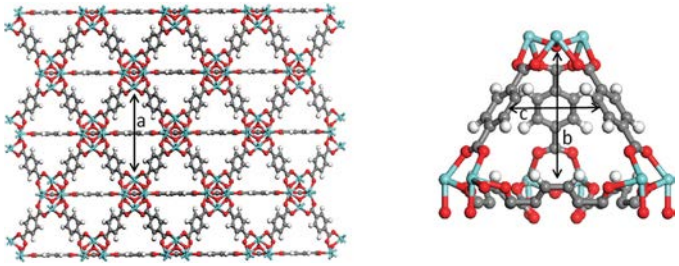

Figure 1. (Left) UiO-66 (zirconium – blue, oxygen – red, carbon – grey, and hydrogen – white) depicted along its axis exhibiting its larger octahedral cages (a) with a diameter of ~1.6 nm. (Right) The smaller tetrahedral cage of UiO-66 is depicted, showing the bisection of the window (b) measuring ~1.0 nm and the distance between the benzene rings (c) measuring 0.6 nm. Pendant functional groups are incorporated into the UiO structure by using an organic linker with the appropriate functional group to replace the hydrogen atom(s).

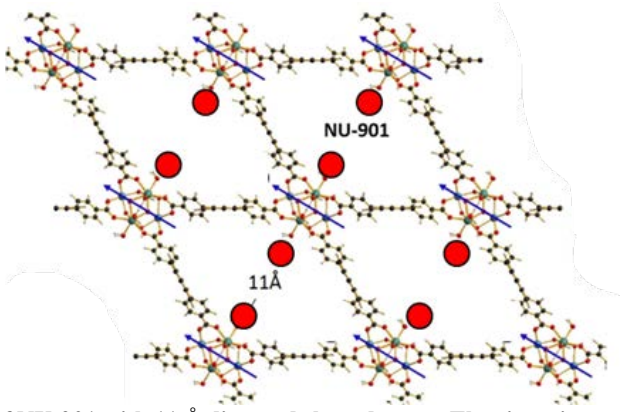

Figure 2. The structure of NU-901 with 11 Å diamond shaped pores. The zirconium nodes can be modified by SALI sticking into the channels as shown by the red circles.

Herein, we report the FY18 findings under the Surface Science Initiative for the adsorption of oxygen by UiO-66 analogs and the adsorption of carbon dioxide by modified NU-901. Some findings from previous years will be presented for clarity of presentation. In short, a combination of DFT and empirical results were used to offer clarity of adsorption of these gases in MOFs and lend insight toward design rules of MOFs and other adsorbents for the adsorption of such gases.

2. METHODOLOGY

2.1 Metal-organic framework synthesis

The synthesis procedure of all UiO-66 analogs was adapted from Biswas et al.[40] Approximately 0.64 mmol of $ZrCl_4$ was mixed with 0.72 mmol of linker in 6 mL of N,N-Dimethylformamide (DMF) and 2 mL of formic acid in a 20-mL scintillation vial. The vial was sonicated for 1 hour to dissolve the precursors. The solution was transferred to a Teflon™-lined Parr bomb and placed in an oven at room temperature. The oven temperature was ramped at 5 °C min^{-1} to 150 °C and held for 24 hours. Once cooled, the solids were filtered and washed 3 times with 10 mL of DMF. The samples were then dried at 90 °C. After drying, the samples were solvent exchanged with 10 mL of methanol for 24 hours. The samples were centrifuged at 6,000 rpm for 5 minutes, decanted, and the exchange procedure was repeated 2 more times. The samples were then dried at 90 °C. Before all measurements, the samples were activated at 90 °C under high vacuum.

For the synthesis of NU-901, 0.3 mmol of $Zr(acac)_4$ (acac = acetyl acetonate) and 22 mmol of benzoic acid (or a benzoic acid analog) were mixed in 8 mL of DMF in an 8-dram vial and ultrasonically dissolved. The clear solution was incubated in an oven at 80 °C for 1 hour. After cooling down to room temperature, H_4TBAPy (40 mg, 0.06 mmol) was added and sonicated for 10 minutes. The yellow suspension was placed in a pre-heated oven at 100 °C for 18 hours. After cooling down to room temperature, yellow polycrystalline material was isolated by centrifuge (5 minutes, 7,500 rpm) and solvent exchanged with fresh DMF three times (10 mL each) followed by methanol three times (10 mL). Yellow polycrystalline NU-901 was collected by centrifugation and dried in a vacuum oven at 80 °C

for 1 hour (yield: ~58 mg). To strip NU-901 of the benzoic acid modulators, the yellow powder was suspended in 12 mL DMF and 0.5 mL of 8 M aqueous HCl in an 8-dram vial and heated in an oven at 100 °C for 18 hours. After cooling to room temperature, the powder was isolated by centrifugation and washed with DMF three times (10 mL each) and acetone three times (10 mL each). The MOF was collected by centrifugation and dried in a vacuum oven at 80 °C for 1 hour.

For the incorporation of various organic ligands in NU-901 via SALI, 0.007 mmol of activated NU-901 was added to a solution containing 0.185 mmol of 4-(methylamino)benzoic acid dissolved in 5 mL of DMF in an 8-dram vial and ultrasonically agitated. The vial was incubated in an oven at 65 °C for 18 hours. After cooling down to room temperature, the yellow suspension was isolated by centrifuge (5 minutes, 7,500 rpm) and solvent exchanged with fresh DMF three times (10 mL each) followed by methanol three times (10 mL each). The MOF was collected by centrifugation and dried in a vacuum oven at 80 °C for 1 hour.

2.2 Metal-organic framework characterization

Nitrogen gas sorption measurements were performed on a Micromeritics 3Flex 3500 instrument at 77 kelvin. Each sample was off gassed overnight under vacuum at 90 °C. The Brunauer–Emmett–Teller model was applied over the pressure range as described by Walton and Snurr to obtain the specific surface area ($m^2\ g^{-1}$).[41]

Powder X-ray diffraction (PXRD) were measured using a Rigaku Miniflex 600UHF X-ray powder diffractometer with a D/Tex detector. Samples were scanned at 40 kV and 15 mA with a scan rate of $2°\cdot min^{-1}$ over a 2θ range of 3–50°. Zero-background discs were used, and a background correction was performed in the Rigaku PDXL software (version 2.1.3.6).

Low-pressure isotherms for O_2 and CO_2 were measured on a Micromeritics 3Flex 3500 instrument. Samples were immersed in a temperature-controlled water bath at the desired temperature during the measurement.

2.3 Computational modeling

Calculations were performed using density functional theory (DFT), as implemented in the Gaussian and Quantum Espresso software packages. In order to model the paramagnetism of molecular oxygen correctly, all cluster calculations were done in the Unrestricted Hatree-Fock formalism, with a triplet state for oxygen. For the periodic calculations of UiO-66, we used a 14.6 Å x 14.6 Å x 20.7 Å supercell with 228 atoms. The functional used was PBE,[42] with projector augmented wave pseudopotentials and an energy wavefunction cutoff of 40 Ry. Dispersion interactions were included under Grimme's DFT-D2 scheme.[43] The calculations were spin-polarized to account for oxygen, and correctly converged to a net magnetic moment of 2 bohr magneton per unit cell containing oxygen.

3. RESULTS AND DISCUSSION

3.1 Effect of UiO-66 functional group on O_2 adsorption

Previously, we reported on the effect of the two –OH groups para to one another on the MOF linker UiO-66, which led to exploration into other MOF linkers with para functional groups. There are very few 2,5 derivatives of terephthalic acid that are available commercially; however, we did attempt to synthesize UiO-66-Br_2, as well as UiO-66-Br_4, via Figure 3. N_2 isotherms and PXRD patterns were able to confirm the synthesis of UiO-66-Br_2, but a lack of crystallinity and low surface area indicated that we were not successful in the synthesis of UiO-66-Br_4 (Figure 4).

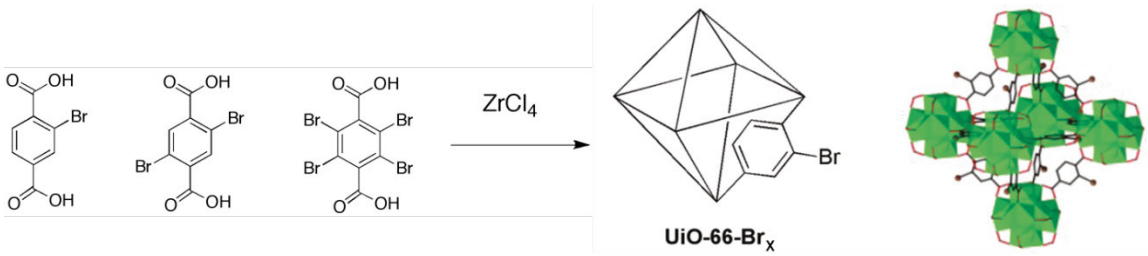

Figure 3. Synthesis and structure for UiO-66-Br_x (x = 1,2,4).

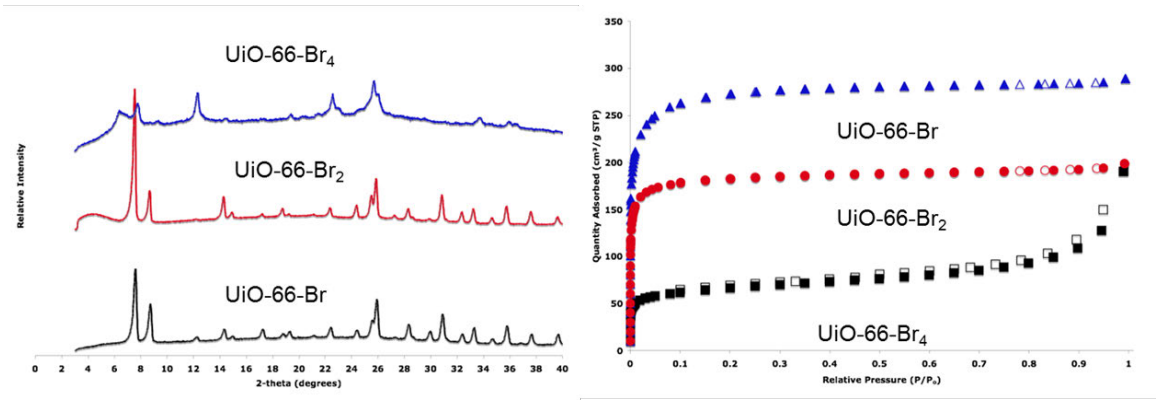

Figure 4. (left) PXRD patterns confirming the crystallinity for the UiO-66-Br$_x$ analogs studied (right) nitrogen isotherms at 77 kelvin used to determine the surface area of each MOF.

Figure 5 shows excess O_2 isotherms at room temperature, compared to other UiO-66 analogs studied previously.[29] It can be seen that these UiO-66-Br$_x$ derivatives were poor performers compared to the other analogs on both a gravimetric and volumetric basis. Previous results indicated that electron donating groups, such as –OH, and –NH_2 tend to enhance the adsorption of O_2, while electron withdrawing groups such as –NO_2 tend to have a negative effect on the adsorption of O_2. Halogens are typically considered weak electron withdrawing groups as they inductively withdraw electrons from the aromatic ring, but they do have non-bonding electrons that they can actually donate back from π-bonding. Furthermore, there is no appreciable enhancement in the adsorption of O_2 for the UiO-66-Br_2, indicating that this enhancement is a direct effect of the –OH groups being electron donating groups, giving a stronger electronic character to the aromatic ring to interact with the oxygen adsorbate.

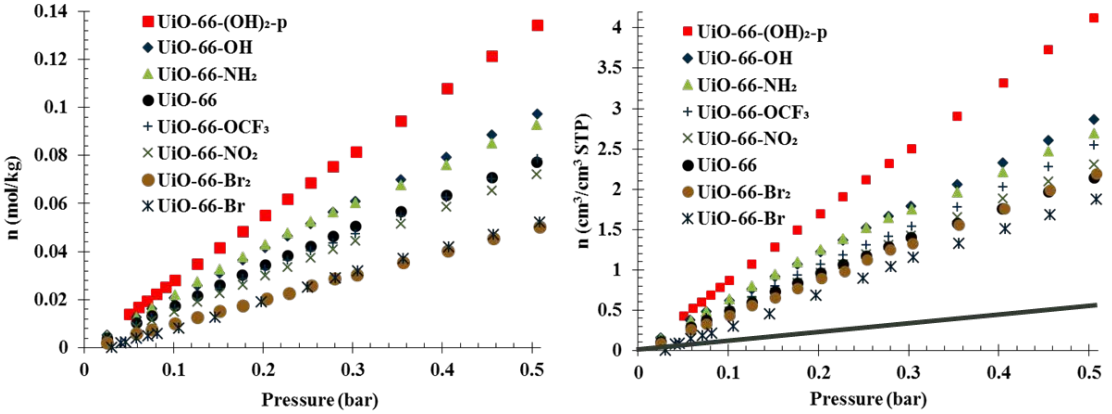

Figure 5. Room-temperature excess O_2 isotherms measured on various functionalized UiO-66 analogs, presented on (a) a gravimetric and (b) a volumetric basis.

3.2 CO_2 adsorption on NU-901 analogs via direct synthesis

Throughout the vast MOF literature there have been ample reports of functionality enhancing CO_2 adsorption. Given its amine functionality, we hypothesized that incorporation of amine groups onto the benzoic acid modulator, as shown in Figure 6, would enhance the CO_2 uptake of the MOFs. Three MOF variants were synthesized with a primary, secondary, and tertiary in the 4-position with NU-901-NH_2, NU-901-$NHCH_3$, and NU-901-$N(CH_3)_2$, respectively.

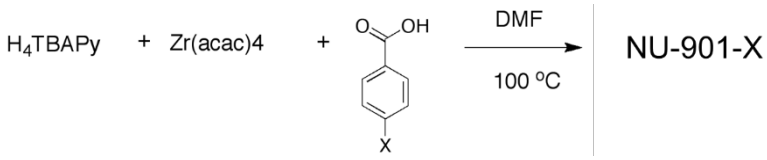

Figure 6. Synthesis and structure for NU-901-X (X = NH_2, $NHCH_3$, $N(CH_3)_2$).

Unfortunately, the only MOF linker that was able to incorporate the theoretical maximum of ~4 linkers per metal node was NU-901-NH_2, as summarized in Table 1. The secondary and tertiary analogs were only able to incorporate

two and one linker, respectively, into their structure. This is hypothesized to do with steric hindrance of the growing linkers within the MOF structure. The enhancement of CO_2 uptake for NU-901-NH_2 is approximately 55 %, compared to 15 % for NU-901-$NHCH_3$, and a decrease in uptake for NU-901-$N(CH_3)_2$. The CO_2 isotherms are presented in Figure 7, along with the NU-901-Br analog for comparison. From this data we were able to show that the CO_2 affinity is 1° amine > 2° amine > 3° amine in a porous structure for CO_2.

Table 1. Surface area, number of incorporated modulator linkers, and CO_2 uptake of each NU-901 analog.

MOF	Surface area (m^2/g)	Modulators incorporated	CO_2 uptake (cm^3/g)
NU-901-act	2276	0	54
NU-901-NH_2	1628	4	84
NU-901-$NHCH_3$	2070	2	62
NU-901-$N(CH_3)_2$	2029	1	51

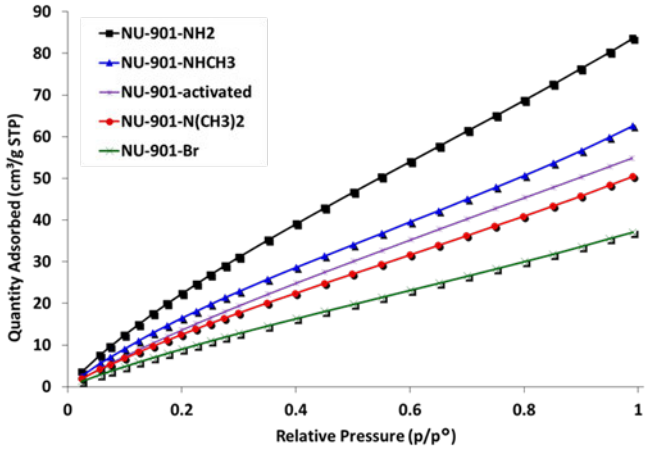

Figure 7. Room-temperature excess CO_2 isotherms measured on various functionalized NU-901-X analogs.

3.3 CO_2 adsorption on NU-901 analogs via solvent-assisted linker incorporation

In a further attempt to increase the uptake of CO_2 in NU-901, 3,5-diamino benzoic acid and 3,4-diamino benzoic acid were incorporated in NU-901-act using SALI. Each of these linkers were only incorporated at a level of 1 per node, meaning there were 50 % less amine groups for CO_2 to interact with compared to NU-901-NH_2. In spite of the fewer amine groups to interact with, the uptake of CO_2 was significantly enhanced for NU-901-SALI-$(NH_2)_2$ to 123 cm^3/g, or approximately an enhancement of 124 % compared to NU-901-act, as shown in Figure 8.

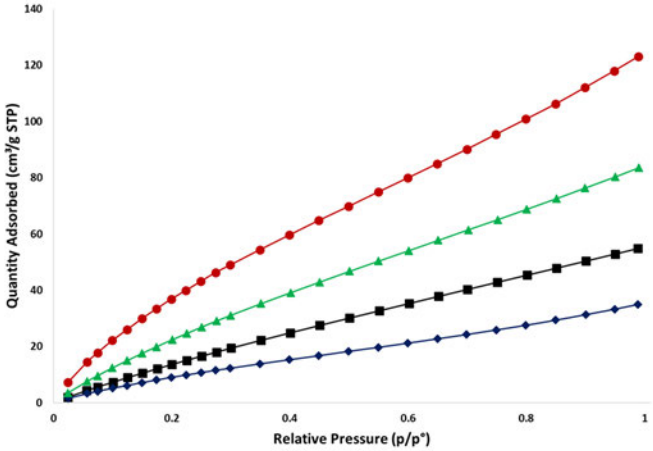

Figure 8. CO_2 isotherms at 273 kelvin of NU-901-SALI-3,5-$(NH_2)_2$ (red circles), NU-901-NH_2 (green triangles), NU-901 (black squares), and NU-901-SALI-3,4-$(NH_2)_2$ (blue diamonds).

3.4 Steric effects on CO_2 adsorption in NU-901

For gas adsorption in microporous materials there can be an extremely fine line between having pores small enough to adsorb the gas of interest and having pores that are too small to fit the adsorbate. Observing an enhancement in the CO_2 adsorption of NU-901-SALI-3,5-$(NH_2)_2$ compared to NU-901-NH_2 when it only had half as many active amine sites raise the question as to whether sterics may be playing a role. Using DFT, crystal structures of NU-901 containing one 3,5-diamino benzoic acid ligand per node, and four 4-amino benzoic acid ligands per node were optimized. The structure for NU-901-NH_2 showed significant geometric concerns for the adsorption of CO_2. It can be seen in Figure 9 that, in the smaller NU-901 pore, the two ligands across from one another were about 3 Å apart, furthermore the –NH_2 groups were about 2 Å from the transverse secondary building unit (SBU), and about 3 Å from the adjacent organic linker of NU-901. All of these distances would cause concern for the adsorption of CO_2, which measures 2.3 Å from oxygen to oxygen. When looking at the larger pore of NU-901 there is still steric considerations that need to be had. The two linkers at again less than 3 Å from one another; however, there is slightly more space across from the –NH_2 in that the transverse SBU is about 5.5 Å away, and the adjacent organic linker of NU-901 is about 4 Å away.

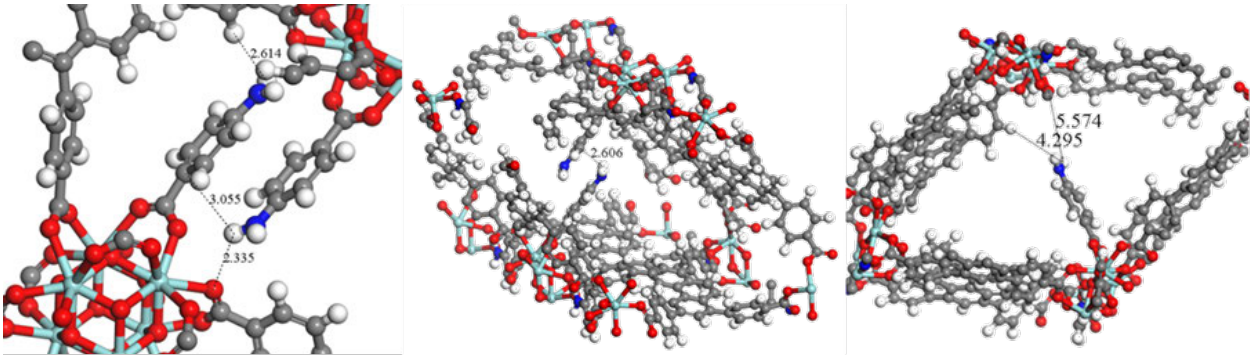

Figure 9. NU-901-NH_2 structures optimized by DFT looking at the (left) small pore, (middle) large pore, and (right) large pore with one linker removed for clarity.

Conversely, the NU-901-SALI-3,5-$(NH_2)_2$ optimized structure shows that there is much more free space for adsorption of CO_2, as seen in Figure 10. Assuming that the linker is in the large pore, as this is more favorable, the SBU is now 6.5 Å from the nearest –NH_2 group and the organic linker is more than 9 Å away. Likely, even more important is the fact that the amine groups actually are in the plane of the pore and not pointing toward the SBU or organic linker, meaning that the optimal adsorption site for CO_2 is effectively even further away from having adverse steric effects. It should be noted at this point that the enhancement in CO_2 uptake for NU-901-SALI-3,5-$(NH_2)_2$ correlates to approximately 1.3 CO_2 molecules per –NH_2 group. While it is only expected that each –NH_2 group would adsorb a single CO_2 molecule, it has been shown in our previous work that preferential adsorption pockets can be created near the SBU when a linker is introduced, such as done here with SALI.[29]

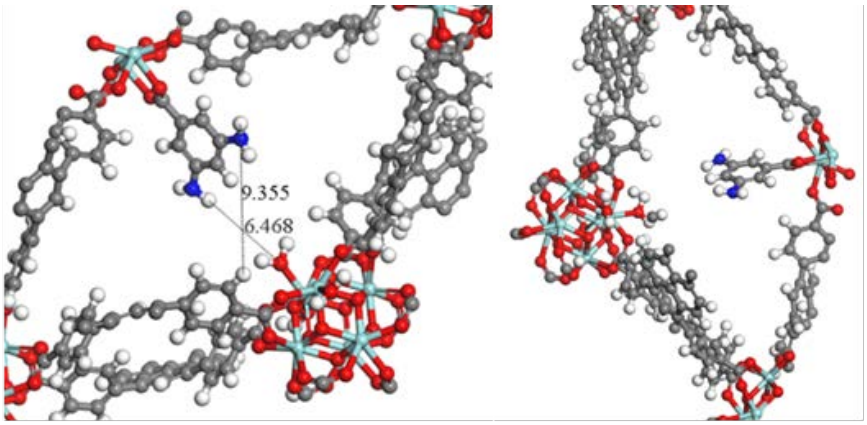

Figure 10. NU-901-SALI-3,5-$(NH_2)_2$ structures optimized by DFT looking at the (left) small pore, (middle) large pore, and (right) large pore with one linker removed for clarity.

4. CONCLUSIONS

Experiments here built on previous reports of the functionalized UiO-66 series of MOFs and the effect that electron-donating groups tend to enhance the adsorption of non-polar adsorbates, like O_2, when compared to electron-withdrawing groups. There was no additional enhancement in the adsorption of O_2 when two –Br groups were placed para to one another, as was previously observed with –OH groups. The adsorption of CO_2 by amine-functionalized derivatives of NU-901 shows that primary amines exhibit the largest uptake enhancement followed by secondary and tertiary amines. Furthermore, we were able to show that a 3,5-diamino derivative was able to show an even larger enhancement in uptake per amine group as compared to the 4-amino derivative due to steric considerations.

ACKNOWLEDGMENTS

Funding was provided by the U.S. Army via the Surface Science Initiative Program (PE 0601102A Project VR9) at the Edgewood Chemical Biological Center. This research was performed while Trenton Tovar and Sergio Garibay held National Research Council Postdoctoral Research Associateship Program positions at the Edgewood Chemical Biological Center.

REFERENCES

[1] Kim, J.; Chen, B.; Reinike, T.M.; Li, H.; Eddaoudi, M.; Moler, D.B.; O'Keefe, M; Yaghi, O.M. Assembly of Metal−Organic Frameworks from Large Organic and Inorganic Secondary Building Units: New Examples and Simplifying Principles for Complex Structures. *J. Am. Chem. Soc.* **2001,** *123* (34), pp 8239–8247.

[2] Sumida, K.; Rogow, D.L.; Mason, J.A.; McDonald, T.M.; Bloch, E.D.; Herm, Z.R.; Bae, T.-H.; Long, J.R. Carbon Dioxide Capture in Metal–Organic Frameworks. *Chem. Rev.* **2012,** *112* (2), pp 724–781.

[3] Lee, J.Y.; Farha, O.K.; Roberts, J.; Scheidt, K.A.; Nguyen S.T.; Hupp, J.T. Metal-Organic Framework Materials as Catalysts. *Chem. Soc. Rev.* **2009,** *38* (5), pp 1450–1459.

[4] Li, J.R.; Sculley J.; Zhou, H.-C. Metal–Organic Frameworks for Separations. *Chem. Rev.* **2012,** *112* (2), pp 869– 932.

[5] Kreno, L.E.; Leong, K.; Farha, O.K.; Allendorf, M.; Van Duyne, R.P.; Hupp, J.T. Metal–Organic Framework Materials as Chemical Sensors. *Chem. Rev.* **2012,** *112* (2), pp 1105–1125.

[6] Wilmer, C.E.; Leaf, M.; Lee, C.Y.; Farha, O.K.; Hauser, B.G.; Hupp, J.T.; Snurr, R.Q. Large-scale screening of hypothetical metal-organic frameworks. *Nat. Chem.* **2012,** *4* (2), pp 83–89.

[7] Wu, H.; Simmons, J.M.; Srinivas, G.; Zhou, W.; Yildirim, T.J. Adsorption Sites and Binding Nature of CO_2 in Prototypical Metal−Organic Frameworks: A Combined Neutron Diffraction and First-Principles Study. *Phys. Chem. Lett.* **2010,** *1* (13), pp 1946–1951.

[8] Mulder, F.M.; Dingemans, T.J.; Schimmel, H.G.; Ramirez-Cuesta, A.J.; Kearley, G.J. Hydrogen adsorption strength and sites in the metal organic framework MOF5: Comparing experiment and model calculations. *Chem. Phys.* **2008,** *351* (1–3), pp 72–76.

[9] Rowsell, J.L.C.; Spencer, E.C.; Eckert, J.; Howard J.A.K.; Yaghi, O.M. Gas Adsorption Sites in a Large-Pore Metal-Organic Framework. *Science*. **2005,** *309* (5739), pp 1350–1354.

[10] Yang, C.; Yang, X.; Omary, M.A. Crystallographic Observation of Dynamic Gas Adsorption Sites and Thermal Expansion in a Breathable Fluorous Metal-Organic Framework. *Agnew. Chem. Int. Ed.* **2009,** *48* (14), pp 2500– 2505.

[11] Düren, T.; Bae, Y.-S.; Snurr, R.Q. Using molecular simulation to characterise metal–organic frameworks for adsorption applications. *Chem. Soc. Rev.* **2009,** *38* (5), pp 1237–1247.

[12] Yang, Q.; Zhong, C. Understanding Hydrogen Adsorption in Metal−Organic Frameworks with Open Metal Sites: A Computational Study. *J. Phys. Chem. B*. **2006,** *110* (2), pp 655–658.

[13] Mallick, A.; Saha, S.; Pachfule, P.; Roy, S.; Banerjee, R.J. Selective CO_2 and H_2 adsorption in a chiral magnesium-based metal organic framework (Mg-MOF) with open metal sites. *J. Mat. Chem.* **2010,** *20* (41), pp 9073– 9080.

[14] Vishnyakov, A.; Ravikovitch, P.I.; Neimark, A.V.; Bulow, M.; Wang, Q.M. Nanopore Structure and Sorption Properties of Cu−BTC Metal−Organic Framework. *Nano. Lett.* **2003,** *3* (6), pp 713–718.

[15] Hamon, L.; Leclerc, H.; Ghoufi, A.; Oliviero, L.; Travert, A.; Lavalley, J.-C.; Devic, T.; Serre, C.; Ferey, G.; Weireld, G.D.; Vimont, A.; Maurin, G. Molecular Insight into the Adsorption of H_2S in the Flexible MIL-53(Cr) and Rigid MIL-47(V) MOFs: Infrared Spectroscopy Combined to Molecular Simulations. *J. Phys. Chem. C.* **2011,** *115* (5), pp 2047–2056.

[16] Glover, T.G.; Peterson, G.W.; Schindler, B.J.; Yaghi, O.M. MOF-74 building unit has a direct impact on toxic gas adsorption. *Chem. Eng. Sci.* **2011,** *66* (2), pp 163–170.

[17] Valenzano, L.; Civalleri, B.; Chavan, S.; Palomino, G.T.; Arean C.O.; Bordiga, S. Computational and Experimental Studies on the Adsorption of CO, N_2, and CO_2 on Mg-MOF-74. *J. Phys. Chem. C.* **2010,** *114* (25), pp 11185–11191.

[18] Atci, E.; Erucar, I.; Keskin, S. Adsorption and Transport of CH_4, CO_2, H_2 Mixtures in a Bio-MOF Material from Molecular Simulations. *J. Phys. Chem. C.* **2011,** *115* (14), pp 6833–6840.

[19] Couck, S.; Denayer, J.F.M.; Baron, G.V.; Remy, T.; Gascon, J.; Kapteijn, F. An Amine-Functionalized MIL-53 Metal−Organic Framework with Large Separation Power for CO_2 and CH_4. *J. Am. Chem. Soc.* **2009,** *131* (18), pp 6326–6327.

[20] McDonald, T.M.; D'Alessandro, D.M.; Krishna, R.; Long, J.R. Enhanced carbon dioxide capture upon incorporation of *N,N′*-dimethylethylenediamine in the metal–organic framework CuBTTri. *Chem. Sci.* **2011**, *2* (10), pp 2022–2028.

[21] DeCoste, J.B.; Weston, M.H.; Fuller, P.E.; Tovar, T.M.; Peterson, G.,W.; LeVan, M.D.; Farha, O.K. Metal-Organic Frameworks for Oxygen Storage. *Agnew. Chem. Int. Ed.* **2014,** *53* (51), pp 14092–14095.

[22] Alezi, D.; Belmakbkhout, Y.; Suyetin, M.; Bhatt, P.M.; Weselinski, L.J.; Solovyeva, V.; Adil, K.; Spanopoulos, I.; Trikalitis, P.N.; Emwas A.-H.; Eddaoudi, M. MOF Crystal Chemistry Paving the Way to Gas Storage Needs: Aluminum-Based soc-MOF for CH_4, O_2, and CO_2 Storage. *J. Am. Chem. Soc.* **2015,** *137* (41), pp 13308–13318.

[23] Sava Gallis, D.F.; Parkes, M.V.; Greathouse, J.A.; Zhang, X.; Nenoff, T.M. Enhanced O_2 Selectivity versus N_2 by Partial Metal Substitution in Cu-BTC. *Chem. Mater.* **2015,** *27* (6), pp 2018–2025.

[24] Wang, Y.; Yang, J.; Li, Z.; Zhang, Z.; Li, J.; Yang, Q.; Zhong, C. Computational study of oxygen adsorption in metal-organic frameworks with exposed cation sites: effect of framework metal ions. *RSC Adv.* **2015,** *5* (42), pp 33432–33437.

[25] Parkes, M.V.; Greathouse, J.A.; Hart, D.B.; Sava Gallis D.F.; Nenoff, T.M. *Ab initio* molecular dynamics determination of competitive O_2 *vs.* N_2 adsorption at open metal sites of M_2(dobdc). *Phys. Chem. Chem. Phys.* **2016,** *18* (16), pp 11528–11538.

[26] Zhang, W.; Banerjee, D.; Liu, J.; Schaef, H.T.; Crum, J.V.; Fernandez, C.A.; Kukkadapu, R.K.; Nie, Z.; Nune, S.K.; Motkuri, R.K.; Chapman, K.W.; Engelhard, M.H.; Hayes, J.C.; Silvers, K.L.; Krishna, R.; McGrail, B.P.; Liu, J.; Thallapally, P.K. Redox-Active Metal–Organic Composites for Highly Selective Oxygen Separation Applications. *Adv. Mater.* **2016,** *28* (18), pp 3572–3577.

[27] Bloch, E.D.; Murray, L.J.; Queen, W.L.; Chavan, S.; Maximoff, S.N.; Bigi, J.P.; Krishna, R.; Peterson, V.K.; Grandjean, F.; Long, G.J.; Smit, B.; Bordiga, S.; Brown C.M.; Long, J.R. Selective Binding of O_2 over N_2 in a Redox– Active Metal–Organic Framework with Open Iron(II) Coordination Sites. *J. Am. Chem. Soc.*, **2011**, *133* (37), pp 14814–14822.

[28] Murray, L.J.; Dinca, M.; Yano, J.; Chavan, S.; Bordiga, S.; Brown C.M.; Long, J.R. Highly-Selective and Reversible O_2 Binding in Cr_3(1,3,5-benzenetricarboxylate)$_2$. *J. Am. Chem. Soc.* **2010,** *132* (23), pp 7856–7857.

[29] Tovar, T.M.; Iordanov, I.; Sava Gallis, D.F.; DeCoste, J.B. Enhancing Van der Waals Interactions of Functinooalized UiO-66 with Non-polar Adsorbates: The Unique effect of para Hydroxyl Groups. *Chem-Eur. J.* **2018,** *24* (8), pp 1931– 1937.

[30] Cavka, J.H.; Jakobsen, S.; Olsbye, U.; Guillou, N.; Lamberti, C.; Bordiga S.; Lillerud, K.P. A New Zirconium Inorganic Building Brick Forming Metal Organic Frameworks with Exceptional Stability. *J. Am. Chem. Soc.* **2008,** *130* (42), pp 13850–13851.

[31] DeCoste, J.B.; Peterson, G.W.; Schindler, B.J.; Killops, K.L.; Browe, M.A.; Mahle, J.J. The effect of water adsorption on the structure of the carboxylate containing metal–organic frameworks Cu-BTC, Mg-MOF-74, and UiO-66. *J. Mater. Chem. A.* **2013,** *1* (38), pp 11922–11932.

[32] DeCoste, J.B.; Peterson, G.W.; Jasuja, H.; Glover, T.G.; Huang, Y.; Walton, K.S. Stability and degradation mechanisms of metal–organic frameworks containing the $Zr_6O_4(OH)_4$ secondary building unit *J. Mater. Chem. A.* **2013,** *1* (18), pp 5642–5650.

[33] Garibay, S.J.; Cohen, S.M.; Walton, K.S. Isoreticular synthesis and modification of frameworks with the UiO-66 topology. *Chem. Commun.* **2010,** *46* (41), pp 7700–7702.

[34] Cmarik, G.E.; Kim, M.; Cohen, S.M.; Walton, K.S. Tuning the Adsorption Properties of UiO-66 via Ligand Functionalization. *Langmuir.* **2012,** *28* (44), pp 15606–15613.
[35] Yang, Q.; Wiersum, A.D.; Llewellyn, P.L.; Guillerm, V.; Serre, C.; Maurin, G. Functionalizing porous zirconium terephthalate UiO-66(Zr) for natural gas upgrading: a computational exploration. *Chem. Commun.* **2011,** 47 (34), pp 9603–9605.
[36] Biswas, S.; Zhang, J.; Li, Z.; Liu, Y.-Y.; Grzywa, M.; Sun, L.; Volkmer, D.; Van Der Voort, P. Enhanced selectivity of CO_2 over CH_4 in sulphonate-, carboxylate- and iodo-functionalized UiO-66 frameworks. *Dalton Trans.* **2013,** *42* (13), pp 4730–4737.
[37] Jasuja, H.; Walton, K.S. Experimental Study of CO_2, CH_4, and Water Vapor Adsorption on a Dimethyl-Functionalized UiO-66 Framework. *J. Phys. Chem. C.* **2013,** *117* (14), pp 7062–7068.
[38] Zlotea, C.; Phanon, D.; Mazaj, M.; Heurtaux, D.; Guillerm, V.; Serre, C.; Horcajada, P.; Devic, T.; Magnier, E.; Cuevas, F.; Ferey, G.; Llewellyn, P.L.; Latroche, M. Effect of NH_2 and CF_3 functionalization on the hydrogen sorption properties of MOFs. *Dalton Trans.* **2011,** *40* (18), pp 4879–4881.
[39] Deria, P.; Mondloch, J.E.; Tylianaki, E.; Ghosh, P.; Bury, W.; Snurr, R.Q.; Hupp, J.T.; Farha, O.K. Perflruoroalkane Functionalized of NU-1000 via Solvent Assitant Ligand Incorporation: Synthesis and CO_2 Adsorption Studies. *J. Am. Chem. Soc.* **2013,** *135* (45), pp. 16801–16804.
[40] Biswas, S.; Van Der Voort, P.A. General Strategy for the Synthesis of Functionalised UiO-66 Frameworks: Characterisation, Stability and CO_2 Adsorption Properties. *Eur. J. Inorg. Chem.* **2013**, *2013* (12), pp 2154– 2160.
[41] Walton, K.S.; Snurr, R.Q. Applicability of the BET Method for Determining Surface Areas of Microporous Metal−Organic Frameworks. *J. Am. Chem. Soc.* **2007,** *129* (27), pp 8552–8556.
[42] Grimme, S. Semiempirical GGA-type density functional constructed with a long-range dispersion correction. *J. Comput. Chem.* **2006,** *27* (15), pp 1787–1799.
[43] Barone, V.; Casarin, M.; Forrer, D.; Pavone, M.; Sambi, M.; Vittadini, A. Role and effective treatment of dispersive forces in materials: Polyethylene and graphite crystals as test cases. *J. Comput. Chem.* **2009,** *30* (6), pp 934–939.

Characterization of opioid conformational changes and their effect on binding and reactivity on surfaces

Monica L. McEntee[a]*, Mark D. Winemiller[a], Andrew J. Walz[a], Fu-Lian Hsu[a], Amanda M. Schenning[a], Michelle L. Sheahy[a], Ivan O. Iordanov[a], John M. Landers[b], Gregory W. Peterson[a]
[a]U.S. Army Edgewood Chemical Biological Center, Research & Technology Directorate, 8198 Blackhawk Rd, Aberdeen Proving Ground, MD 21010
[b]National Research Council, 500 5th St NW, Washington, D.C. 20001

ABSTRACT

The basic knowledge about the structure, chemical, and physical properties of opioid molecules has not been fully established. Nuclear magnetic resonance spectroscopy data suggests that carfentanil has more than one solvent-dependent conformer whereas remifentanil has only one structure. Studies of these opioids in different salt forms show that conformation is independent of the anion. Density functional theory calculations convey carfentanil conformers are stable at lower energies than remifentanil conformers. Additionally, the neutral (freebase) molecules contain more labile functional groups than the protonated (salt) forms, which suggests the protonated opioids contain more stable conformers than the neutral species. As a result, it is reasonable to assume that conformational diversity could have important implications for the binding and reactivity of this class of molecules on surfaces. Preliminary uptake studies were performed for both carfentanil and remifentanil on SiO_2 and several Zr-based metal organic frameworks, and the results show both a porosity and solvent dependence.

Keywords: carfentanil, remifentanil, conformational changes, surface binding, opioid, protonated, nuclear magnetic resonance

1. INTRODUCTION

The fentanyl class of synthetic opioids has generated an immense interest outside the medical field recently due to increasing drug overdoses and chemical attacks worldwide. Developed in the 1960s by Janssen and colleagues,[1–3] fentanyl (N-(1-(2-phenylethyl)-4-piperidinyl)-N-phenylpropanamide) and carfentanil are 100 and 10,000 times[4] more potent than morphine, respectively. Further research led to the development of remi- and su-fentanil with short onset times[5] and high lipid solubility increasing their pharmaceutical efficiency and potency.

Previous opioid studies have focused primarily on two separate research paths: 1) characterization of the opioid binding to different pain receptors and determination of their potency in the human body, and 2) synthesis in order to improve synthetic steps[6] and to create analogs. Following path 1, this class of opioids is known to bind to the μ-receptor but could also bind and act through δ- and κ-opiate receptors.[7] Weltrowska et al.[8] researched carfentanil and carba-carfentanil binding to the μ-receptor via the Asp147 residue. The binding affinity to the Asp147 residue was reduced when the N atom in carfentanil is replaced with a C atom in carba-carfentanil and the binding orientation of the molecule also changed; however, the potency (agonist activity) remained, which indicates that the Asp147 residue was not the necessary site for receptor activation. Further theoretical studies done by Snyder's group[9] determined that there are two important regions on the fentanyl molecule: the benzene ring with the amine nitrogen (referred to as ring A) and the phenethyl group (referred to as ring F). Ring A is crucial for potent activity; however, when they calculate the F ring in different conformational orientations, only one specific conformation performs agonist activity. Clearly, a more fundamental understanding of these conformational changes and how they affect binding to a surface is required.

Following path 2, previous synthetic routes were investigated to improve the yield of this class of molecules. Janssen et al. found by changing the phenethyl group (ring F) to a phenylmethyl group drastically enhanced reactivity and yield of an amide analog from a cyanide analog;[10] however, the reason is still unclear. A possible explanation may

lie in a conformational change affecting functional group reactivity just as was emphasized in path 1 for the affected potency when binding to a receptor.

A change in the conformational structure of a flexible molecule can promote a change in the molecule's physical and chemical properties. Li et al.[11] found a transmembrane protein in three different conformations each having different binding affinities. Conformational changes can also be affected/changed by environmental factors such as temperature, pH, solvent, concentration, and other species. Thus, the importance of understanding the impact changing the conformational structure has on binding and reactivity on surfaces cannot be overemphasized and can help in the future understanding of these class of molecules in many different research fields such as synthesis, decontamination, toxicology, aerosols and obscurants, and medicine. The novelty of studying the conformers' effect on reactivity lies within discovering a better mechanistic understanding of how these potent compounds bind to sites of interest. Here, we study the conformational changes of two opioids (carfentanil and remifentanil) and their constituents in solution and the effect their conformer changes have on the binding and reactivity on surfaces of different porosities.

2. METHODS AND PROCEDURES

2.1 Synthesis of opioids

Carfentanil and remifentanil salts were synthesized from a derivation from the literature.[10] Commercially available 1-benzyl-4-piperidone was used as the starting material. Formation of the imine, followed by hydrocyanation across the carbon-nitrogen bond, produced the cyano-substituted salt. From the CN-opioid, propionyl chloride generated amide bond formation to form the ketone group on the nitrogen atom away from the piperidine ring on the opioid structure. The ketone-opioid was then treated with methanolic HCl to replace the CN group with a methyl ester functional group. Purification generated the precipitation of the oxalate salt. Ammonium formate was then employed to produce the free amine at the N-piperidine ring removing the methylphenyl group. Lastly, the amine was alkylated with phenylethyl chloride to form neutral carfentanil. When a Michael addition using methyl acrylate was performed on the amine, neutral remifentanil was produced instead. Treating these two opioids with the desired acid produces the salt form.

2.2 Nuclear magnetic resonance spectroscopy

All ^{1}H NMR spectra were recorded on a Bruker Avance III HD 500 MHz instrument and referenced to the residual solvent peaks. All ^{1}H NMR spectra for kinetic runs were performed on the same 500 MHz instrument. A macro was used so that gradient shimming would be performed before the collection of each ^{1}H spectrum after a specified time interval. At the conclusion of a run, another macro was used to process and integrate all the ^{1}H NMR spectra back against the internal standard allowing for a greater number of points to be collected and eliminating bias during analysis.

2.3 Liquid chromatography-mass spectrometry

Uptake studies were performed by preparing aqueous solutions of carfentanil citrate and remifentanil HCl, separately, in mixtures of 0 %, 20 %, 40 %, 60 %, 80 %, and 100 % by volume of water with methanol as the other solvent. Approximately 10 mg of solid material (SiO_2, UiO-66, UiO-66-NH_2, UiO-67, and NU-1000) were added to each set of solution mixtures and stirred at ambient temperature for 18-24 hours. The samples were then centrifuged to drive the surface material to the bottom of the vial. The top aqueous portion was pipetted into a vial and transferred into the LC-MS. A control set of vials was made for both carfentanil and remifentanil salts with no solid material for comparison.

2.4 IR spectroscopy

In order to differentiate between the various functional groups of the opioid structures, diffuse reflectance infrared Fourier transform spectroscopy (DRIFTS) was utilized after the opioids were synthesized. The opioid salt (~0.9 mg) was placed into the DRIFTS cell (Harrick) oriented in the internal compartment of a Thermo Nicolet 6700 FTIR spectrometer under a CO_2- and H_2O-free air purge for approximately 10 minutes. Then an IR spectrum was taken with an average of 256 scans at a 2 cm^{-1} resolution. A KBr powder was used as the background spectrum.

2.5 Density functional theory

Plane wave density functional theory (DFT) calculations were done using the Quantum Espresso software package. Core electrons were approximated using projector augmented wave pseudopotentials with a 40/400 Ry corresponding wavefunction/electron density cutoff. The exchange correlation was approximated using the Perdew–Burke-Ernzerhof functional. All presented structures were geometry optimized with convergence thresholds of $10^{-5}/10^{-4}$ Ry for the energies/forces. All calculations included only the Γ-point due to size constraints.

3. RESULTS AND DISCUSSION

3.1 Characterization of protonated opioid salts

Before analyzing the opioids in solution, one major knowledge gap in the literature was where the was opioid protonated when in the salt form. A DRIFTS spectrum was taken of carfentanil oxalate salt after synthesis under a CO_2- and H_2O-free air purge for ~10 minutes (Figure 1). The likely sites for protonation on the opioid structure are the oxygen atoms on the C=O moieties and the nitrogen atoms. In IR spectroscopy, the wavenumber (cm^{-1}) shifts are sensitive and the difference between C=O modes and C–O–H modes are large and distinct. Figure 1 shows all of the C=O modes are present at 1740 cm^{-1} assigned to the ester group,[12] 1666 cm^{-1} assigned to the ketone group,[12] and 1605 cm^{-1} assigned to the oxalate group, respectively, of the carfentanil oxalate salt. If any or all of the groups were protonated, the IR peak(s) would redshift down in frequency below 1600 cm^{-1}.[12] Since the redshift does not occur, the opioid is not protonated at the oxygen atoms.

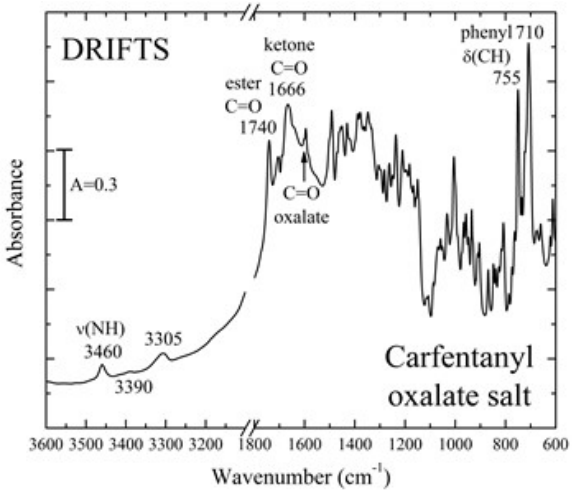

Figure 1. IR spectrum of dry carfentanil oxalate salt.

For further verification that the oxygen atoms are not the protonated sites, DFT calculations were performed to determine the most likely protonated site. A hydrogen atom was placed on each oxygen and nitrogen atom and the opioid structure was allowed to geometrically optimize. The lowest energy site was the protonation of the nitrogen on the piperidine ring. Others in the literature have theorized this site to be the protonated site as well.[13]

3.2 Characterization of opioids in solution

The synthesis of carfentanil salt has been studied previously in the literature[14] and characterized in methanol solvent. The 1H NMR shifts for carfentanil oxalate salt in methanol were assigned as δ 7.52–7.44 (m, 3H), 7.37–7.35 (m, 2H), 7.30–7.19 (m, 5H), 3.80 (s, 3H), 3.53–3.48 (m, 2H), 3.34–3.23 (m, 4H), 2.99–2.95 (m, 2H), 2.50–2.45 (m, 2H), 1.97–1.89 (m, 4H), and 0.92 (t, 3H, J = 7.33 Hz),[14] where each peak splitting corresponds to a group of atoms on the opioid structure. However, when carfentanil was dissolved in different solvents, the NMR spectra changed. Figure 2 shows a 0.016M solution of carfentanil oxalate salt in different solvents. When carfentanil oxalate is in methanol, the peaks at 3.8 ppm, 3.5 ppm, 3.3 ppm, 3.0 ppm, 2.5 ppm, and 2.0 ppm correspond to the O–CH_3, N–CH_2, N–CH_2–CH_2, Ph–CH_2, C–CH_2, and OC–CH_2–CH_3 groups which are consistent with literature values.[14] Interestingly, new NMR peaks are observed in dimethyl sulfoxide (green curve) and water (blue curve) solvents. Using the (n + 1) rule, the NMR peak in methanol at 3.8 ppm is assigned to the methoxy (O–CH_3) moiety on the opioid and should be a singlet

since its next nearest neighbor contains zero hydrogen bonds. Interestingly in water, the singlet peak is observed as a doublet. From 2D NMR spectroscopy (not shown here), the doublet is actually two singlet peaks. Another example of this doubling effect is shown at 3.0 ppm, which is assigned to the CH_2 moiety next to the phenyl ring of the opioid. The CH_2 group shows a triplet NMR band in methanol and shows two triplets in water. The doubling effect is consistent with the theory that two geometrically different carfentanil molecules are observed in water and are not observed in methanol. Two molecules with the same chemical formula but with different geometric structures are called conformers.

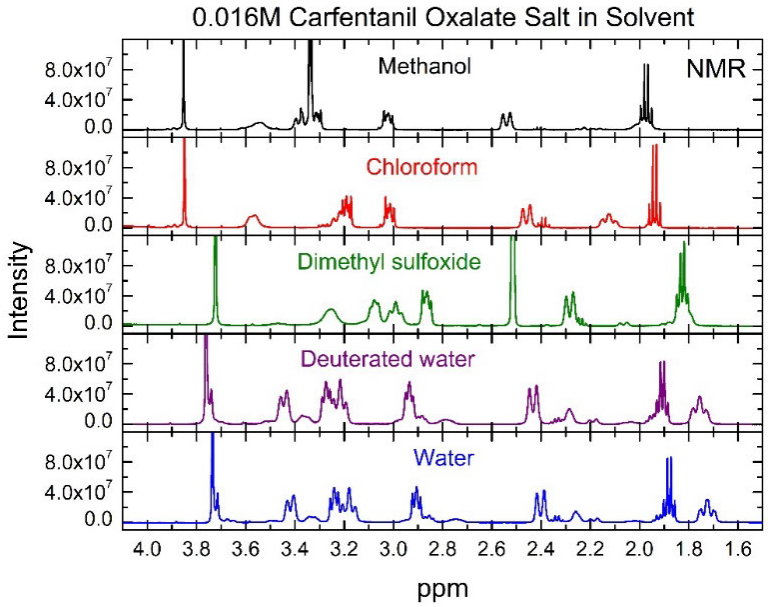

Figure 2. NMR spectra of 0.016 M carfentanil oxalate salt in different solvents. The salt is dissolved in methanol (black), chloroform (red), dimethyl sulfoxide (green), deuterated water (purple), and water (blue curve).

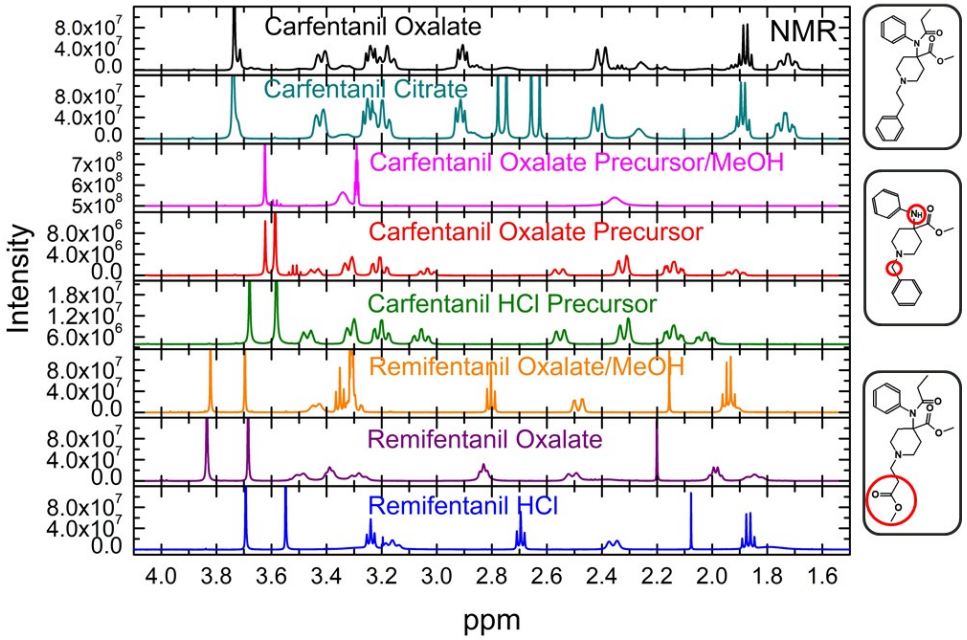

Figure 3. NMR spectra of 0.016 M opioid salts in methanol (depicted with /MeOH) or water. The salts are carfentanil oxalate (black), carfentanil citrate (cyan), carfentanil oxalate precursor in methanol (pink), carfentanil oxalate precursor in water (red), carfentanil HCl precursor (green), remifentanil oxalate in methanol (orange), remifentanil oxalate in water (purple), and remifentanil HCl (blue curve). The red circles on the right correspond to the functional group changed compared to the carfentanil structure.

Control experiments were performed to determine what caused the conformer effect. Figure 3 shows a systematic approach of changing one variable in the opioid salt solution such as the anion or a functional group of the opioid structure in order to discover insight into the possible cause of the conformer changes. Firstly, the carfentanil oxalate (black curve) was replaced with the carfentanil citrate (cyan curve) salt to determine if the anion in the salt had an impact on the conformation. The results show the anion has no effect on conformation. All of the NMR peaks in the carfentanil oxalate salt solution in water are present in the citrate salt solution; therefore, the conformation is likely affected by the solvent, as shown previously, and the opioid structure itself. The next step required the synthesis of a different opioid, the carfentanil precursor, which replaces the ketone group with an NH group. In methanol, the carfentanil oxalate precursor (pink curve) displayed one distinct NMR peak at 3.6 ppm assigned to the methoxy moiety; and in water, both the oxalate and HCl precursors (red and green curves) show two distinct singlet peaks. Not only do the oxalate precursor salts give conformers in water, but the intensities of the two singlet peaks portray a closer affinity for a 1:1 ratio of the conformers compared to the carfentanil salt conformers.

Since the side of the opioid molecule that contains the ester and ketone groups did not quench the measured conformer effect, the side of the opioid molecule that contains the phenylethyl moiety was changed. By replacing the phenylethyl moiety with an ester group, the new molecule synthesized is called remifentanil salt. Figure 3 shows remifentanil oxalate in methanol (orange curve) and water (purple curve). Now with two methoxy moieties on remifentanil, two distinct singlet peaks are present in the NMR spectrum in methanol. Surprisingly, no new NMR peaks were present when remifentanil salt was dissolved in water signifying no conformer changes in contrast to the carfentanil salts.

3.3 Characterization of neutral and protonated opioids

The replacement of the phenyl group in the carfentanil structure to the ester group in the remifentanil structure caused a significant conformer change in the NMR spectra and to help understand this change DFT calculations were performed. The first step in the process was to systematically break each bond of the opioid molecule and reattach it in different orientations to create over a hundred different possible structures. These structures were then plotted with their relative energies compared to the ground state structure. Figure 4 shows carfentanil and remifentanil structures in their neutral states (green and blue dots respectively) and their protonated states (orange and red dots respectively) with each structure's optimization energy normalized to the ground state structure's energy. From these results, one major trend shows that the carfentanil structures (green and orange dots) have relatively lower energy structures than the remifentanil structures. High energy structures could explain why remifentanil salt water solution NMR spectra do not show multiple conformers because the remifentanil conformers might have energy too high to be stable at ambient conditions.

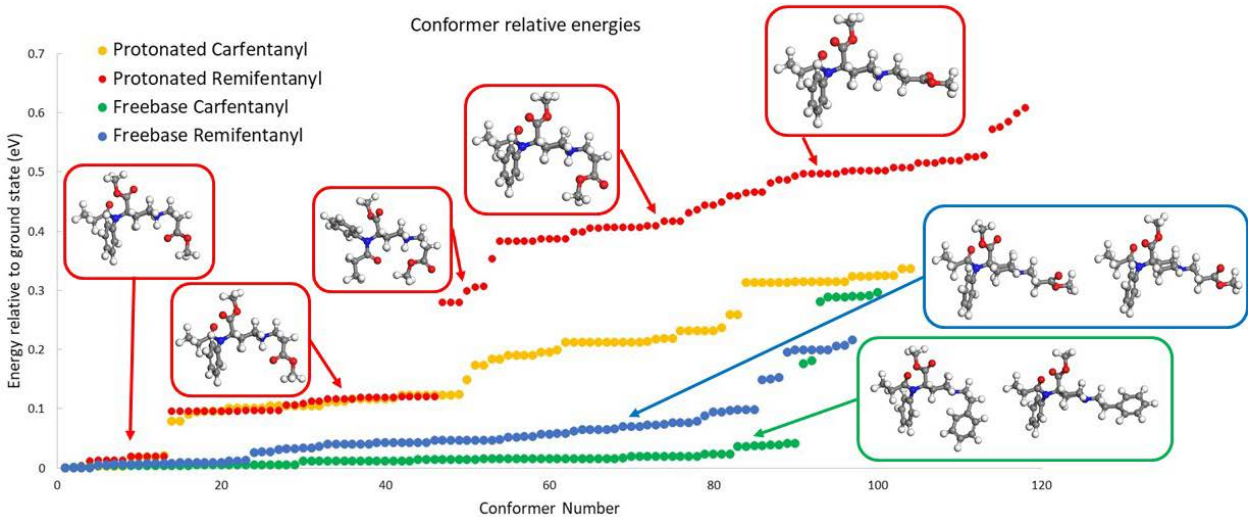

Figure 4. Energies of different conformer structures relative to the ground state structure. The neutral carfentanil (green dots) and remifentanil (blue dots) are compared to the protonated carfentanil (yellow dots) and remifentanil (red dots) structures. The boxes hold the molecular structures of specific conformers where the C, H, O, and N atoms are grey, white, red, and blue, respectively.

Another trend appears when the energies of the neutral structures are compared to the protonated structures. By adding one hydrogen to the neutral opioid structure, the structures become more rigid with larger energy differences from the

ground state. Some explanation behind this trend can be understood by focusing on the geometries of the different structures. For the neutral carfentanil and remifentanil structures (green and blue boxes), if the ester group is twisted, the phenylethyl group is folded, or even the ethyl ester group is folded, the conformer structure energies do not change significantly compared to the ground state conformer. The lack of energy changes for the neutral structures indicates their conformer structures are not stable and any twists or folds formed during conformation will easily change back to the original ground state orientation. Overall, the neutral species are flexible and labile and do not want to form stable conformer structures. On the other hand, adding the hydrogen atom to the N-piperidine ring, creates a rigidity that stabilizes the conformers in their geometries. As shown in Figure 4 for protonated remifentanil, if the ester group next to the ketone group was twisted, the relative energy jumped to 0.1 eV, and so on as each functional group is oriented differently, the relative energy increased signifying the larger rigidity of the protonated structures compared to the neutral structures. Further studies are ongoing to understand why the rigidity changes.

3.4 Characterization of opioids on surfaces

Conformational changes in the opioid structures might potentially affect binding on surfaces. Therefore, we chose five surfaces to initially study: SiO_2, UiO-66, UiO-66-NH_2, UiO-67, and NU-1000. Silica contains polar –OH surface sites that have the ability to hydrogen bond with the oxygen and protonated nitrogen groups of the opioids. The UiO series of surfaces are a class of Zr-based materials called metal organic frameworks (MOFs). MOFs contain inorganic oxide nodes called secondary building units (SBUs) connected by organic linkers that form three-dimensional crystal lattices. Several advantages of using the Zr-based MOFs are their stability in water, high surface areas (∼500–2,000 m^3/g), and their controllable pore sizes. Additionally, MOFs contain both polar and nonpolar groups that may allow for multiple binding sites for the opioid molecules. Figure 5 shows both carfentanil (top) and remifentanil (bottom) uptake normalized to the control, which contained no surface material. The opioid of interest was dissolved into 0 %, 20 %, 40 %, 60 %, 80 %, and 100 % water mixtures with the remaining percentages being solvent methanol. Then, ∼10 mg of surface material was added to the solution mixtures, stirred, centrifuged, and the supernatant was transferred to the LC-MS for analysis.

Carfentanil citrate results show no binding (complete recovery) of the opioid on SiO_2, which contains no pores. The hydrogen bonding is likely too weak in energy to interact strongly enough with the opioid. Similarly, carfentanil does not absorb into UiO-66, which contains pore diameters of ∼6 Å that are too small for carfentanil to penetrate into the pores. On the other hand, once the pore size increases to ∼12 Å for UiO67, carfentanil uptake increases, but only when the water content is high. For NU-1000 with a pore diameter of ∼30 Å, uptake occurs in both methanol and water, with more uptake in water. At this time, the cause of the changes in uptake seem to stem from a solvent effect, but a conformational effect cannot be ruled out. Since polar OH sites showed minimal carfentanil uptake, the organic linker was changed to include an amine (–NH_2) group in order to see if the C=O modes in the opioid might interact with the amine group more strongly than the –OH groups on the MOF surface. Indeed, the uptake increased with the addition of the amine group in the MOF called UiO-66-NH_2, and the trend continued with water increasing the uptake of the opioid on the surface compared to in methanol. Future studies are pending to try and elucidate these results.

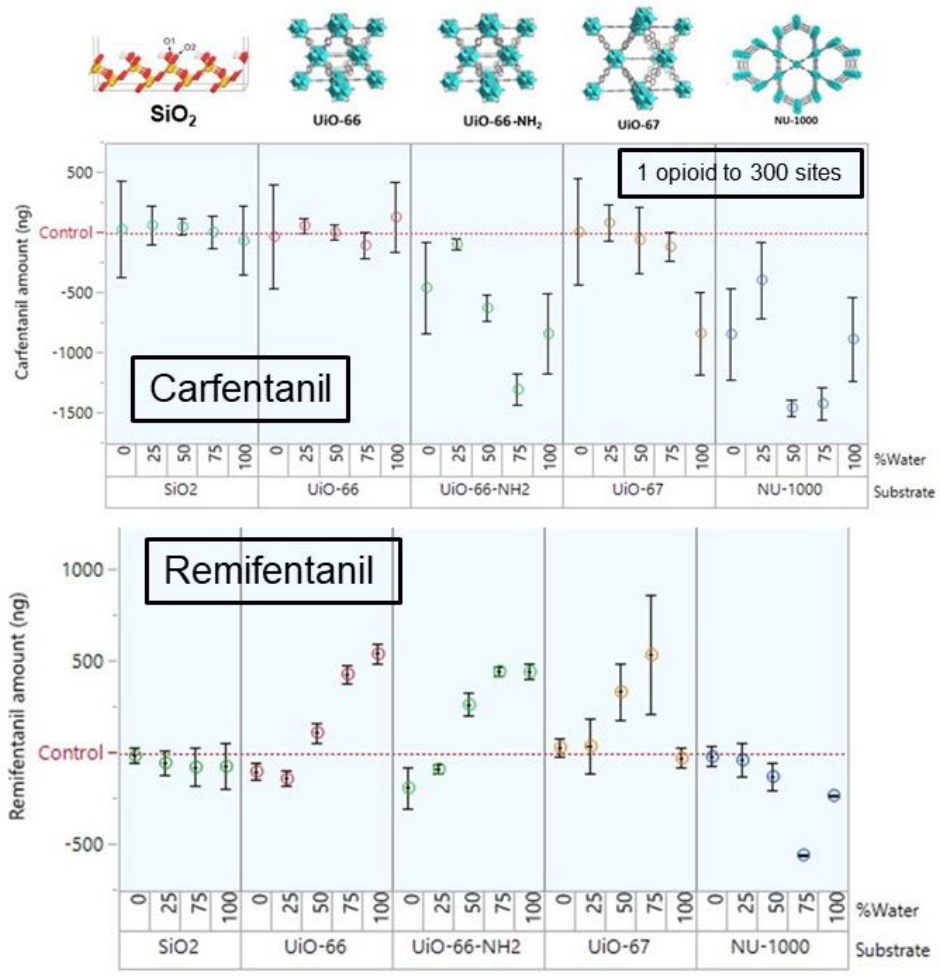

Figure 5. Uptake studies of carfentanil citrate (top) and remifentanil HCl (bottom) on surfaces. The opioids were dissolved in 0 %, 20 %, 40 %, 60 %, 80 %, and 100 % water mixtures with the remaining percentages in methanol. The surfaces used were SiO_2, UiO-66, UiO-66-NH_2, UiO-67, and NU-1000 in order of increasing porosity from left to right.[15]

Surprisingly, remifentanil HCl uptake on surfaces produced a different result when the opioid was introduced to the MOFs. As expected, no uptake occurred on SiO_2 in methanol or in water. However, positive amounts of remifentanil were measured after uptake when remifentanil was mixed with UiO-66, UiO-66-NH_2, and UiO-67. It is impossible to retain more than 100 % recovery of the opioid unless a reaction occurs; therefore, a phenomenon seemed to be occurring in the control mixture, which consisted of remifentanil HCl salt and solvent mixture without any surface material present. After further analysis of the LC-MS chromatograms, a new peak grew in the control mixtures as water content increased, and that peak was found to be hydrolyzed remifentanil product (not shown). Thus, remifentanil salt was decomposing in water; however, with the addition of the MOF surfaces, the solution mixture likely became more acidic and stabilized the remifentanil from becoming hydrolyzed. If remifentanil became more stable in the MOF solutions, then normalizing to the control would portray the illusion that more remifentanil formed than was present originally. Since NU-1000 has such a high affinity for opioid binding, the remifentanil results look normal with the similar trend that more water shows more uptake.

4. CONCLUSIONS

Opioid characterization in solution and on surfaces unrelated to the human body can now be more understood. We found that the opioid salts are protonated at the N-piperidine ring of the opioid structure, which is consistent with literature theory. Carfentanil salts form conformers in more polar solvents such as water, whereas remifentanil salts portray one structure in water. Calculations show trends that remifentanil conformer structures require higher energies

than carfentanil conformers. Additionally, neutral opioid structures are more labile, and lack stable conformers compared to the protonated opioid salt forms. When these opioid salts are put on surfaces, increased water content increased uptake of the opioids on the surface. Carfentanil overall showed little uptake on MOFs until the pore sizes were large enough to accommodate the opioid. Remifentanil stabilized in the acidic MOF solution. The cause of uptake on surfaces is still unclear; however, many previous knowledge gaps have been solved and the next step in understanding lies on the surface.

ACKNOWLEDGMENTS

Funding was provided by the U.S. Army via the Surface Science Initiative Program (PE 0601102A Project VR9) at the Edgewood Chemical Biological Center. This research was performed while John Landers held a National Research Council Postdoctoral Research Associateship Program position at the Edgewood Chemical Biological Center.

REFERENCES

[1] Van Daele, P.G.H.; De Bruyn, M.F.L.; Boey, J.M.; Sanczuk, S.; Agten, J.T.M.; Janssen, P.A.J. Synthetic analgesics: N-(1-[2-arylethyl]-4-substituted 4-piperidinyl) N-arylalkanamides. *Arzneim. Forsch.* **1976,** *26* (8), pp 1521–1531.

[2] Niemegeers, C.J.E.; Schellekens, K.H.L.; Van, Bruyn, W.F.M.; Janssen, P.A.J. Sufentanil, a very potent and extremely safe intravenous morphine-like compound in mice, rats and dogs. *Arzneim. Forsch.* **1976,** *26* (8), pp 1551–1556.

[3] Janssens, F.; Torremans, J.; Janssen, P.A.J. Synthetic 1, 4-disubstituted 1, 4-dihydro-5H-tetrazol-5-one derivatives of fentanyl: alfentanil (R 39209), a potent, extremely short-acting narcotic analgesic. *J. Med. Chem*. **1986,** *29* (11), pp 2290–2297.

[4] Stanley, T.H. New developments in opioid drug research for alleviation of animal pain. *J. Am. Vet. Med. Assoc.* **1987,** *191* (10), pp 1252–1253.

[5] Scholz, J.; Steinfath, M.; Schulz, M. Clinical pharmacokinetics of alfentanil, fentanyl and sufentanil. *Clin. Pharmacokinet.* **1996,** *31* (4), pp 275–292.

[6] Feldman, P.L.; Brackeen, M.F. A novel route to the 4-anilido-4-(methoxycarbonyl) piperidine class of analgetics. *J. Org. Chem.* **1990,** *55* (13), pp 4207–4209.

[7] Maguire, P.; Tsai, N.; Kamal, J.; Cometta-Morini, C.; Upton, C.; Loew, G. Pharmacological profiles of fentanyl analogs at μ, δ and κ opiate receptors. *Eur. J. Pharmacol.* **1992,** *213* (2), pp 219–225.

[8] Weltrowska, G.; Lemieux, C.; Chung, N.N.; Guo, J.J.; Wilkes, B.C.; Schiller, P.W. 'Carba'-carfentanil (trans isomer): a μ opioid receptor (MOR) partial agonist with a distinct binding mode. *Bioorg. Med. Chem.* **2014,** *22* (17), pp 4581–4586.

[9] Feinberg, A.P.; Creese, I.; Snyder, S.H. The opiate receptor: a model explaining structure-activity relationships of opiate agonists and antagonists. *Proc. Nati. Acad. Sci.* **1976,** *73* (11), pp 4215–4219.

[10] Walz, A.J.; Hsu, F.L. Synthesis of 4-anilinopiperidine methyl esters, intermediates in the production of carfentanil, sufentanil, and remifentanil. *Tetrahedron Lett.* **2014,** *55* (2), pp 501–502.

[11] Li, J.; Su, Y.; Xia, W.; Qin, Y.; Humphries, M.J.; Vestweber, D.; Cabañas, C.; Lu, C.; Springer, T.A. Conformational equilibria and intrinsic affinities define integrin activation. *EMBO J.* **2017,** *36* (5), pp 629–645.

[12] Zimmerman, D.C. A new product of linoleic acid oxidation by a flaxseed enzyme. *Biochem. Biophys. Res. Commun.* **1966,** *23* (4), pp 398–402.

[13] Mayer, B.P.; Kennedy, D.J.; Lau, E.Y.; Valdez, C.A. Solution-state structure and affinities of cyclodextrin: fentanyl complexes by nuclear magnetic resonance spectroscopy and molecular dynamics simulation. *J. Phys. Chem. B.* **2016,** *120* (9), pp 2423–2433.

[14] Walz, A.J.; Hsu, F.L. *Scaled-up synthesis: salts of carfentanil and remifentanil*. ECBC-TR-1473; U.S. Army Edgewood Chemical Biological Center: Aberdeen Proving Ground, MD, **2017;** UNCLASSIFIED Report (AD1039337).

[15] Liu, Y.; Howarth, A.J.; Vermeulen, N.A.; Moon, S.Y.; Hupp, J.T.; Farha, O.K. Catalytic degradation of chemical warfare agents and their simulants by metal-organic frameworks. *Coord. Chem. Rev.* **2017,** *346*, pp 101–111.

Novel MXene/titania nanocomposite fibers for enhanced charge injection

Shaun M. DeBow[a]*, Brendan G. DeLacy[a], Yuri Gogotsi[b], Yi Rao[c]
[a]U.S. Army Edgewood Chemical Biological Center, Research & Technology Directorate, 8198 Blackhawk Rd, Aberdeen Proving Ground, MD 21010
[b]Drexel University Materials Science & Engineering, 3141 Chestnut St, Philadelphia, PA 19104
[c]Utah State University Department of Chemistry & Biochemistry, 0300 Old Main Hill, Logan, UT 84322

ABSTRACT

MXenes are a recently-discovered class of materials with exceptional electrical, thermal, mechanical, and electromagnetic properties. They were first discovered by Gogotsi and co-workers in 2011 at Drexel University. This class of materials originally included carbides of transition metals, but it has expanded to include carbonitride and nitride materials. All are produced by selective etching and delaminating early transition metal compounds to form nanoparticles with two dimensional structures. MXenes have the ability to 1) efficiently absorb light of varying wavelengths (visible thru infrared), 2) efficiently store charge and act as supercapacitors, and 3) exhibit photoluminescence. We hypothesized that MXenes should have a superior ability to inject electrons into an adjacent acceptor substrate, i.e., a suitable semiconductor, so a MXene nanostructure that is efficiently grown or attached to a semiconductor substrate (with suitable band gap) will efficiently absorb light, generate excited electrons, store that charge, and inject that charge into the semiconductor. In order to test this hypothesis, we fabricated novel TiO_2/Ti_3C_2 fiber nanocomposites and subsequently measure its charge injection properties using transient absorption measurements. We teamed with Dr. Yuri Gogotsi to fabricate these novel nanocomposites and leveraged our relationship with Dr. Yi Rao of Utah State University to determine the charge transfer characteristics of the composites. This project provides a new and exciting material to be explored in a range of applications including filtration, decontamination, energy conversion, and obscuration.

Keywords: obscurants, nanoparticles

1. INTRODUCTION

MXenes are a recently-discovered new class of materials. They are two-dimensional in structure and made of transition metal carbides, carbonitrides, and nitrides.[1] They exhibit exceptional electrical, thermal, mechanical, and electromagnetic properties. The first class of two-dimensional transition metal carbides were originally discovered and characterized by Dr. Yuri Gogotsi and co-workers in 2011 at Drexel University[2] and referred to as MXenes. These materials have since expanded to include carbonitride and nitride materials, all produced by selective etching and delaminating layers using a range of early transition metal compounds.[3,4] Large material diversity contributes to their wide-ranging properties, and theoretical and experimentally-created MXenes are shown in Figure 1.

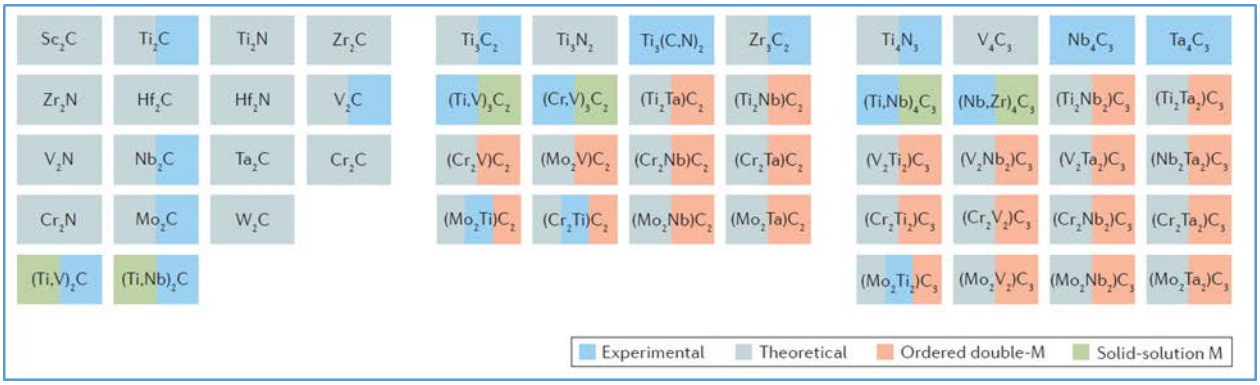

Figure 1. 2D metal carbides and nitrides (MXenes) for energy storage.[3]

Recently, these materials have found applications in microwave absorbing and shielding,[5,6] water splitting,[7] water purification and desalination,[2] methane adsorption,[8] transparent conductors,[9] photocatalysis,[10,11] chemical sensing,[12] photoluminescence quantum dots,[13] flexible and conducting films,[14] and super capacitors.[14–18]

These composites are generally described by the formula $M_{x+1}AX_n$, where M is an early transition metal, A is selected from group IIIA or IVA elements, and X is C or N, with n = 1, 2, or 3. This composite is referred to as the MAX Phase. To separate the layers, the A layer is etched away, typically by using HF or LiF and HCl. This produces a multilayered MXene phase which now has a functionalized surface containing –OH, –F, or =O groups.[6] This resulting MXene laminate is weakly bound together and may be delaminated by sonication or vigorous shaking. This process is described in Figure 2. These materials share similarities with graphene, both start with stacked tightly bound phases and are exfoliated to monolayers by the use of intercalants and mechanical agitation or sonication.[14] Unlike graphene, however, MXenes are more resistant to van der Waals restacking, so while graphene reforms graphite, MXenes do not reform the MAX phase due to the functionalized surface.[5] This characteristic in particular allows MXene to retain its unique electrical properties, and also makes it an attractive additive in various nanocomposites. In terms of conductivity, some MXenes exhibit over three-times greater conductivity, when compared with reduced graphene oxide.[9]

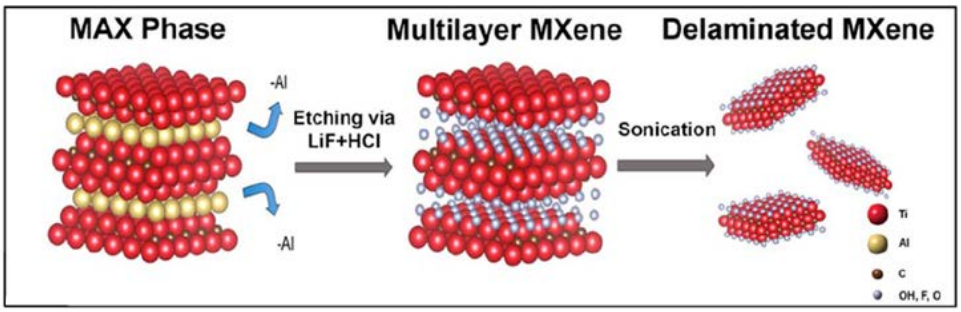

Figure 2. Steps detailing the transformation from MAX phase to multilayer MXene to exfoliated particles.[19]

Due to the above MXene characteristics, we anticipated that this exciting class of materials should also exhibit superior charge injection characteristics. This is supported by the material's ability to efficiently absorb incident radiation, the ability to store charge (e.g., as a supercapacitor), high conductivity, ability to transfer charge, and exhibit photoluminescence.

Assuming an efficient electron acceptor is near or adjacent to the MXene, it was hypothesized that the excited electron should hop or inject into the acceptor material. Photoluminescence would be quenched in this scenario. This is readily observable in analogous composite systems where plasmonic nanoparticles are decorated on semiconductor substrates. In this analagous composite structure, the plasmonic nanoparticles absorb light, generate electrons in excited states, and subsequently inject the "hot" electrons into the adjacent semiconductor. Due to their superior quality to store charge, it stands to reason that MXenes should also have a superior ability to inject electrons into an adjacent acceptor substrate, assuming that the acceptor has the appropriate band gap. Indeed, in one initial study, titania-Ti_3C_2 hybrid materials have already exhibited excellent interfacial charge transfer properties.[20] This was achieved through separation of photogenerated carriers from photogenerated holes, which was then shown to promote photocatalytic activity of TiO_2.[20]

Hence, our central hypothesis in this study was that a MXene nanostructure efficiently grown or attached to a semiconductor substrate (with suitable band gap) will efficiently absorb light, store that charge in a controllable fashion, and inject that charge into the adjacent semiconductor substrate. Furthermore, we hypothesize that the way in which the 2D sheets of MXene are prepared or attached to the semiconductor substrate will greatly impact the charge injection process.

To test this hypothesis, we identified TiO_2 as a suitable semiconductor substrate that could be used to study the transfer of charge between the MXene to the TiO_2. TiO_2 is an ideally suited material for this study, due to its inherent band gap, its ease of fabrication, and its ability to grow or attach other nanostructures, such as a MXene. Hence, a primary goal during year one of this study was to fabricate and characterize MXene/TiO_2 composites.

Several aspects of this study are of particular interest to the U.S. Army and the Warfighter. The properties of the materials indicate that they could provide advantages as a new type of catalyst for industrial chemicals or as an attenuating aerosol for use in a complex electromagnetic environment. MXenes are hydrophilic after suitable processing, which reduces the organic solvent waste burden that is inherent with hydrophobic materials. Their hydrophilic characteristic indicates that they can be suspended in a water solution, this may facilitate their dispersal as an aerosol fog, rather than using incendiary or energetic dispersal methods. Previous research, available in the scientific literature, has described a method to achieve specific lateral size distributions through the use of gradient centrifugation.[21] This selectivity may allow better performance by properly matching the flake size with intended wavelengths of electromagnetic radiation to absorb or reflect. Alternatively, the flakes could be used in broad lateral size distribution, this may produce a broadband absorber covering a wider range of wavelengths, e.g., from microwave to visible radiation. In comparison to MXene, graphitic materials, such as graphene, are well-studied two-dimensional conductive materials; however, their electrical efficiencies are reduced through lattice and surface defects that are an inherent byproduct in their synthesis. In addition to defect-related performance degradation, graphitic materials are typically hydrophobic, and this hydrophobicity increases their processing costs and handling burden by requiring potentially hazardous organic solvents for processing or forming dispersions.

2. MATERIALS

The choice of testing Ti_3C_2-TiO_2 nanocomposites was based on the following considerations. TiO_2 was included in the composite since our laboratory has extensive experience in fabricating and characterizing spherical-, nanorod-, and fiber-shaped TiO_2. Additionally, TiO_2 has a band gap near 3.2 eV, making it a suitable candidate for accepting electron injection from various electron donors. We have recently explored the charge injection properties of plasmonic/TiO_2 nanocomposites. The MXene Ti_3C_2 was chosen because it is the most well-known and well-characterized material in this class.

The following approach to fabricate and characterize Ti_3C_2-TiO_2 nanocomposites was used.

2.1 TiO_2 fiber substrates

Our laboratory has both the expertise and equipment to electrospin titania fibers with controllable dimensions. These fibers will be used as the substrate for embedding, growing, or attaching MXene nanostructures. The fibers were characterized in terms of composition and size via XRD and SEM.

2.2 MXene fabrication

Dr. Yuri Gogotsi, and his Nanomaterials Group at Drexel University, is the preeminent leader in the field of MXene synthesis and preparation. Collaborating with his expertise reduced the time and labor needed to generate usable material. We focused on Ti_3C_2 MXene in this study, but a wide range of other compounds, made by varying the transition metal, are options for future study.

2.3 Charge injection

Charge injection studies were done in collaboration with Dr. Yi Rao, who is a leader in the field of transient absorption. Dr. Rao was funded by our group and assisted in the characterization of these nanocomposites during year one. Transient absorption is a pump/probe technique in which the injection of charge into a substrate may be monitored by pumping the composite with a femtosecond laser of a given wavelength and power, and subsequently

probing/monitoring the absorption properties of the substrate (at a different wavelength) to determine whether charge is injected.

2.4 TiO_2/Ti_3C_2 nanocomposite fabrication

An approach for fabricating a TiO_2/Ti_3C_2 nanocomposite is to electrospin TiO_2 fibers containing the MXene. This approach is based upon a prior study in which electrospun polymer fibers and thin films were loaded with MXenes. These composites were shown to have greater electrical conductivity, when compared with the corresponding neat polymer.[19,22] The electrical conductivity of polymers loaded with MXene increased by three orders of magnitude when compared with the neat polymer.[19] An example of these electrospun Ti_3C_2/Poly(ethylene oxide) (PEO) fibers is shown in Figure 3. We employed a similar approach.

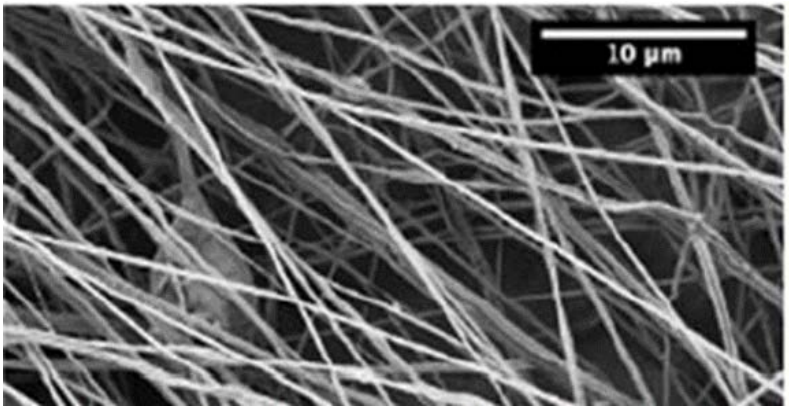

Figure 3. Electrospun $Ti_3C_2T_x$/PEO fibers.[19]

Layered Ti_3C_2 MXene was obtained from the A.J. Drexel Nanomaterials Institute, Drexel University, Philadelphia, PA. Polymethyl methacrylate (M_w = 996,000 Da), chloroform ($CHCl_3$), N,N–dimethylformamide (DMF), and titanium isopropoxide (TTiP) were procured from Sigma-Aldrich®; these chemicals were used without additional purification. Water used during MXene self-assembly was 18.2 MΩ deionized water and was purified by a Millipore® Direct-Q® 5 water purification system.

3. EXPERIMENTAL

3.1 Synthesis of MXene-TiO_2 and TiO_2 composite nanofibers

A laboratory quantity of Ti_3C_2 MXene was fabricated by Gogotsi's group following procedures similar to those previously disclosed by Ghidiu et al.[23] In brief, this method involves etching a Ti_2AlC MAX phase with an acid, followed by sonication to delaminate into monolayers.

The resulting Ti_3C_2 monolayers from Gogotsi were incorporated into electrospun TiO_2 fibers at ECBC following electrospinning procedures reported by Liu et al,[22] with modifications to incorporate Ti_3C_2 MXene, and applying concepts similar to those implemented by Mayerberger et al.[19] and Kiennork et al.[24] Mayerberger discovered that the polymer jet ejection characteristics vary depending upon Ti_3C_2 concentration, due to changes in viscosity and electrical conductivity. They determined the ideal concentration for electrospun Ti_3C_2 in a polymer solution is a 1 % w/w. This concentration was the starting point for TiO_2 electrospinning; however, these parameters—in addition to electrospinning voltage potentials, needle size, and pump rate—required tuning in order to be optimized.

As a control, TiO_2 fibers (without MXenes) were also fabricated using a simple a sol-gel synthesis process. This sol-gel process disperses MXene and Titanium isopropoxide (TTiP) into a uniform suspension containing polymethyl methacrylate (PMMA) that is ideal for electrospinning. Fibers were electrospun using the sol-gel suspension, then a thermal treatment was used in a controlled environment to evaporate PMMA and convert the TTiP to TiO_2.

A brief description of the procedure follows: 320 mg of PMMA was slowly added to 2 mL of chloroform while stirring, the solution was stirred until the PMMA was completely dissolved, for approximately 30 minutes. TTiP was added dropwise to the stirring solution—the volume varied from 0.29 mL to 0.67 mL, depending upon the desired MXene-to-TTiP concentration. The solution was allowed to stir for an additional 30 minutes. Following the addition

of TTiP, 2 mL of DMF was added and allowed to stir for 2 hours, with a variable mass (34–275 mg) of MXene flake added to the stirring solution 30 minutes prior to electrospinning. Fibers were electrospun using an MTI KJ Group Electrospinning cabinet, model MSK-NFES-3LDV (Richmond, CA). The solution was drawn into a syringe with an 18 ga needle attached. The syringe was clamped into a syringe pump, with the needle positioned 8 cm away from a horizontally-rotating drum mandrel. The following process parameter were used: the mandrel operated at 400 rpm, the syringe pump flow was set to 0.12 mL/min, and a 10kV potential was applied to the syringe tip. A diagram of the process is detailed in Figure 4. For clarity, DMF and chloroform were omitted from the diagram but were included in the electrospinning solution.

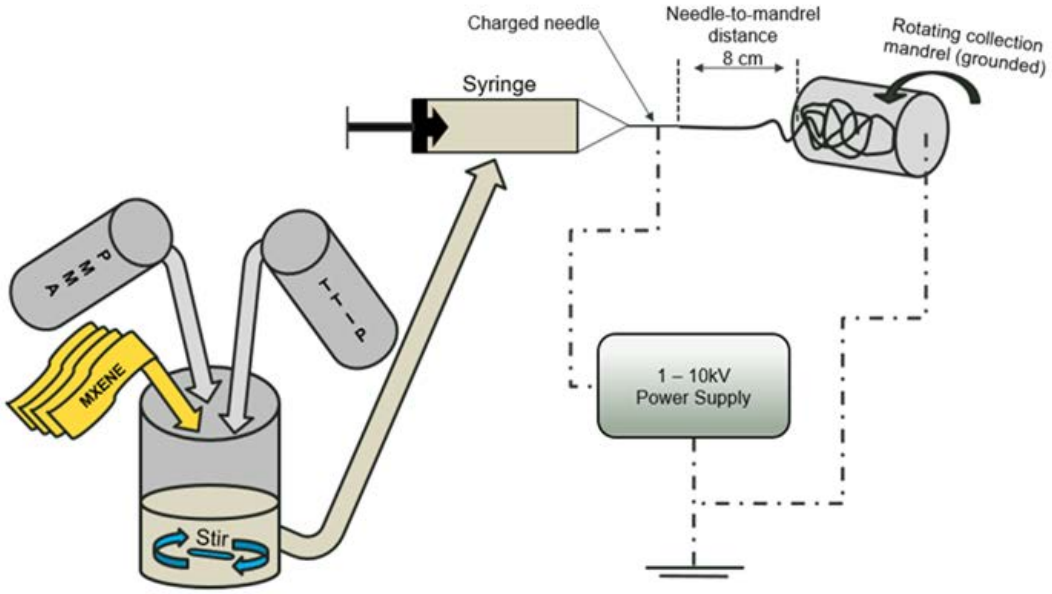

Figure 4. Electrospinning process for MXene-TiO_2 composite, portions adapted from Shahreen, et al.[25]

Electrospun TiO_2 nanofibers were fabricated by applying the sol-gel synthesis process previously described for MXene-TiO_2 fibers. These fibers didn't contain MXene and were produced using 0.67 mL of TTiP and 320 mg of PMMA.

The resulting MXene-TTiP-PMMA and TTiP-PMMA nanofibers mats were allowed to stand for 24 hours under ambient conditions. This allowed the TTiP in the electrospun fibers to hydrolyze into $Ti(OH)_4$ and then further condensation to amorphous TiO_2 prior to thermal treatment.[26]

Fibers were thermally treated by calcining in a Thermo Scientific Lindberg Blue M TF55035A-1 Tube Furnace (White Deer, PA) tube furnace for four hours at 400 °C under an Ar-H_2(10 %) atmosphere. A weight difference was noted between the pre-calcined and post-calcined fibers, this difference was consistent with PMMA evaporation and water loss.

3.2 Synthesis of MXene-TiO_2 composite nanofibers with self-assembled surface MXene

MXene flake was self-assembled to the surface of electrospun TTiP-PMMA and MXene-TTiP-PMMA fibers. The self-assembly process started with as-spun fiber mats that were electrospun following procedures outlined in Section 3.1, prior to the calcination step. Briefly, a colloidal suspension of MXene in water was produced by adding 0.0330 g of MXene to 40 mL of deionized water. This solution was sonicated at 24 watts for 70 minutes using a Misonix Sonciator 3000 (Farmingdale, NY) with a horn having a one-inch diameter tip operating at 20 kHz. Following sonication, 0.129 g of electrospun fibers were added to the colloidal suspension and stirred for 15 minutes. During this time, MXene self-assembled onto the fiber surface. The resulting fibers were centrifuged at 4,100 rpm for 15 minutes, then filtered. A diagram illustrating the process is shown in Figure 5. Coated fibers were thermally treated using the previously-described procedures. Post calcination fibers prepared using this procedure and resulting in a MXene-TiO2 composite with a self-assembled MXene surface are hereafter referred to as MXene-TiO_2-MXene fibers.

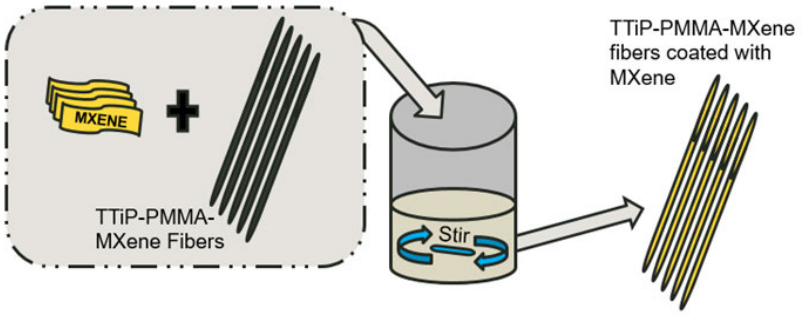

Figure 5. MXene TTiP-PMMA-MXene fiber self-assembly process.

3.3 Visible pump-transient IR absorption

The experimental setup for the visible pump-transient IR absorption experiments was described previously.[27] A schematic of the experimental pump-probe setup is provided in Figure 6. Briefly, a regenerative-amplified 100 fs Ti:Sapphire laser system (Quantronix; San Jose, CA), operating at 800 nm and 1 kHz repetition rate, was used for the experiments. A typical output power of the laser was 2.5 W. 40 % of the 800 nm output was frequency doubled in a BBO crystal to generate a pump pulse of 400 nm with a pulse energy of 3 µJ. The remaining 60 % of the output laser pulse was used to pump a Palitra-FS IR Optical Parametric Amplifier (Quantronix; San Jose, CA) to produce an IR pulse of 5260 nm (1900 cm^{-1}) with a pulse energy of 1.5 µJ. The IR beam was attenuated by more than 1,000 times before the samples. The IR probe was detected by a Teledyne Judson liquid nitrogen cooled HgCdTe detector, model J15D14-M204B-S01M-60-D31316 (Montgomeryville, PA) followed by an amplifier. The pump pulse was modulated by a New Focus (Santa Clara, CA) modulated chopper, Model 3501, operating at 500 Hz. The amplified IR signal from the detector was sent to a lock-in amplifier (Stanford Research, SR830). The digitized outputs were processed and recorded by a home-made Labview (National Instruments; Austin, TX) program. The instrumentation response function for the transient IR was 300 fs. The samples of TiO_2 and Ag-TiO_2 powders were pressed into thin slices, respectively. A typical thickness of the samples is around 100 µm for the transient IR absorption measurements.

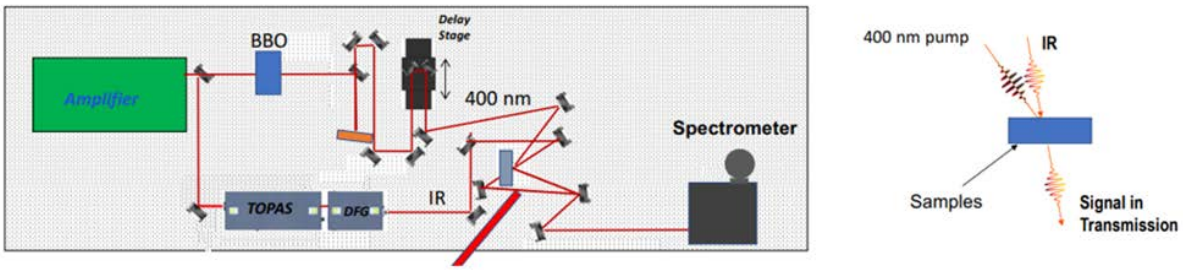

Figure 6. Transient pump-probe experimental setup schematic (left) and transmission geometry (right).

4. RESULTS AND DISCUSSION

4.1 Electrospun MXene-TTiP-PMMA fibers

The primary goal for the first-year of this multi-year project was to identify and develop methods and procedures that would enable MXene to be grown or attached to a semiconductor substrate having a suitable band gap that would efficiently absorb light. It was unknown at the inception of this project if MXene could actually form an intermediate or composite that would allow for easily handling and processing (e.g., electrospinning). No literature references were found to indicate this had been done before. By the end of the first year, we had developed a method to do just that—producing a MXene-semiconductor composite that demonstrated charge transfer between the MXene and TiO_2 semiconductor. Method development began by trying a 2.5-wt% loading of MXene to TTiP solution for electrospinning. The concentration of MXene was gradually increased over several electrospinning cycles. A solution having a MXene to TTiP ratio of 50/50-wt% with a PMMA support matrix was finally selected as the best alternative. PMMA polymer was selected as the support matrix because it provided an inert matrix that allowed the fibers to be electrospun and aided in post processing but would be cleanly evaporate during thermal treatment. The electrospun fibers were examined by electron microscopy and evaluated through electron injection studies.

A visible difference exists between fibers electrospun without and with MXene. Figure 7 illustrates this difference, the fibers shown on the left do not contain MXene and are snow white in appearance. The fibers on the right in Figure 7 contain a 50/50-wt% loading of MXene to TTiP; these fibers appear dark gray in their as-spun form, when the fibers turn black when they are consolidated and rolled under load. The visible difference between samples, electrospun without and with MXene, led us to believe that MXene was successfully electrospun into the fibers.

Figure 7. The physical appearance of TTiP-PMMA electrospun fibers (left), and MXene-TTiP-PMMA electrospun fibers (right).

Fibers were imaged by SEM to determine their morphology and to compare any differences between those electrospun without and with MXene. Fibers electrospun without MXene are smooth in appearance and have a consistent diameter along the fiber length; an SEM micrograph of these fibers is shown in the left panel of Figure 8. Fibers that were elecrospun with a MXene and having a MXene to TTiP loading of 50/50-wt% are shown in the right panel of Figure 8. These fibers appeared similar to the fibers in the left panel of Figure 8, with the exception of nodules long the fiber axis. These nodules appear to be MAX phase (unetched or unexfoliated MXene).

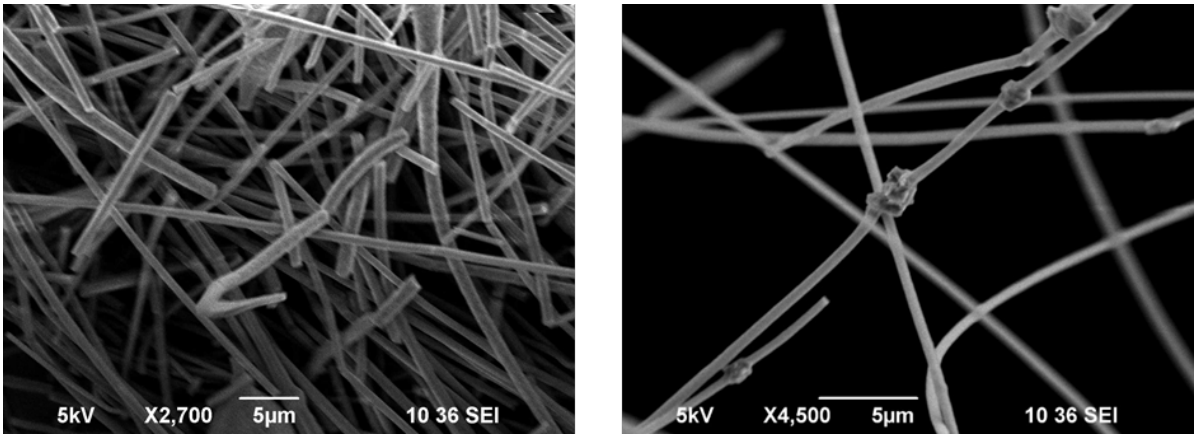

Figure 8. (left) SEM micrograph of TTiP-PMMA fibers, prior to calcination. (right) SEM micrograph of MXene-TTiP-PMMA fibers, prior to calcination.

4.2 MXene self-assembly onto MXene-TTiP-PMMA and TTiP-PMMA fiber surfaces

MXene self-assembly to the TTiP-PMMA and MXene-TTiP-PMMA fiber surfaces is demonstrated by the SEM micrographs shown in Figure 9. The successful self-assembly is clear when the images shown in Figure 9 are compared with the images shown in Figure 8.

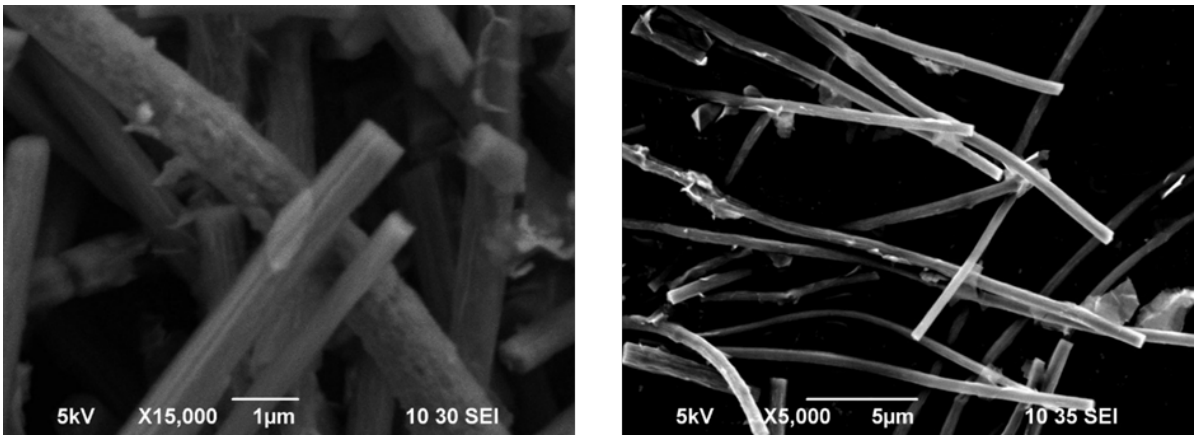

Figure 9. (left) SEM micrograph of TTiP-PMMA fibers with self-assembled MXene, prior to calcination. (right) SEM micrograph of MXene-TTiP-PMMA fibers with self-assembled MXene, prior to calcination.

To further verify that MXene sheets had self-assembled to the fibers, a specimen of the fibers shown in the right panel of Figure 9 was loaded on to a lacey carbon grid and imaged using TEM. Layered structures on the fiber surface are clearly visible in Figure 10 and are indicative of MXene.

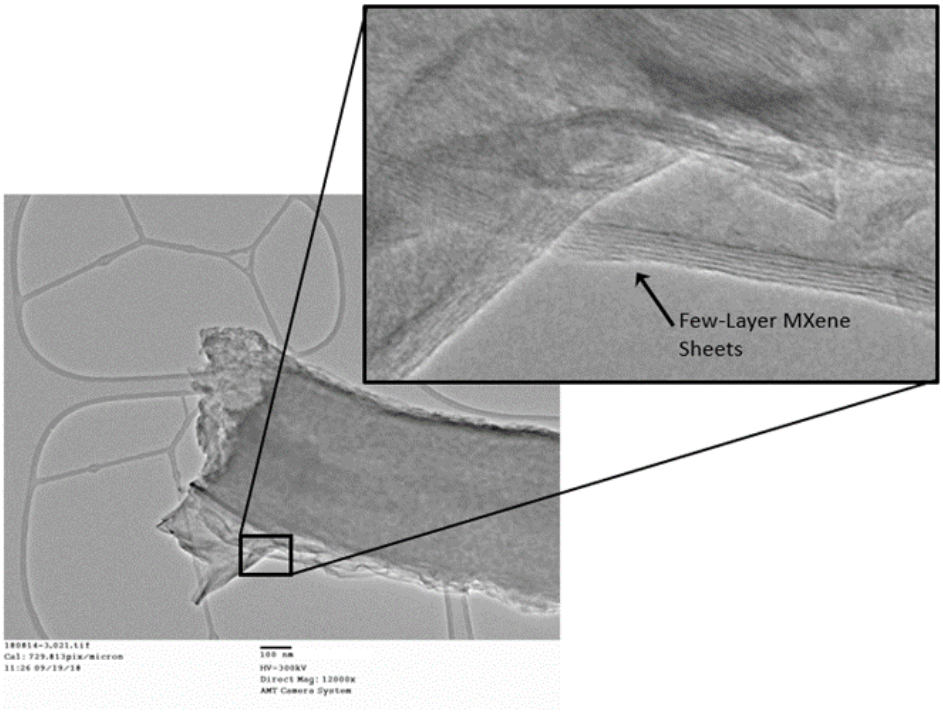

Figure 10. TEM micrograph of MXene-TTiP-PMMAfibers illustrating self-assembled MXene, prior to calcination.

4.3 Calcined fibers

After electrospinning and any post treatment steps (e.g., MXene self-assembly to the fiber surface) were complete, the fibers were calcined in an Ar-H_2 (10 %) atmosphere at 400 °C for 4 hours. A weight difference was noted between the pre-calcined and post-calcined fibers, this difference was consistent with PMMA evaporation and water loss. The post-calcined fibers retained their original morphologies and physical appearance. Nodules are still present in the fibers (see left panel of Figure 11), as well as MXene, which had self-assembled to the fiber surface (see right panel of Figure 11).

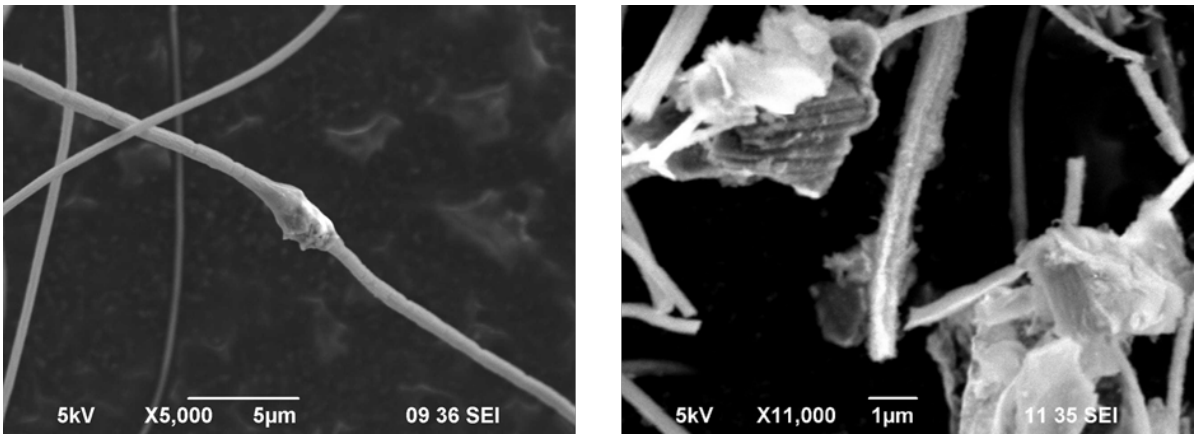

Figure 11. (left) SEM micrograph of MXene-TiO_2 fibers after calcination. (right) SEM micrograph of MXene-TiO_2 fibers with self-assembled surface MXene after calcination, "MXene-TiO_2-MXene."

4.4 Transient absorption measurements (pump-probe)

In collaboration with Yi Rao at Utah State University, studies of two laser pump-probe optical properties were studied on several films. Electron injection studies were performed for the samples using transient absorption spectroscopy.

To determine if the injection of electrons from MXene to the conduction band of TiO_2 occurs after photo-illumination, transient IR absorption spectroscopy was used for the as-prepared TiO_2 fibers and the as-prepared MXene/TiO_2 composite fibers. The IR at 1900 cm^{-1} is transparent to any chemical groups, but sensitive to the change in the absorption of free carriers. Therefore, the transient IR absorption measures the absorption of free carriers inside the conduction band of TiO_2, following the 400 nm pump excitation of electron from its valence band. As demonstrated in Figure 12, a prominent change in the transient IR absorption was observed for all MXene/TiO_2 composite fibers. This fast electron injection suggests that the MXene electrons rapidly transfer into the conduction band of the semiconductor. Figure 12 also presents the decay of the transient IR absorption for the MXene/TiO_2 nanofibers. This decay is likely due to the electron redistribution caused by a back-electron transfer process.

In addition to a traditional femtosecond transient absorption, microscopy was combined with the ultrafast measurements for the purpose of determining the response of single microparticles and small crystal samples. This is a custom-built microscope for both transmission-type and reflection-type transient absorption experiments, which is not commercially available. This micro-transient absorption spectrometer, combined with UV absorption, Raman, and photoluminescence, is especially good for characterizing linear, nonlinear, ultrafast optical properties of particle materials.

As shown in Figure 12 for several samples, three of the films have very different performance for the MXene components of the composite material, with two of the films very similar and one different. In particular, sample 180814-4 shows electron charge injection, storage and transfer. Transient absorption showed interesting results for sample 180814-4 since these fibers appeared to allow electron injection, charge storage and fast transfer. The reasons for the differences in the three films are under study.

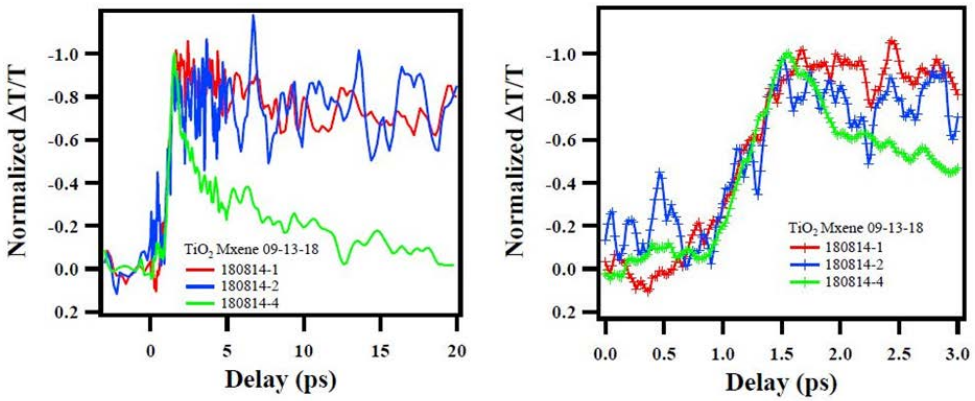

Figure 12. Dynamics for different MXene-TiO_2 samples. The sample 180814-4 has faster signal decay than samples 180814-1 and 180814-2.

4.5 Addition of platinum nanocrystals

Due to our observations of the propensity of MXenes to inject electrons into TiO_2, we hypothesized that this propensity could also be used to enhance chemical reduction reactions. To test this hypothesis, we added Pt nanoparticles to the MXene-TiO_2-MXene composite using the following procedure: 5 mg of MXene-TiO_2-MXene was ultrasonically dispersed in 20 mL of water for two hours and subsequently mixed with an aqueous solution of K_2PtCl_6 (0.02 mM). The resulted aqueous suspension was further dispersed for an hour. Then, $NaBH_4$ (30 mg) was added into the mixture, resulting in the generation of catalyst as a dark suspension. The mixture was stirred for another half an hour at room temperature to fully deposit the metallic nanoparticles onto the support. Finally, the desired catalyst Pt-MXene-TiO_2-MXene was collected by centrifuging and washed with de-ionized water for three times and then dried in vacuum at room temperature.

Electrodes were then prepared as follows. The electrodes were prepared by casting catalyst inks on carbon paper (0.5 cm × 0.5 cm). The catalyst inks (Pt-MXene-TiO_2-MXene or MXene-TiO_2-MXene) were prepared by dispersing the catalyst in water with 0.05 wt% Nafion®. The catalyst ink was deposited on carbon paper and dried in vacuum at room temperature, resulted in a metal loading of 1 mg Pt/MXene-TiO_2-MXene cm^{-2} and 1 mg MXene-TiO_2-MXene cm^{-2}.

Initial results indicate an increased hydrogen evolution from the electrode materials at lower applied voltage, as a reaction of Pt nanoparticles on MXene-TiO_2-MXene. In particular, sample 180814-4 showed good activity when it was decorated with Pt nanocrystals. The observed performance increase is illustrated in Figure 13, MXene-TiO2-MXene composite electrodes compared with Pt-decorated MXene-TiO2-MXene composite electrodes.

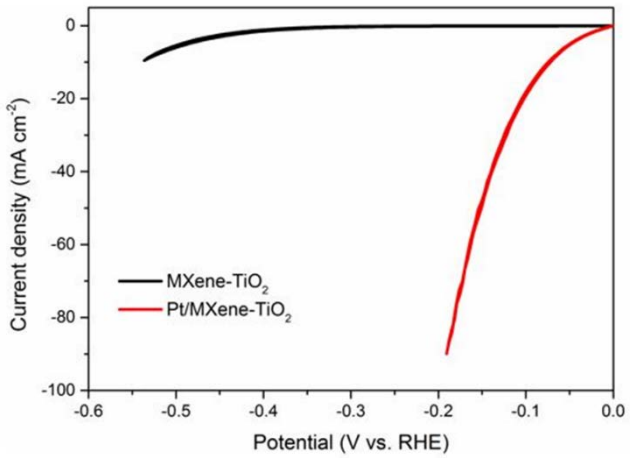

Figure 13. Hydrogen generation as a function of voltage of Pt-treated MXene/TiO_2 film.

5. CONCLUSIONS

MXene/TiO_2 composites were successfully fabricated during year one of this study. Specifically, MXenes were first incorporated into the electrospinning TiO_2 process. This approach resulted in the MXenes residing on the inside of the TiO_2/MXene composite fibers. Concurrently, MXenes were successfully self-assembled onto the surface of TiO_2 and TiO_2/MXene fibers. Transient absorption measurements confirmed the transfer of charge from the MXene to the TiO_2 for all fabricated composite fibers. This injection rate was extremely fast, on the order of one picosecond. For the specific case in which the MXenes were present on the inside of the TiO_2 fibers, a gradual decay rate in transient absorption was observed. This decay is likely due to the electron redistribution caused by a back-electron transfer process. For the case in which the MXenes were both on the interior and exterior of the fiber, an increase in the decay rate was observed. Future studies will attempt to elucidate why the presence of MXene on the outside of the fiber enhances this decay rate. In addition to the charge injection studies that were completed, initial efforts to explore water splitting were made by growing Pt nanoparticles onto the surface of the MXene/TiO_2 composite fibers. Initial results indicate that this novel composite is capable of splitting water.

ACKNOWLEDGMENTS

Funding was provided by the U.S. Army via the Surface Science Initiative Program (PE 0601102A Project VR9) at the Edgewood Chemical Biological Center. The authors further extend their gratitude to the Senior Research Scientists (ST), internal and external senior scientists, and professionals who invested their time to evaluate the initial proposal and participate during the year-end Technical Advisory Board review. The authors acknowledge and thank the professionals at the W. M. Keck Center for Advanced Microscopy and Microanalysis at the University of Delaware for use of their instrumentation and support of this project.

REFERENCES

[1] Naguib, M.; Mochalin, V.N.; Barsoum, M.W.; Gogotsi, Y. 25th anniversary article: MXenes: a new family of two-dimensional materials. *Adv. Mater.* **2014,** *26* (7), pp 992–1005.

[2] Li, R.; Zhang, L.; Shi, L.; Wang, P. MXene Ti3C2: An Effective 2D Light-to-Heat Conversion Material. *ACS Nano.* **2017,** *11* (4), pp 3752–3759.

[3] Anasori, B.; Lukatskaya, M.R.; Gogotsi, Y. 2D metal carbides and nitrides (MXenes) for energy storage. *Nat. Rev. Mater.* **2017,** *2*, p 16098.

[4] Naguib, M.; Kurtoglu, M.; Presser, V.; Lu, J.; Niu, J.; Heon, M.; Hultman, L.; Gogotsi, Y.; Barsoum, M.W. Two-dimensional nanocrystals produced by exfoliation of $Ti_3 AlC_2$. *Adv. Mater.* **2011,** *23* (37), pp 4248–4253.

[5] Han, M.; Yin, X.; Li, X.; Anasori, B.; Zhang, L.; Cheng, L.; Gogotsi, Y. Laminated and Two-Dimensional Carbon-Supported Microwave Absorbers Derived from MXenes. *ACS Appl. Mater. Interfaces.* **2017,** *9* (23), pp 20038–20045.

[6] Li, X.L.; Yin, X.W.; Han, M.K.; Song, C.Q.; Xu, H.L.; Hou, Z.X.; Zhang, L.T.; Cheng, L.F. Ti_3C_2 MXenes modified with in situ grown carbon nanotubes for enhanced electromagnetic wave absorption properties. *J. Mater.Chem. C.* **2017,** *5* (16), pp 4068–4074.

[7] Le Formal, F.; Pendlebury, S.R.; Cornuz, M.; Tilley, S.D.; Gratzel, M.; Durrant, J.R. Back electron-hole recombination in hematite photoanodes for water splitting. *J. Am. Chem. Soc.* **2014,** *136* (6), pp 2564–2574.

[8] Liu, F.; Zhou, A.; Chen, J.; Jia, J.; Zhou, W.; Wang, L.; Hu, Q. Preparation of Ti_3C_2 and Ti_2C MXenes by fluoride salts etching and methane adsorptive properties. *Appl. Surf. Sci.* **2017,** *416*, pp 781–789.

[9] Mariano, M.; Mashtalir, O.; Antonio, F.Q.; Ryu, W.H.; Deng, B.; Xia, F.; Gogotsi, Y.; Taylor, A.D. Solution-processed titanium carbide MXene films examined as highly transparent conductors. *Nanoscale.* **2016,** *8* (36), pp 16371–16378.

[10] Pan, X.; Zhao, Y.; Liu, S.; Korzeniewski, C.L.; Wang, S.; Fan, Z. Comparing graphene-TiO(2) nanowire and graphene-TiO(2) nanoparticle composite photocatalysts. *ACS Appl. Mater. Interfaces.* **2012,** *4* (8), pp 3944–3950.

[11] Peng, C.; Yang, X.; Li, Y.; Yu, H.; Wang, H.; Peng, F. Hybrids of Two-Dimensional Ti_3C_2 and TiO_2 Exposing {001} Facets toward Enhanced Photocatalytic Activity. *ACS Appl. Mater. Interfaces.* **2016,** *8* (9), pp 6051–6060.

[12] Xiao, B.; Li, Y.C.; Yu, X.F.; Cheng, J.B. MXenes: Reusable materials for NH3 sensor or capturer by controlling the charge injection. *Sens. Actuators, B.* **2016,** *235*, pp 103–109.

[13] Xue, Q.; Zhang, H.; Zhu, M.; Pei, Z.; Li, H.; Wang, Z.; Huang, Y.; Huang, Y.; Deng, Q.; Zhou, J.; Du, S.; Huang, Q.; Zhi, C. Photoluminescent Ti3 C2 MXene Quantum Dots for Multicolor Cellular Imaging. *Adv. Mater.* **2017,** *29* (15), p 1604847.
[14] Ling, Z.; Ren, C.E.; Zhao, M.Q.; Yang, J.; Giammarco, J.M.; Qiu, J.; Barsoum, M.W.; Gogotsi, Y. Flexible and conductive MXene films and nanocomposites with high capacitance. *Proc. Natl. Acad. Sci. USA.* **2014,** *111* (47), pp 16676–16681.
[15] Tian, Y.P.; Yang, C.H.; Que, W.X.; Liu, X.B.; Yin, X.T.; Kong, L.B. Flexible and free-standing 2D titanium carbide film decorated with manganese oxide nanoparticles as a high volumetric capacity electrode for supercapacitor. *J. Power Sources.* **2017,** *359*, pp 332–339.
[16] Wen, Y.; Rufford, T.E.; Chen, X.; Li, N.; Lyu, M.; Dai, L.; Wang, L. Nitrogen-doped $Ti_3C_2T_x$ MXene electrodes for high-performance supercapacitors. *Nano Energy.* **2017,** *38*, pp 368–376.
[17] Xin, Y.; Yu, Y.X. Possibility of bare and functionalized niobium carbide MXenes for electrode materials of supercapacitors and field emitters. *Mater. Des.* **2017,** *130*, pp 512–520.
[18] Xu, S.; Wei, G.; Li, J.; Ji, Y.; Klyui, N.; Izotov, V.; Han, W. Binder-free $Ti_3C_2T_x$ MXene electrode film for supercapacitor produced by electrophoretic deposition method. *Chem. Eng. J.* **2017,** *317*, pp 1026–1036.
[19] Mayerberger, E.A.; Urbanek, O.; McDaniel, R.M.; Street, R.M.; Barsoum, M.W.; Schauer, C.L. Preparation and characterization of polymer-$Ti_3C_2T_x$ (MXene) composite nanofibers produced via electrospinning. *J. Appl. Polym. Sci.* **2017,** *134* (37), p 45295.
[20] Peng, C.; Wang, H.; Yu, H.; Peng, F. (111) TiO_2-x/Ti_3C_2: Synergy of active facets, interfacial charge transfer and Ti^{3+} doping for enhance photocatalytic activity. *Mater. Res. Bull.* **2017,** *89*, pp 16–25.
[21] Maleski, K.; Ren, C.E.; Zhao, M.Q.; Anasori, B.; Gogotsi, Y. Size-Dependent Physical and Electrochemical Properties of Two-Dimensional MXene Flakes. *ACS Appl. Mater. Interfaces.* **2018,** *10* (29), pp 24491–24498.
[22] Liu, J.; McCarthy, D.L.; Cowan, M.J.; Obuya, E.A.; DeCoste, J.B.; Skorenko, K.H.; Tong, L.; Boyer, S.M.; Bernier, W.E.; Jones Jr, W.E. Photocatalytic activity of TiO_2 polycrystalline sub-micron fibers with variable rutile fraction. *Appl. Catal., B.* **2016,** *187*, pp 154–162.
[23] Ghidiu, M.; Lukatskaya, M.R.; Zhao, M.Q.; Gogotsi, Y.; Barsoum, M.W. Conductive two-dimensional titanium carbide 'clay' with high volumetric capacitance. *Nature.* **2014,** *516* (7529), pp 78–81.
[24] Kiennork, S.; Nakhowong, R.; Chueachot, R.; Tipparach, U. Preparation and Characterization of Electrospun TiO_2 Nanofibers via Electrospinning. *Integr. Ferroelectr.* **2015,** *165* (1), pp 131–137.
[25] Shahreen, L.; Chase, G.G. Effects of Electrospinning Solution Properties on Formation of Beads in TiO_2 Fibers with PdO Particles. *J. Eng. Fibers Fabr.* **2015,** *10* (3), pp 136–145.
[26] Mahshid, S.; Askari, M.; Ghamsari, M.S. Synthesis of TiO2 nanoparticles by hydrolysis and peptization of titanium isopropoxide solution. *J. Mater. Process. Technol.* **2007,** *189* (1-3), pp 296–300.
[27] Monahan, N.R.; Sun, D.; Tamura, H.; Williams, K.W.; Xu, B.; Zhong, Y.; Kumar, B.; Nuckolls, C.; Harutyunyan, A.R.; Chen, G.; Dai, H.L.; Beljonne, D.; Rao, Y.; Zhu, X.Y. Dynamics of the triplet-pair state reveals the likely coexistence of coherent and incoherent singlet fission in crystalline hexacene. *Nat. Chem.* **2017,** *9* (4), pp 341–346.

Matrix-free assisted laser desorption ionization using metal-organic frameworks

Rabih E. Jabbour*, Gregory W. Peterson, Jared B. DeCoste
U.S. Army Edgewood Chemical Biological Center, Research & Technology Directorate,
8198 Blackhawk Rd, Aberdeen Proving Ground, MD 21010

ABSTRACT

Metal-organic frameworks are gaining wide-spread applicability across many fields. We utilized metal-organic frameworks to develop a universal matrix for a new matrix-assisted laser desorption ionization mass spectrometry technique. The matrix-assisted laser desorption ionization technique is a powerful ionization method used to improve mass spectrometry characterization of biological samples. The current matrices used in the matrix-assisted laser desorption ionization process are not universal, and usually depend heavily on the nature of the analytes being analyzed. As such, there are many matrices that are used and based on the nature and type of analytes suitable matrices will be selected to provide optimal matrix-assisted laser desorption ionization mass spectrometry analysis. We proposed to utilize metal-organic framework compounds with multifunctional groups and various pores structures to address this technological gap. Understanding the basic mechanism of ionization during matrix-assisted laser desorption ionization-mass spectrometry process is vital to design an effective metal-organic framework surface to act as universal matrix. Metal-organic frameworks can be synthesized with regular or predicted geometry. In this report, we investigated the utilization of modified HKUST-1 with isonicotinic and nicotinic acids to address some fundamental questions about the type of interactions and binding mechanisms between metal-organic frameworks and analytes of interest on the surface. The data showed that there are different potential interactions and that HKUST-1 modified with isonicotinic acids had highest matrix-assisted laser desorption ionization-mass spectrometry response as compared to that of the conventional matrix-assisted laser desorption ionization matrix.

Keywords: metal-organic frameworks, mass spectrometry, matrix-assisted laser desorption ionization, charge transfer, desorption, matrix, film

1. INTRODUCTION

Matrix-assisted laser desorption ionization (MALDI), is a soft ionization technique that has witnessed wide application in the characterization of large biomolecules using various mass spectrometry analyzers, specifically time-of-flight ones.[1–4] The MALDI process involves the deposition of an analyte solution onto a metal substrate followed by the addition of a matrix.[5] The matrix/analyte dry spot is exposed to a UV laser, and the laser energy absorbed by the matrix/analyte is converted into heat energy that initiates charge transfer, resulting in the desorption of the matrix and analyte molecules in ionized form. The positive ions are then accelerated through a vacuum into mass spectroscopy (MS) analyses. Nevertheless, MALDI has faced a lack of guiding systematic principles, which has resulted in mostly empirical work. For example, there is no universal matrix that can be used in the MALDI-MS analysis of biomolecules. Hundreds of compounds have been tried with several analytes and were given qualitative ratings.[6–8] these variables were the result of differences in charge transfer efficiency between the matrix and analytes due to chemical and structural factors[7]. This problem requires an urgent analytical need that can advance the MALDI process toward mechanistic understanding. Metal-organic frameworks (MOF) are an emerging class of porous materials that have been studied in multiple areas, including gas storage,[9,10] sensing,[11] air purification,[12] and catalysis.[13] MOFs are typically synthesized from metal oxide secondary building units (SBU) connected by organic linkers to form a reticulated, porous network. MOFs are utilized because of their versatility and thermal stability. The unique physical and chemical properties of MOFs provide the potential to serve as a MALDI matrix capable of ionizing a wide range of analytes. However, because of their structural complexity, we attempted to determine first if there is any interaction between analytes and the MOFs when they are mixed together. Low-frequency Raman spectroscopy (LFRS) was used to determine the intermolecular and intramolecular changes between free MOFs, and when mixed with analytes in an amorphous environment.[1–16] The LFRS is an emerging technique that provides, concurrently, vibrational spectra for tested compounds in the terahertz and normal Raman spectral regions that are indicative of any potential physical and

chemical changes in a given analyte. Using LFRS can provide a wealth of information about material properties in a fast and non-destructive manner. In the case of MOFs, LFRS can be used to investigate the binding properties of MOFs with analytes of interest, and to determine the nature of such binding.

Currently, there are two different mechanisms that explain the ionization process in MALDI-MS analysis. The first mechanism is based on the coupled chemical and physical dynamics (CCPD) model, which involves charge transfer during the excitation stage of a matrix-analyte mixture, resulting from exposure to laser power.[17] The second mechanism is based on a cluster model, which involves a combination of proton and intra-cluster charge transfer during the desolvation step of the MALDI process.[18] Accordingly, we designed our experimental approach for MOF-analyte interaction during the MALDI process to determine which ionization model is governing their ionization step. This report addresses the modification of the MOF surfaces with nicotinic and isonicotinic acids to provide a carboxylic acid group as a potential source for charge transfer during the MALDI-MS process. This report will also address the utilization of MOFs in film-form to compare the MALDI-MS response to that of the powder form. The latter investigation was performed to determine the feasibility of using MOF-film to simplify the MALDI-MS sample preparation steps.

The overall goal of this project is to study the mechanism of ionization, and determine the factors that affect the charge transfer process during the MALDI-MS ionization process. This year, we also addressed the binding affinity issue between MOF and analytes using LFRS to determine intermolecular and intramolecular changes between crystalline and amorphous states of the MOFs with different analytes. Those analytes studied were classified as acidic or basic compounds. Understanding the basic properties of the MOF-analyte mixture, we will be able to determine how to design MOFs that enhance the ionization efficiency for a wide range of compounds during MALDI-MS analysis. This knowledge will be used to design and develop a reliable, functionalized MOF substrate that can desorb biomolecules and selectively capture analytes of interest.

This study addressed the potential intramolecular and intermolecular changes for MOF-analyte mixtures using LFRS and MALDI-MS techniques. The MOFs used in this year's effort were UiO-66-COOH and UiO-66-NH_2, HKUST-1, modified HKUST-1 with nicotinic or isonicotinic acids (HKUST-NA and HKUST-INA), and the analytes used were aniline, benzoic acid, benzylamine, and lauric acid. More MOFs than those tested by the LFRS technique were used for the MALDI-MS analyses. Most of the MOFs were obtained from internal sources either through synthesis or leveraged from already funded projects that utilize MOFs. The structures for some of the MOFs used are shown in Figure 1.

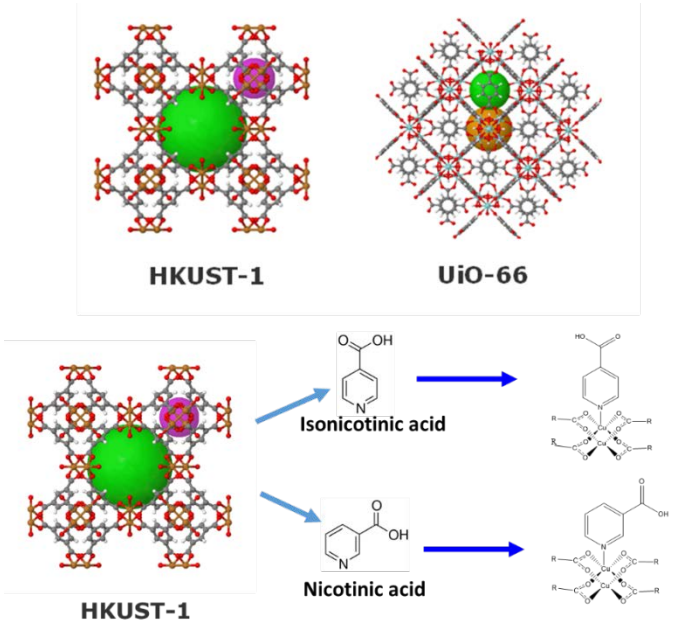

Figure 1. Representative MOFs used in this study including HKUST-1, UiO-66 with –COOH and –NH_2 functional groups, and modified HKUST-1 with nicotinic and isonicotinic acids.

2. MATERIALS AND METHODS

2.1 Metal-organic framework network synthesis

The MOFs used in this study—UiO-66, UiO-66-COOH, UiO-66-NH_2, and Copper(ii) benzene-1,3,5-tricarboxylate (Cu-BTC/HKUST-1)—were synthesized according to the reported literature.[19–21] Briefly, the synthesis of UiO-66-NH_2 was performed by dissolving 1.5 g of $ZrCl_4$ and 1.5 g of 2-Amino-1,4-benzenedicarboxylic acid in 180 mL of dimethyl formamide at room temperature in a volumetric flask. The resulting mixture was preheated in an oven at 80 °C for 12 hours, and then held at 100 °C for 24 hours. After cooling to room temperature in air, the resulting solid was filtered and repeatedly washed with absolute ethanol for 3 days at 60 °C in a water bath. The resulting yellow powder was filtered and transferred for drying under vacuum at room temperature. All the tested MOF substrates were characterized and validated using appropriate techniques to ensure the formation of the desired chemical network and determine the surface coverage area, pore size, and volume.[22,23]

2.2 Low-frequency Raman spectroscopy measurements

The measurement of the low-frequency Raman scattering from a MOF sample was taken in Stokes and anti-Stokes vibrational spectra. The Raman spectroscopy experiments were performed using a WItec alpha300 R confocal Raman microscopy system. A 100X microscope objective in the Raman microscopy was used. A Rayshield™ notch filter was used to provide LFRS features (from a wavenumber of 10 cm^{-1}). The laser used was a solid-state laser with a wavelength of 532.1 nm. A wavelength of 532 nm was used for excitation, with a power of ∼2 mW incident on the substrate. The Raman-scattered light was collected in the backscattering configuration and transmitted through a 100-μm slit to a 600 grooves/mm grating, which dispersed the light onto a thermoelectrically cooled CCD camera (WItec DV401 A). A spectral resolution of approximately 5 cm^{-1} was obtained. Spectra were acquired with 5-second to 10-second acquisition times. At a lower Raman shift, spurious contributions from the elastic line can be detected by measuring the scattering from a metal surface. In the anti-Stokes side, our spectrometer instrument response is better, which allowed us to measure the Raman spectrum down to 5 cm^{-1} of the Raman shift. The sample image in the entrance spectrometer plane was selected in such a way that the contribution from the glassy slide did not come into the spectrometer. No polarization selection was used.

2.3 MALDI-MS analysis

The standard sample preparation protocol for conventional MALDI-MS was used to perform all of the MALDI-MS analyses. Briefly, mass spectra were recorded with a MALDI Synapt® G2-S high-definition mass spectrometer (Waters®, Milford, MA). The buffer gas was adjusted using the default gas line connected to the hexapole ion guide compartment. The standard MALDI matrices and analytes kit were purchased from Sigma-Aldrich® (St. Louis, MO). The kit contains 1 mg of cinnamic acid (CA), 1 mg of 98 % sinnapic acid (SA), 4,6-dinitrophloroglucinol (97 %), insulin (from bovine pancreas), ubiquitin (from bovine erythrocytes), and carbonic anhydrase (from bovine erythrocytes). Each kit also contained a sufficient amount of MALDI solvent composed of acetonitrile (ACN), high-performance liquid chromatography-grade water, and triflouroacetic acid (TFA). High-performance liquid chromatography-grade methanol (MeOH) and water were purchased from Thermo Fisher Scientific, Inc. (Waltham, MA). A saturated solution of the matrices was prepared at a concentration of 1 μg/mL and dissolved in 50 % ACN:50 % H_2O:0.1 % TFA for CA and SA. The standard calibration analytes supplied in the same MALDI kit were diluted in the same solvent composition as that of the MALDI matrix. A MALDI target plate was spotted with 1–2 μL of the samples using a stacking or a mixing approach. The stacking approach consisted of spotting 1 μL of the matrix solution on the MALDI plate, allowing it to dry, followed by spotting with 1 μL of the analyte solution. The mixing approach utilized was the conventional MALDI spotting approach in which a 1:10 mixture of analytes:matrix is mixed prior to spotting on the MALDI substrate. Once mixed, 1–2 μL was spotted on the MALDI target plate and allowed to dry prior to insertion of the plate into the MALDI instrument. The same sample preparation protocol used in the conventional MALDI setup was also utilized with the tested MOFs. Every MOF:analyte mixture was spotted in triplicates on the MALDI target plate and allowed to dry prior to MS analysis.

A Waters® SYNAPT® G2-Si mass spectrometer equipped with a commercial MALDI source and operated with a Nd:YAG laser (355 nm, 200 Hz) was used. The mass spectral acquisitions were performed in positive ion mode using the following MALDI settings: 0 V on the sample plate holder, 10 V for extraction, 350 V for hexapole, and 10 V for aperture. The laser power used was 250 mW for 25–50 % laser fluence and at a 200 Hz firing rate. The sample plate voltage was held at 10 kV. Calibration was performed using polyethylene glycol adducts between 300 *m/z* and 3000 *m/z*.

The mass spectra were acquired using the reflectron positive ion mode with a reflectron voltage of 18 kV and an ion source lens voltage of 10 kV. Laser repetition rate was set at 20 Hz and increments of 20 laser shots were used to acquire the mass spectrum with a total of 100 shots per each mass spectrum. The MALDI instrument's vendor software was used to process the data and to obtain the MALDI mass spectra of the studied MOFs.

3. RESULTS AND DISCUSSION

3.1 Effect of MOF UiO-66-COOH on the LFRS analysis of acidic and basic compounds

LFRS was used to study the potential chemical and physical changes when the UiO-66-COOH was mixed with different acidic and basic analytes. The mixture was suspended in water and allowed to mix for 20 minutes using vortexing. The mixture was then centrifuged, the supernatant and the pellet were aliquoted and deposited on aluminum oxide slides, allowed to dry, then followed by LFRS analysis. Figure 2 shows the Stokes and anti-Stokes spectra for UiO-66-COOH mixed with lauric acid and benzylamine. The LFRS results showed that there is a subtle difference in the spectral signatures for the MOF-analyte mixtures in the normal Raman and terahertz regions. The terahertz region showed a similar pattern but with significant different in signal intensity between the UiO-66-COOH+lauric acid mixture vs. that of UiO-66-COOH+benzyl amine. However the terahertz had more differentiated signals for UiO-66-COOH+lauric acid than that for UiO-66-COOH+benzylamine; indicating that the physical changes with benzylamine and the MOF surface are more intense than those observed with the UiO-66-COOH+lauric acid mixture. Moreover, there is a loss of crystalline structure as evident by the terahertz data at around 0 cm^{-1} Raman shift, which indicates a physical change to the structure of the UiO-66-COOH when mixed with analytes, as shown in Figure 2. The LFRS data showed that UiO-66-COOH+lauric acid retains some crystalline properties as compared to UiO-66-COOH+benzylamine. This subtle difference in the terahertz region supports the observation seen in the Raman shift for the UiO-66-COOH interaction with different analytes, in which all of these mixtures showed loss of crystalline structures as evident by loss of Stokes and anti-Stokes peaks in the terahertz region.

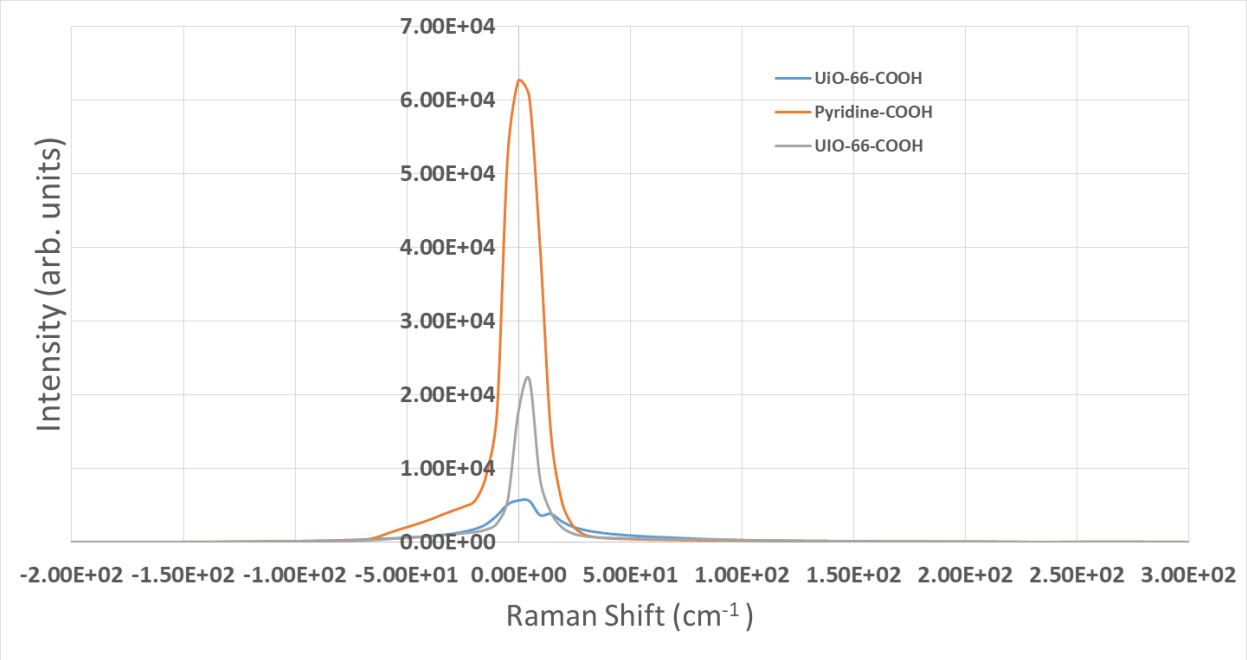

Figure 2. The LFRS spectra for UiO-66-COOH and different analytes. All samples were mixed with the MOF, UiO-66-COOH, and the resulting LFRS are stacked.

In the normal Raman shift region, there are differences in the Raman signature of the analyzed mixtures. The UiO-6-COOH+lauric acid mixture has Raman shifts at 405 cm^{-1}, 2260 cm^{-1}, and 2910 cm^{-1} that are not presented in the mixture of UiO-66-COOH+benzylamine. Moreover, there are differences between the standard MOF and its mixture where the Raman spectra shows a shift in the signal indicating that a chemical interactions are occurring

between the MOF and the analytes. These potential chemical interactions are more visible in the mixture of the MOF and benzylamine as compared to that of MOF and lauric acid, Figure 3.

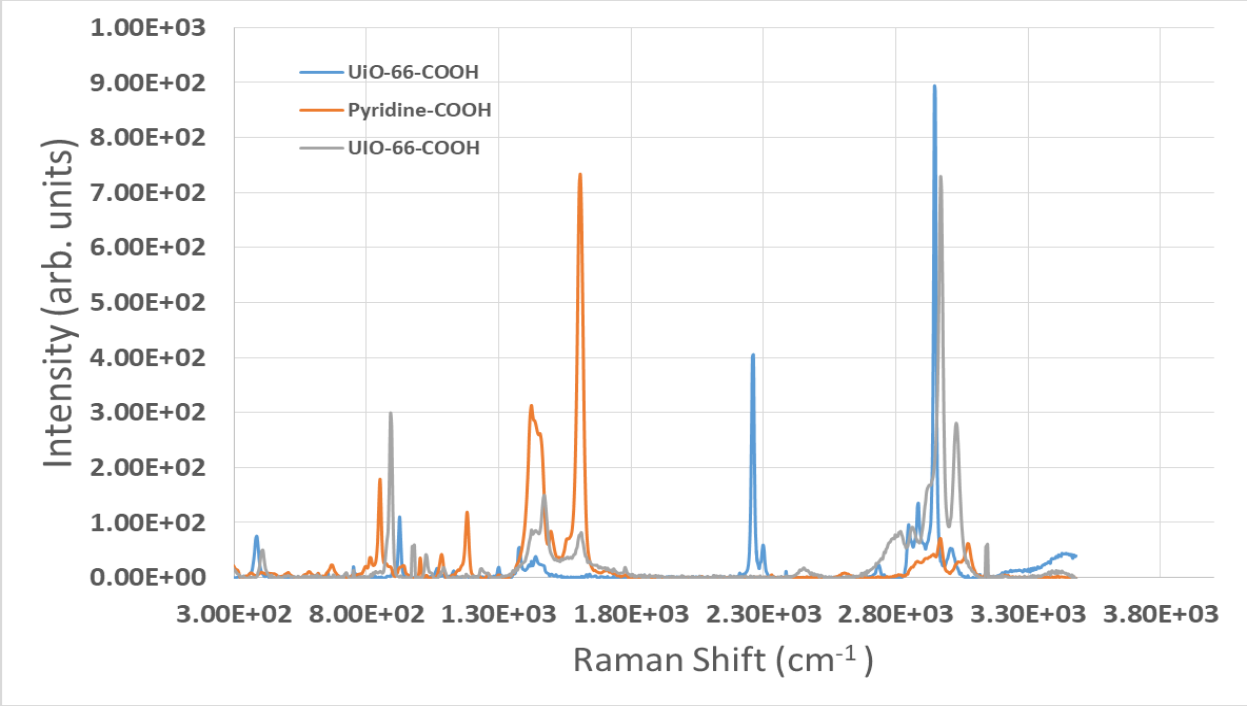

Figure 3. The normal Raman region spectra for UiO-66-COOH and different analytes. All samples were mixed with the MOF, UiO-66-COOH, and the resulting spectra are stacked.

3.2 Effect of the functional groups of MOFs on the MALDI-MS analysis of acidic and basic compounds

The MALDI-MS analyses were performed on benzylamine using different MOFs such as HKUST-1, HKUST-isonicotinic acid, HKUST-nicotinic acid, and using MALDI conventional matrix α-Cyano-4-hydroxycinnamic acid (CHCA). The MALDI-MS analyses were done in triplicate and the shown spectra represent the average of the obtained MALDI-MS spectra. Figure 4. Shows the MALDI-MS spectral signature of benzylamine using the mentioned MOFs and the conventional MALDI matrix, CHCA. The MALDI-MS data showed that the optimal response was obtained using the modified HKUST with isonicotinic acid as compared to the other investigated MOFs. The MS spectra showed the dominance of the MH+ ions as compared to others fragments. These MALDI-MS spectra show that the MOFs have a lower noise level than the CHCA spectrum. This could be due to the MOFs being stable and not decomposing into small fragment within the mass spectral signatures of benzylamine. However, the CHCA spectrum has relatively higher noise peaks that could be attributed to interferences from the matrix itself, which has a mass spectral signature within that of benzylamine. Moreover, the highest MALDI-MS response was observed with the HKUST-isonicotinic acid MOF as compared to the other MOFs. This could be due to the ease of interaction between benzylamine and the carboxylic group of the immobilized isonicotinic acid on the surface of the HKUST-1. The HKUST with nicotinic acid has the carboxylic group in the meta position as compared to that on isonicotinic acid, which is in the para position; thus, the latter carboxylic group has less steric hindrance to interact with the analyte molecules. The acid–base chemistry between the benzyl amine and the immobilized carboxylic group demonstrates that the presence of the electron-donating group in the para position (tertiary amine) reduces the acidity of isonicotinic acid more than nicotinic acid—which has the electron-donating group at the meta position. The reduction in acidity of the isonicotinic acid resulted in weaker acid–base interactions between the analyte and the immobilized phase, but potentially enhanced the charge transfer efficiency during MALDI-MS ionization. Overall, surface modification of the MOF affected the MALDI-MS response when acidic and basic compounds were analyzed with the mentioned MOFs. Such differences in acidic and basic properties of the analytes, and to a lesser extent the MOFs, were the major factors that affected the MALDI-MS responses for the modified HKSUT-isonicotinic and HKUST-nicotinic acid MOFs.

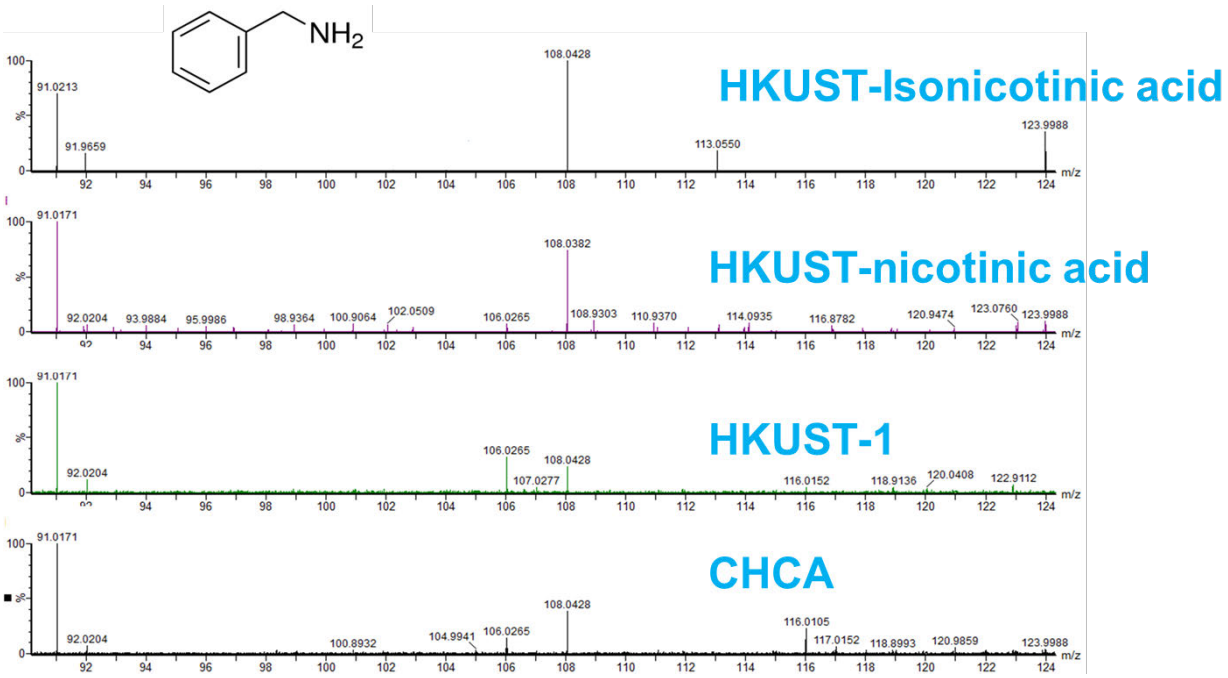

Figure 4. Comparative MALDI-MS response for benzylamine using different MOFs: HKUST-1, HKUST-isonicotinic, HKUST-nicotinic, and a conventional MALDI matrix (CHCA).

3.3 Effect of the acid/base interaction between MOFs and analytes on the MALDI-MS analyses

We examined the MALDI-MS ionization response to different acidic and basic compounds mixed with MOFs containing different modifying groups. The MOFs used were HKUST-1, HKUST-isonicotinic acid, and HKUST-nicotinic acid. The HKUST-1 is a neutral coordination polymer that has dimeric cupric tetracarboxylate units and twelve carboxylate oxygen atoms from the two BTC ligands bound to four coordination sites for each of the three Cu^{2+} ions.[22] These copper complex units form a face-centered crystal lattice. HKUST-1 has main pores of approximately 0.9 nm in diameter and forms a cubic network (Figure 1). The modified HKUST-1 with isonicotinic and nicotinic acids were synthesized and verified using different surface analysis techniques, such as NMR, ATR and XRD. Surface analysis data showed that the modified HKUST have an immobilized isonicotinic acid or nicotinic acid.

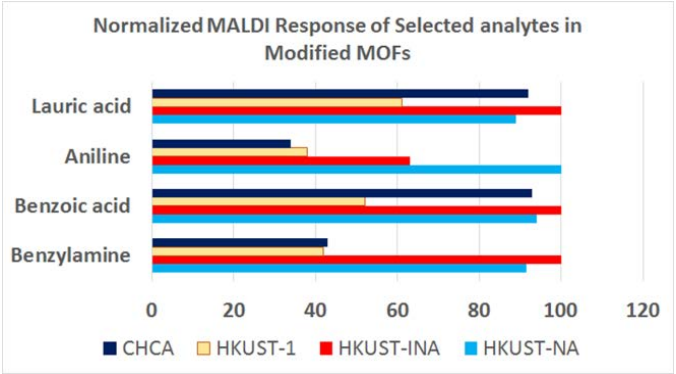

Figure 5. Normalized MALDI response of selected analytes in modified MOFs (HKUST-1, HKUST-isonicotinic acid, and HKUST-nicotinic acid) and a conventional MALDI matrix (CHCA).

Figure 5 shows the normalized MALDI-MS responses of different analytes and MOF mixtures. Lauric acid, benzoic acid, and benzylamine have the highest responses when mixed with HKUST-isonicotinic acid; however, aniline has the highest response with HKUST-nicotinic acid. It should be noted that benzylamine and benzoic acid have a more than 90 % MALDI-MS response signal with HKUST-nicotinic acid. The latter analyte seems to have the same MALDI response pattern when mixed with the HKUST-isonicotinic acid and HKUST-nicotinic acid. However, the data showed that the CHCA matrix has a better MALDI-MS response with acidic compounds than with basic compounds by a margin of almost 2X. Also, this latter observation was observed with acidic compounds and HKUST-1, which

has acidic dominant properties on the surface. This is another example of the impact acid/base chemistry has on the MALDI-MS characteristics of the analyzed acidic and basic compounds. The aromatic-containing analytes showed a similar pattern with the three different MOFs—with aniline having the highest MALDI-MS response with HKUST-NA instead of HKUST-INA. Though the rest of the MOFs have the same pattern for all the aromatic analytes, this is not the case with the aliphatic chain of lauric acid. There is a steric hindrance possibility on the MOF surface with aromatic compounds, but less evident with lauric acid, where the cumulative MALDI-MS responses of most of its mixtures had comparative signal intensity, with the exception of HKUST-1+lauric acid mixture.

Furthermore, we investigated the binding properties of the acidic and basic analytes with the mentioned modified MOFs and the non-modified MOF. In this approach, two sets of samples were obtained—one set from the precipitated solid and the other one from the supernatant of the same mixture solution. These samples were centrifuged at 8,000 rpm for 10 minutes to ensure sufficient separation of the supernatant from the suspended solid MOFs or CHCA matrices. A 2-µL aliquot was deposited on the MALDI plate surface and allowed to dry at room temperature. After that the MALDI-MS analyses were performed, the resulting data (Figure 6) shows the difference in the MALDI-MS responses to the different supernatant and precipitate samples of the dissolved benzylamine. The MALDI-MS data showed that the benzylamine and MOFs mixtures collected from the centrifuged precipitates have a higher MALDI-MS response as compared to their corresponding supernatant mixtures. However, the supernatant mixture of benzylamine and CHCA matrix has a higher MALDI-MS signal response than that of its corresponding precipitate mixture. Such a difference could be indicative of different binding affinities between the analyte and the MOF mixture in different phases, possibly caused by the solvation or the binding characteristics of the MOFs surfaces.

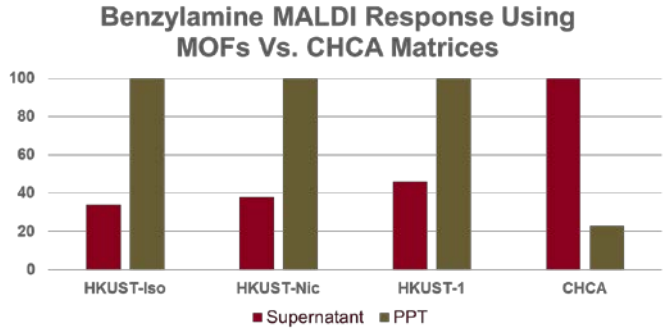

Figure 6. Comparison of the MALDI-MS response to different supernatant and precipitate aliquots for mixtures of benzylamine and different MOFs and CHCA matrices.

It is noteworthy to mention that the MOFs, when dissolved in the 50 % ACN/50 % H_2O/0.1 % TFA solution, did not show sufficient solvation and remain suspended in the liquid. However, the conventional MALDI matrix, CHCA, had a higher degree of solubility than that of the investigated MOFs. Such difference in the solvation properties of the matrices could have resulted in such a drastic difference among all the MALDI-MS analyzed samples. Also, there is a binding interaction between the surface of the MOFs and the analytes because the MALDI-MS signal responses from the precipitates were higher than that of the supernatant portions. This observation was the same for all investigated analytes (data not shown). The potential binding between the analyte and the MOF's surface could be supported by the Raman spectroscopy data, which showed physical and chemical changes occurred upon mixing the analytes with the MOF (see Figure 2 and Figure 3). Determining the specific type of binding is of interest and could provide better understanding of the MOF's interaction with acidic and basic molecules and help determine the specific types of interaction—whether size exclusion, dipole-dipole, H-bonding, ionic, or a combination of these potential interactions. Further experimentation is required to narrow down the type of interactions, this could be accomplished by the utilization of other MOFs that are drastically different in the chemical properties that could provide complimentary and useful information to decipher this contrasted behavior between the MOFs and the conventional MALDI matrix.

3.4 Effect of MOF form on the MALDI-MS analyses of acidic and basic compounds

Transitioning the MOF to be used in MALDI-MS applications will require providing the efficient and practical form of MOF to make it a desirable matrix. As such, different MOFs have only been used in the powder form in MALDI-MS applications. No reported literature has shown the implication on MALDI-MS spectral signatures when the MOF is used in film format. We utilized HKUST-1 in a film format since it is easily made in such form and its thickness could

be altered from 10 µm to around 100 µm. It is anticipated that using a MOF in a film form as a matrix in MALDI-MS analysis will simplify sample preparation steps required for MALDI-MS analysis. This approach allowed the deposition of the analyte samples directly on the surface of the MOF film follow by MALDI-MS analysis. The HKUST-1 film used in this study was compared to the powder format, also the HKUST-1 powder has been previously reported to show promising, and in this report as well, utilization as a MALDI-MS matrix due to its comparative MS responses to that of CHCA. Same experimental conditions applied to both the HKUST-1 film and powder forms during the MALDI-MS experiments. The HKUST-1 film form was coated to a silica surface, wetted with the 50 % ACN/50 % H_2O/0.1 % TFA solution and followed by a direct deposition of 2-µL aliquots, from the acidic and basic compounds solutions, on the film. The MALDI-MS results showed that the signal intensity for all of the acidic and basic compounds were similar to their responses when using HKUST-1 in powder form.

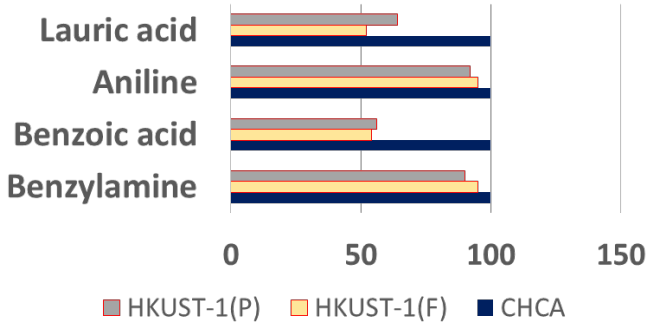

Figure 7. Effect of HKUST-1 forms, powder versus film, on the MALDI-MS analyses of acidic and basic compounds.

Figure 7 shows the MALDI-MS results for HKUST-1 film (HKUST-1(F)), HKUST-1 powder (HKUST-1(P)), and CHCA matrix. The mixtures of aniline and benzylamine with HKUST-1 (F) and HKUST-1(P) yielded the highest MALDI-MS responses as compared to the lauric and benzoic acids mixtures with same MOFs. The HKUST-1(F) had lower MALDI-MS signal intensity for all tested analytes as compared to that of HKUST-1(P). Also, the two MOF forms had lower MALDI-MS signal intensity than that of CHCA matrix ones. The HKUST-1 showed the same MALDI-MS response with the same analytes as previously reported. While the HKUST-1(F) did give similar level of MALDI-MS responses to that of the powder form, still more optimization is needed to increase its MALDI-MS signal responses to reach that of the conventional MALDI's matrix, CHCA. The acid/base chemistry of the MOFs in the two forms did not change drastically as shown by their MALDI-MS responses.

3.5 Comparison of the reproducibility of the MALDI-MS response for HKUST-1 in film and powder forms

The reproducibility of the HKUST-1 in film and powder forms were investigated using MALDI-MS. In this set of experiments, multiple MALDI-MS spectra were acquired on the same deposited spot for the HKUST-1 in film and powder forms and compared to that of CHCA MALDI-matrix. At least five different MALDI-MS spectra for each type of matrix were acquired. The HKUST-1 film showed the least reproducibility in which only two exposures resulted in MS spectra before the spectral signals completely diminished as shown in Figure 8.

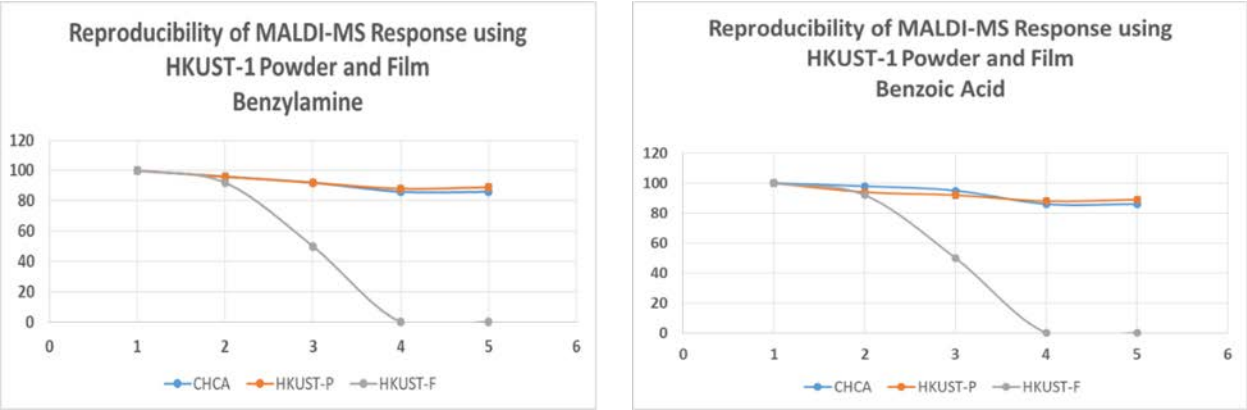

Figure 8. Comparative stability of the HKUST-1 film and powder forms during MALDI-MS analyses of benzylamine and benzoic acid.

However, the HKUST-1 powder form showed a stable acquisition of mass spectra, even after five different consecutive spectra, and was comparable to that of CHCA matrix. The drop-in signal intensity for the HKUST-1 powder started at the fourth day of the MALDI-MS analysis and the drop-in signal was around 16 % by the acquisition of the fifth spectra, which is comparable to CHCA matrix (Figure 8). Upon visual examination of the HKUST-1 film, it showed ablation of the spot that was exposed to the repetitive MALDI-laser; this could be due to the method of attaching the MOF film not being strong enough, or the unsustainability of the MOF film to the laser power period during the MALDI-MS analysis. It should be noted that the exposed spots of the HKUST-1 films were the only parts that got ablated by the MALDI laser with repetitive exposure. While it is normally observed that the exposed spot on MALDI plates during typical experimentation shows ablation as well, the HKUST-1 film was expected to sustain repeated exposure to the MALDI laser longer than its powder form. Overall, the MALDI-MS response for the analyzed MOFs showed variable response with the powder being more stable than the film form. Still, the MOF film was able to produce similar spectral features for the investigated analytes in MALDI-MS analyses as those of the MOF in powder form. This is encouraging from the practical aspect of utilizing MOFs in MALDI analysis, as it is imperative to obtain reproducible responses using the same MOFs for repetitive runs. The efficient MOFs in film format will reduce the consumption of matrix material, as is the case with conventional MALDI-MS matrices, and eventually, when bound to the MALDI plate surface as a film, it may potentially result in a faster MALDI-MS process and more practical approach for detection and identification of a wider range of chemical and biological molecules.

4. CONCLUSIONS

The experimental results showed that MOF substrates can provide an alternative, yet useful, venue to investigate the ionization mechanism during the MALDI-MS process. While there is still more work needed to confirm these reported findings, these results will help in designing more efficient MOFs to enhance the MALDI-MS response and to act as a multifunctional surface that could be used for the MALDI-MS analyses of more diverse chemical classes. This is not the case with the current MALDI-MS matrices, which are selected arbitrarily based on their experimental MALDI-MS response and one cannot be used for a wide range of chemical compounds. Changing the current approach of matrix selection for MALDI-MS analysis by having a multifunctional matrix/matrices—such as MOFs—will help reduce the burden on sample preparation steps and make it more economical and practical. The modification of the HKUST-1 surface with isonicotinic or nicotinic acids support such expectation, in which the MALDI-MS data from these modified MOFs showed significant improvements over the standard HKUST-1 MOF or the CHCA matrices. Even when comparing the modified HKUST-1 with isonicotinic acid versus that of the modified HKUST-1 with nicotinic acid, there are difference in their respective MALDI-MS responses—with the former modified MOF showing higher signal intensities for analytes as compared to the latter one. Clearly, there is an acid/base chemistry taking place between the MOFs and the acidic and basic analytes. This mechanism needs to be explored further to determine and understand all the factors involved in the acid/base or proton exchange during the MOF-analyte MALDI-MS process. The determination of the charge transfer mechanism and its correlation with the MALDI desorption is beneficial—understanding will provide broader benefits to the utilization of MOFs in biocatalysis, biomimetics, and bioprocesses.

Using HKUST-1 in film form showed a novel approach to utilizing MOFs in MALDI-MS analysis that could have appreciable advantage over powder MOFs. The HKSUT-1 film had a comparable MALDI-MS response to that of the powder form, although it was less stable due to various reasons. If successful in improving the stability of the HKUST-1 film during MALDI-MS analyses, it will be a promising approach to simplify the sample preparation steps and save time during the MALDI-MS process. However, more work is needed in this approach to ensure the stability of the film during MALDI-laser exposure, to determine the cause of ablation, and to determine if the film thickness will diminish or eliminate this deterioration issue. Overall, these MALDI-MS data showed that there exists a possibility to explore an in-depth approach to determine the parameters that need to be optimized in order to utilize MOFs as efficient and simplified alternative matrices to the conventional MALDI ones.

ACKNOWLEDGMENTS

Funding was provided by the U.S. Army via the Surface Science Initiative Program (PE 0601102A Project VR9) at the Edgewood Chemical Biological Center.

REFERENCES

[1] Rosinke, B.; Strupat, K.; Hillenkamp, F.; Rosenbusch, J.; Dencher, N.; Krüger, U.; Galla, H.J. Matrix-assisted laser desorption/ionization mass spectrometry (MALDI-MS) of membrane proteins and non-covalent complexes. *J. Mass Spectrom.* **1995,** *30* (10), pp 1462–1468.

[2] Cohen, S.L.; Chait, B.T. Influence of matrix solution conditions on the MALDI-MS analysis of peptides and proteins. *Anal. Chem.* **1996,** *68* (1), pp 31–37.

[3] Fenselau, C.; Demirev, P.A. Characterization of intact microorganisms by MALDI mass spectrometry. *Mass Spectrom. Rev.* **2001,** *20* (4), pp 157–171.

[4] Chaurand P; Norris J.L.; Cornett, D.S.; Mobley, J.A.; Caprioli, R.M. New developments in profiling and imaging of proteins from tissue sections by MALDI mass spectrometry. *J.Prot. Res*. **2006,** *5* (11), pp 2889–900.

[5] Tanaka, K.; Waki, H.; Ido, Y.; Akita, S.; Yoshida, Y.; Yoshida, T.; Matsuo, T. Protein and polymer analyses up to m/z 100 000 by laser ionization time-of-flight mass spectrometry. *Rapid Comm. Mass Spec.* **1988,** *2* (8), pp 151–153.

[6] Demeure, K.; Quinton, L.; Gabelica, V.; De Pauw, E. Rational selection of the optimum MALDI matrix for top-down proteomics by in-source decay. *Ana. Chem.* **2007,** *79* (22), pp 8678–8685.

[7] Cohen, S.L.; Chait, B.T. Influence of matrix solution conditions on the MALDI-MS analysis of peptides and proteins. *Anal. Chem.* **1996,** *68* (1), pp 31–37.

[8] Dong, X.; Cheng, J.; Li, J.; Wang, Y. Graphene as a novel matrix for the analysis of small molecules by MALDI-TOF MS. *Anal. Chem.* **2010,** *82* (14), pp 6208–6214.

[9] Farha, O.K.; Yazaydın, A.Ö.; Eryazici, I.; Malliakas, C.D.; Hauser, B.G.; Kanatzidis, M.G.; Nguyen, S.T.; Snurr, R.Q.; Hupp, J.T. De novo synthesis of a metal–organic framework material featuring ultrahigh surface area and gas storage capacities. *Nat. Chem.* **2010,** *2* (11), pp 944–948.

[10] Kaye, S.S.; Dailly, A.; Yaghi, O.M.; Long, J.R. Impact of preparation and handling on the hydrogen storage properties of Zn4O (1, 4-benzenedicarboxylate) 3 (MOF-5). *J. Am. Chem. Soc.* **2007,** *129* (46), pp 14176–14177.

[11] Kreno, L.E.; Leong, K.; Farha, O.K.; Allendorf, M.; Van Duyne, R.P.; Hupp, J.T. Metal–organic framework materials as chemical sensors. *Chem. Rev.* **2012,** *112* (2), pp 1105–1125.

[12] DeCoste, J.B.; Peterson, G.W. Metal-organic frameworks for air purification of toxic chemicals. *Chem. Rev.* **2014,** *114* (11), pp 5695–5727.

[13] Lee, J.; Farha, O.K.; Roberts, J.; Scheidt, K.A.; Nguyen, S.T.; Hupp, J.T. Metal–organic framework materials as catalysts. *Chem. Soc. Rev.* **2009,** *38* (5), pp 1450–1459.

[14] Colaianni, S.M.; Nielsen, O.F. Low-frequency Raman spectroscopy. *J. Mol. Struct.* **1995,** *347*, pp 267–283.

[15] Puretzky, A.A.; Liang, L.; Li, X.; Xiao, K.; Sumpter, B.G.; Meunier, V.; Geohegan, D.B. Twisted MoSe2 bilayers with variable local stacking and interlayer coupling revealed by low-frequency Raman spectroscopy. *ACS Nano.* **2016,** *10* (2), pp 2736–2744.

[16] Ferrari, A.C.; Basko, D.M. Raman spectroscopy as a versatile tool for studying the properties of graphene. *Nat. Nano.* **2013,** *8* (4), pp 235–246.

[17] Kirmess, K.M.; Knochenmuss, R.; Blanchard, G.J.; Kinsel, G.R. MALDI ionization mechanisms investigated by comparison of isomers of dihydroxybenzoic acid. *J. Mass Spectrom.* **2016,** *51* (1), pp 79–85.

[18] Knochenmuss, R. Ion formation mechanisms in UV-MALDI. *Analyst.* **2006,** *131* (9), pp 966–986.

[19] Wadas, T.J.; Wong, E.H.; Weisman, G.R.; Anderson, C.J. Coordinating Radiometals of Copper, Gallium, Indium, Yttrium and Zirconium for PET and SPECT Imaging of Disease. *Chem Rev*. **2010,** *110* (5), pp 2858–2902.

[20] Shih, Y.H.; Chien, C.H.; Singco, B.; Hsu, C.L.; Lin, C.H.; Huang, H.Y. Metal–organic frameworks: new matrices for surface-assisted laser desorption–ionization mass spectrometry. *Chem. Comm.* **2013,** *49* (43), pp 4929–4931.

[21] Cavka, J.H.; Jakobsen, S.; Olsbye, U.; Guillou, N.; Lamberti, C.; Bordiga, S.; Lillerud, K.P. A new zirconium inorganic building brick forming metal organic frameworks with exceptional stability. *J. Am. Chem. Soc.* **2008,** *130* (42), pp 13850–13851.

[22] An, J.; Farha, O.K.; Hupp, J.T.; Pohl, E.; Yeh, J.I.; Rosi, N.L. Metal-adeninate vertices for the construction of an exceptionally porous metal-organic framework. *Nat. Comm.* **2012,** *3*, p 604.

[23] Morris, W.; Volosskiy, B.; Demir, S.; Gándara, F.; McGrier, P.L.; Furukawa, H.; Cascio, D.; Stoddart, J.F.; Yaghi, O.M. Synthesis, structure, and metalation of two new highly porous zirconium metal–organic frameworks. *Inorg. Chem.* **2012,** *51* (12), pp 6443–6445.

Probing the connection between low-frequency vibrational modes and macroscopic structural behavior of metal organic frameworks

Neal D. Kline[a*], Bernard Goetz[b], Ashish Tripathi[a], Jose L. Mendoza-Cortes[c,d], Christian Serre[b]
[a]U.S. Army Edgewood Chemical Biological Center, Research & Technology Directorate, 8198 Blackhawk Rd, Aberdeen Proving Ground, MD 21010
[b]Institut des Materiaux Poreux de Paris, CNRS Ecole Normale Superieure, Ecole Superieure de Physique et de Chimie Industrielles, PSL research university, Paris, France 75005
[c]Florida State University College of Engineering, Tallahassee, FL 32306
[d]National High Magnetic Field Laboratory, Tallahassee, FL, 32310

ABSTRACT

Metal-organic frameworks are hybrid porous materials that have been widely studied due to their promising applications in fields such as gas storage, catalysis, and sensing. Among the variety of reported metal-organic frameworks is a sub group that have been observed to display large scale structural flexibility. The flexibility in the metal-organic framework corresponds to a fully reversible transition between different framework conformations triggered by external stimuli including temperature, pressure, and guest molecule. This study will investigate the MIL-53 family of metal-organic frameworks by systematically varying the components (metal node, functionalization of linker) and examining the collective vibrations of the frameworks (located in the THz region) using low frequency Raman spectroscopy. The Al^{3+}, Fe^{3+}, Cr^{3+}, and Ga^{3+} derivatives of the MIL-53 metal-organic frameworks were synthesized along with two functionalized derivatives of Al^{3+} incorporating the $–NH_2$ and $–NO_2$ functional groups on the linker. The low frequency Raman spectra collected on the metal-organic framework samples show clearly resolved bands for all of the systems under study. Minor differences in line shape/peak position were observed in the low frequency bands while varying the metal node, however significant differences were observed for the functionalized Al^{3+} versions. Theoretical modeling is ongoing to assign the spectra.

Keywords: metal organic frameworks, lattice dynamics, terahertz vibrations, low-frequency Raman spectroscopy, MIL-53

1. INTRODUCTION

Metal-organic frameworks (MOF) are porous crystalline materials with metal ions or clusters as the nodal points and organic linkers regularly arranged in between them. The periodic and porous structures give MOFs advantages for applications such as gas storage, gas separations, catalysis and sensing.[1,2] While MOFs are similar to other microporous materials, such as inorganic zeolites and activated carbon, they have greater surface areas and can be processed at much lower temperatures. MOFs can also be built from a wider range of constituents allowing the ability to fine tune structural aspects of the material or a specific interaction with an adsorbate. However, in contrast to the rigid structure of zeolites and carbon materials, a limited number of MOFs display large scale structural flexibility upon the application of external stimuli that can drastically alter their characterisctics.[3,4]

This unique large-scale structural flexibility of MOFs has stimulated research to specifically study the phenomenon. Several techniques have been used including X-ray diffraction methods, NMR, and IR/Raman.[5,6] These methods are usually implemented as an *in situ* characterization approach performed by applying an external stimulus—such as introducing guest molecules, and applying pressure, or temperature—and probing the MOF under the influence of the stimuli.

Recently, investigations studying the low frequency vibrational modes of the zeolitic imidazolate framework family of MOFs located in the THz region (0.1–10 THz, 3–300 cm^{-1}) have been performed.[7–9] The authors discovered that the low frequency modes of MOFs showed the standard lattice vibrations but also physical properties unique to the particular MOFs included in the study. It also allowed the authors to identify possible phase change mechanisms through which the framework may destabilize, distort, or collapse when mechanical force is applied. Several

techniques were used to uncover these low frequency vibrational modes including inelastic neutron scattering, low-frequency Raman spectroscopy, synchrotron radiation far-infrared absorption spectroscopy, and terahertz time domain spectroscopy. The experimental investigations were also supported by theoretical density functional theory calculations in order to help assign the spectra that were obtained. Combining spectroscopic techniques capable of reaching the THz region with theoretical calculations to model the low frequency vibrations provides an approach for a comprehensive description of MOF framework properties much more efficiently than current methods.

The structural flexibility of MOFs is associated with an anisotropic stiffness of the crystal pore which allows the material to be deformed easily in one direction but not in another. Because of this directional flexibility, the barrier between structural conformations is small allowing the material to transition to different conformations. Ferey and Serre[4] have identified a number of structural characteristics that are indicative of framework flexibility including the nature of the organic ligand, the characteristics of the secondary building unit present in the MOF, the periodic structure of the MOF, and the coordination of the metal nodes. There are also different categories of flexibility which generally illustrate the dynamic structural transformation that the MOF undergoes when exposed to the proper stimulus. One category of flexibility that will be investigated in this study is breathing (Figure 1).

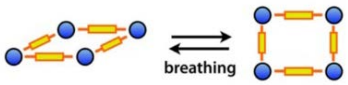

Figure 1. Structural flexibility in MOFs illustrated by the breathing phenomenon in MIL-53.[10]

Breathing is defined as reversible structural transitions between different framework conformations of a MOF during which the substantial displacement of atoms of the framework is accompanied by a change in unit cell volume.[2] In breathing, characteristic distances and angles of the unit cell change and the crystallographic space groups of the two distinct phases (narrow pore and large pore) may be different. The representative example of this kind of flexibility is the MIL-53 family of MOFs ([M(bdc)(OH)] where bdc = 1,4-benzenedicarboxylate and M = Al^{3+}, Fe^{3+}, Cr^{3+}, Sc^{3+}, Ga^{3+}, In^{3+}.

The present study reports the results of a low frequency analysis of the Al^{3+}, Fe^{3+}, Cr^{3+}, and Ga^{3+} derivatives of the MIL-53 family along with two functionalized derivatives of Al^{3+} incorporating the $–NH_2$ and $–NO_2$ functional groups on the linker. Previous findings have indicated that changing the metal node and functionalizing the MOF can affect its macroscopic structural behavior and also the low frequency vibrations that are intrinsically linked to the observed physical phenomena such as breathing. Our primary hypothesis is that the differences observed in the overall structural behavior of the MIL-53 MOFs from changing the metal node originate in the lattice dynamics of the MOF, which can be studied using spectroscopic techniques capable of reaching very low frequencies (< 100 cm^{-1}). We can then use differences in the low frequency spectra of these MOFs to help explain their differing structural behavior.

2. EXPERIMENTAL PROCEDURE

2.1 Metal-organic framework synthesis

The various MIL-53 MOFs were synthesized according to methods reported in the literature. All chemicals were obtained from Sigma-Aldrich® and were used without further purification.

2.1.1 MIL-53 Al^{3+}

MIL-53(Al) was synthesized by a solvothermal method. First, 6.5 g (17.3 mmol) of aluminum nitrate nonahydrate ($Al(NO_3)_3{\cdot}9H_2O$) and 1.44 g (8.7 mmol) of 1,4-benzenedicarboxylic acid (BDC) were mixed with 25 mL of deionized water in a Teflon™-lined stainless steel Parr bomb under autogenous pressure at 220 °C for 72 hours. The resulting white powder was then washed with deionized water. The sample was activated by heating in a furnace at 360 °C (heating rate of about 3 °C/minute) under air atmosphere for 13 hours, in order to remove unreacted acid molecules.

2.1.2 MIL-53 Ga^{3+}

MIL-53(Ga) was hydrothermally synthesized under mild conditions (210 °C, 3.5 hours). First, 0.997 g (3.9×10^{-3} mol) of $Ga(NO_3)3{\cdot}xH_2O$ and 0.764 g (4.6×10^{-3} mol) of BDC) were mixed with 20 mL of deionized water in a 125-mL Teflon™-lined stainless steel Parr bomb. After the reaction, the white powder obtained was washed with 50 mL of

N,N-Dimethylformamide (DMF) in a 125-mL Teflon™-lined stainless-steel Parr bomb (200 °C, 36 hours). The sample was washed again with MeOH to remove DMF, and dried in a furnace at 65 °C.

2.1.3 MIL-53 Fe^{3+}

MIL-53(Fe) was synthesized in a 250-mL laboratory flask. First, 6.75 g of $FeCl_3 \cdot xH_2O$ (2.5×10^{-3} mol) and 4.15 g terephthalic acid (2.5×10^{-3} mol) of each in 5 mL of DMF and 4 mL of HCl (5 M) were reacted in 125 mL of DMF at 150 °C for 48 hours. After filtration, the crude product was washed with 100 mL of MeOH at 65 °C for 12 hours and dried in an oven to remove MeOH.

2.1.4 MIL-53(Al)-NH_2

MIL-53(Al)-NH_2 was synthesized by mixing aluminum chloride ($AlCl_3 \cdot 6H_2O$) with benzene-2-amino-1,4-dicarboxylic acid (BDC-NH_2) and NaOH in a 1.56:1:2 molar ratio. First, 3.95 g (16.4 mmol) of aluminum chloride was added to 30 mL of water in a 100-mL round-bottom flask and stirred until dissolved. Then, 1.9 g (10.5 mmol) of BDC-NH_2 dissolved in 7.5 mL of water was added, followed by 10.5 mL of NaOH solution (2 M/ 21 mmol). The mixture was heated in reflux conditions overnight. After the reaction, a pale-yellow powder was collected by filtration and dried in oven at 65 °C. The solid was washed with DMF (150 °C, 8 hours) to remove non-reacted BDC-NH_2, washed again with MeOH to remove DMF, and dried in an oven to remove MeOH.

2.1.5 MIL-53(Al)-NO_2

MIL-53(Al)-NO_2 was synthesized by a procedure similar to MIL-53(Al)-NH_2, using benzene-1,4-dicarboxylic-2-nitro-acid (BDC-NO_2) as a linker. First, 3.95 g (16.4 mmol) of aluminum chloride ($AlCl_3 \cdot 6H_2O$) were added to 30 mL of water in a 100-mL round-bottom flask and stirred until dissolution. Then, 2.21 g (10.5 mmol) of BDC-NO_2 dissolved in 7.5 mL of water and 10.5 mL of NaOH solution (2 M/ 21 mmol) were added to the round-bottom flask and refluxed overnight. The resulting white solid was filtered and dried at 65 °C in an oven before being washed with DMF (150 °C, 8 hours) to remove non-reacted BDC-NO_2, washed again with MeOH to remove DMF, and dried in an oven to remove MeOH.

2.2 MOF characterization

2.2.1 X-ray diffraction

X-ray powder diffraction (XRPD) of the MOFs were collected with a Bruker D8 Advance diffractometer equipped with a LYNXEYE XE-T detector and with a copper radiation source (Cu Kα, λ =1.5406 Å), operating at 45 kV and 40 mA. XRPD of the MOFs were collected in a Siemens D5000 (θ–2θ) diffractometer with Cu Kα1 radiation (λ = 1.54056 Å) from 3–30° (2θ) using a step size of 0.02° and 4 seconds per step in continuous mode.

2.2.2 Fourier-transform infrared spectroscopy

Fourier-transform infrared spectroscopy (FTIR) spectra were taken using a Perkin-Elmer Spectrum 100. Twelve scans were averaged over a range of 4000 cm^{-1} to 400 cm^{-1} with a resolution of 3 cm^{-1}.

2.2.3 Low-frequency Raman measurements

Samples for Raman analysis were prepared by casting thin films of the various MIL-53 MOFs on aluminum coated slides. Raman spectra were recorded using an Alpha 300R confocal microscope with a 100X objective and with a 532-nm laser with the following laser power for each sample: 2.0 mW for MIL-53 Al^{3+}, 600.0 µw for MIL-53 Fe^{3+}, 3.0 mW for MIL-53 Cr^{3+}, 600.0 µw for MIL-53 Ga^{3+}, 1.0 mW for MIL-53 Al^{3+} NH_2, and 1.5 mW for MIL-53 Al^{3+} NO_2. Raman spectra were acquired with a 20 s integration time with 10 co-added spectra for the high frequency (-250 cm^{-1}–2000 cm^{-1}) portion of Raman spectra recorded using the 600 line/mm grating, while the low frequency data (-200 cm^{-1}–1000 cm^{-1}) was recorded using the 1,800 line/mm grating with a 30 s integration time and 15 co-added spectra.

2.3 Theoretical methods

Calculations have been performed using first-principles calculations at the level of unrestricted hybrid DFT, with the UB3LYP functional, as implemented in the *ab initio* CRYSTAL14 suite code. The van der Waals weak interactions

were taken account using the semi-empirical Grimme's (-D2) dispersion corrections. Triple-zeta valence with polarization quality (TZVP) Gaussian basis sets were used for light elements (H, B, C, N, O) and transition metal (TM) atoms. The convergence of energy, electron density, and forces were set to 10–7 atomic units for all geometry optimizations. The spin states were allowed to relax unrestricted wave functions calculations. The harmonic vibrational frequencies at the optimized geometries were analyzed at the respective levels of theory to reveal the nature of the stable structure. This method was used for geometry optimization because densities and energies obtained with the method are less affected by spin contamination than other approaches, and it has been proved effective for related materials calculations. Integrations inside of the first Brillouin zone were sampled on 4 × 4 × 16 MonkhorstPack k-mesh grids for the MOF during geometry optimization. In other words, the reciprocal space for all the structures was sampled by a Γ-centered Monkhorst-Pack scheme with a resolution of around 2π x 1/60 Å-1

3. RESULTS AND DISCUSSION

3.1 X-ray diffraction and FTIR analysis

The MIL-53 family of MOFs is composed of terephthalate anions and trans chains of metal (III) octahedral-sharing –OH groups, creating a three-dimensional framework with a one-dimensional pore channel system. Their formulas are $M^{III}(OH)\cdot[O_2C\text{-}C_6H4\text{-}CO_2]H_2O$ (M^{III}=Al, Cr, Fe) for the hydrated forms (MIL-53lt; "lt"=low temperature or "np"=narrow pore) are $M^{III}(OH)\cdot[O_2C\text{-}C_6H_4\text{-}CO_2]$ for the dehydrated compounds (MIL-53ht; "ht"=high temperature or "lp"=large pore). XRD and FTIR (Figures 2 and 3) data were collected on the activated compared to literature sources to confirm their identity.[11,12] The FTIR spectra of the Fe^{3+}, Ga^{3+}, and Al^{3+} derivatives all exhibit vibrational bands in the 1400–1700 cm^{-1} region which indicates the presence of a carboxylic acid functionality. The vibrational bands around 1580 cm^{-1} and 1403 cm^{-1} are characteristic of the $–CO_2$ asymmetric and symmetric stretching, respectively.

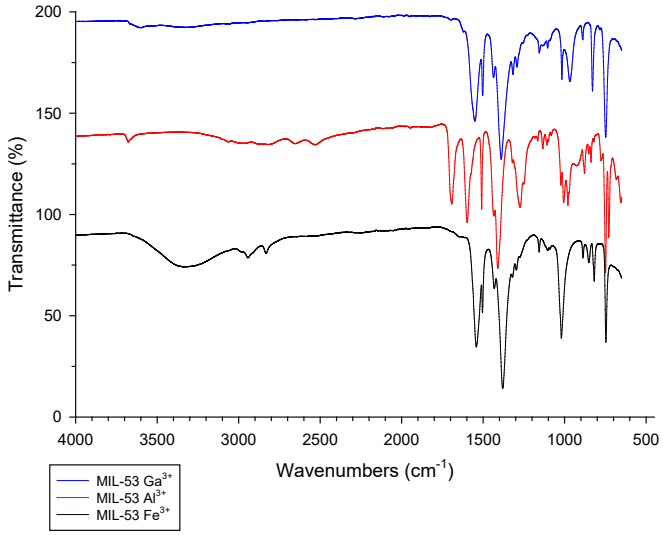

Figure 2. FTIR data for the Fe^{3+}, Cr^{3+}, and Al^{3+} MIL-53 analogues.

Further confirmation of the synthesis of the MIL-53 compounds was performed by collecting XRD data (Figure 3) of the synthesized powders and comparing to literature. The XRD was performed on the powder samples after activation which would render the MOFs in the hydrated "np" form. Fe^{3+}, Ga^{3+}, and Al^{3+}analogues are depicted in Figure 4 and appear to correlate well to what has been reported in the literature[11–13] The XRD pattern of the "np" form should look roughly the same for the different MIL-53 analogues as the main difference between the structures will be the metal center with minor changes in the structural parameters due to differing metal size.

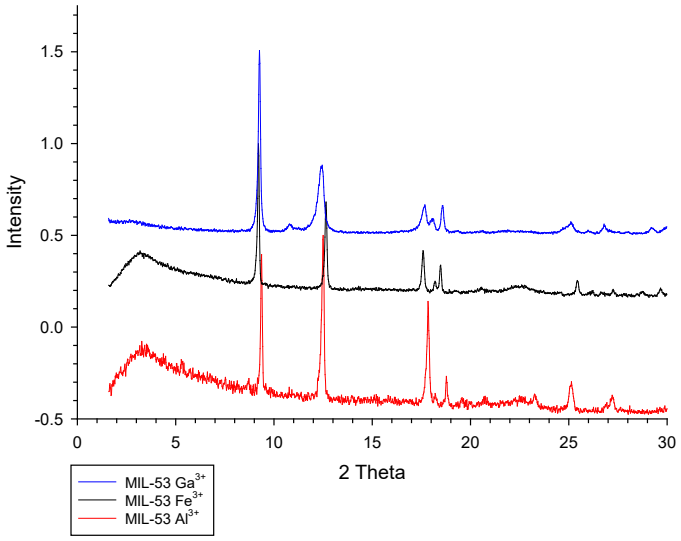

Figure 3. XRD data for the Al^{3+}, Ga^{3+} and Fe^{3+} derivatives of MIL-53.

3.2 Raman analysis

The Raman spectra for the Al^{3+}, Fe^{3+}, Ga^{3+}, and Cr^{3+} analogues of MIL-53 is shown in Figure 4. The low frequency data (< 200 cm^{-1}) collected is indicative of the lattice vibrations of the MOF while the higher frequency data details chemical information. In fact, the spectral features > 500 cm^{-1} of the different analogues is dominated by signatures from the 1,4-benzenedicarboxylate linker indicating a very high chemical similarity between the different species. However, in the low frequency spectra there are subtle differences between the Al^{3+}, Ga^{3+}, and Cr^{3+} MIL-53 species while the Fe^{3+} derivative displays very low frequency behavior.

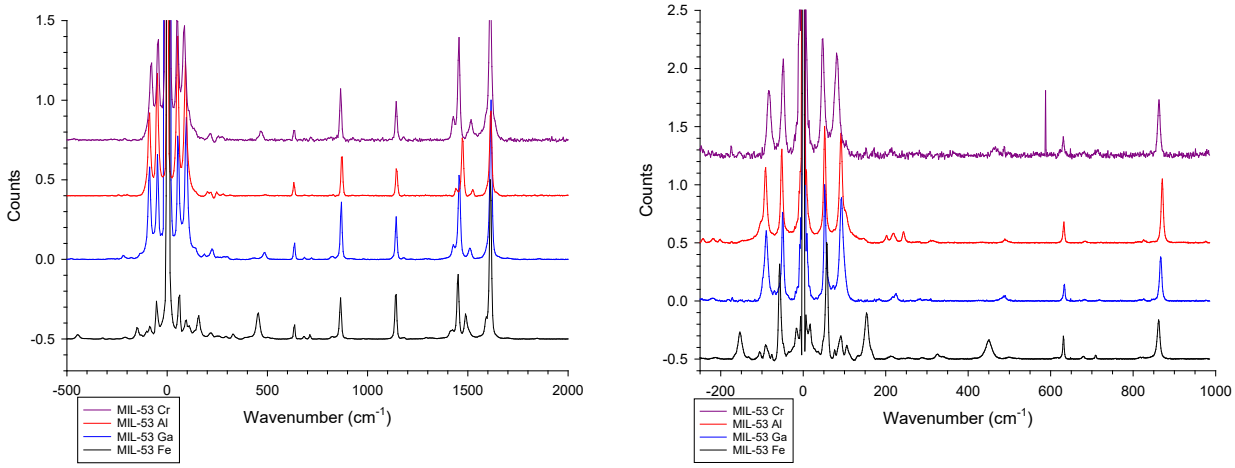

Figure 4. High-frequency (left panel) and low-frequency (right panel) Raman data for the different MIL-53 analogues.

Table 1 also contains a list of the observed spectral features below 200 cm^{-1} for the different derivatives. The Al^{3+} and Ga^{3+} MIL-53 have the most similar spectra with the two main bands appearing below 200 cm^{-1} having almost identical peak position and spacing. The only differences are a small third feature that appears in between the two main bands in the Ga^{3+} spectrum and the appearance of a shoulder on the blue side of the band observed at 92.3 cm^{-1} in the Al^{3+} spectrum. The Cr^{3+} spectrum also is dominated by two strong bands below 200 cm^{-1}, but they are slightly red shifted from where they appear in the Ga^{3+} and Al^{3+} spectra and the spacing between them is also smaller.

Table 1. Peak position of observed spectra bands < 200 $^{cm-1}$ for MIL-53 derivatives.

MIL-53 species	Position of observed spectral bands <200 $^{cm-1}$
Cr^{3+}	48.2 cm^{-1}, 81.2 cm^{-1}
Al^{3+}	53.0 cm^{-1}, 92.3 cm^{-1}
Ga^{3+}	52.7 cm^{-1}, 73.9 cm^{-1}, 93.3 cm^{-1}
Fe^{3+}	58.8 cm^{-1}, 76.3 cm^{-1}, 91.9 cm^{-1}, 106.4 cm^{-1}

The Raman spectra for the singly substituted derivatives of the Al^{3+} MOF incorporating the $–NH_2$ functional group and $–NO_2$ functional group are shown in Figure 5, along with the unsubstituted MIL-53 Al^{3+} spectrum for reference. The functionalized MOFs display very different spectral characteristics below 200 cm^{-1} than the original MOF. In both substituted MOFs, the two predominant bands are replaced by one band at 79.3 cm^{-1} in the $–NH_2$ analogue, while the $–NO_2$ MOF shows one very broad, featureless band extending from 31 cm^{-1} to 110 cm^{-1} and an additional band at 150 cm^{-1}. Theoretical modeling is underway to aid in the band assignments of the low-frequency features.

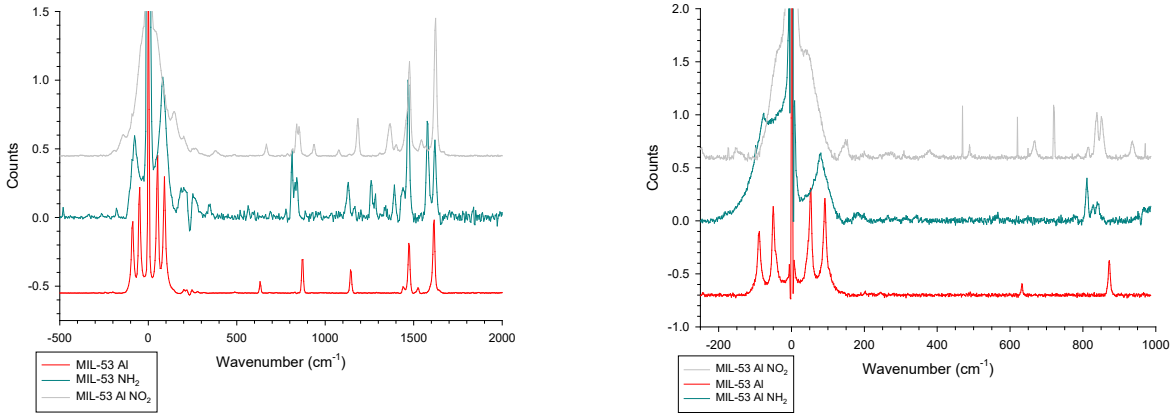

Figure 5. High-frequency (left panel) and low-frequency (right panel) Raman data for substituted MIL-53 Al^{3+} analogues.

4. CONCLUSIONS

Several MIL-53 derivatives were synthesized and characterized in this investigation to study their low-frequency vibrational modes. The low-frequency Raman data collected shows that there are signatures related to collective lattice vibrations for the MIL-53 series of MOFs. The Al^{3+}, Fe^{3+}, Ga^{3+}, and Cr^{3+} MIL-53 derivatives were successfully synthesized along the with two singly substituted Al^{3+} MIL-53 MOFs, and their low-frequency data compared. There were subtle differences related to peak positioning and line shape in the low-frequency data when comparing the Al^{3+}, Ga^{3+}, and Cr^{3+} MOFs, while the Fe^{3+} MOF gave very different low-frequency spectra. Incorporating the $–NH_2$ and $–NO_2$ functional groups into the Al^{3+} analogue also dramatically changed the low-frequency behavior. According to previous research, these changes in low-frequency behavior can be linked to changes in the macroscopic properties of the MOF. Modeling is underway to help assign the Raman spectra and elucidate the lattice dynamics of these species.

ACKNOWLEDGMENTS

Funding was provided by the U.S. Army via the Surface Science Initiative Program (PE 0601102A Project VR9) at the Edgewood Chemical Biological Center.

REFERENCES

[1] Furukawa, H.; Cordova, K.E.; O'Keeffe, M.; Yaghi, O.M. The chemistry and applications of metal-organic frameworks. *Science.* **2013,** *341* (6149), p 1230444.

[2] Kuppler, R.J.; Timmons, D.J.; Fang, Q.R.; Li, J.R.; Makal, T.A.; Young, M.D.; Yuan, D.Q.; Zhao, D.; Zhuang, W.J.; Zhou, H.C. Potential applications of metal-organic frameworks. *Coord. Chem. Rev.* **2009,** *253* (23– 24), pp 3042–3066.
[3] Schneemann, A.; Bon, V.; Schwedler, I.; Senkovska, I.; Kaskel, S.; Fischer, R.A. Flexible metal-organic frameworks. *Chem. Soc. Rev.* **2014,** *43* (16), pp 6062–6096.
[4] Ferey, G.; Serre, C. Large breathing effects in three-dimensional porous hybrid matter: facts, analyses, rules and consequences. *Chem. Soc. Rev.* **2009,** *38* (5), pp 1380–1399.
[5] Miller, S.R.; Wright, P.A.; Devic, T.; Serre, C.; Ferey, G.; Llewellyn, P.L.; Denoyel, R.; Gaberova, L.; Filinchuk, Y. Single crystal X-ray diffraction studies of carbon dioxide and fuel-related gases adsorbed on the small pore scandium terephthalate metal organic framework, Sc2(O2CC6H4CO2)3. *Langmuir.* **2009,** *25* (6), pp 3618–3626.
[6] Klein, N.; Herzog, C.; Sabo, M.; Senkovska, I.; Getzschmann, J.; Paasch, S.; Lohe, M.R.; Brunner, E.; Kaskel, S. Monitoring adsorption-induced switching by (129)Xe NMR spectroscopy in a new metal-organic framework Ni(2)(2,6-ndc)(2)(dabco). *Phys. Chem. Chem. Phys.* **2010,** *12* (37), pp 11778–11784.
[7] Ryder, M.R.; Civalleri, B.; Bennett, T.D.; Henke, S.; Rudic, S.; Cinque, G.; Fernandez-Alonso, F.; Tan, J.C. Identifying the role of terahertz vibrations in metal-organic frameworks: from gate-opening phenomenon to shear-driven structural destabilization. *Phys. Rev. Lett.* **2014,** *113* (21), p 215502.
[8] Ryder, M.R.; Civalleri, B.; Cinque, G.; Tan, J.-C. Discovering connections between terahertz vibrations and elasticity underpinning the collective dynamics of the HKUST-1 metal–organic framework. *CrystEngComm.* **2016,** *18* (23), pp 4303–4312.
[9] Tan, N.Y.; Ruggiero, M.T.; Orellana-Tavra, C.; Tian, T.; Bond, A.D.; Korter, T.M.; Fairen-Jimenez, D.; Zeitler, J.A. Investigation of the terahertz vibrational modes of ZIF-8 and ZIF-90 with terahertz time-domain spectroscopy. *Chem. Commun. (Cambridge, U. K.)* **2015,** *51* (89), pp 16037–16040.
[10] Coudert, F.-X.; Boutin, A.; Fuchs, A.H.; Neimark, A.V. Adsorption Deformation and Structural Transitions in Metal–Organic Frameworks: From the Unit Cell to the Crystal. *J. Phys. Chem. Lett.* **2013,** *4* (19), pp 3198–3205.
[11] Horcajada, P.; Serre, C.; Maurin, G.; Ramsahye, N.A.; Balas, F.; Vallet-Regi, M.; Sebban, M.; Taulelle, F.; Ferey, G. Flexible porous metal-organic frameworks for a controlled drug delivery. *J. Am. Chem. Soc.* **2008,** *130* (21), pp 6774–6780.
[12] Loiseau, T.; Serre, C.; Huguenard, C.; Fink, G.; Taulelle, F.; Henry, M.; Bataille, T.; Ferey, G. A rationale for the large breathing of the porous aluminum terephthalate (MIL-53) upon hydration. *Chemistry.* **2004,** *10* (6), pp 1373–1382.
[13] Li, Z.; Wu, Y.N.; Li, J.; Zhang, Y.; Zou, X.; Li, F. The metal-organic framework MIL-53(Al) constructed from multiple metal sources: alumina, aluminum hydroxide, and boehmite. *Chemistry.* **2015,** *21* (18), pp 6913–6920.
[14] Volkringer, C.; Loiseau, T.; Guillou, N.; Ferey, G.; Elkaim, E.; Vimont, A. XRD and IR structural investigations of a particular breathing effect in the MOF-type gallium terephthalate MIL-53(Ga). *Dalton Trans.* **2009,** (12), pp 2241–2249.

SEEDLING

PROJECTS

Effect of opioids on the pulmonary microvascular endothelium

Daniel J. Angelini*, Christopher S. Phillips, Todd M. Sickler, Michael G. Feasel
U.S. Army Army Edgewood Chemical Biological Center, Research & Technology Directorate,
8198 Blackhawk Rd, Aberdeen Proving Ground, MD 21010

ABSTRACT

Translating responses seen at the *in vitro* level to the *in vivo* level is a challenge faced by the entire scientific community but is additionally challenging for the defense research community due to the limited availability of human exposure data. Opioid analgesics are an exception to this trend since they are widely used in human clinical medicine. Acute toxicities associated with opioid use and overdose include respiratory depression and apnea, cardiac arrhythmias, and vomiting. A less studied, but relevant, side-effect of opioid agonists is pulmonary edema. This phenomenon is sometimes observed in overdose patients, but it is currently not known whether these observations are due to direct interaction with the endothelium by an opioid compound or some other mechanism. This study aimed to assess the propensity of opioids to cause cellular-level changes that generate pulmonary edema.

Keywords: barrier function, endothelial cells, fentanyl, morphine, opioids

1. INTRODUCTION

1.1 Opioids

Opiates refer only to substances that have been derived from the opium poppy plant—including morphine, heroin, and codeine.[1] Opioid is a broader term that is defined as any substance, either natural or synthetic, that directly interacts with one or more opioid receptor(s),[1] including all opiates as well as the synthetic substances oxycodone, methadone, fentanyl, and derivatives. Opioids are routinely used in clinical medicine for pain management and anesthesia, but also have the potential for abuse.[2] The synthetic opioids are of particular concern because fentanyl has been reported to be 100X more potent than morphine, and its analog, carfentanil, 100X more potent than fentanyl.[3] Carfentanil is so potent that it has no application in human clinical medicine; although, it is approved for large animal veterinary use and has been used to anesthetize polar bears in wildlife tracking studies.[4] In addition, synthetic opioids can be cutaneously absorbed or inhaled, increasing the risk of exposure. Accidental exposures have led to life-threatening presentations of law enforcement agents following exposure to illicit drugs containing these substances.[5]

1.2 Opioid receptors

Opioid receptors have been characterized to include four major subtypes: mu (MOR), delta (DOR), and kappa (KOR) opioid receptors, and the nociception receptor (NOP).[6] Fentanyl and its analogues are known to be MOR agonists of varying potency, efficacy, and duration. The MOR is responsible for the desirable effects of opioid administration such as euphoria, sedation, and analgesia but is also known to play a major role in respiratory depression, central nervous system depression, constipation, emesis, and addiction. It is unknown if the MOR or any of the other opioid receptors play a role in cellular responses that evoke structural changes that manifest as pulmonary edema.

1.3 Endothelial barrier function

Endothelial cells (EC) play a crucial role in maintaining homeostasis; these cells tightly regulate the passage of fluid, nutrients, and immune cells from the intravascular compartment to tissues throughout the body.[7,8] Transenodthelial flux of molecules occurs through either the paracellular pathway (intercellular gaps) or the transcellular pathway (transcytosis or vesicular transport). Edema formation—fluid accumulation within tissues—typically occurs through the paracellular pathway.[9] This pathway is regulated at the cell-cell level by at least two distinct junctional complexes—adherens junctions (AJ), and tight junctions (TJ).[8] The number of these specific junctions in an EC is dependent on its location within the vascular tree. For example, brain microvascular ECs contain many more TJs than ECs from any other regional vascular bed.[8] AJs and TJs are both tethered to the actin cytoskeleton, but AJs play a prominent role in the regulation of barrier function throughout almost the entire vasculature.[10] AJs consist of the

membrane-spanning vascular endothelial (VE)-cadherin, and the cytoplasmic proteins α-, β-, and γ-catenin and p120.[8] The VE-cadherin ectodomain participates in calcium-dependent, homophilic cell-cell adhesion, and is tethered to the actin cytoskeleton through the catenin proteins. Both rapidly acting (e.g., thrombin) and late-acting (e.g., tumor necrosis factor-α) regulators of barrier function increase tyrosine phosphorylation of VE-cadherin; these phosphorylation events induce a loss of cell-cell adhesion and actin depolymerization, leading to intercellular gap formation and increased paracellular permeability.[8,11,12]

1.4 Opioid-induced pulmonary microvascular injury

Opioids have been shown to affect almost every organ, including the lung,[13] and non-cardiogenic pulmonary edema has been associated with opioid overdose deaths.[13–16] The molecular mechanism(s) underpinning this pathologic process is currently unclear, but potentially involves hypoxia, direct effects of the opioid compound (e.g., apoptosis), or increased capillary permeability.[13] In the laboratory, studies have demonstrated that the opiate morphine can increase pulmonary endothelial permeability *in vitro*[17] as well as enhance the endothelial permeability response to endotoxin exposure.[18] In other studies, it has been shown that the synthetic opioid fentanyl is readily absorbed into the pulmonary endothelium.[19]

2. METHODOLOGY

2.1 Culture of human lung microvascular endothelial cells

Primary human lung microvascular ECs (HMVEC-L) were obtained from Lonza (Walkersville, MD) and were cultured in EC basal medium (EBM-2, Lonza) supplemented with 5 % fetal bovine serum (FBS), human recombinant epidermal growth factor (rhEGF), human recombinant vascular endothelial growth factor (rhVEGF), human recombinant fibroblast growth factor (rhFGF) with heparin, long R3 insulin-like growth factor I (IGF), hydrocortistone, ascorbic acid, gentamicin, and amphotericin B (Lonza Bulletkit, CC-3202) as we have described.[12,20–22] Only HMVEC-Ls from passages 5–10 were studied.

2.2 Selection of opioid compounds

In these studies, we examined two different opioid compounds—morphine (opium alkaloid) and fentanyl (synthetic opioid). Morphine was obtained from Cayman Chemical (Ann Arbor, MI) and fentanyl was obtained from Sigma-Aldrich® (St. Louis, MO). Stock solutions of the powdered opioids were then diluted in dimethyl sulfoxide (DMSO) (Sigma-Aldrich®) to a concentration of 10 mM for use in the cell culture experiments. The prepared stock solutions were then stored at -20 ºC until use.

2.3 Cellular impedance assay

Cellular impedance was measured using the xCELLigence® Real-Time Cell Analyzer (ACEA Biosciences, Inc.; San Diego, CA) as described.[23,24] HMVEC-L (5×10^4) were plated on specially designed impedance plates (E-Plate® 16s; ACEA Biosciences, Inc.) and grown to post-confluence in the incubator (72 hours, 37 ºC/5 % CO_2). During this time, cellular impedance measurements were taken hourly to monitor the progress of the development of the endothelial barrier. These results were reported as Cell Index (CI). Once the barrier had been developed (48–72 hours), the CI was normalized, and the ECs were exposed to increasing concentrations of either morphine or fentanyl (1–1,000 μM diluted in DMSO). As controls, the HMVEC-Ls were treated with vehicle (0.1 % or 1% DMSO) or media alone. Following treatment, impedance readings were taken every 15 minutes over the course of the 24-hour experiment. Evidence of endothelial barrier dysfunction was indicated by a decrease in the normalized CI compared to media alone and/or vehicle control.

3. RESULTS

3.1 Effect of morphine on the pulmonary endothelial barrier

HMVEC-Ls were grown to confluence over a 72-hour period on impedance plates as stated above. The CI was normalized, and the ECs were exposed to increasing concentrations of morphine (1–1,000 μM), vehicle (0.1 % or 1 % DMSO), or media alone for 24 hours. Normalized CI was measured every 15 minutes following exposure (shown

in Figure 1). In morphine-treated HMVEC-Ls, concentrations of either 300 µM or 1,000 µM induced a reduction in normalized CI compared to media or vehicle (0.1 % or 1% DMSO). This reduction began to separate from vehicle (1 % DMSO) at approximately 4 hours post-treatment and persisted for several hours. Changes in normalized CI in HMVEC-Ls treated with 300 µM morphine persisted throughout the 24-hour study; however, HMVEC-Ls treated with 1,000 µM morphine seemed to recover from this effect between 15–16 hours post-treatment. This reduction appears to return to baseline by the end of the 24-hour study. The peak reduction of normalized CI was approximately 25 % and was observed between 8–9 hours post-exposure. Lower doses of morphine (1 µM, 10 µM, 30 µM and 100 µM) did not disturb the normalized CI in these experiments.

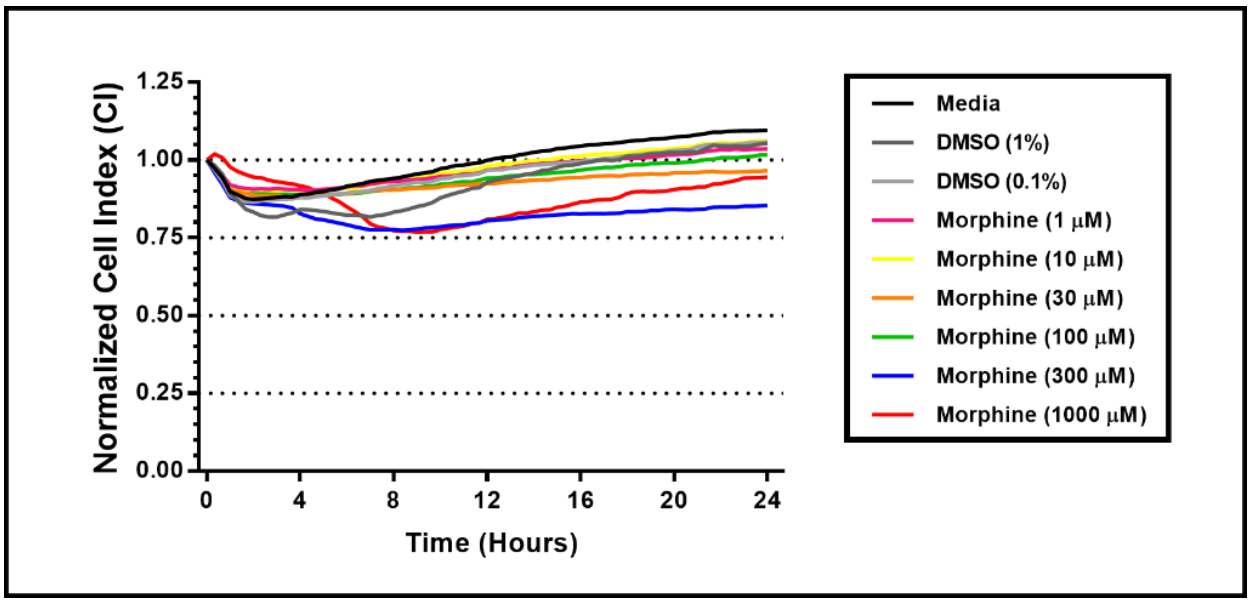

Figure 1. Normalized cellular impedance changes in cultured HMVEC-L following treatment with morphine. HMVEC-Ls were exposed to media alone, vehicle (0.1 % or 1 % DMSO), or increasing concentrations of morphine (1–1,000 µM). The results are expressed as the mean of the normalized CI; $n \geq 3$ for each experimental condition.

3.2 Effect of fentanyl on the pulmonary endothelial barrier

HMVEC-Ls were grown to confluence over a 72-hour period on impedance plates as stated above. Prior to testing, the CI was normalized, and the ECs were exposed to increasing concentrations of fentanyl (1–1,000 µM), vehicle (0.1 % or 1 % DMSO), or media alone for 24 hours. Normalized CI was measured every 15 minutes following the exposures (Figure 2). In these experiments, fentanyl concentrations < 100 µM appeared to have no effect on normalized CI compared to either media or vehicle controls. A fentanyl concentration of 300 µM induced a reduction in normalized CI compared to media or vehicle (0.1 % or 1% DMSO) and this reduction began to separate from vehicle (1 % DMSO) at approximately 4 hours post-treatment and persisted for several hours. Toward the end of the 24-hour experiment, the HMVEC-Ls appeared to begin to recover from the fentanyl treatment at this concentration. Exposure to 1,000 µM produced an interesting result. The normalized CI increased following fentanyl treatment which peaked at approximately 8 hours following initial exposure. Once the normalized CI reached this peak, it was followed by a rapid reduction in normalized CI. This reduction reached 0.00 at 40 hours post-initial exposure (data not shown), suggesting that fentanyl is cytotoxic at 1,000 µM for HMVEC-Ls.

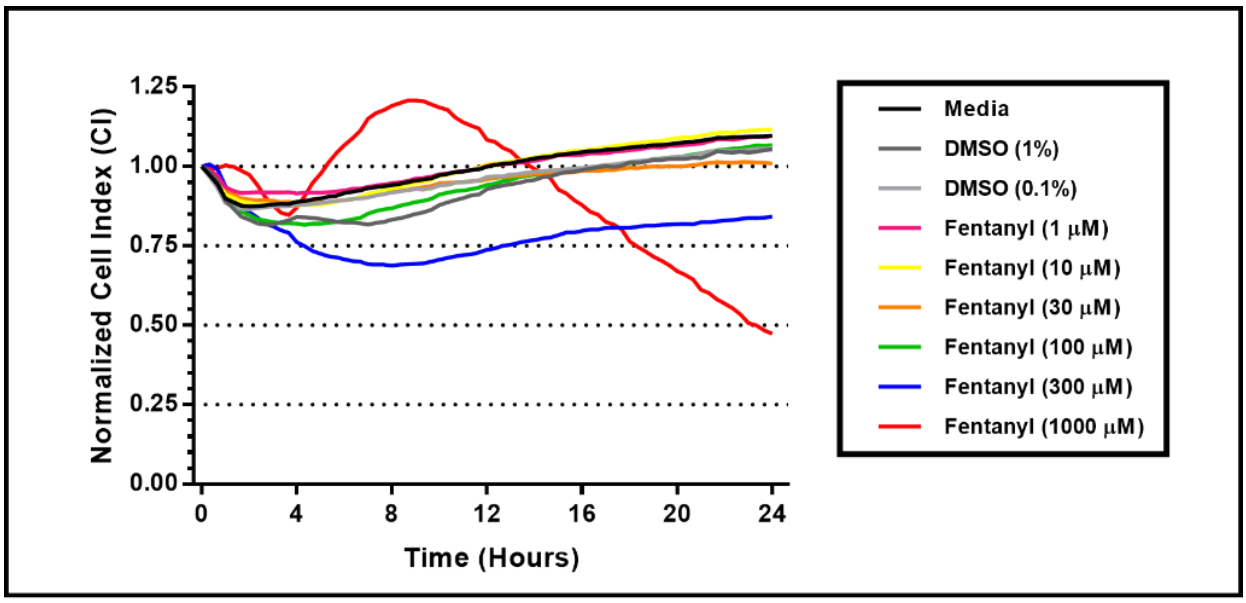

Figure 2. Normalized cellular impedance changes in cultured HMVEC-L following treatment with fentanyl. HMVEC-Ls were exposed to media alone, vehicle (0.1 % or 1% DMSO), or increasing concentrations of fentanyl (1–1,000 μM). The results are expressed as the mean of the normalized CI; $n \geq 3$ for each experimental condition.

4. CONCLUSIONS

In this study, we demonstrated that the opioids morphine and fentanyl induce both a dose- and time-dependent decrease in normalized CI in cultured HMVEC-Ls. These results suggest that these opioids are acting directly on the ECs to disrupt the endothelial barrier at concentrations ≥ 300 μM. The maximum reduction in normalized CI appears to occur between 8–9 hours following initial exposure. Following this peak reduction, the HMVEC-Ls seem to begin to recover from the barrier disruption for the remainder of the study. In addition to barrier disruption, these results suggest that fentanyl is cytotoxic to HMVEC-L at concentrations ≥ 1,000 μM. Whether this cytotoxicity is occurring through apoptosis or necrosis, is currently unclear; determining the pathway of this observation will require further examination.

ACKNOWLEDGMENTS

Funding was provided by the Director, Edgewood Chemical Biological Center under the authorities and provisions of Section 2363 of the FY 2018 NDAA to develop new technologies, engineer innovations, and introduce game-changing capabilities. The authors would also like to thank Dr. Augustus W. Fountain, Ms. Rebecca Braun, Dr. Kelly Basi, Dr. Kyle Glover, and Mrs. Davi Kristovich for continued scientific and administrative support.

REFERENCES

[1] Moallem, S.A.; Balali-Mood, K.; Balali-Mood, M., Opioids and Opiates. In *Handbook of Drug Interactions*, Mozayani, A.; Raymon, L., Eds. Humana Press: 2011; pp 159–191.
[2] Inturrisi, C.E., Clinical pharmacology of opioids for pain. *Clin. J. Pain.* **2002,** *18* (4 Suppl), pp S3–13.
[3] Van Bever, W.F.; Niemegeers, C.J.; Schellekens, K.H.; Janssen, P.A., N-4-Substituted 1-(2-arylethyl)-4-piperidinyl-N-phenylpropanamides, a novel series of extremely potent analgesics with unusually high safety margin. *Arzneimittelforschung.* **1976,** *26* (8), pp 1548–1551.
[4] Haigh, J.C.; Lee, L.J.; Schweinsburg, R.E., Immobilization of polar bears with carfentanil. *J. Wildl. Dis.* **1983,** *19* (2), pp 140–144.

[5] Rondinone, N., 11 Hartford SWAT Officers Exposed to Heroin, Fentanyl During Drug Raid. *Hartford Courant,* Sep 16, 2016.
[6] Waldhoer, M.; Bartlett, S.E.; Whistler, J.L., Opioid receptors. *Annu. Rev. Biochem.* **2004,** *73*, pp 953–990.
[7] Garcia, J.G.; Schaphorst, K.L., Regulation of endothelial cell gap formation and paracellular permeability. *J. Investig. Med.* **1995,** *43* (2), pp 117–126.
[8] Sukriti, S.; Tauseef, M.; Yazbeck, P.; Mehta, D., Mechanisms regulating endothelial permeability. *Pulm. Circ.* **2014,** *4* (4), pp 535–551.
[9] Lucas, R.; Verin, A.D.; Black, S.M.; Catravas, J.D., Regulators of endothelial and epithelial barrier integrity and function in acute lung injury. *Biochem. Pharmacol.* **2009,** *77* (12), pp 1763–1772.
[10] Gavard, J., Endothelial permeability and VE-cadherin: a wacky comradeship. *Cell Adh. Migr.* **2014,** *8* (2), pp 158–164.
[11] Angelini, D.J.; Hasday, J.D.; Goldblum, S.E.; Bannerman, D.D., Tumor Necrosis Factor-α-Mediated Pulmonary Endothelial Barrier Dysfunction. *Curr. Respir. Med. Rev.* **2005,** *1* (3), p 14.
[12] Angelini, D.J.; Hyun, S.W.; Grigoryev, D.N.; Garg, P.; Gong, P.; Singh, I.S.; Passaniti, A.; Hasday, J.D.; Goldblum, S.E., TNF-alpha increases tyrosine phosphorylation of vascular endothelial cadherin and opens the paracellular pathway through fyn activation in human lung endothelia. *Am. J. Physiol. Lung. Cell Mol. Physiol.* **2006,** *291* (6), pp L1232–1245.
[13] Radke, J.B.; Owen, K.P.; Sutter, M.E.; Ford, J.B.; Albertson, T.E., The effects of opioids on the lung. *Clin. Rev. Allergy Immunol.* **2014,** *46* (1), pp 54–64.
[14] Bazoukis, G.; Spiliopoulou, A.; Mourouzis, K.; Grigoropoulou, P.; Yalouris, A., Non-cardiogenic pulmonary edema, rhabdomyolysis and myocardial injury following heroin inhalation: a case report. *Hippokratia.* **2016,** *20* (1), pp 84–87.
[15] Mell, H.K.; Sztajnkrycer, M.D., Clinical images in medical toxicology: heroin overdose with non-cardiogenic pulmonary edema. *Clin. Toxicol. (Phila).* **2006,** *44* (4), p 399.
[16] Riccardello, G.J., Jr.; Maldjian, P.D., Pulmonary hemorrhage in acute heroin overdose: a report of two cases. *Emerg. Radiol.* **2017,** *24* (6), pp 709–712.
[17] Singleton, P.A.; Moreno-Vinasco, L.; Sammani, S.; Wanderling, S.L.; Moss, J.; Garcia, J.G., Attenuation of vascular permeability by methylnaltrexone: role of mOP-R and S1P3 transactivation. *Am. J. Respir. Cell. Mol. Biol.* **2007,** *37* (2), pp 222–231.
[18] Liu, H.C.; Anday, J.K.; House, S.D.; Chang, S.L., Dual effects of morphine on permeability and apoptosis of vascular endothelial cells: morphine potentiates lipopolysaccharide-induced permeability and apoptosis of vascular endothelial cells. *J. Neuroimmunol.* **2004,** *146* (1–2), pp 13–21.
[19] Waters, C.M.; Avram, M.J.; Krejcie, T.C.; Henthorn, T.K., Uptake of fentanyl in pulmonary endothelium. *J. Pharmacol. Exp. Ther.* **1999,** *288* (1), pp 157–163.
[20] Angelini, D.J.; Su, Q.; Yamaji-Kegan, K.; Fan, C.; Teng, X.; Hassoun, P.M.; Yang, S.C.; Champion, H.C.; Tuder, R.M.; Johns, R.A., Resistin-like molecule-beta in scleroderma-associated pulmonary hypertension. *Am. J. Respir. Cell Mol. Biol.* **2009,** *41* (5), pp 553–561.
[21] Nguyen, C.; Feng, C.; Zhan, M.; Cross, A.S.; Goldblum, S.E., Bacillus anthracis-derived edema toxin (ET) counter-regulates movement of neutrophils and macromolecules through the endothelial paracellular pathway. *BMC Microbiol.* **2012,** *12*, p 2.
[22] Sui, X.F.; Kiser, T.D.; Hyun, S.W.; Angelini, D.J.; Del Vecchio, R.L.; Young, B.A.; Hasday, J.D.; Romer, L.H.; Passaniti, A.; Tonks, N.K.; Goldblum, S.E., Receptor protein tyrosine phosphatase micro regulates the paracellular pathway in human lung microvascular endothelia. *Am. J. Pathol.* **2005,** *166* (4), pp 1247–1258.
[23] Angelini, D.J.; Phillips, C.; Prugh, A.M.; Glaros, T.; Tran, B., *Signaling Pathways Associated with VX Exposure in Mesenchymal Stem Cells*; ECBC-TR-1452; U.S. Army Edgewood Chemical Biological Center: Aberdeen Proving Ground, MD, **2017;** UNCLASSIFIED Report.
[24] Ke, N.; Wang, X.; Xu, X.; Abassi, Y.A., The xCELLigence system for real-time and label-free monitoring of cell viability. *Methods Mol. Biol.* **2011,** *740*, pp 33–43.

Effect of Laponite® clay platelet incorporation on performance of metal-organic framework-polyethylene oxide composite membranes for permeation applications

Matthew A. Browe[a*], Trenton M. Tovar[a,b], John M. Landers[a,b], John J. Mahle[a], Paul D. Butler[c], Masafumi Fukuto[d], Christopher J. Karwacki[a]
[a]U.S. Army Edgewood Chemical Biological Center, Research & Technology Directorate, 8198 Blackhawk Rd, Aberdeen Proving Ground, MD 21010
[b]National Research Council, 500 5th St NW, Washington, D.C. 20001
[c]Center for Neutron Research, National Institute for Standards and Technology, 100 Bureau Dr, Gaithersburg, MD 20899
[d]National Synchrotron Light Source II, Brookhaven National Laboratory, 743 Brookhaven Ave, Building 743, Upton, NY 11973

ABSTRACT

Composite polymer membranes of polyethylene oxide, Laponite® clay platelets, and the metal-organic frameworks UiO-66-NH_2, PCN-250, ZIF-8, and NU-1000 were synthesized and evaluated to examine the effect of the clay platelet filler on the properties of the composite, with the UiO-66-NH_2 membranes evaluated at pH 8, 9, and 10 to probe the extrema of the stability of the metal-organic framework and the clay platelet to more fully map the potential design range of the material for future applications. It was found that UiO-66-NH_2 at pH 8 was able to preserve the thermal stability of the composite membrane, for which the polyethylene oxide-Laponite® clay analogue at that pH without a metal-organic framework otherwise appeared to greatly lose connectivity of the platelets to the polymer substrate. Further, the ability of the metal-organic framework and Laponite® to produce a tortuous diffusion path in the membrane was found to directly impact the fractional utilization of the active material and corresponding failing breakthrough time in permeation experiments involving the mustard gas simulant chloroethyl ethyl sulfide, with UiO-66-NH_2 observing the greatest synergistic tortuosity effect with Laponite® among all the metal-organic frameworks utilized.

Keywords: permeation, Laponite®, metal-organic framework, polymer, filler, mechanical strength, tortuosity

1. INTRODUCTION

Polymers are favorable materials for utilization in membrane-based separation applications due to their flexibility, stability, and durability. However, diffusion of permeant in polymer-based membranes is inherently complex, as polymer chain distribution in film morphology is highly heterogenous in nature. Therefore, permeant behavior is heavily influenced by the spatial distribution of void regions within the material, which is largely reflected in free-volume theories of diffusive transport in polymer membranes. This directly influences interaction of the film material with the permeant and can often lead to great underutilization of the active species and subsequent suboptimal barrier performance of the composite membrane.

It has been shown that the barrier properties of polymers can be altered and greatly enhanced by inclusion of impermeable filler components in these void regions to alter the diffusion path of permeant molecules by forcing them to follow longer and more tortuous pathways in passing through the film.[1] Early theory developed by Nielsen[2] attempted to parameterize the relative enhancement of the diffusion path length of a permeant molecule through a polymer film through the concept of tortuosity—described as the ratio of the diffusion path length of a permeant through a polymer film with filler components to the diffusion path length of a permeant through a polymer film without filler. The morphology of the filler component was found to heavily influence tortuosity—specifically, the ratio of the length of the filler component in the direction normal to the film surface to the length of the filler component in the direction tangent to the film surface, which is commonly referred to as the aspect ratio. It was shown that thin plate-shaped particles with a large aspect ratio serve as an optimal morphology for increasing tortousity (and

subsequently decreasing permeability) if they can be oriented within the polymer so that their faces are parallel to the surface of the film.

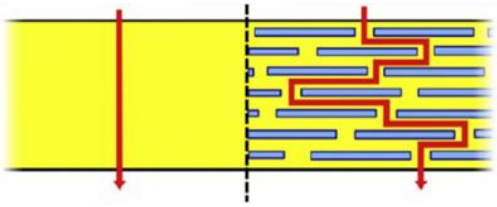

Figure 1. Depiction of diffusion path of gas-phase permeant without filler particles (left) and with high-aspect-ratio filler particles (right).[3]

Clay platelets are a common polymer filler material of thin plate-shaped morphology utilized as such a diffusion barrier. Polymer-clay composite materials have been heavily studied since the discovery by the Toyota Research Center in Japan that a composite of nylon-6 with as little as two volume percent of montmorillonite showed significantly enhanced mechanical and thermal properties.[4] Such enhancement of composite properties with very small amounts of added clay filler has been found to extend to many other polymeric systems as well.[5]

Polyethylene oxide (PEO), specifically, has long been a model polymer used in a platelet composite system due to its high affinity for interaction with cations on the platelet surface[6] It has been shown that in solution, synthetic clay nanoparticles are exfoliated and act as multifunctional cross-links to PEO polymers, building a network.[7] Upon applied shear to the precursor PEO/platelet solution, stretching of the polymer is induced, which favors alignment of the platelets. With PEO, it has been found that polymer-clay interactions become stronger as the clay particle size is reduced.

Given these findings, a common clay platelet filler utilized with PEO has been Laponite® RD (LRD). LRD is a synthetic and trioctahedral smectite clay with a layered structure similar to that of the natural clay hectorite,[8] and it has a chemical composition of 66.2 % SiO_2, 30.2 % MgO, 2.9 % Na_2O, and 0.7 % Li_2O, corresponding to the molecular formula $Si_8(Mg_{5.5}Li_{O.4}H_{4.0}O_{24.0})^{0.7-}(Na_{0.7})^{0.7+}$.[9] LRD has the advantages over natural clays of being chemically pure, free from crystalline silica impurities, and composed of a very monodisperse platelet size of approximately 25-nm diameter and 0.9-nm thickness, resulting in a uniform aspect ratio of 30:1.[10]

Metal-organic frameworks (MOF)[11] are attractive reactive filler components in polymeric membranes due to their high surface area, tunable porosity and functionalities, and high decontaminative performance against a wide variety of toxic chemicals[12]—including nerve agents[13] and vesicants.[14] MOFs have emerged as promising filler materials for mixed-matrix membranes (MMM) containing MOF and polymer components, since the first MOF-polymer MMM was synthesized by Yehia et al.[15] When incorporating MOFs into these systems, suitability for reaction must be considered, and zirconium-based MOFs have high potential. Among these are the UiO series of MOFs, in which UiO-66-NH_2 in particular has demonstrated superior reactivity against a wide range of nerve agents, vesicants, and simulants. In permeation applications, performance of vesicants—such as mustard gas—are of paramount interest, as they represent severe percutaneous threats and possess low molecular dimensions relative to other chemical warfare agents,[16] thus allowing for easier diffusion through a membrane. A commonly-employed simulant utilized to represent mustard gas is 2-chloroethyl ethyl sulfide (CEES), of which the reaction chemistry has been elucidated with UiO-66-NH_2.[17] CEES was shown to bind to the amine group of the linker in UiO-66-NH_2, releasing HCl.

Other MOFs with 31 Å channels—such as the Zr_6-based MOF NU-1000 in particular—are very promising for these applications as well.[18] NU-1000 offers larger pore apertures than the other MOFs, possibly facilitating diffusion of larger molecules such as CEES to the interior space of the MOF where a majority of the reactive sites are located. Diffuse reflectance infrared fourier transform (DRIFT) spectral data has suggested interaction between NU-1000 and CEES via hydrogen bonding between the thioether and chloro groups of 2-CEES with the Zr–OH groups at the nodes of the MOF. The interaction mechanism has been attributed to the interaction between the sulfur group of 2-CEES and the zirconium nodes of the MOF.[19] Lastly, polymer-clay interactions are probed utilizing the MOFs PCN-250 and ZIF-8. Neither has been evaluated against CEES in the open literature to the best of our knowledge, but both are known to present wide thermal, hydrolytic, and chemical stability and offer differing surface chemistries for evaluation of compatibility as fillers in PEO-LRD systems.

The aim of this current effort is to evaluate the MOFs UiO-66-NH_2, NU-1000, PCN-250, and ZIF-8 in PEO films, with and without LRD platelets. This will probe a full range of interactions among film components with major commercially-produced MOFs which have the potential to survive the synthesis conditions. The effect of each of these

filler combinations on utilization of active material in permeation properties, breathability, and mechanical stability of the resultant films will be explored and elucidated.

2. PROCEDURE

For all films synthesized, the effort was made to limit the PEO concentration in distilled water to 5 % by volume to avoid approaching solubility limits. For films containing solely PEO and LRD, the synthesis procedure was followed according to previous literature[20] in which LRD/PEO films were synthesized in a 20/80 weight/percent ratio at an ionic strength of 0.001 M (adjusted with NaCl) and a synthesis pH of either 10, 9, or 8. The different pHs were utilized in the effort to compare with corresponding samples utilizing MOF.

For samples containing MOF, LRD, and PEO, the MOF was first tip-sonicated for 5 minutes to promote optimal dispersion before proceeding via the same procedure as the PEO-LRD samples, with weight percents of 20/20/60 of MOF/LRD/PEO. All samples containing LRD were mixed vigorously for two weeks to promote optimal exfoliation of the platelets. The UiO-66-NH_2 samples were synthesized at pH of 10, 9, and 8 to gauge the tradeoffs between stability of the MOF and stability of the LRD platelets, as X-ray diffraction patterns showed that UiO-66-NH_2 was found to have a maximally-stable pH of 8. Samples utilizing PCN-250, ZIF-8, and NU-1000 were all synthesized solely at a pH of 10. Samples containing solely PEO or solely PEO and MOF were only mixed overnight. After mixing, the precursor solutions were pipetted onto a quartz tray and spread layer-by-layer with a wet film applicator in the effort to achieve a thickness of 100 microns. Layers took approximately 1–2 hours to dry and yielded an average thickness of 2–3 microns per layer. A full list of films synthesized is shown in Table 1.

Table 1. Films synthesized.

Sample	PEO Wt %	LRD Wt %	MOF utilized	MOF Wt %	pH
PEO	100	0	None	0	9 (not adjusted)
PEO-LRD-pH 8	80	20	None	0	8
PEO-LRD-pH 9	80	20	None	0	9
PEO-LRD-pH 10	80	20	None	0	10
PEO-U-AR	80	0	UiO-66-NH_2	20	6 (not adjusted)
PEO-U-pH 8	80	0	UiO-66-NH_2	20	8
PEO-U-pH 9	80	0	UiO-66-NH_2	20	9
PEO-U-pH 10	80	0	UiO-66-NH_2	20	10
PEO-U-LRD-pH 8	60	20	UiO-66-NH_2	20	8
PEO-U-LRD-pH 9	60	20	UiO-66-NH_2	20	9
PEO-U-LRD-pH 10	60	20	UiO-66-NH_2	20	10
PEO-PCN	80	0	PCN-250	20	10
PEO-PCN-LRD	60	20	PCN-250	20	10
PEO-ZIF	80	0	ZIF-8	20	10
PEO-ZIF-LRD	60	20	ZIF-8	20	10
PEO-NU	80	0	NU-1000	20	10
PEO-NU-LRD	60	20	NU-1000	20	10

3. CHARACTERIZATION METHODS

3.1 Water isotherm

Water isotherms were conducted at 25 °C for each of the baseline MOFs, the polyethylene oxide powder, and the LRD powder to parameterize the relative wettability of each component for the solvent utilized in the synthesis. A sample of 20–30 mg of sorbent material was dried overnight in a convection oven at a temperature determined to be the maximum thermally stable temperature of the material to optimally remove water and solvent impurities. This was determined to be 50 °C for PEO, 80 °C for LRD, 120 °C for UiO-66-NH_2, NU-1000, and ZIF-8, and 200 °C for PCN-250. Once removed from the oven, the sample was placed in a desiccator and cooled to room temperature. It was then arranged as a monolayer into the sample holder to promote rapid mass transfer of water vapor from the bulk stream to the sample surface, and the sample holder was then attached to a Cahn™ Model D-200 microbalance. Water

was delivered from a saturator cell to a temperature-controlled microbalance containing the sorbent to be evaluated. The concentration of water vapor in the air stream (the relative humidity), was systematically increased (or decreased) by changing the temperature of the saturator cell in accordance with vapor pressure values calculated from the Antoine coefficients for water. By measuring the change in weight, the amount of water adsorbed on the material was calculated.

3.2 Scanning electron microscopy

SEM images were obtained using a Phenom ProX GSR desktop SEM. Samples were submerged in liquid nitrogen and cracked to form a clean break, and then mounted on double-sided carbon tape with the cracked edge facing upwards. Samples were scanned at 15 kV, analysis mode, and 1024 cm^{-1} resolution.

3.3 Nitrogen isotherm

Nitrogen isotherms were measured using a Micromeritics® ASAP™ 2420 analyzer at 77 kelvin. Samples were degassed at 50 °C under vacuum for approximately 16 hours. The Brunauer–Emmett–Teller (BET) theory was used to calculate specific surface area in $m^2\ g^{-1}$.

3.4 X-ray diffraction

XRD measurements were collected using a Rigaku MiniFlex600 X-ray powder diffractometer with a D/Tex detector. Samples were scanned at 40 kV and 15 mA, using Cu Kα radiation (λ = 1.54 Å) at a scan rate of 5° min^{-1} over a 2θ range of 2° to 50°. Zero-background discs were used for XRD measurements. A background correction was performed in the Rigaku PDXL software (version 2.1.3.6).

3.5 Fourier transform infrared

Attenuated total reflectance fourier transform infrared (ATR-FTIR) spectra of the baseline powders and composite films were obtained using a Bruker TENSOR 27 spectrometer. A wavenumber range of 400–4000 cm^{-1} was scanned at a resolution of 2 cm^{-1}.

3.6 Tensile strength

Tensile strength testing was performed in accordance with ASTM D882-02. Briefly, a 4-inch-by-0.5-inch strip of polymer film was cut and mounted into a tensiometer. Sample thickness was measured beforehand on a SEM using a vertically-mounted sample holder to view the film cross-section. The tensiometer grips overlapped the specimen by 1 inch on each side. Stress-strain curves were measured using a pull rate of 5 cm/min.

3.7 Thermogravimetric analysis

Thermogravimetric analysis (TGA) was conducted using a TA Instruments TGA Q500 analyzer. A temperature range of 25–600 °C was utilized with a nominal heating rate of 10 °C/min utilizing a dynamic high-resolution heating algorithm that more distinctly differentiates distinct thermal events occurring at similar temperatures than purely linear heating methods.

3.8 Differential scanning calorimetry

Differential scanning calorimetry (DSC) measurements were conducted on a TA Instruments SDT Q600 with aluminum pans. The temperature was ramped from 25 °C to 600 °C at a rate of 10 °C/min after an initial 10-minute hold at ambient temperature. Nitrogen was used as a carrier gas and flowed at 20 mL/min.

3.9 Small-angle neutron scattering

Small-angle neutron scattering (SANS) measurements were performed on the 30-m SANS NG7 instrument at the Center for Neutron Research at the National Institute of Standards and Technology (Gaithersburg, MD). Both 2D scans and azimuthal scans were performed on the films. In the 2D scans, both the spreading plane (typically designated as the x-z plane) and the sample edge plane (typically designated as the x-y plane) were scanned to give a visual of the platelet alignment in the films. Azimuthal scans parallel and perpendicular to the vector normal to the film spreading surface were conducted at an intensity of q = 0.003 $Å^{-1}$.

3.10 CEES microbreakthrough

Microbreakthrough testing of CEES was conducted on the films to gauge their ideal maximum capability for removal, as the transport phenomena involved in a microbreakthrough exposure ostensibly favor full utilization of the active material in the films. The apparatus and general procedure used has been previously described in literature.[21] Briefly, approximately 10–20 mg of composite film was cut into pieces that could pass through a size 20 sieve (0.1-mm size mesh) and loaded into a 4-mm i.d. fritted glass tube. The tube was loaded into a water bath so as to conduct testing isothermally at 20 °C. A flow rate was programmed through a saturator cell filled with neat CEES liquid and mixed with a diluent dry air stream at flow rates necessary to achieve 300 mg/m^3 concentration. The contaminated air stream was passed through the fritted glass tube. The effluent concentration was measured as a function of time using a gas chromatograph equipped with a photoionization detector. Data of effluent concentration versus time was integrated to determine the mass eluting the tube, and then subtracted from the total amount of feed to give the loading of the composite sample.

3.11 CEES and octane permeation

CEES and octane permeation testing were conducted in accordance with ASTM F739-12. Briefly, a 1.25-inch-by-1.25-inch segment of film was cut, weighed, and measured for thickness with a SEM, as outlined in Section 3.2, and placed in a 1-inch-diameter Pesce PTC 700 permeation test cell. An equal countercurrent flow of 0 % relative humidity and 300 mL min^{-1} air was applied to both sides of the swatch with a feed side concentration of 300 mg/m^3 of chemical. The chemical concentration was monitored at three locations in the PTC 700 cell—the inlet stream to the cell apparatus (designated as the feed line), the outlet stream from the cell apparatus (designated as the retentate line), and the outlet stream from the cell apparatus on the opposite side of the swatch (designated as the permeate line). The test was considered complete when the two outlet stream concentrations summed to equal the value of the feed concentration, closing the mass balance and satisfying the condition of the equation

$$C_{feed} - C_{retentate} - C_{permeate} = 0. \quad (1)$$

For octane, only the steady state permeation rate value was recorded. For CEES, both the steady state permeation rate and the loading of CEES in the membrane were tracked. The loading of CEES in the composite membrane was calculated analogously to the microbreakthrough loading, in that the difference between the feed and effluent concentrations was differentially integrated and divided by the product of the mass density of the film and the cross-sectional area of the film exposed to CEES to calculate the total mass of CEES adsorbed in the film.

3.12 Water vapor transport rate

Water vapor transport rate (WVTR) measurements through the swatches were conducted in accordance with the Water Method of ASTM E-96-16. Briefly, a swatch of material was sealed over a 1.75-cm-diameter container filled to a headspace of 0.5 inches with distilled water and placed in an environmentally-controlled chamber at 25 °C and 50 % relative humidity for 24 hours. The total mass of the apparatus was weighed before and after the exposure, and the mass difference was divided by the cross-sectional area of the top of the container and the exposure time to generate a WVTR value. The WVTR value was reported in units of grams of water lost per square meter of surface area exposed to the humidity gradient in the test system per hour of exposure time

4. RESULTS

4.1 SEM

SEM is a very useful tool for visualizing the dispersion on the MOF on the polymer substrate. It is ideal for the MOF to be evenly dispersed throughout the polymer substrate to avoid agglomeration and subsequent development of voids to occur. SEM images of all films are shown in Figure 2. It is seen for the PEO-LRD samples that surface roughness generally increases with a decrease in the pH, which may result from leaching of ions from the clay platelets. UiO-66-NH_2 was well-dispersed on the surface of the film at pH 8, but became more clustered on the surface at higher pH. This may be due to the decomposition of the MOF in this realm, thus generating an environment in which the MOF fragments lack the aminated moiety for binding to the polymer backbone. With films of UiO-66-NH_2 with LRD and PEO, as the pH of the film is increased from 8 to 10, the MOF became less evenly dispersed in the film. The UiO-66-NH_2 particles also appeared to be more clustered in the LRD composites than in the baseline PEO film. It was

shown that PCN-250 was reasonably dispersed in the baseline PEO film, but upon incorporation with LRD, it was more heterogeneously dispersed. Significant voids were also observed in the PEO-PCN film. Together, this suggested that low affinity exists between PCN and PEO and high affinity exists between PCN and LRD, all of which are contradictory to the desired scenario. ZIF-8 appeared to be better dispersed on the baseline PEO film. In a composite with PEO and LRD, the MOF appeared more clustered, possibly due to affinity of the ZIF-8 particles with the LRD platelets. NU-1000 appeared to remain better intact when combined with LRD than with simply PEO alone, as the rod-shaped particles appeared fragmented.

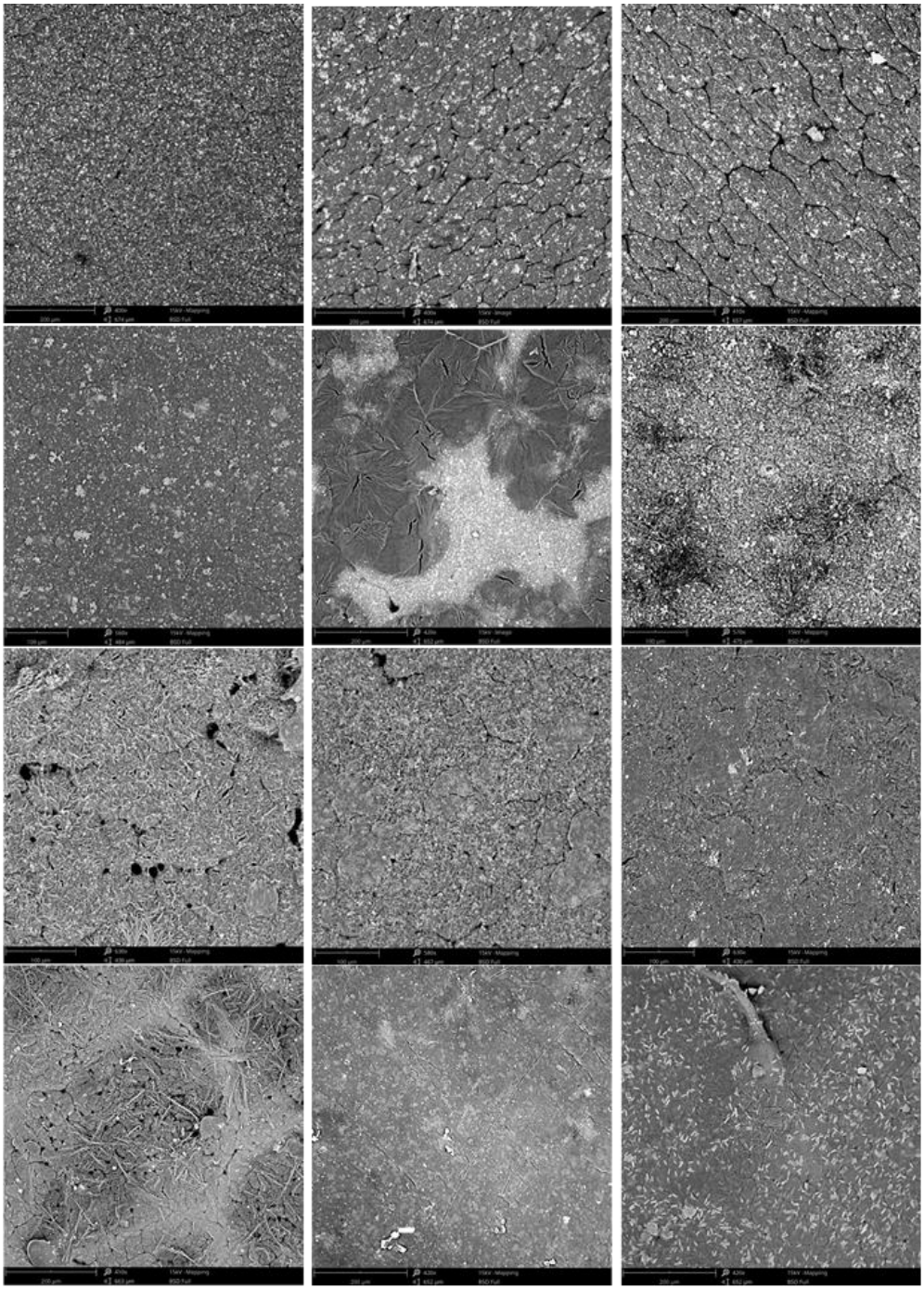

Figure 2. SEM images of (all specified from left to right) top row: PEO-U-pH 8, PEO-U-pH 9, and PEO-U-pH 10; second row: PEO-U-LRD-pH 8, PEO-U-LRD-pH 9, and PEO-U-LRD-pH 10; third row: PEO-PCN, PEO-ZIF, and PEO-NU; and fourth row: PEO-PCN-LRD, PEO-ZIF-LRD, and PEO-NU-LRD.

4.2 N_2 isotherm

BET surface areas of the composite membranes are depicted in Table 2. Baseline BET surface areas of powder-form UiO-66-NH_2, PCN-250, ZIF-8, NU-1000, and LRD were 1635 m^2/g, 1769 m^2/g, 1807 m^2/g, 1904 m^2/g, and 375 m^2/g, respectively. All of the UiO-66-NH_2-based films exhibited a lower surface area with their LRD analogues than the analogues without LRD, but the opposite trends were observed with the other three MOFs.

Table 2. Nitrogen isotherm data for films synthesized.

Sample	BET Surface Area (m^2/g)
PEO film	0.1
PEO-LRD-pH 8	2.7
PEO-LRD-pH 9	0.1
PEO-LRD-pH 10	2.3
PEO-U-AR	1.1
PEO-U-pH 8	1.9
PEO-U-pH 9	3.8
PEO-U-pH 10	2.9
PEO-U-LRD-pH 8	0.3
PEO-U-LRD-pH 9	2.1
PEO-U-LRD-pH 10	2.8
PEO-PCN	4.2
PEO-PCN-LRD	5.9
PEO-ZIF	6.0
PEO-ZIF-LRD	11.2
PEO-NU	1.5
PEO-NU-LRD	5.6

4.3 XRD

XRD was used as a complementary technique with FTIR to confirm preservation of the MOF, LRD, and PEO components within the composite framework of the films. With these systems, LRD is known to produce a diffraction pattern at a 2-theta value of 5 °.[20] Further, the PEO substrate is known to produce distinct peaks at 2-theta values of 20 ° and 23 °.[20] In this experiment, the PEO and LRD components were well-incorporated into the composite film at a pH of 9 or 10, but low structural integrity was observed at a pH of 8. As alluded to earlier, the LRD particles experienced leaching of magnesium and lithium ions at lower pH, and so this variable was likely at play in this range. Further, the natural pH of 5 % PEO in distilled water is around 9, so this range is acidic relative to the natural PEO environment and may serve to compromise the PEO structure as well. Additionally, a pH of 9 seems to be an optimal value for preserving both the PEO and LRD components. There was a hint of evidence of the MOF peak present in the as-received PEO-UiO-66-NH_2 film, which became depleted at pH of 8 and above. However, in the samples containing PEO, UiO-66-NH_2, and LRD, this peak was preserved in the pH 8 and pH 9 samples, indicating that presence of the clay filler component aided in preserving the stability of the MOF. Further, the peak corresponding to LRD was much better preserved in the pH 8 sample containing UiO-66-NH_2 than for the corresponding sample with just PEO and LRD at pH 8, suggesting that the added MOF aided in preserving the integrity of the platelets. However, the LRD peak at pH of 9 was not as strong as the baseline PEO-LRD-pH 9 sample, suggesting that full preservation of the MOF may be necessary for aiding in subsequent preservation of the LRD component.

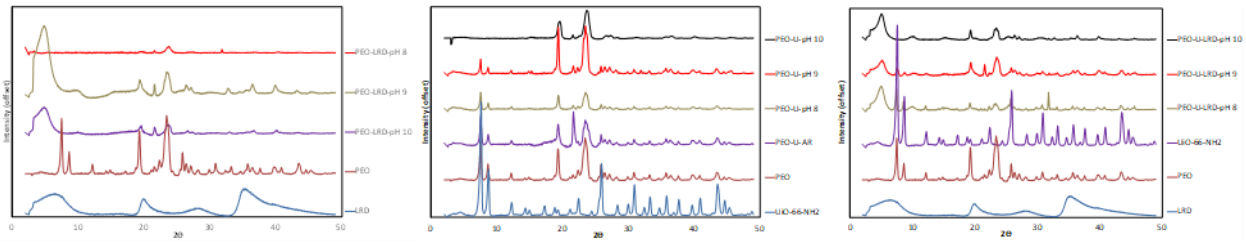

Figure 3. XRD patterns of baseline PEO-LRD and PEO-UiO-66-NH_2 films.

For the other MOFs, only a small amount of the PCN-250 component remained present in both PEO and PEO-LRD composite films, but the PEO and LRD peaks were preserved in all cases. ZIF-8 was present with both PEO alone and

PEO with LRD in the composite. LRD was also preserved in the composite; however, the peaks corresponding to ZIF-8 and PEO in the PEO-ZIF-LRD composite were greatly reduced, potentially indicating predominance of LRD on the surface of the film. The NU-1000 filler was maintained well in both the composite with PEO and the composite with PEO and LRD. The PEO structure was also maintained well in both composites, but the LRD peaks are scarcely present—possibly indicating that the alignment of the LRD component was greatly affected by incorporation of NU-1000 into the composite film.

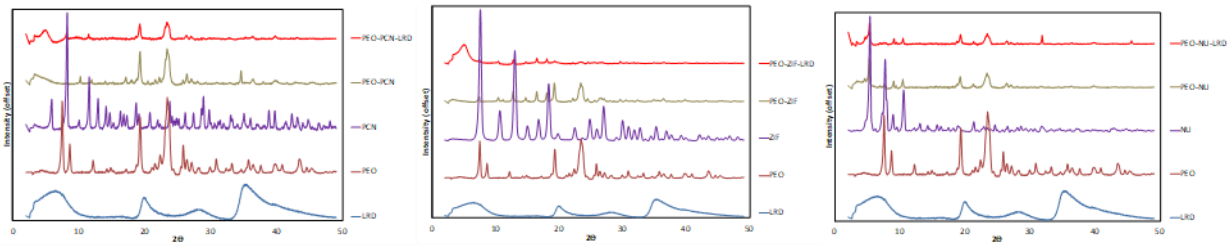

Figure 4. XRD patterns of PEO-PCN (left), PEO-ZIF (middle), and PEO-NU (right) films.

4.4 FTIR

FTIR can be used to assess the MOF-polymer binding environment and preservation of the MOF in general, as there is the potential for new peaks to form upon interaction with MOFs. The FTIR spectra of baseline PEO and PEO-LRD composites at pH values of 8, 9, and 10 are consistent with the XRD spectra in that the peaks corresponding to the PEO and LRD components show greatest integrity for the pH 9 samples. The characteristic peaks of LRD are greatly diminished in the pH 8 sample, reflecting that significant leaching of magnesium and lithium ions has occurred from the structure and compromised the platelet structural integrity. As expected, this peak sequentially diminishes in intensity with increasing pH and is completely depleted at pH of 10. In the composites of PEO, UiO-66-NH_2, and LRD, both the MOF and LRD components show signs of stability at pH values outside of their stable range observed in isolation, with MOF peaks still present at pH of 10 and LRD peaks still present at pH of 8.

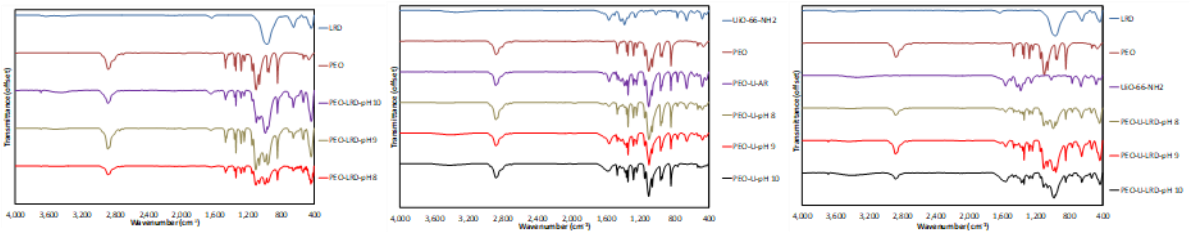

Figure 5. FTIR spectra of PEO-LRD and PEO-UiO-66-NH_2 films.

In the other MOFs, it is seen that PCN-250 is only faintly present in both composite films and that LRD is marginally incorporated in the composite as well, consistent with the XRD spectra. Results showed that ZIF-8 is heavily present in the composite film with PEO, but peaks for all three components are heavily truncated in the PEO-ZIF-LRD composite. This is consistent with the XRD patterns, which only showed significant presence of LRD. Presence of PEO, NU-1000, and LRD is maintained well in all composites. This suggests that the lack of characteristic LRD peaks in the XRD pattern for PEO-NU-LRD can be attributed to poor platelet alignment rather than dissolution.

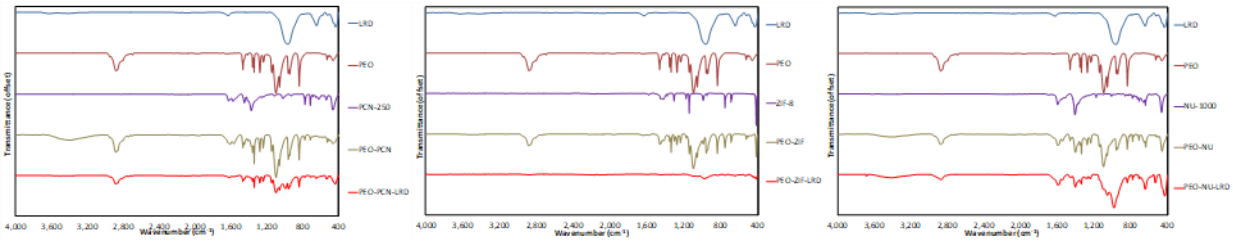

Figure 6. FTIR spectra for PEO-PCN (left), PEO-ZIF (middle), and PEO-NU (right) films.

4.5 TGA

TGA was conducted to gauge the thermal stability of the composite membranes. It is seen that PEO-LRD composite films at pH of 9 and 10 have a higher thermal decomposition temperature than baseline PEO, with the pH 9 film exhibiting the greatest thermal stability, and the PEO-LRD-pH 8 film having a lower stability than the baseline film. This supports the XRD and FTIR data and suggests that the clay platelets are not well incorporated into the PEO structure at this lower pH, possibly existing in a dissolved state due to leaching of magnesium ions from the clay that is known to occur in this regime. If leaching and dissolution of the platelets is indeed occurring, this effect appears to compromise the thermal stability of the composite to the extent that it exhibits a lower decomposition temperature than the baseline PEO film.

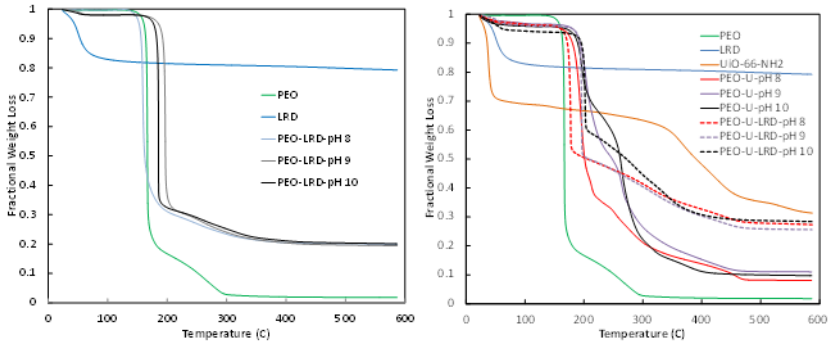

Figure 7. TGA profiles for PEO-LRD (left) and PEO-UiO-66-NH_2 (right) films.

In contrast to the films with solely PEO and LRD, the composites with PEO, UiO-66-NH_2, and LRD all exhibited a higher decomposition temperature than the baseline PEO, at all pH values evaluated. In comparison to the films with just PEO and UiO-66-NH_2, the PEO-U-LRD composite films show lower thermal stability at pH 8 and pH 9 and slightly higher stability at pH 10. This suggests that UiO-66-NH_2 enhances the thermal stability of the composite film but does not display a synergistic thermal stability effect with LRD. All films containing PCN-250 exhibit a lower decomposition temperature than the baseline PEO film, with the composite of PEO, PCN-250, and LRD exhibiting the lowest thermal stability. This suggests that PCN-250 does not integrate favorably with PEO or LRD. Presence of ZIF-8 alone in PEO enhanced the thermal stability of the composite film to a greater extent than presence of LRD alone, but the composite of ZIF-8 and LRD in PEO had a lower decomposition temperature than the baseline PEO film. This suggested high affinity between the two filler components, which is undesirable for cofillers in a polymeric matrix. This is consistent with previous literature data where ZIF-8 and the zeolite silicate-1 (a high-SiO_2-based filler, as is LRD), were deemed to be too chemically similar to be synergistic fillers. Presence of both NU-1000 and LRD in the PEO membrane, separately, enhances the thermal stability, with the PEO-LRD composite having a higher decomposition temperature than the PEO-NU composite. However, when both fillers are combined, the composite thermal stability is lower than that of the baseline PEO film.

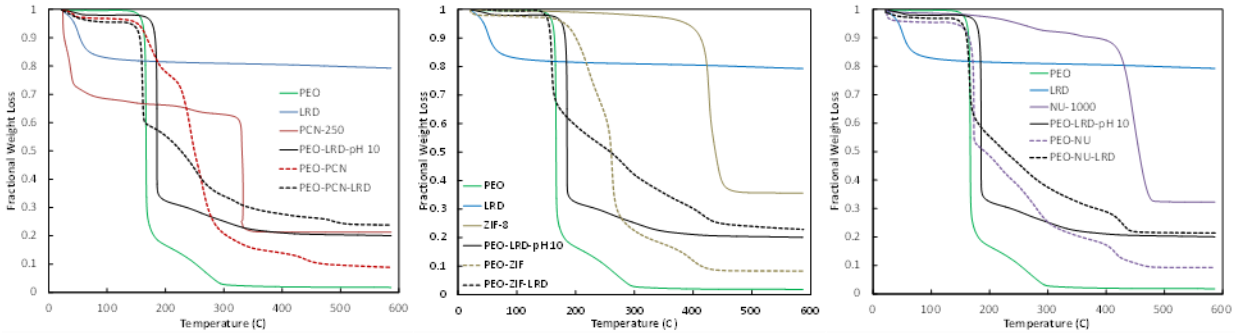

Figure 8. TGA profiles for PEO-PCN (left), PEO-ZIF (middle), and PEO-NU (right) films.

4.6 DSC

The endotherms from DSC on the baseline PEO and baseline PEO-LRD composite samples are shown in Figure 9. Integration of the endotherms, applying an appropriate correction factor for the weight fraction of polymer in the films,

yields the crystallization enthalpy of the composite membranes. Dividing these values by the crystallization enthalpy for the pure PEO film yields percent crystallinities of 90.8, 91.2, and 98.1 for the PEO-LRD films at pH 10, 9, and 8, respectively, with the literature crystallization percentage of PEO-LRD(20 %)-pH 10 reported around 94 %. This supports the TGA results and confirms that, at pH of 8, connectivity between the polymer and clay components alone is greatly diminished, likely due to partial dissolution of the clay.

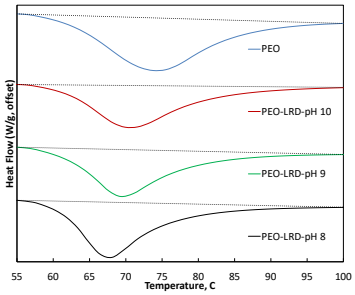

Figure 9. DSC endotherm at the literature crystallization temperature for PEO-LRD films.

4.7 Tensile strength

Tensile strength testing was conducted on all films to monitor changes in the mechanical integrity of the composite films from addition of filler. It is shown in Table 3 that, for the baseline films containing PEO and LRD, the maximum load reaches a relative maximum at pH of 9, consistent with the TGA data suggesting higher overall stability of the polymer-clay composite at this pH. Percent elongation increased moving down from pH of 10 to pH of 8, increasing increase in elasticity of the composite film going down in pH. Maximum load and percent elongation are, together, used to indicate the overall toughness of a material. For the films containing solely MOF and PEO, only the film with UiO-66-NH_2 at pH of 8 exhibits higher values of these parameters than the baseline PEO film. For the films containing the other three MOFs, it is seen that the Young's modulus and maximum load are higher for all the composite films that do not contain LRD. Further, the percent elongation values are higher for the films containing LRD for all the MOFs except NU-1000.

Table 3. Tensile strength data for all PEO-based films.

Sample	Maximum Load (N)	% Elongation	Young's Modulus (MPa)
PEO	11.59	151.6	408.4
PEO-LRD-pH 8	5.87	723.6	296.0
PEO-LRD-pH 9	10.43	433.3	471.7
PEO-LRD-pH 10	5.64	49.7	164.1
PEO-U-pH 8	15.74	873.1	833.1
PEO-U-pH 9	4.04	220.7	117.7
PEO-U-pH 10	12.55	38.8	85.8
PEO-U-LRD-pH 8	2.37	163.9	565.7
PEO-U-LRD-pH 9	7.51	173.4	497.3
PEO-U-LRD-pH 10	6.99	148.3	461.0
PEO-PCN	2.84	37.6	375.2
PEO-PCN-LRD	2.75	63.3	288.1
PEO-ZIF	1.21	64.6	166.0
PEO-ZIF-LRD	0.66	290.7	141.1
PEO-NU	5.41	20.9	532.5
PEO-NU-LRD	0.48	13.3	239.0

4.8 SANS

Both the 2D scans (Figure 10) and azimuthal SANS profiles (Figure 11) show high anisotropy in the baseline PEO-LRD films, particularly with the analogues synthesized at pH of 9 and pH of 8. This confirms successful reproduction of the literature synthesis and alignment results for the PEO-LRD system. It is interesting to note the PEO-LRD analogue synthesized at pH of 8 exhibits strong anisotropy despite having low connectivity to the polymer, suggesting that only minimal bonding between the two moieties is necessary to achieve shear-based alignment in the system during the synthesis.

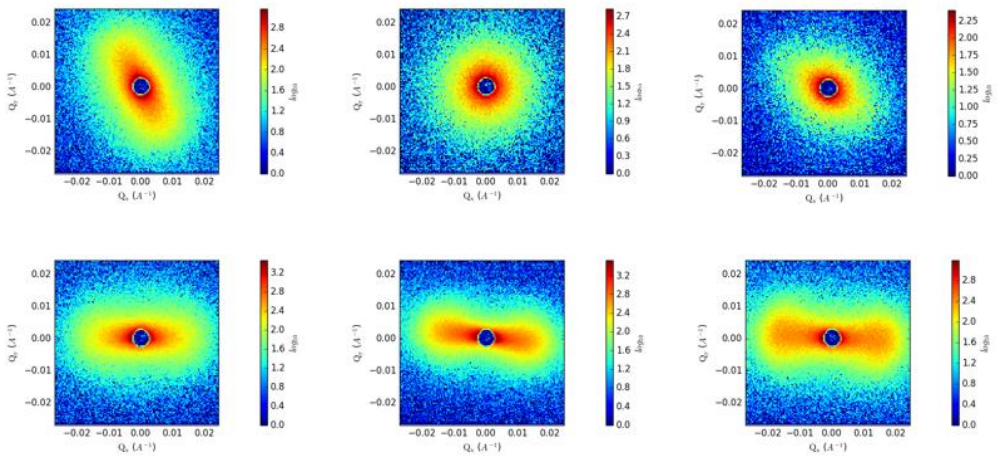

Figure 10. Top view (top row) and side view (bottom row) 2D SANS data of (left to right) PEO-LRD-pH 10, PEO-LRD-pH 9, PEO-LRD-pH 8 films.

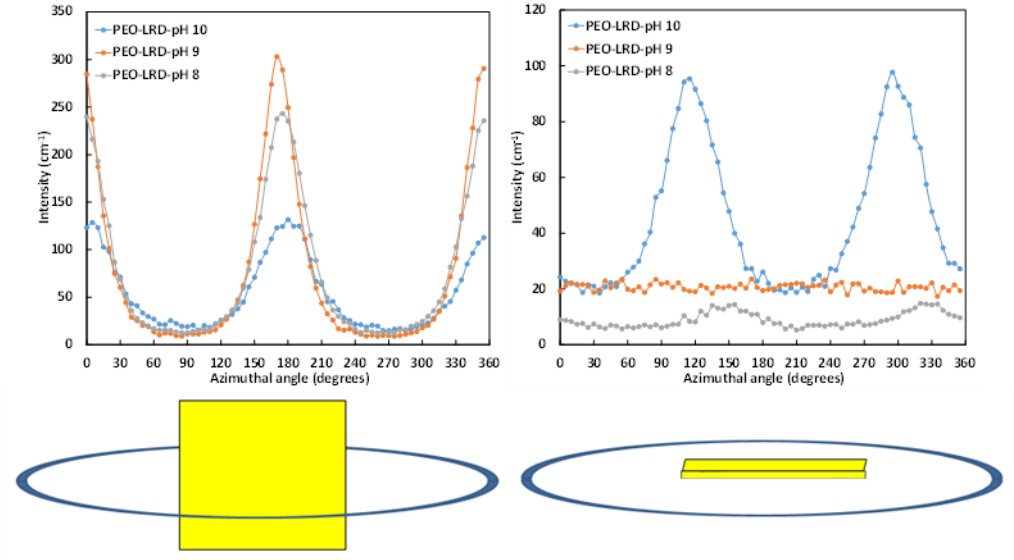

Figure 11. SANS azimuthal scans of PEO-LRD films in the parallel (left) and perpendicular (right) planes.

4.9 Octane permeation

Octane permeation testing was conducted on the samples in an effort to gauge the relative length of the diffusion path of an inert gas-phase permeant of similar molecular dimensions as CEES. As with CEES and mustard gas, octane is a linear molecule with a very similar van der Waals volume, as calculated from known correlations.[22] This roughly gauges the effectiveness of filler incorporation in the composite films, and ideal incorporation of the platelets would result in a greatly elongated diffusion path of octane through the composite film.

Several trends are observed from the data. Interestingly, the PEO-LRD composite prepared at pH of 10 observed the lowest tortuosity factor relative to baseline PEO of all three baseline PEO-LRD samples, with the composite at a pH of showing the highest tortuosity. This may be an artifact of agglomeration of the clay filler in this sample. Further, all samples containing UiO-66-NH_2 displayed an increased tortuosity factor when decreasing the pH from 10 to 9 to 8. This is logical, as the structural integrity of the UiO-66-NH_2 component is preserved to a greater extent as the pH is reduced and maintaining the integrity of the second filler component will generate a greater amount of filled space within the void regions of the polymer for octane to diffuse around. Further, the composite films with UiO-66-NH_2 and LRD all showed a greater tortuosity factor than the corresponding films without MOF, suggesting favorable dispersion of the two filler components. Finally, notable conclusions were found when comparing tortuosity effect across the different MOFs. UiO-66-NH_2 and ZIF-8 were able to generate a significant synergistic tortuosity effect when combined with LRD, PCN-250 only generated a moderate effect, and NU-1000 actually generated a lower

tortuosity factor in combination with the platelet filler than with the MOF alone. This would reflect the XRD and SEM data in that the more intact NU-1000 particles combined with LRD platelets that are not well-aligned actually impede the diffusion path to a lesser extent than the fragmented NU-1000 particles alone.

Table 4. Tortuosity factors of films synthesized.

Sample	Tortuosity factor relative to baseline PEO	Tortuosity factor relative to analogue without LRD
PEO-LRD-pH 8	268.3	-
PEO-LRD-pH 9	838.5	-
PEO-LRD-pH 10	4.2	-
PEO-U-pH 8	4.5	-
PEO-U-pH 9	5.3	-
PEO-U-pH 10	0.5	-
PEO-U-LRD-pH 8	1376.1	303.6
PEO-U-LRD-pH 9	1064.8	202.4
PEO-U-LRD-pH 10	383.3	766.7
PEO-PCN	0.3	-
PEO-PCN-LRD	3.7	12.8
PEO-ZIF	3.4	-
PEO-ZIF-LRD	575.0	169.1
PEO-NU	6.6	-
PEO-NU-LRD	2.5	0.4

4.10 WVTR

WVTR data are shown in Table 5. It is noted here that only the films containing LRD could be evaluated with this technique. As PEO is highly soluble in water, all baseline films not containing the LRD filler displayed noticeable loss of structural integrity for this test. Therefore, an immediate structural integrity benefit was displayed for all films through incorporation of LRD platelets. Values are similar for all films with the exception of PEO-U-LRD-pH 9 and PEO-ZIF-LRD. The SEM images show that PEO-U-LRD-pH 9 has significantly heterogenous dispersion of MOF on the surface, and the MOF regions may prove to aid in facilitating diffusion of water molecules through the composite. For PEO-ZIF-LRD, the highly hydrophobic nature of the MOF component may aid in preventing water from penetrating through the film.

Table 5. WVTR data for LRD-containing films.

Sample	WVTR ($g/m^2/hr$ per 100-µm film thickness)
PEO-LRD-pH 8	19.5
PEO-LRD-pH 9	17.7
PEO-LRD-pH 10	18.9
PEO-U-LRD-pH 8	15.0
PEO-U-LRD-pH 9	29.5
PEO-U-LRD-pH 10	19.7
PEO-PCN-LRD	13.4
PEO-ZIF-LRD	8.8
PEO-NU-LRD	15.5

4.11CEES permeation and microbreakthrough

Steady-state permeation rate values of CEES through the membranes are shown in Table 6 and compared to octane tortuosity factors to gauge any differences in trends. Generally, CEES steady-state permeation rates reflect the octane tortuosity factor data in that higher tortuosity factors resulted in lower steady-state permeation rates of CEES through the composite membranes.

Table 6. CEES steady-state permeation rates of films synthesized, normalized to 100-µm thickness.

Film	CEES steady-state permeation rate (µg/cm²/min)
PEO	0.259
PEO-LRD-pH 10	0.000
PEO-LRD-pH 9	0.000
PEO-LRD-pH 8	0.035
PEO-U-pH 10	6.050
PEO-U-pH 9	1.170
PEO-U-pH 8	0.360
PEO-U-LRD-pH 10	0.000
PEO-U-LRD-pH 9	0.000
PEO-U-LRD-pH 8	0.045
PEO-PCN	10.632
PEO-PCN-LRD	0.253
PEO-ZIF	1.370
PEO-ZIF-LRD	0.117
PEO-NU	2.450
PEO-NU-LRD	2.121

Microbreakthrough and permeation loadings of CEES in all the composite films are shown in Table 7, along with the standard deviations calculated to assign relative confidence intervals to the data. Results of the average values of the tests for all composite films are shown in Figure 12. All tests were performed in a minimum of three replicates to establish confidence intervals to the data.

Table 7. CEES permeation and microbreakthrough loadings of films synthesized, with standard deviations included.

Film	CEES Micro Loading (mol/kg)	Micro Stand. Dev. (+/-, mol/kg)	CEES Perm Loading (mol/kg)	Perm. Stand. Dev. (+/-, mol/kg)	Perm to Micro Ratio
PEO	0.0332	0.0047	0.0048	0.0028	0.144
PEO-LRD-pH 10	0.0370	0.0100	0.0015	0.0010	0.041
PEO-LRD-pH 9	0.0220	0.0150	0.0021	0.0020	0.096
PEO-LRD-pH 8	0.0300	0.0100	0.0018	0.0010	0.060
PEO-U-pH 10	0.0673	0.0195	0.0026	0.0022	0.038
PEO-U-pH 9	0.0850	0.0080	0.0127	0.0034	0.150
PEO-U-pH 8	0.1050	0.0160	0.0043	0.0031	0.041
PEO-U-LRD-pH 10	0.0597	0.0160	0.0038	0.0020	0.063
PEO-U-LRD-pH 9	0.0774	0.0160	0.0055	0.0053	0.071
PEO-U-LRD-pH 8	0.1040	0.0240	0.0903	0.0475	0.869
PEO-PCN	0.1080	0.0110	0.0096	0.0041	0.088
PEO-PCN-LRD	0.1490	0.0100	0.0089	0.0068	0.060
PEO-ZIF	0.1950	0.0320	0.0110	0.0041	0.057
PEO-ZIF-LRD	0.1180	0.0060	0.0202	0.0024	0.171
PEO-NU	0.2620	0.0090	0.0883	0.0309	0.337
PEO-NU-LRD	0.2130	0.0350	0.0358	0.0094	0.168

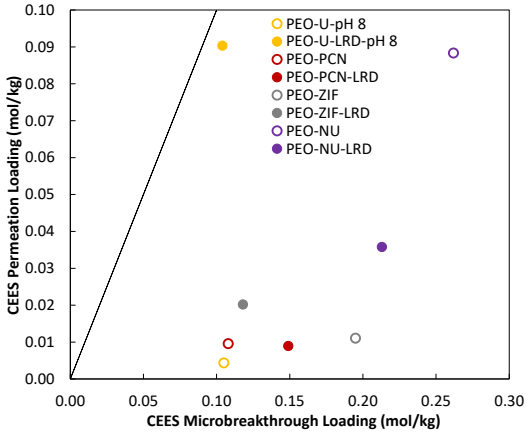

Figure 12. Plot of average permeation and average microbreakthrough loadings for MOF-containing films.

While the loading values are all very small for the MOF-containing films, notable trends can be discerned upon close examination of the data. It is seen that the incorporation of LRD filler into the films can have a distinctly different effect depending on the MOF utilized. The LRD may circumstantially have a deleterious effect on overall potential of the film for removing toxic chemical, as represented in the microbreakthrough loading. This may be a rough parameterization of the affinity of the MOF to the clay and is certainly anticipated for ZIF-8, as it has shown high affinity for the zeolite filler silicate-1, chemically similar to LRD, in previous studies upon incorporation into a polymer film. Further, it is apparent that the overall removal of the film in permeation applications can be either greatly hindered or greatly enhanced upon incorporation of the filler, but via different criteria than the microbreakthrough trends.

Full elucidation of this requires thorough consideration of the governing transport phenomena in permeation experiments. As diffusion is the dominant mechanism, one naturally would conclude that a longer diffusion path would favor greater interaction with the active material in the film. Therefore, this relationship was considered by plotting the fractional difference in permeation loading upon filler incorporation in the PEO-MOF films versus fractional difference in the octane steady state permeation rate (parameterized via the octane tortuosity factor), as shown in Figure 13. Results reveal a strong trend suggesting that, indeed, it is this tortuosity factor that governs the utilization of the active material in permeation experiments.

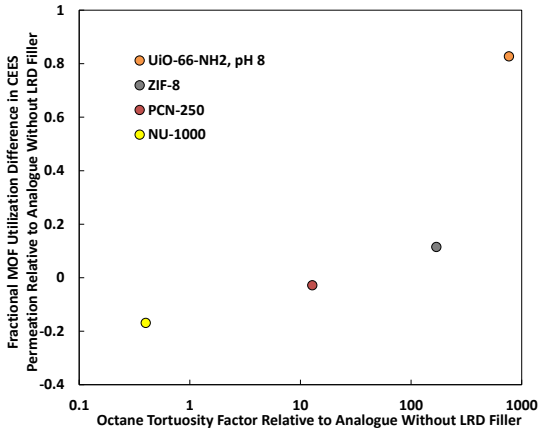

Figure 13. Plot of fractional utilization difference in CEES permeation to microbreakthrough loading ratio for MOF-LRD samples compared to non-LRD analogues versus fractional difference in octane tortuosity factor for MOF-LRD samples compared to non-LRD analogues.

5. CONCLUSIONS

A series of MOFs were incorporated into the known PEO-LRD system to investigate the ability for enhancing mechanical and permeation properties of the composite. While TGA and tensile strength data reveal that none of the

MOFs exhibit full thermal and mechanical synergy with LRD as the filler, notable trends are observed with broad implications. First, it is shown through FTIR and XRD that, selectively, incorporation of MOF into the PEO-LRD composite can extend the pH stability range at which the LRD platelets are structurally intact. This is paramount for consideration for more detailed studies into this system and suggests that synthesis conditions can be selectively relaxed from the previously rigid guidelines in literature, enhancing opportunities for consideration of additional MOFs into the framework that could not survive the standard pH of synthesis conditions.

Further, it is found through permeation and breakthrough experiments that a direct relationship does indeed exist between tortuosity factor and fractional utilization of active component in the PEO-MOF films. It is elucidated that a tortuosity factor of 10^2 to 10^3, corresponding to a reduction in the steady-state permeation rate of octane that is two to three orders of magnitude lower than that of the baseline polymer, may promote a suitable diffusion path for proper interaction of gas-phase permeant with active material. Future efforts in this study should involve elucidating the full range of baseline conditions under which the PEO-LRD system will align. Namely, utilization of solvents other than water will ultimately be essential for incorporation of the wide range of MOFs into the framework, as the limited water stability of many MOFs greatly limits possibilities when maintaining distilled water as the solvent of choice.

ACKNOWLEDGMENTS

Funding was provided by the Director, Edgewood Chemical Biological Center under the authorities and provisions of Section 2363 of the FY 2018 NDAA to develop new technologies, engineer innovations, and introduce game-changing capabilities.

REFERENCES

[1] Carrera, M.C.; Erdmann, E.; Destefanis, H.A. Barrier Properties and Structural Study of Nanocomposite of HDPE/Montmorillonite Modified with Polyvinylalcohol. *J. Chem.* **2013,** *2013*, pp 1–7.

[2] Nielsen, L.E. Models for the Permeability of Filled Polymer Systems. *J. Macromol. Sci., Part A: Pure Appl.Chem.* **1967,** *1* (5), pp 929–942.

[3] Duncan, T.V. Applications of nanotechnology in food packaging and food safety: barrier materials, antimicrobials and sensors. *J. Colloid Interface Sci.* **2011,** *363* (1), pp 1–24.

[4] Krishnamoorti, R.; Vaia, R.A.; Giannelis, E.P. Structure and dynamics of polymer-layered silicate nanocomposites. *Chem. Mater.* **1996,** *8* (8), pp 1728–1734.

[5] Woo, R.S.C.; Zhu, H.; Chow, M.M.K.; Leung, C.K.Y.; Kim, J.-K., Barrier performance of silane–clay nanocomposite coatings on concrete structure. *Compos. Sci. Technol.* **2008,** *68* (14), pp 2828–2836.

[6] Aranda, P.; Ruiz-Hitzky, E. Poly(ethylene oxide)-silicate intercalation materials. *Chem. Mater*. **1992,** *4* (6), pp 1395–1403.

[7] Loizou, E.; Butler, P.; Porcar, L.; Kesselman, E.; Talmon, Y.; Dundigalla, A.; Schmidt, G. Large scale structures in nanocomposite hydrogels. *Macromolecules.* **2005,** *38* (6), pp 2047–2049.

[8] Thuresson, A.; Segad, M.; Turesson, M.; Skepo, M. Flocculated Laponite-PEG/PEO dispersions with monovalent salt, a SAXS and simulation study. *J. Colloid Interface Sci*. **2016,** *466*, pp 330–342.

[9] Tawari, S.L.; Koch, D.L.; Cohen, C. Electrical Double-Layer Effects on the Brownian Diffusivity and Aggregation Rate of Laponite Clay Particles. *J. Colloid Interface Sci*. **2001,** *240* (1), pp 54–66.

[10] Michot, L.J.; Bihannic, I.; Thomas, F.; Lartiges, B.S.; Waldvogel, Y.; Caillet, C.; Thieme, J.; Funari, S.S.; Levitz, P. Coagulation of Na-montmorillonite by inorganic cations at neutral pH. A combined transmission X-ray microscopy, small angle and wide angle X-ray scattering study. *Langmuir*. **2013,** *29* (10), pp 3500–3510.

[11] Yaghi, O.M.; O'Keeffe, M.; Ockwig, N.W.; Chae, H.K.; Eddaoudi, M.; Kim, J. Reticular synthesis and the design of new materials. *Nature.* **2003,** *423* (6941), pp 705–714.

[12] DeCoste, J.B.; Peterson, G.W. Metal-organic frameworks for air purification of toxic chemicals. *Chem. Rev.* **2014,** *114* (11), pp 5695–5727.

[13] Mondal, S.S.; Holdt, H.J. Breaking Down Chemical Weapons by Metal-Organic Frameworks. *Angew. Chem. Int. Ed. Engl.* **2016,** *55* (1), pp 42–44.

[14] Liu, Y.Y.; Howarth, A.J.; Vermeulen, N.A.; Moon, S.Y.; Hupp, J.T.; Farha, O.K. Catalytic destruction of chemical warfare agents and their stimulants by metal-organic frameworks. *Coord. Chem. Rev*. **2017,** *346*, pp 101–111.

[15] Yehia, H.; Pisklak, T.J.; Ferraris, J.P.; Balkus, K.J.; Musselman, I.H. Methane Facilitated Transport Using Copper(II) Biphenyl Dicarboxylate-Triethylenediamine/Poly (3-Acetoxyethylthiophene) Mixed Matrix Membranes, *Presented at the 227th National Meeting of the American Chemical Society, 28 March–1 April 2004*, *Anaheim, CA;* published in *Polym. Prepr*. **2004,** *45* (1), pp 35–36.

[16] Webster, C.E.; Drago, R.S.; Zerner, M.C. Molecular dimensions for adsorptives. *J. Am. Chem. Soc.* **1998,** *120* (22), pp 5509–5516.

[17] Ploskonka, A.M.; DeCoste, J.B. Tailoring the Adsorption of Reaction Chemistry of the Metal Organic Frameworks UiO-66, UiO-66-NH_2, and HKUST-1 via the Incorporation of Molecular Guests. *ACS Appl. Mater. Interfaces.* **2017,** *9* (25), pp 21579–21585.

[18] Mondloch, J. E.; Bury, W.; Fairen-Jimenez, D.; Kwon, S.; DeMarco, E. J.; Weston, M. H.; Sarjeant, A. A.; Nguyen, S. T.; Stair, P. C.; Snurr, R. Q.; Farha, O. K.; Hupp, J. T., Vapor-phase metalation by atomic layer deposition in a metal-organic framework. *J. Am. Chem. Soc.* **2013,** *135* (28), pp 10294–10297.

[19] Asha, P.; Sinha, M.; Mandal, S. Effective removal of chemical warfare agent stimulants using water stable metal-organic frameworks: mechanistic study and structure-property correlation. *RSC Adv.* **2017,** *7* (11), pp 6691–6696.

[20] Stefanescu, E.A.; Schexnailder, P.J.; Dundigalla, A.; Negulescu, I.I.; Schmidt, G. Structure and thermal properties of multilayered Laponite/PEO nanocomposite films. *Polymer.* **2006**, *47* (21), pp 7339–7348.

[21] Glover, T.G.; Peterson, G.W.; Schindler, B.J.; Britt, D.; Yaghi, O. MOF-74 building unit has a direct impact on toxic gas adsorption. *Chem. Eng. Sci.* **2011,** *66* (2), pp 163–170.

[22] Zhao, Y.H.; Abraham, M.H.; Zissimos, A.M. Fast calculation of van der Waals volume as a sum of atomic and bond contributions and its application to drug compounds. *J. Org. Chem.* **2003,** *68* (19), pp 7368–7378.

Impact of metal-organic framework pore size on the diffusion of toxic industrial chemicals and chemical warfare agent simulants measured by concentration-swing frequency response

Trenton M. Tovar, Jared B. DeCoste*
U.S. Army Edgewood Chemical Biological Center, Research & Technology Directorate,
8198 Blackhawk Rd, Aberdeen Proving Ground, MD 21010

ABSTRACT

A set of general predictive parameters is desired to help determine which metal-organic frameworks to explore for protection from toxic compounds. This study aims to provide guidance on minimum required pore sizes for effective mass transfer. A series of isoreticular metal-organic frameworks with varying pore sizes—UiO-66-N, UiO-66, and UiO-67—were synthesized in single-crystal form for diffusion studies. Diffusion of two hydrocarbons—*n*-octane and β-pinene—with molecular sizes similar to certain chemical warfare agents was measured using concentration-swing frequency response. This type of system parameterization eliminates the impact of different intermolecular interactions on diffusion as a variable and looks only at the impact of pore size. For octane diffusion, UiO-66 and UiO-67 are similar, but the functionalized UiO-66-N shows significantly reduced diffusivity. Even when the larger β-pinene molecule is tested, still no significant differences in diffusivity were found between UiO-66 and UiO-67.

Keywords: metal-organic frameworks, UiO-66, micropore diffusion, hydrocarbons, single crystal

1. INTRODUCTION

Highly toxic compounds such as toxic industrial chemicals (TIC) and chemical warfare agents (CWA) pose significant risks to society. These risks can come from state sanctioned warfare, terrorist threats, or industrial accidents. Development of protective equipment for soldiers or first responders at these types of incidents is a key goal of the military. The most widely deployed protective measure from chemical attacks is the gas mask. The development of military respirators began shortly after the use of Cl_2 gas as a weapon during World War I. Despite a century of research, the adsorbent material, which is the key component of gas mask filters, has almost exclusively been based on activated carbons.

The difficulty in developing new adsorbent materials for military respirators is the requirement to effectively filter a wide array of possible threats with very different chemical properties. Metal-organic frameworks (MOF) are a new class of porous material with the potential to replace carbon adsorbents. One of the biggest advantages of MOFs over other adsorbents is the high degree of chemical tunability by varying the metal nodes or organic linkers.[1] Many functionalities can also be incorporated post-synthetically to further enhance adsorption properties.[2] These properties have led to significant research efforts on developing MOFs for filtration of toxic chemicals from air.[3]

Since filtration is a dynamic process, mass transfer can significantly impact performance. Figure 1 shows the impact mass transfer can have on the breakthrough of an adsorbent bed. Due to bed depth restraints on a gas mask, slow adsorption kinetics could lead to instantaneous breakthrough. Thus, in order to rationally design a MOF for use in a gas mask, it is critically important to understand its diffusional properties. Due to the large number of reported MOF structures and the inherent dependence of diffusion on both the adsorbate as well as the adsorbent, the bulk of diffusion studies on MOFs have been computational.[4,5] While molecular dynamics (MD) simulations are an important tool for understanding the intermolecular interactions that govern the behavior in an adsorbate-adsorbent system, the force fields used have limitations for quantitative predictions,[6] particularly due to difficulties in calculating atomic charges within MOF structures.[7] While there have been experimental diffusion studies on MOFs, the adsorbates of interest have mainly been confined to those relevant for industrial separations such as H_2,[8] CH_4,[9] CO_2,[10] and low molecular weight hydrocarbons.[6] Experimentally measured diffusion rates of TICs and CWAs in MOFs is non-existent in the literature.

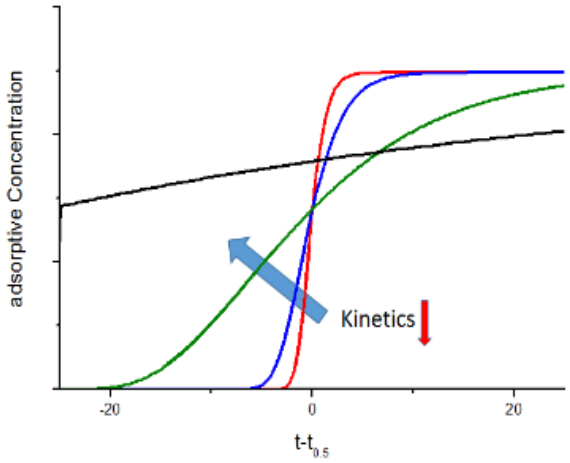

Figure 1. Dependence of breakthrough curves on mass transfer.

The measurement of diffusion rates in porous materials is a complex problem due to the presence of multiple mass transfer mechanisms that are dependent on adsorbent morphology. In micropores, intermolecular interactions and steric effects dominate surface diffusion. While in macropores, surface forces play very little role and mass transfer is controlled by collisions between adsorbate molecules. Intermediate size mesopores create a transitional area where surface forces are not yet dominant but collisions between the adsorbate and the adsorbent surface can result in Knudsen diffusion. Sometimes, the outermost surface of a particle may have collapsed or blocked pores, creating a barrier resistance. For multi-component systems, there is also the possibility of external resistance through a fluid film boundary layer. Temperature gradients generated by heat of adsorption can also complicate measurements. For any given system, the overall mass transfer rate can be the result of multiple mechanisms. Due to this complexity, many experimental techniques have been developed to measure diffusion rates including NMR, quasi-elastic neutron scattering, uptake rates, chromatography, differential adsorption bed, zero-length column, and frequency response.[11]

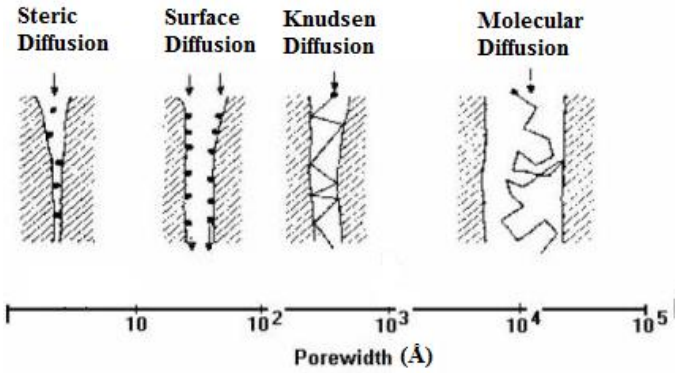

Figure 2. Visualization of steric hindrance, surface diffusion, Knudsen diffusion, and molecular diffusion in different pore sizes.

Frequency response (FR) is a perturbation technique which introduces small, typically sinusoidal, oscillations around the equilibrium set point of a system variable. The response of a second variable is measured, and mass transfer data can be extracted through a mathematical model in Laplace space. As the periodic measurements are not dependent on initial conditions, experimental error is reduced, and data are highly reproducible. FR is a powerful technique as it introduces an additional degree of freedom, with measurements taken over a range of frequencies, which helps decouple the impacts of multiple diffusive mechanisms, allowing for determination of a rate-limiting mass transfer mechanism.[12] The batch volume-swing FR technique was used extensively by Yasuda to study adsorption and diffusion in zeolites.[13] Flow-through FR methods, like pressure-swing (PSFR) and concentration-swing (CSFR), have the advantages of reduced heat effects due to convective cooling and operating over pressure ranges relevant to ambient conditions. While PSFR has been useful for studying diffusion in carbon molecular sieves, zeolites, activated carbons, and MOFs, it can only be used to study pure component systems. The relevant conditions for studying

diffusion of TICs and CWAs would be in dilute systems at ambient pressure, which can be done using CSFR. Previously, CSFR has been used to measure diffusion in MOF single crystals[14] and in pelletized MOF particles.[15]

In this work, we will explore the impact of MOF pore size on mass transfer. There are many types of MOFs with different pore sizes and topologies that could potentially be used. Of interest to the Army is the Zr-based UiO series of MOFs. The UiO family is highly stable, where pore size can be controlled by varying linker lengths which creates an isoreticular topology with a variation in pore size. Two such MOFs are UiO-66 and UiO-67 which have cage window openings of approximately 7 Å and 12 Å, respectively. In addition to those, the functionalized UiO-66-naphthalene (UiO-66-N), which has an aromatic ring that can reduce the pore space, was also studied. Figure 3 shows the pore topology of the MOFs and the size of the linkers used. While the ultimate goal is to understand mass transfer of toxic compounds, an approach using hydrocarbons was used in order to limit the impact of intermolecular interactions and explore only the steric effects. The two adsorbates in this work, also shown in Figure 3, are the linear hydrocarbon *n*-octane and a terpene β-pinene. When comparing data sets of each adsorbate on the UiO series of MOFs, we hypothesized that there will be a step increase in diffusion rate as a function of pore size that indicates the minimum pore size necessary for effective diffusion. This information could lead to some generic design rules for MOFs used to filter toxic chemicals.

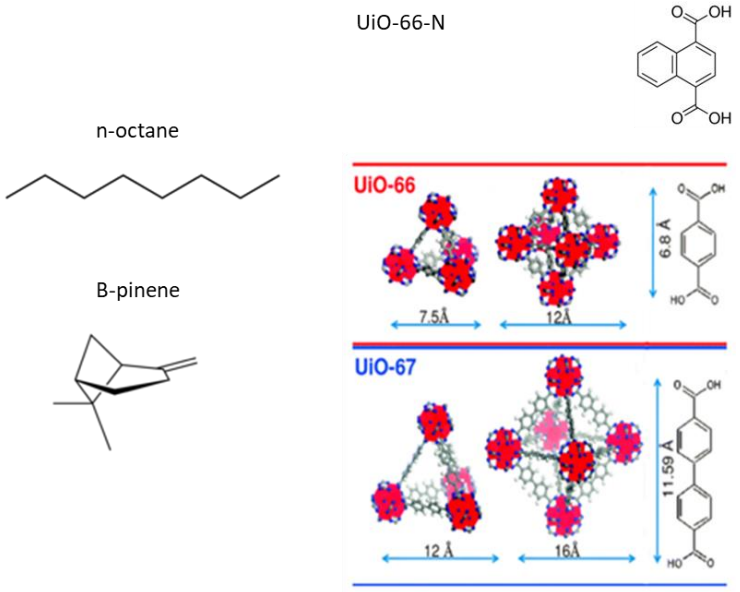

Figure 3. Image of the linkers and pore structure of UiO-66-N, UiO-66, and UiO-67. The chosen adsorbates are also shown (not to scale).

2. EXPERIMENTAL METHODS

2.1 Synthesis

All reagents were purchased from Sigma-Aldrich® and used as received.

2.1.1 UiO-66 and UiO-66-N

Crystals of UiO-66 and UiO-66-N were synthesized according to a procedure modified from Zhao et al.[16] $ZrCl_4$ and acetic acid (AA) were dissolved in 140 mL of dimethylformamide (DMF). The solution was heated at 120 °C for 1 hour to form the secondary building unit (SBU). A second solution of linker, terephthalic acid or 1,4-naphthalenedicarboxylic acid for UiO-66 and UiO-66-N respectively, and triethylamine (TEA) was mixed in 10 mL of DMF. The $ZrCl_4$ solution was cooled to room temperature and the two solutions were mixed. The molar ratios of the reactants were 4 mmol:4 mmol:2.4 mol:0.5 mmol of $ZrCl_4$:linker:AA:TEA. The solution was heated to 120 °C for 72 hours. After reaction, the product was centrifuged at 6,000 rpm and washed with 10 mL of fresh DMF. The washing procedure was repeated 3 times. After the third wash, the sample was solvent exchanged with 10 mL of methanol for 24 hours.

2.1.2 UiO-67

UiO-67 was synthesized according to a procedure reported by Schaate et al.[17] $ZrCl_4$ and 5 equivalents of benzoic acid were dissolved in 10 mL of DMF. The solution was heated at 120 °C for 1 hour to form the SBU. A second solution of biphenol-4,4'-dicarboxylic acid was dissolved in 10 mL DMF. The two solutions were mixed and heated at 120 °C for 72 hours. The product was centrifuged and washed with fresh DMF 3 times. The sample was then solvent exchanged with acetone for 24 hours.

2.2 Characterization

2.2.1 Scanning electron microscopy

SEM images were obtained using a Phenom GSR desktop SEM. Typical settings for the instrument use an accelerating voltage of 15 kV at a nominal working distance of 10 mm. Particle size was determined by averaging the measurement of each side length of the octahedral crystals.

2.2.2 Thermogravimetric analysis

Thermogravimetric analysis (TGA) measurements were conducted with a TA Instruments Q500 instrument from a range of 20–800 °C using the Hi-Res variable temperature ramp program with a sensitivity factor of 5.

2.2.3 N_2 physisorption

N_2 isotherms were measured using a Micromeritics ASAP 2420 analyzer at 77 kelvin. Samples were off-gassed at 90 °C under vacuum for ~16 hours. The Brunauer–Emmett–Teller (BET) method was used to calculate specific surface area in m^2/g.

2.3 Diffusion measurements

Figure 4 shows a schematic of a CSFR apparatus. The apparatus consists of two feed streams that mix before flowing into an adsorbent bed. One stream is an inert carrier gas while the second stream contains the adsorbate of interest. In the case of low vapor pressure compounds, the adsorbate stream is prepared by flowing an inert carrier gas through a liquid sparger system to generate a saturated feed stream. The steady-state adsorbate feed concentration is determined by the combined flowrates of the two streams, which are controlled by mass flow controllers. The pressure in the adsorbent bed is controlled by a Baratron pressure controller and the effluent gas from the adsorbent bed is sampled by mass spectrometry. A constant, unperturbed feed is passed through the bed until the system reaches steady-state at the desired gas-phase concentration. Then, the flowrates of the two feed streams are set to undergo sinusoidal perturbations 180 degrees out of phase. The resulting feed stream to the adsorbent bed has constant total flowrate with a sinusoidal adsorbate concentration swing around the steady-state concentration. The sinusoidal perturbations can be performed over a frequency range of 0.0001–0.1 Hz. The amplitude of the concentration swing exiting the bed is measured and divided by the amplitude of the concentration swing entering the bed in order to determine the amplitude ratio. The data is presented as a plot of the amplitude ratio versus the frequency of oscillation. Model fitting of the results is conducted using a frequency or Laplace domain and thus is not more complex analytically.[18] In addition to rate data, frequency response results provide information on the adsorption equilibrium at the operating conditions; thus, providing an easy way to check the consistency between the CSFR results and equilibrium isotherms.

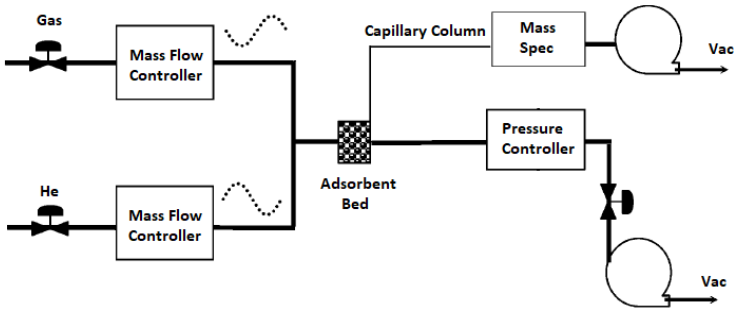

Figure 4. CSFR apparatus.

3. RESULTS

The first task for this effort was to bring frequency response capability to ECBC by assembling a new apparatus. The correct operation of the system was then verified by replicating results from the literature. Figure 5 shows an amplitude ratio plot of octane on BPL activated carbon fitted using a micropore diffusion model. Table 1 gives the regressed isotherm slope, K, and mass transfer coefficient, D/r^2, along with values from Wang et al.[19] An octane concentration of 4,000 ppm gives an isotherm slope of 31.5 mol/kg/bar which is between the two literature values for 4,900 ppm and 3,100 ppm. The D/r^2 value is faster than the literature value which is expected since a smaller particle mesh size was used.

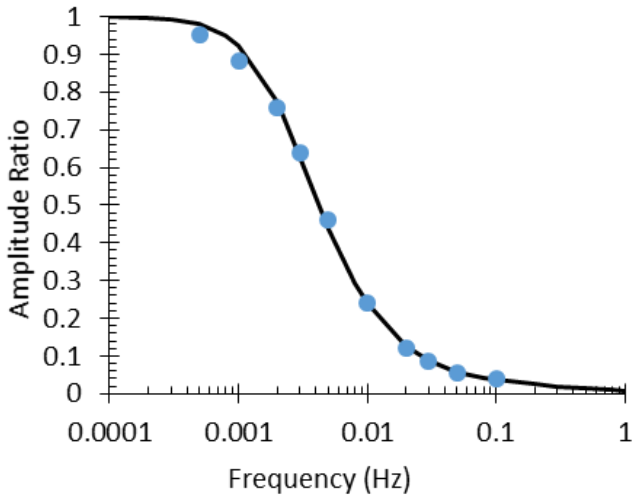

Figure 5. Amplitude ratio curve for 4,000 ppm *n*-octane on BPL activated carbon.

Table 1. Micropore diffusion model parameters for octane compared with literature results from Wang et al.[19]

Octane concentration	K	D/r^2	Mesh
(ppm)	(mol/kg/bar)	(1/s)	
4900[19]	23.2	0.0023	6x16
4000	31.5	0.0064	12x32
3100[19]	63.9	0.0019	6x16

After confirmation of the apparatus working as expected, a sample of UiO-66 made with no modulators was tested under different operating conditions. A standard UiO-66 synthesis produces agglomerated particles of very small intergrown crystals. Because of this morphology, diffusion is likely not governed by the micropores given the extremely short diffusion length scale. Figure 6 shows amplitude ratio curves for octane on UiO-66 at high and low octane concentrations of 4,000 ppm and 860 ppm and with a high and low mass of sample used in the bed. As expected, the micropore diffusion model cannot recover the curve shape for any of the experiments indicating that diffusion in the micropores is not the rate-limiting mass transfer mechanism. While the mass transfer coefficient is meaningless, the regressed isotherm slope shows expected trends. K values were 23.6 mol/kg/bar and 101.5 mol/kg/bar for 4,000 ppm and 1,000 ppm respectively. This decrease in slope as concentration increases is consistent with a favorable isotherm. When the sample mass was varied but the concentration remained the same, K values were 101.5 mol/kg/bar and 106.9 mol/kg/bar which are within experimental error.

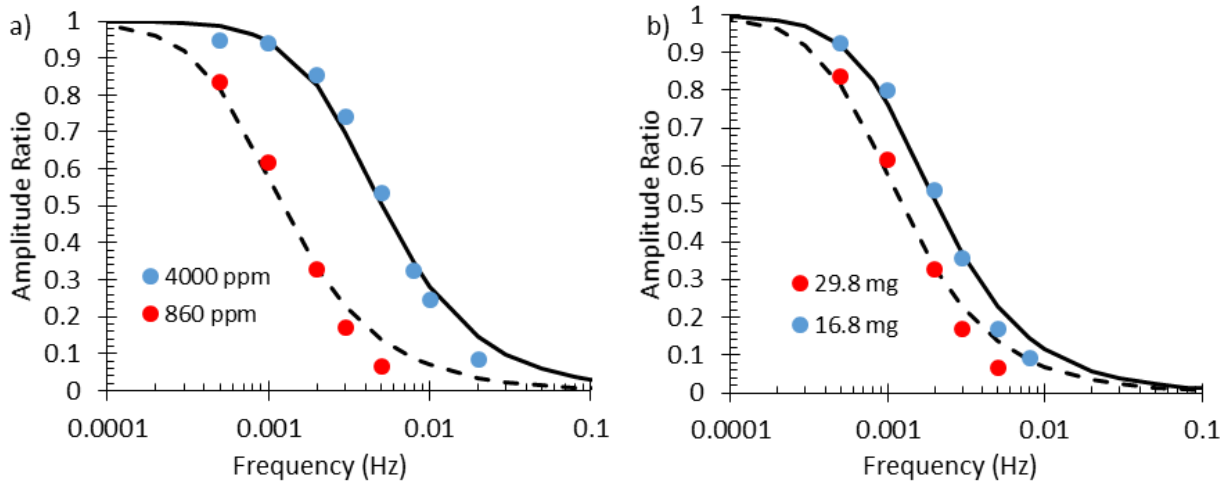

Figure 6. Amplitude ratio curves for *n*-octane on standard UiO-66 at different operating conditions.

In order to overcome the issue of mass transfer not being controlled by diffusion in the micropores of the MOF, larger single crystals of UiO-66 needed to be synthesized in order to increase the length scale of micropore diffusion. Two methods from the literature, one using triethylamine and acetic acid and the other using benzoic acid as modulators, were chosen to make crystals of UiO-66-N, UiO-66, and UiO-67. Detailed synthesis procedures are described in Section 2.1. Figure 7 shows SEM images of each type of crystal along with the standard UiO-66. The crystals produced have an octahedral shape with sizes ranging from 300–1,000 nm. N_2 physisorption was used to prove the crystal porosity and measured BET surface areas were 593 m^2/g, 924 m^2/g, and 1792 m^2/g for UiO-66-N, UiO-66, and UiO-67 respectively. UiO-66 is known to have defect sites that can be the result of missing linkers or SBUs. Surface area is known to increase with the number of defects and surface areas greater than 1,800 m^2/g have been reported.[20] The low surface area of 924 m^2/g indicates low defect density and TGA was used to confirm this by calculating a value of 0.68 defects per unit cell. For comparison, high defect samples can have 3–4 defects per unit cell. The combination of these characterization techniques indicate that the synthesized crystals are of high quality and can be used for CSFR.

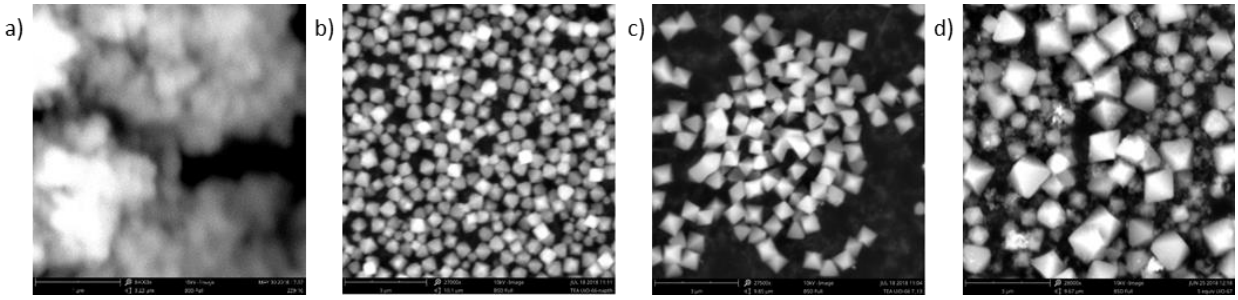

Figure 7. SEM images of a) standard UiO-66, b) UiO-66-N crystals, c) UiO-66 crystals, and d) UiO-67 crystals.

Figure 8 shows amplitude ratio curves for *n*-octane on each of the MOF crystals. The operating condition for the CSFR experiments was 9,000 ppm octane with a flowrate of 40 sccm. Approximately 20 mg of sample was used for each experiment. A micropore diffusion model clearly fits each of the curves and a control curve shows clear impact from adsorption and desorption compared to bed effects. Table 2 gives the regressed parameters and calculates a diffusivity based on the average particle size of each sample. While no trends can be seen in the mass transfer parameter, when normalized by the particle size to calculate a diffusivity, UiO-66-N has a significantly lower diffusion coefficient than UiO-66 and UiO-67. Since there is no jump in diffusivity between UiO-66 and UiO-67, the pore size of UiO-66 allows uninhibited surface diffusion of the linear alkane. Because we expect the intermolecular forces between octane and UiO-66 and UiO-67 to be similar, it makes since that the diffusivity plateaus once steric hindrances are eliminated.

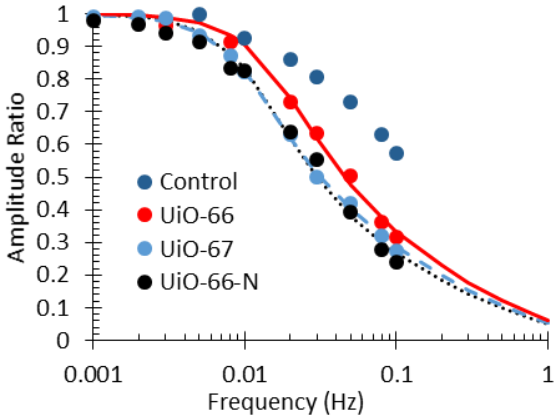

Figure 8. Amplitude ratio curves for *n*-octane on UiO-66-N, UiO-66, and UiO-67 crystals.

Table 2. Micropore diffusion parameters and diffusivity calculations for *n*-octane on each MOF crystal.

	UiO-66-N	UiO-66	UiO-67
D/r^2 (1/s)	0.00419	0.00532	0.00324
K (mol/kg/bar)	12.5	8.1	11.8
Avg. size (nm)	432	591	701
Diffusivity (nm^2/s)	195	462	396

Since octane diffusion does not show any difference between UiO-66 and UiO-67, a larger molecule needs to be used to investigate possible steric effects between the two pore sizes. β-pinene is a hydrocarbon that has a six-member ring with a bridging carbon and three branching carbons. It was chosen since the structure has a significant cross-sectional area in all three dimensions. Figure 9 shows amplitude ratio curves for pinene on UiO-66 and UiO-67 crystals along with fits based on the micropore diffusion model. The regressed parameters are given in Table 3. As expected, the C_{10} hydrocarbon pinene has significantly higher *K* values compared with octane. This is expected due to stronger dispersion forces from the additional carbon and from the significantly lower vapor pressure of pinene. The significantly higher *K* value for UiO-67 indicates a greater flux through the crystal likely due to a higher adsorption capacity in the larger pore. However, the calculated diffusivity once again shows that the smaller pore size of UiO-66 does not have a negative effect on the diffusion rate compared to UiO-67. This result is not unreasonable as Grissom et al. showed with IR that aromatic (BTX) compounds could reach all sites within UiO-66.[21]

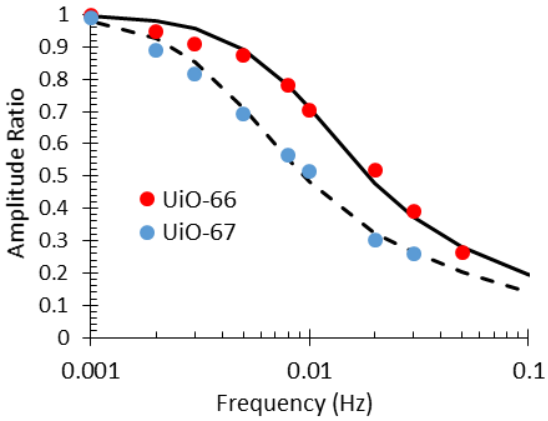

Figure 9. Amplitude ratio curves for β-pinene on UiO-66 and UiO-67 crystals.

Table 3. Micropore diffusion model parameters and diffusivity of β-pinene on UiO-66 and UiO-67 crystals.

	UiO-66	UiO-67
D/r^2 (1/s)	0.00357	0.00168
K (mol/kg/bar)	19.1	34
Diffusivity (nm^2/s)	312	206

While the diffusion rate of the hydrocarbons *n*-octane and β-pinene were not sterically hindered by the smaller pore size of UiO-66 compared with UiO-67, these results may not translate to other adsorbates. For adsorbates with functional groups that have stronger intermolecular interactions with the MOFs, surface diffusion could be significantly lowered even without steric hindrance effects. Also, in cases of irreversible adsorption, the chemisorbed species could end up blocking diffusion pathways in a similar manner as the aromatic ring in UiO-66-N that caused reduced diffusivity. Moving forward, it will be important to investigate these effects in systems of greater interest to the Army's mission.

4. CONCLUSIONS/FUTURE WORK

Single crystals of UiO-66-N, UiO-66, and UiO-67 were synthesized with good porosity and low defects. Diffusion rates of *n*-octane and β-pinene were measured using CSFR. Octane diffusion was faster than pinene for each of the MOFs. When comparing octane diffusion rates between the different MOFs, no difference is seen between UiO-66 and UiO-67. However, UiO-66-N has a significantly lower diffusion rate indicating that the pore blockage is impacting diffusion. Despite the larger molecular size of pinene, no difference in diffusion rate was seen between UiO-66 and UiO-67. This indicates that UiO-66 does not have any steric limitations for molecules up to the size of pinene. In the future, it is of interest to investigate the impact of MOF functionalities and defects and also to measure data for adsorbates with stronger intermolecular interactions.

ACKNOWLEDGMENTS

Funding was provided by the Director, Edgewood Chemical Biological Center under the authorities and provisions of Section 2363 of the FY 2018 NDAA to develop new technologies, engineer innovations, and introduce game-changing capabilities. This research was performed while Trenton Tovar held a National Research Council post-doctoral research associateship award at ECBC.

REFERENCES

[1] Eddaoudi, M.; Kim, J.; Rosi, N.; Vodak, D.; Wachter, J.; O'Keeffe, M.; Yaghi, O.M. Systematic design of pore size and functionality in isoreticular MOFs and their application in methane storage. *Science.* **2002,** *295* (5554), pp 469–472.

[2] Wang, Z.; Cohen, S.M. Postsynthetic modification of metal-organic frameworks. *Chem. Soc. Rev.* **2009,** *38* (5), pp 1315–1329.

[3] DeCoste, J.B.; Peterson, G.W. Metal-organic frameworks for air purification of toxic chemicals. *Chem. Rev.* **2014,** *114* (11), pp 5695–5727.

[4] Haldoupis, E.; Watanabe, T.; Nair, S.; Sholl, D.S. Quantifying large effects of framework flexibility on diffusion in MOFs: CH4 and CO2 in ZIF-8. *Chemphyschem.* **2012,** *13* (15), pp 3449–3452.

[5] Dubbeldam, D.; Snurr, R.Q. Recent developments in the molecular modeling of diffusion in nanoporous materials. *Mol. Simulat.* **2007,** *33* (4-5), pp 305–325.

[6] Chmelik, C.; Karger, J.; Wiebcke, M.; Caro, J.; van Baten, J.M.; Krishna, R. Adsorption and diffusion of alkanes in CuBTC crystals investigated using infra-red microscopy and molecular simulations. *Micropor. Mesopor. Mat.* **2009,** *117* (1–2), pp 22–32.

[7] Hamad, S.; Balestra, S.R.G.; Bueno-Perez, R.; Calero, S.; Ruiz-Salvador, A.R. Atomic charges for modeling metal–organic frameworks: Why and how. *J. Solid State Chem.* **2015,** *223*, pp 144–151.
[8] Rosenbach, N., Jr.; Jobic, H.; Ghoufi, A.; Salles, F.; Maurin, G.; Bourrelly, S.; Llewellyn, P.L.; Devic, T.; Serre, C.; Ferey, G. Quasi-elastic neutron scattering and molecular dynamics study of methane diffusion in metal organic frameworks MIL-47(V) and MIL-53(Cr). *Angew. Chem. Int. Ed. Engl.* **2008,** *47* (35), pp 6611–6615.
[9] Salles, F.; Jobic, H.; Maurin, G.; Koza, M.M.; Llewellyn, P.L.; Devic, T.; Serre, C.; Ferey, G. Experimental evidence supported by simulations of a very high H2 diffusion in metal organic framework materials. *Phys. Rev. Lett.* **2008,** *100* (24), p 245901.
[10] Prakash, M.; Jobic, H.; Ramsahye, N.A.; Nouar, F.; Damasceno Borges, D.; Serre, C.; Maurin, G. Diffusion of H2, CO2, and Their Mixtures in the Porous Zirconium Based Metal–Organic Framework MIL-140A(Zr): Combination of Quasi-Elastic Neutron Scattering Measurements and Molecular Dynamics Simulations. *J. Phys. Chem. C.* **2015,** *119* (42), pp 23978–23989.
[11] Kärger, J.; Ruthven, D.M.; Theodorou, D.N., Diffusion in Nanoporous Materials. Wiley-VCH Verlag GmbH & Co. KGaA: 2012.
[12] Song, L.J.; Rees, L.V.C. Adsorption and diffusion of cyclic hydrocarbon in MFI-type zeolites studied by gravimetric and frequency-response techniques. *Microporous Mesoporous Mater.* **2000,** *35–6*, pp 301–314.
[13] Yasuda, Y. Determination of Vapor Diffusion-Coefficients in Zeolite by the Frequency-Response Method. *J. Phys. Chem.* **1982,** *86* (10), pp 1913–1917.
[14] Tovar, T.M.; Zhao, J.; Nunn, W.T.; Barton, H.F.; Peterson, G.W.; Parsons, G.N.; LeVan, M.D. Diffusion of CO_2 in Large Crystals of Cu-BTC MOF. *J. Am. Chem. Soc.* **2016,** *138* (36), pp 11449–11452.
[15] Liu, J.; Wang, Y.; Benin, A.I.; Jakubczak, P.; Willis, R.R.; LeVan, M.D. CO_2/H_2O adsorption equilibrium and rates on metal-organic frameworks: HKUST-1 and Ni/DOBDC. *Langmuir.* **2010,** *26* (17), pp 14301–14307.
[16] Zhao, Y.; Zhang, Q.; Li, Y.; Zhang, R.; Lu, G. Large-Scale Synthesis of Monodisperse UiO-66 Crystals with Tunable Sizes and Missing Linker Defects via Acid/Base Co-Modulation. *ACS Appl. Mater. Interfaces.* **2017,** *9* (17), pp 15079–15085.
[17] Schaate, A.; Roy, P.; Godt, A.; Lippke, J.; Waltz, F.; Wiebcke, M.; Behrens, P. Modulated synthesis of Zr-based metal-organic frameworks: from nano to single crystals. *Chemistry.* **2011,** *17* (24), pp 6643–6651.
[18] Wang, Y.; LeVan, M.D. Master curves for mass transfer in bidisperse adsorbents for pressure-swing and volume-swing frequency response methods. *AlChE J.* **2011,** *57* (8), pp 2054–2069.
[19] Wang, Y.; Mahle, J.J.; Furtado, A.M.; Glover, T.G.; Buchanan, J.H.; Peterson, G.W.; LeVan, M.D. Mass transfer and adsorption equilibrium for low volatility alkanes in BPL activated carbon. *Langmuir.* **2013,** *29* (9), pp 2935–2945.
[20] Shearer, G.C.; Chavan, S.; Bordiga, S.; Svelle, S.; Olsbye, U.; Lillerud, K.P. Defect Engineering: Tuning the Porosity and Composition of the Metal–Organic Framework UiO-66 via Modulated Synthesis. *Chem. Mater.* **2016,** *28* (11), pp 3749–3761.
[21] Grissom, T.G.; Sharp, C.H.; Usov, P.M.; Troya, D.; Morris, A.J.; Morris, J.R. Benzene, Toluene, and Xylene Transport through UiO-66: Diffusion Rates, Energetics, and the Role of Hydrogen Bonding. *J. Phys. Chem. C.* **2018,** *122* (28), pp 16060–16069.

Chemical imaging of decontamination reactions on surfaces

Erik D. Emmons*, Ashish Tripathi
U.S. Army Edgewood Chemical Biological Center, Research & Technology Directorate,
8198 Blackhawk Rd, Aberdeen Proving Ground, MD 21010

ABSTRACT

Decontamination reactions on surfaces are an important area of research due to the necessity of finding new materials such as fabrics for protecting soldiers from chemical warfare agents. It would be advantageous if these materials could also decontaminate the agents in addition to serving their other purposes; therefore, it is necessary to develop a technique for assessing the performance of these materials from a decontamination perspective. In this work, Raman chemical imaging was used in order to image decontamination reactions of chemical warfare agent simulants on surfaces. The organophosphate chemical ethyl paraoxon was chemically imaged with spatial and temporal resolution as it underwent hydrolysis on a roughened glass substrate. The production of thiophenolate ion reaction products could be tracked as the hydrolysis reaction proceeded. The results and techniques developed on this model system can be further developed to handle progressively more realistic situations.

Keywords: Raman chemical imaging, vibrational spectroscopy, decontamination reactions, hydrolysis, reaction kinetics

1. INTRODUCTION

Decontamination following chemical warfare agent exposure is a crucial capability for the Army and the defense and security communities in general. New types of decontamination materials are constantly being developed in order to better protect soldiers and civilians. There is significant interest in multifunctional materials which can combine the capability for decontaminating toxic chemicals with other purposes. For example, a uniform could be made of a composite material which contains components, including catalysts that can decontaminate chemical agents to which it is exposed. It is important to develop methods for assessing the performance of these multifunctional materials. Chemical imaging techniques are capable of imaging reactions on complex surfaces and have the potential for application in testing new multifunctional materials. These techniques are capable of obtaining both spatially and temporally resolved information on the chemical identity of materials. As has been stated by Bentrup in a review article, "knowledge of spatiotemporal gradients in heterogeneous catalysts is of essential importance for the rational design of catalysts and catalytic processes."[1] In particular, the group of Prof. Weckhuysen at Utrecht University in the Netherlands has been working on using chemical imaging to observe catalytic reactions with both spatial and temporal resolution.[2]

One of these techniques, Raman chemical imaging (RCI), is particularly promising. Raman spectroscopy uses a monochromatic light source, such as a laser, which illuminates the sample. A small fraction of the laser photons excite vibrations of the molecules in the sample. A new photon is emitted which varies in energy from the original photon by an amount equal to the vibrational energy of the mode that was excited. Molecular vibrational energies and the band intensities observed are highly specific to molecular identity, providing a type of molecular fingerprint. Raman spectroscopy requires minimal sample preparation and can be used to obtain definitive information on chemical identity. Some challenges of Raman spectroscopy, however, include sensitivity to laser-induced damage of colored samples, fluorescence interference, and low-signal intensities.

This study focused on alkaline hydrolysis of ethyl paraoxon—a model system for chemical warfare agent decontamination. A scheme of the chemical reaction is shown below in Figure 1, with NaOH serving to catalyze the reaction by producing a basic solution. The hydrolysis reaction involves the cleavage of a P–O bond to produce 4-nitrophenol and diethyl phosphate. In basic solution, 4-nitrophenol deprotonates to produce 4-nitrophenolate anions, since the pKa value of nitrophenol is ~7. These anions exhibit a bright yellow color and produce Raman scattering bands much more intense than diethyl phosphate, due to the presence of the disubstituted aromatic ions which likely exhibit resonance Raman enhancement. A detailed study of the Raman spectra of nitrophenol and related molecules

is given by Kumar and Carey.[3] If the solution containing the ions dries out, a crystal will be formed. In the present experiments, NaOH was used to produce a basic solution. Therefore, the crystal that would be precipitated would be sodium 4-nitrophenolate.

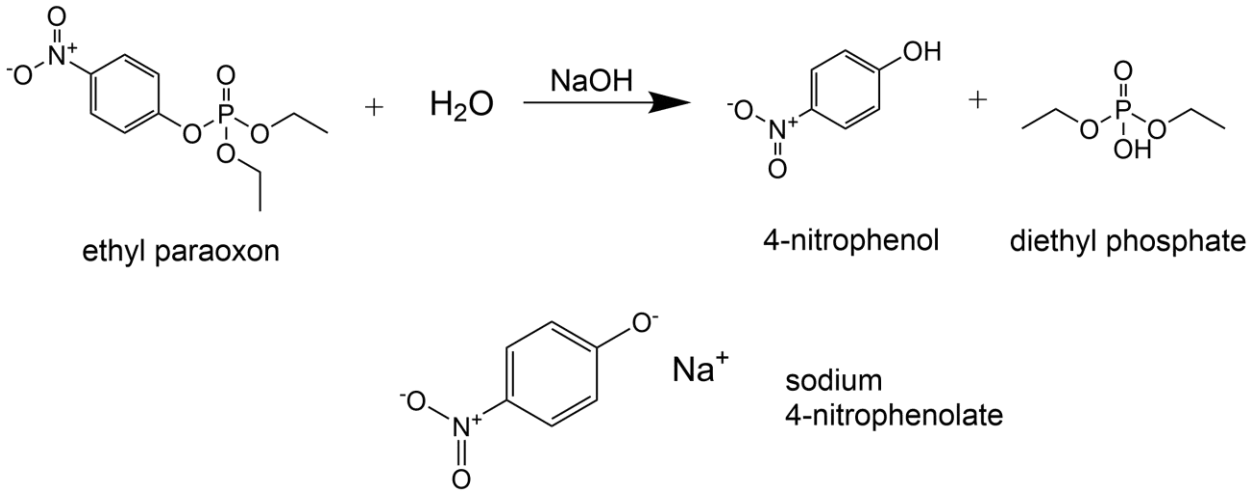

Figure 1. Reaction scheme for hydrolysis of ethyl paraoxon. The reaction is catalyzed by the base sodium hydroxide. Following cleavage of the P–O bond, 4-nitrophenol and diethyl phosphate are produced. In basic solution, the nitrophenol molecules deprotonate to form nitrophenolate ions.

2. EXPERIMENTAL

The RCI experiments were performed with a Witec Alpha 300R RCI microscopy system. A 532 nm laser was used to excite the samples. A 10X magnification microscope objective was used to focus the laser light on the sample, and to collect the Raman scattered light in a backscattering configuration. A notch filter with a very narrow blocking range around the laser line was used to prevent the Rayleigh scattered light from overwhelming the detector. This allowed for observation of Raman scattered light down to around 10–20 cm^{-1}, including the observation of low-frequency crystalline lattice modes. A 600-grooves/mm diffraction grating was used to disperse the Raman scattered light onto a thermoelectrically-cooled charge-coupled device detector to obtain spectra. The entire spectrum from the Rayleigh line through the CH and OH stretching modes (> 3000 cm^{-1}) could be obtained with this grating. The sample was rastered with a precision XYZ stage in order to obtain chemical images. Time-resolved chemical imaging could be performed by repeatedly imaging the same region of the sample. Typical laser powers used were on the order of 10 mW and integration times of 0.1–1.0 seconds-per-point were used.

Ethyl paraoxon and sodium hydroxide were obtained from Sigma-Aldrich® and Thermo Fisher Scientific, Inc., respectively, and used without further purification. Ultrapure deionized water (> 18.2 MΩ × cm resistivity) was used to make all solutions of sodium hydroxide. A ground BK7 glass diffuser (Thorlabs, Inc.) was used as a substrate. Figure 2 shows the library Raman spectra of three molecular species of relevance in the current work. The top (red) trace shows the spectrum of neat liquid ethyl paraoxon. The second spectrum (green) is for a 0.1 % (v/v) solution of ethyl paraoxon in 0.5 M aqueous NaOH. The third (blue) spectrum is for crystalline 4-nitrophenol. The spectra of 4-nitrophenol and its corresponding anion are consistent with the literature.[3] Finally, the bottom spectrum (light blue) is from the crystalline deposit of 0.1 % ethyl paraxon in 0.5 M NaOH after drying. This is presumed to be crystalline 4-nitrophenolate ions and is labeled as such. All four of the spectra show intense Raman peaks in the range of 1270–1350 cm^{-1}. These peaks are due to symmetric NO_2 stretching vibrations of the molecules. These bands will feature prominently in the analysis to follow. Another region of note is the range around 0 cm^{-1}. This is the area around the Rayleigh line, which is due to intense inelastic scattering of laser photons from the molecules. Note that 4-nitrophenol, which is a crystalline material, has at least three sharp peaks at less than 200 cm^{-1}. These low-frequency modes are indicative of the presence of crystalline material and are due to vibrational motions where entire molecules or ions in a unit cell translate or rotate relative to each other. These sharp bands are a simple indicator for tracking the phase of the material. Liquids or amorphous solids, by contrast, show broad structures in this frequency region. In the RCI experiments, droplets of ethyl paraoxon and aqueous sodium hydroxide were deposited on top of each other on

the ground glass surfaces. The deposits were then measured using RCI to determine the progress of the reactions with spatial and temporal resolution. The same region of the sample was imaged sequentially in a "video" mode.

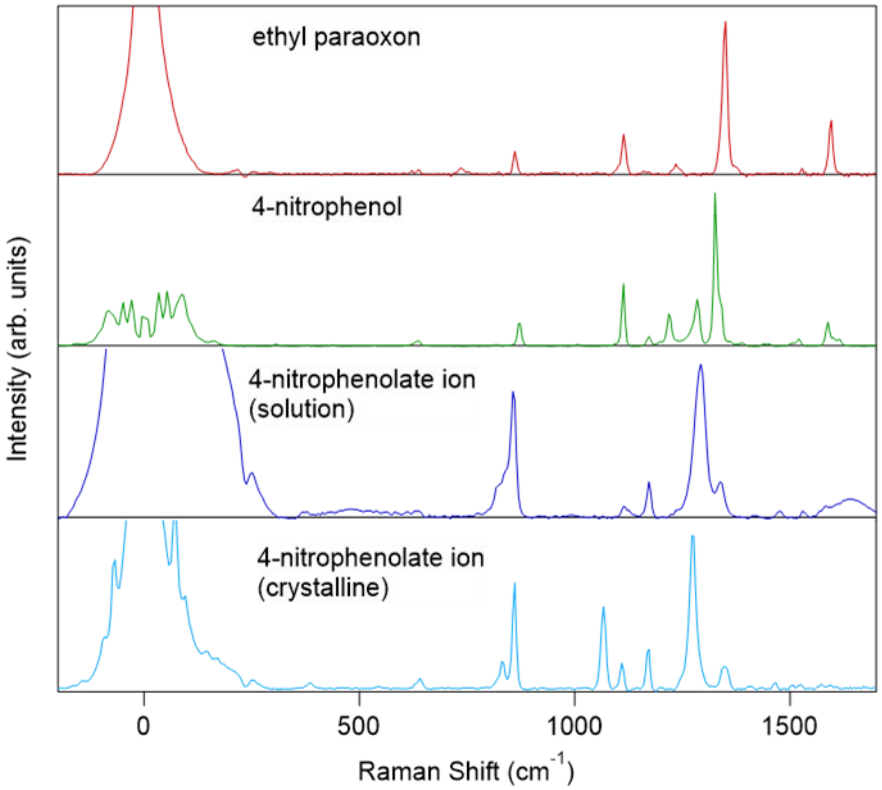

Figure 2. Library Raman spectra of relevant molecular species. The most intense bands near 1275–1350 cm^{-1} in all three species are due to symmetric NO_2 stretching.

3. RESULTS AND DISCUSSION

As described in the previous section, the experiments were performed by co-depositing droplets of ethyl paraoxon and concentrated sodium hydroxide solution on a ground glass substrate. RCI was then used to track the progress of the decontamination reaction. The results of one experiment are shown in Figure 3. In this experiment, a 0.5-µL droplet of ethyl paraoxon was placed on the ground glass substrate, and a 2.5-µL droplet of 5 M sodium hydroxide was placed on top of it as a decontamination solution. The far-left frame shows a brightfield montage microscope image of the droplet soon after deposition and immediately prior to the measurement. A series of RCI measurements were then performed to image the sample as a function of time. Each frame of the RCI measurements consisted of a 60 x 60 grid of pixels with an integration time of 90 ms per pixel. Each frame required approximately 360 seconds to acquire. A laser power of 10 mW and a 10X microscope objective were used. The red images shown in Figure 3 were obtained by integrating the intensity of the 1344 cm^{-1} band of ethyl paraoxon at each pixel. The blue images were obtained by integrating the intensity of the 1378 cm^{-1} band of nitrophenolate ions at each pixel. Selected frames at each time period are shown from right to left. In the figure, frames 1, 31, 61, and 91 are shown, which were obtained at t = 0 minutes, 180 minutes, 360 minutes, and 480 minutes, respectively. The geometrical redistribution and transformation of the material is shown. In this case, there was insufficient decontamination solution to completely decontaminate the droplet. As a result, some ethyl paraoxon still remains after 480 minutes. The presence of the degradation product 4-nitrophenolate steadily grows as the reaction proceeds. However, due to the limited amount of sodium hydroxide solution used, the reaction was not completed as unreacted ethyl paraoxon remained at the end.

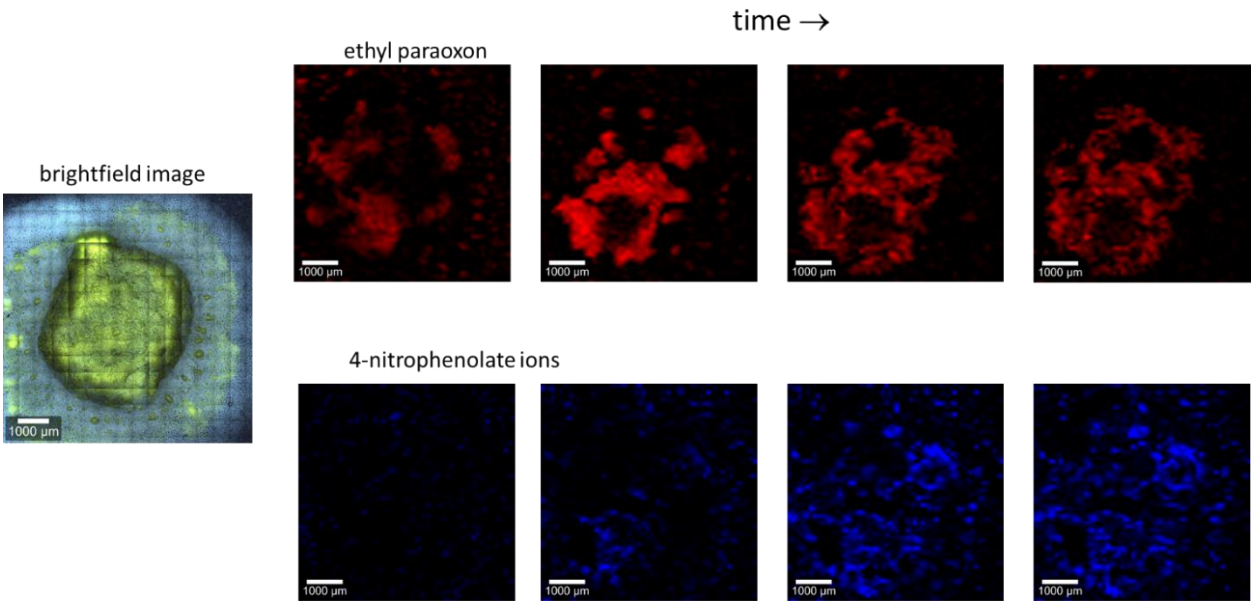

Figure 3. Raman chemical images as a function of time for decontamination of ethyl paraoxon. On the far left is a brightfield montage of the deposit of ethyl paraoxon and aqueous sodium hydroxide prior to the measurement. The red chemical images track the presence of ethyl paraoxon as a function of time from left to right. The blue images track the presence of nitrophenolate ions.

Figure 4 shows a more detailed spectroscopic analysis of one frame in the successive RCIs. Figure 4(a) shows the RCIs of ethyl paraoxon (red) and 4-nitrophenolate ions (blue) superimposed on each other. Where contributions from both species are present in a spectrum from a single pixel, the spectrum is shown as purple. Again, these intensity maps were obtained by integrating under the peaks as in Figure 3. Spectra of three different spots as indicated in Figure 4(a) are shown in Figure 4(b–d). They are compared to the library spectra of ethyl paraoxon and 4-nitrophenolate in the crystalline form. Spot 1 (Figure 4(b)) is red in the RCI, indicating it is predominantly unreacted ethyl paraoxon, as can be seen by the comparison of the single pixel spectrum (black) with the two library spectra. In contrast, spot 2 is colored blue and its spectra is consistent with crystalline 4-nitrophenolate ions, indicating that the ethyl paraoxon had hydrolyzed and then precipitated out as a crystal. The sharp low-frequency bands can be observed, indicating that the phase is indeed crystalline. Finally, spot 3 is colored purple, indicating that it is a mixture of unreacted ethyl paraoxon and 4-nitrophenolate ions. Features from both ethyl paraoxon and crystalline 4-nitrophenolate can be observed, including the low-frequency bands of 4-nitrophenolate. From these results, it is clearly seen that RCI can be used to track decontamination reactions with both spatial and temporal resolution, and in addition it can give material phase information as well.

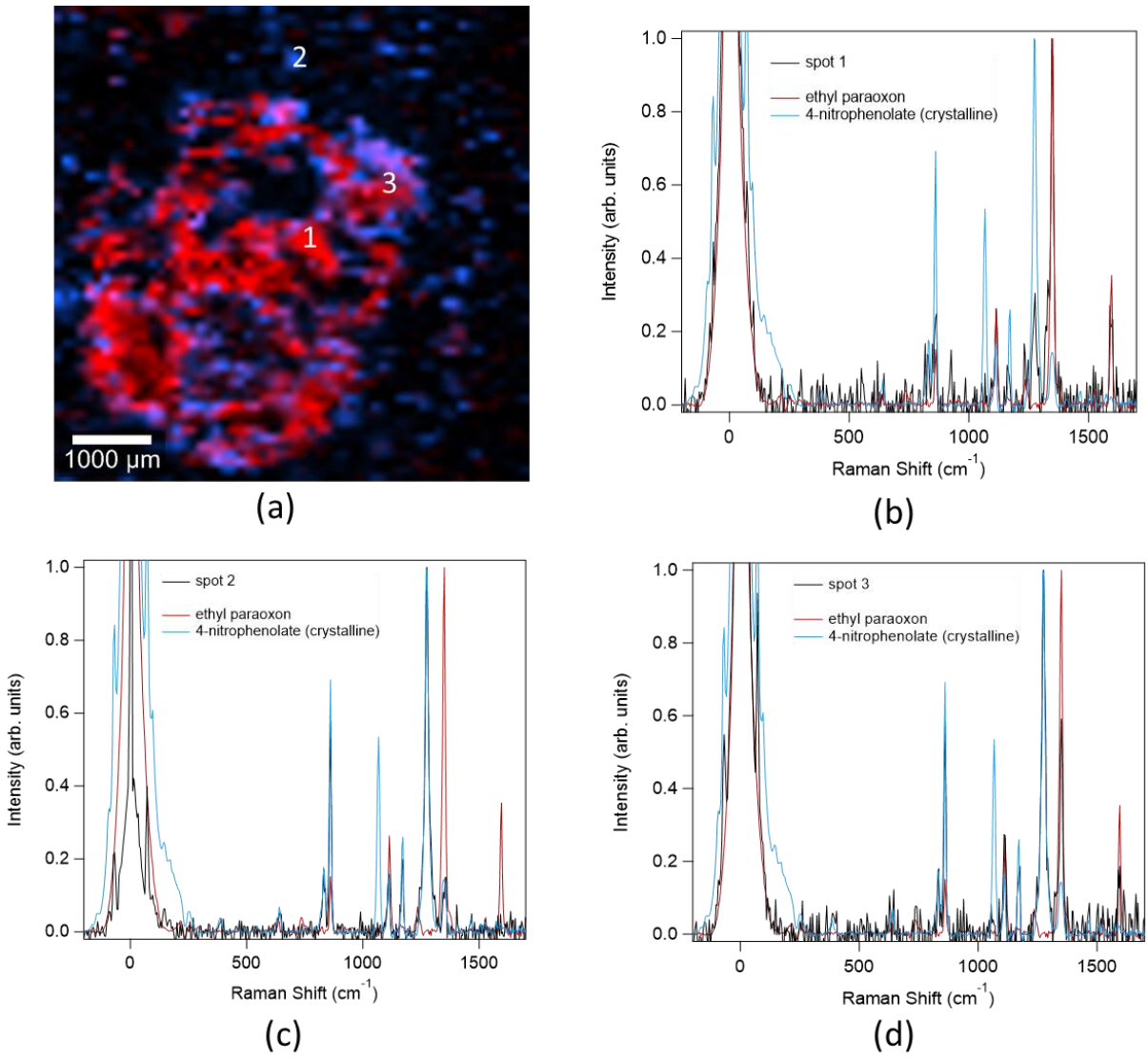

Figure 4. (a) RCI map of the decontamination process for ethyl paraoxon. Red indicates the intensity of the 1344 cm^{-1} band of ethyl paraoxon while blue indicates the intensity of the 1278 cm^{-1} band of nitrophenolate ions. Mixtures of the two are shown as purple. (b) Raman spectra of a single spectrum indicated by the label '1' in part (a). The library spectra are also shown indicating that the spectrum at spot 1 corresponds to ethyl paraoxon. (c) Plot similar to (b) indicating that spot 2 corresponds to 4-nitrophenolate ions. (d) Plot similar to (b) indicating that spot 3 corresponds to a mixture of ethyl paraoxon and 4-nitrophenolate ions.

4. CONCLUSIONS

RCI microscopy was used to track the process of decontamination reactions on surfaces with both spatial and temporal resolution. These initial measurements were performed with a model system involving hydrolysis of the pesticide ethyl paraoxon by a basic sodium hydroxide solution and were performed on a ground glass substrate. In addition to information on the progress of the reaction, the phase of the products (amorphous or crystalline) can be tracked. Additional analysis is in progress and the measurements are planned to be extended to other systems and more complex substrates. One such system is 2-chloroethyl phenyl sufide (an aromatic sulfur mustard simulant) oxidation by peroxides. These measurements are being performed using a proposed decon material known as peroxydone, which is a polymer with embedded peroxide. Hopefully RCI microscopy and chemical imaging in general can find an application in benchmarking the performance of decontamination materials on complex surfaces.

ACKNOWLEDGMENTS

Funding was provided by the Director, Edgewood Chemical Biological Center under the authorities and provisions of Section 2363 of the FY 2018 NDAA to develop new technologies, engineer innovations, and introduce game-changing capabilities. The authors thank Dr. John Landers and Dr. Chris Karwacki for helpful discussions.

REFERENCES

[1] Bentrup, U., Combining in situ Characterization Methods in One Set-Up: Looking with More Eyes Into the Intricate Chemistry of the Synthesis and Working of Heterogeneous Catalysts. *Chem. Soc. Rev.* **2010,** *39* (12), pp 4718–4730.

[2] Stavitski, E.; Weckhuysen, B. M., Infrared and Raman Imaging of Heterogeneous Catalysts. *Chem. Soc. Rev.* **2010,** *39* (12), pp 4615–4625.

[3] Kumar, K.; Carey, P. R., Resonance Raman spectra and structure of some complex nitroaromatic molecules. *J. Chem. Phys.* **1975,** *63* (9), pp 3697–3707.

Combining point and standoff detection data

Tom Ingersoll
U.S. Army Edgewood Chemical Biological Center, Research & Technology Directorate,
8198 Blackhawk Rd, Aberdeen Proving Ground, MD 21010

ABSTRACT

Based on their spatial sensitivity, sensors for chemical and biological warfare agents fall into two classes—point detectors and standoff detectors. Simulated data from standoff and point sampling devices containing two types of observation errors were combined using hierarchical occupancy modeling. These observation errors included both underreporting and false-positives, which are known to introduce bias in parameter estimation. Two modeling methods, based on differences in discriminating power of point sampling devices, were developed and tested for bias when estimating threat distribution using the occupancy probability. Bias was measured by the median absolute deviance between estimated and true occupancy probabilities. Median absolute deviance was found to be reduced, typically to negligible levels, through the hierarchical modeling process. Thus, the modeling process was robust to false-positive errors. Maps indicating chemical and biological threat distribution corrected for observation errors were produced.

Keywords: Hierarchical models, occupancy, false-positives, underreporting, standoff sensors, point sensors

1. INTRODUCTION

Based on their spatial sensitivity, sensors for chemical and biological (CB) warfare agents fall into two classes. Point detectors—which can include certain optical sensors, sample collectors, and identification devices—are restricted to sampling at the immediate location of the sensor, thus producing point data. Standoff detectors—such as LIDAR—can sample remotely across a distance, producing line, surface, or volume data. Thus, data from point and standoff sensors are of disparate spatial dimensions. Furthermore, the two sensor classes produce data of differing discrimination (or specificity), the ability to properly classify agents. They also differ in sensitivity, the ability to detect agents that are sparsely distributed. Data from point-sensors tend to have high specificity and low sensitivity. Standoff detectors tend to be highly sensitive but have low specificity. Clearly, an advantage in CB threat early-warning systems would be gained by combining the scale and sensitivity of standoff detectors with the specificity of point detectors. Currently, such data are combined informally through the judgment of skilled analysts and decision-makers, following a time-consuming review of confirmatory samples. A formal analytic process that provides objective estimates from data and automates map production of threat likelihood in near real-time is more elusive.

Combining data of differing sensitivity and discriminatory power into a unified descriptive model presents several technical challenges. Imperfect sensitivity and non-specificity introduce observation errors into data—under-reporting and false positives, respectively. Our group completed an FY17 Seedling project which presented a method using capture/recapture to eliminate estimation bias caused by under-reporting and false positives in alarm data. Such a method allows data from sensors of unequal sensitivity and specificity to be combined but has limitations due to confounding of false-positive and underreporting rate estimation. To provide locally heterogeneous estimates of both these errors, each must be represented separately by models based on orthogonal terms. A model of observation error representing environmental conditions in addition to sensor configuration, which affects both underreporting and false-positives, must be provided. Given these caveats, capture/recapture modeling can be used to estimate threat distribution, along with sensitivity (detection probability), and discrimination errors (the probability of false-positives).

Differences in sensitivity between point and standoff detectors can be readily explained for many detection systems. Highly specific point samplers, such as systems that include species identifiers for particular biological agents, are responding to multiple explanatory variables at the fine scale. For example, in PCR methods, DNA samples must match primers across a large number of loci, so samples must be of high quality. Furthermore, environmental DNA

samples are small, relative to the environment sampled. All conditions must be met simultaneously. Thus, the probability of detection in a single sample is a product of many probabilities, each less than one as shown in

$$P = \prod_{x=1}^{n} {p_x}^n, \quad (1)$$

where P is the overall probability of allocation, p_x is the probability associated with matching at each locus, and n is the number of loci. As the number of conditions required increases in number, such a product tends towards zero. Thus, in order to be effective, many point samples must typically be collected.

Many standoff detectors collect samples of a single explanatory variable repeatedly across distances or time intervals. For an agent to be detected, it need only be detected in any of individual repetitions. Thus, the probability that an agent is detected is the complement of the probability that it is not detected in any of the repetitions as shown in

$$P = \prod_{x=1}^{n} 1 - (1 - p_x)^n, \quad (2)$$

where P is the overall probability of detection, p_x is the per repetition detection probability, and n is the number of repetitions. Such a probability approaches one as the number of repeated measures increases.

Thus, under the right conditions, high-sensitivity standoff detectors, such as LIDAR, can approach a state where underreporting is negligible, but false-positives are significant. Alternatively, high discrimination point detection methods, such as PCR, can approach a state where the false-positives are negligible, but underreporting is significant. Other devices, including spectroscopic point-samplers, produce mixed errors with intermediate sensitivity and discrimination. These intermediate sensors retain low but significant levels of both underreporting and false positives.

Combining data of differing spatial dimension presents an additional problem. Many current methods reduce the standoff data to match the dimension of the point data but doing-so at a loss of information that would otherwise be available in the standoff data. An alternative would be to interpolate the point data to match the spatial dimensions of the standoff data. In this case, no information is lost. The difficulty then becomes proper incorporation of uncertainty associated with the interpolation, and adjustment for differences in observation errors between the different sensors.

Occupancy modeling is a method for estimating incidence when detection is imperfect.[1] The probability of occupancy, often denoted by Ψ, is the probability that a state, such as the presence of a threat, is incident on a geographic patch, regardless of observation error. Thus, Ψ is a robust and unbiased estimator of spatial distribution. Occupancy models use repeated measures to compensate for both underreporting and false-positives in data.[2] Because incidence is binomial, thus restricted to values of zero or one, it can be evenly distributed within polygonal regions, and remains constant within repeated measures as long as the interval between measures is adequately minute. Thus, differences within regional boundaries or within repeated measures can be attributed to observation errors, allowing these errors to be estimated. This is the basis for hierarchical modeling.[3] Occupancy modeling retains certain advantages of robustness over other distribution metrics such as density.

2. METHODS

All computation and graphics were done in the computational language R version 3.5.1.[4] Standoff and point incidence data with fixed underreporting, and false-positive rates were simulated using true values of threat occupancy that were known *a priori*. Occupancy probability was then estimated using the occupancy with false-positives (OccuFP) model found in the R library unmarked,[5] which is described by Royle and Link.[2] Bias was measured using the median absolute deviance between estimated and true threat probability. Maps were then produced using the R library *raster*,[6] displaying the geographical distribution of threat probabilities.

A system was developed for modeling data from high discrimination devices conditional on data from high sensitivity devices to produce geographic maps indicating threat distribution. That is, a data of insignificant underreporting and high false-positives, were combined with data having underreporting, but low false-positives (Method 1). A second method for combining data from intermediate devices conditional on data from high sensitivity devices was also developed (Method 2). Method 2 required careful selection of model terms and monitoring for spurious results in order to control confounding of false-positive and underreporting error terms.

By taking advantage of the high sensitivity of standoff devices and the binomial properties of incidence, the author developed simplified assumptions for spatial interpolation. Assuming that standoff surveillance was of an intensity that rendered underreporting insignificant, standoff data mapped into polygonal regions of evenly distributed

incidence. The analytic problem then became estimation of the true state within each reported polygon, either occupied or falsely-positive. A region where agent was present and indicated in standoff data was simulated along with a region where false-positives in standoff occurred due to presence of an obscurant (Figure 1a). Point samples for Methods 1 and 2 were also simulated. OccuFP was then used to discriminate the agent from the obscurant and plot the corrected distribution of agent on the map Figure 1b). Ψ values were assigned to five bins of 0.2 breadth each for grayscale indexing. These maps were produced from rasters of threat occupancy probability automated directly from the model output.

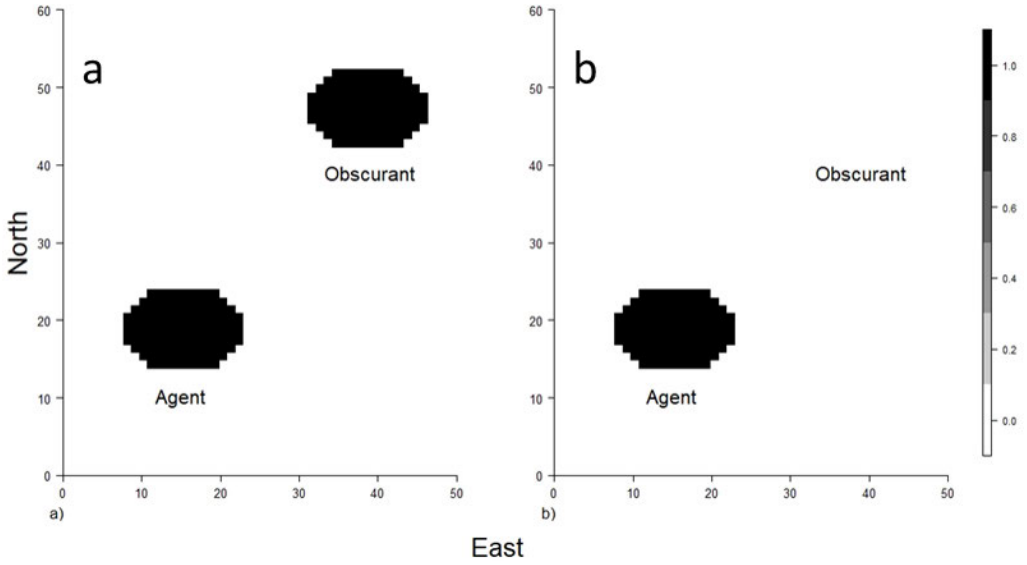

Figure 1. Mapped threat probabilities. a) Two plumes are in the raw data, including false-positives due to the obscurant. b) False-positives at the obscurant plume have been removed by modeling.

3. RESULTS

Maps indicating the location of threat agents corrected for false-positives and underreporting were produced using Method 1 (Figure 2). Bias was found to be very low even with point samples as few as 40, and detection probabilities as low as 0.2.

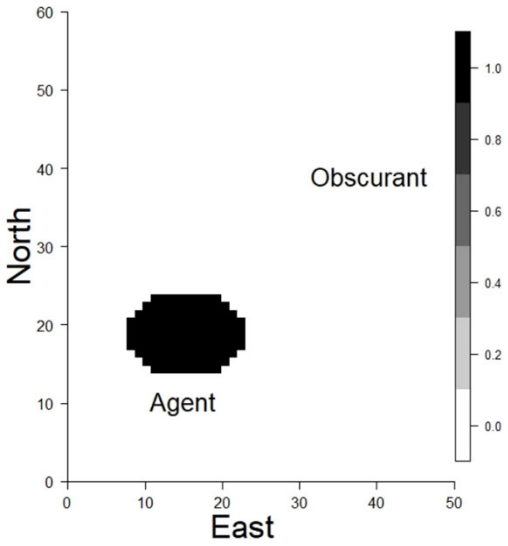

Figure 2. Mapped threat probability via Method 1, fusion of data between highly sensitive and highly discriminating devices. The threat probability attributed to obscurant is removed by the modeling process.

Typical model outputs are given in Table 1–Table 3; logit-scale occupancy, detection probabilities, and predicted threat probabilities, respectively. Standard errors—and thus uncertainties—were large, and 95 % confidence intervals (C.I.) were especially broad for the obscurant class.

Table 1. Occupancy (logit-scale) via Method 1.

Level	Estimate	Standard Errors
Obscurant	-9.49	39.8
Agent	9.57	39.8

Table 2. Detection probability (logit-scale) via Method 1.

Estimate	Standard Errors
-0.4	1.15

Table 3. Predicted threat probabilities via Method 1.

Level	Predicted	Standard Errors	Lower C.I.	Upper C.I.
Obscurant	0.00003	0.019	0	1
Agent	0.998	0.0006	0.069	0.941

Maps indicating the location of threat agents corrected for false-positives and underreporting were produced using Method 2 (Figure 3). Bias was found to be generally low with large numbers of samples, high detection probabilities, and low false-positive rates, increasing with reduced sample number, lower detection probabilities, and higher false-positive rates.

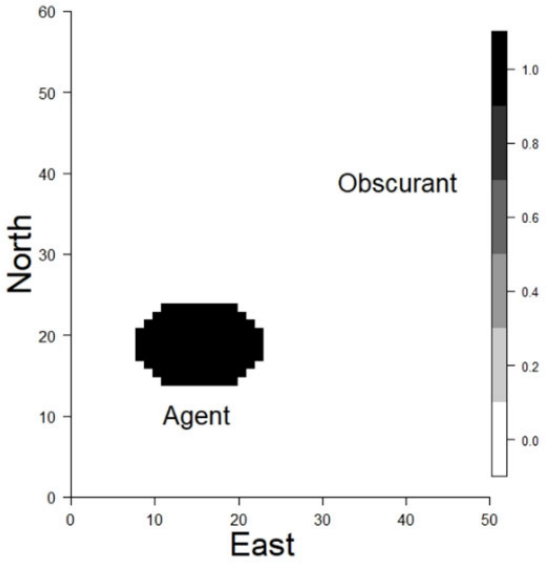

Figure 3. Mapped threat probability via Method 2, fusion of data between highly sensitive and intermediate devices. The threat probability attributed to obscurant is removed by the modeling process.

Typical model outputs are given in Table 4–Table 7; logit-scale occupancy, detection probabilities, false-positive probabilities, and predicted threat probabilities, respectively. Standard errors, and uncertainties, were broad.

Table 4. Occupancy (logit-scale) via Method 2.

Level	Estimate	Standard Errors
Obscurant	-8.6	23.3
Agent	21.1	133.4

Table 5. Detection probability (logit-scale) via Method 2.

Level	Estimate	Standard Errors
Obscurant	-15.7	4487
Agent	17.3	4487

Table 6. False-positive probability (logit-scale) via Method 2.

Level	Estimate	Standard Errors
Obscurant	22.5	4334
Agent	-23.8	4334

Table 7. Predicted threat probabilities via Method 2.

Level	Predicted	Standard Errors	Lower C.I.	Upper C.I.
Obscurant	0.0002	0.0043	0	1
Agent	0.9999	0.0005	0	1

4. DISCUSSION

Method 1 was found to be sensible, easy-to-automate, and reliable, assuming high quality point samples as might be produced by methods such as PCR. Method 2 was found to be less reliable and harder to automate than Method 1, due to confounding of error terms and false-positives in the lower quality point samples. However, Method 2 was reliable with careful selection of model terms and monitoring of results for spurious estimates.

Using the methods provided in the R library *unmarked*, both methods produced very broad confidence intervals. Repeated simulations only rarely resulted in predicted values far from true values, and the median absolute deviance between these values was typically less than 1 %. This suggested that confidence intervals calculated in *unmarked* were unrealistically high, and confidence intervals unrealistically broad. More realistic values might be estimated using a different method, such as bootstrap.

The author found that current Kriging processes used for interpolation and available in the R generalized geostatistics package was prone to producing spurious effects, such as edge effects, and was of limited reliability for modeling threat distribution. Instead, occupancy values were assumed to be constant within the borders of plumes as indicated by standoff data. This could become problematic when plumes are of mixed composition, including both agent and obscurant. Other interpolative methods, such as using the correlation between near neighbors, might be developed instead.

Method 2 could be used to enhance the usefulness of sensor data in a wide variety of future applications.

Threat maps are particularly easy to interpret in operational situations and provide increased situational awareness of hazard conditions. Results of hazard transport and dispersion models, such as the Defense Threat Reduction Agency Hazard Prediction and Assessment Capability, could be updated and refined using sensor data in near real-time. Tools for power analysis could be incorporated to identify optimal locations to deploy additional surveillance resources such as unmanned ground or air vehicles.

In general, these methods allowed data from point sampling devices to be mixed with surfaces from highly sensitive standoff devices for the production of threat maps. Bias due to false-positives and underreporting was reduced through this data mixture. Error estimation associated with computational libraries will need to be improved to provide commanders with an objective tool for evaluating model uncertainty. Likely risks associated with spatial distribution of CB agents can be mapped, along with regions likely to produce false alarms. The probability that specific threat agents are absent from the regions in sampling area can be estimated.

ACKNOWLEDGMENTS

Funding was provided by the Director, Edgewood Chemical Biological Center under the authorities and provisions of Section 2363 of the FY 2018 NDAA to develop new technologies, engineer innovations, and introduce game-changing capabilities.

REFERENCES

[1] MacKenzie, D.I.; Nichols, J.D.; Lachman, G.B.; Droege, S.; Royle, J.A.; Langtimm, C.A. Estimating Site Occupancy Rates When Detection Probabilities Are Less Than One. *Ecology.* **2002,** *83* (8), p 2248.

[2] Royle, J.A.; Link, W.A. Generalized site occupancy models allowing for false positive and false negative errors. *Ecology.* **2006,** *87* (4), pp 835–841.
[3] Royle, J.A.; Dorazio, R.M., *Hierarchical Modeling and Inference in Ecology*, Royle, J.A.; Dorazio, R.M., Eds. Academic Press: San Diego, 2009.
[4] R Development Core Team. R: A language and environment for statistical computing; The R Foundation for Statistical Computing, Vienna, Austria, 2011. http://www.R-project.org/
[5] Fiske, I.; Chandler, R. unmarked: AnRPackage for Fitting Hierarchical Models of Wildlife Occurrence and Abundance. *J. Stat. Softw.* **2011,** *43* (10).
[6] Hijmans, R.J. *raster: Geographic Data Analysis and Modeling*, version 2.6-7; 2017. https://CRAN.R-project.org/package=raster

Deep learning for the prediction of experimental spectra

Patrick C. Riley[a*], Samir V. Deshpande[b], Brian C. Hauck[b]
[a]U.S. Army Edgewood Chemical Biological Center, Research & Technology Directorate,
8198 Blackhawk Rd, Aberdeen Proving Ground, MD 21010
[b]Science and Technology Corporation, 111 Bata Blvd, Suite C, Belcamp, MD 21017

ABSTRACT

Increasingly, the design of alarm algorithms to alert Soldiers of danger grows more complex as new threats emerge. These algorithms need to be robust enough to prevent false alarms to interferents and sensitive enough to alarm to the incredibly small doses that prove lethal. The design of these algorithms has left a plethora of data that can be leveraged to train deep neural networks that could improve current algorithms, predict experimental spectra of new threats, and potentially determine chemical species from spectra. Deep neural networks are a technique in machine learning that imitate the function of a human brain by passing inputs through a series of hidden layers, where a neuron, representative of a piece of data, is activated based on a mathematical function. These deep neural networks need a large data set to be trained and developed. A mature chemical detection technology where a large data set exists is ion mobility spectrometry, and past work has been done using neural networks to predict either chemical class based on spectra or spectra from molecular property inputs. However, in either case the resulting network could not be generalized to additional detectors. Here the design of a theoretical deep neural network framework is presented that considers both instrument parameters and molecular properties to simulate the chemistry of a detection technology for which it was trained and predict experimental spectra.

Keywords: deep neural network, machine learning, ion-mobility spectrometry, false alarm reduction

1. INTRODUCTION

Machine learning (ML) is a field of computer science that uses a set of programming and statistical techniques to enable computers to "learn" from input data without being explicitly programmed. One approach is a neural network (NN) algorithm—a series of computations structured as interconnected nodes, or "neurons," to model non-linear data. The network is formed by using data transform functions, called the activation function, in a hidden layer to determine the neurons that are passed from the input to the output layer. Measurable properties of a phenomenon being observed, or "features," are used to define each neuron. This ML technique has drawbacks because features require extensive engineering, which can introduce bias in the model toward a particular output. Deep learning is a NN that contains multiple hidden layers between the input and output, and when retraining through these multiple hidden layers, the network is impeccable at removing this feature bias. These deep neural networks (DNN) are being used in both industry and academia for speech recognition, image analysis, to predict chemical reactions,[1] and in the modeling of infrared spectra.[2]

Chemical detection is one field well-suited to DNN use due to the number of mature technologies with large and previously collected data sets that can be used to train and develop DNNs. One such mature chemical detection technology that the Army has a wealth of data for is ion mobility spectrometry (IMS). IMS alerts a Soldier to danger by measuring the reduced mobility (K_0) values of surveyed ions and comparing them to a previously collected library of K_0 values for chemical threats. K_0 values are calculated using the equation

$$K_0 = \frac{L^2}{V t_d}\left(\frac{273.15}{T}\right)\left(\frac{P}{760}\right), \quad (1)$$

where L is the length traveled by the ion within the instrument, V and t_d are the voltage applied and drift time of the ion, respectively, across L, and T and P are the temperature and pressure, respectively, of a neutral drift gas inside the instrument. The theory of IMS has been previously discussed at length but relies on the separation of ions as a function of their collision cross section (ccs) with the counter flow of neutral drift gas. An ion's ccs is an empirical measurement

of its size and shape, and larger ions will experience a greater number of collisions with the drift gas and will have lower K_0 values. The ccs of the ion in a particular drift gas is calculated using the equation

$$\Omega = \frac{3e}{16N}\left(\frac{2\pi}{\mu kT}\right)^{1/2}\left(\frac{1}{K}\right), \quad (2)$$

where e is the elementary charge, N is the drift gas number density, μ is the reduced mass of the ion-neutral pair, k is Boltzmann's constant, T is the neutral drift gas temperature, and K is the mobility of the ion (not normalized against standard pressure and temperature).

While IMS is extremely sensitive and can be placed in a small form factor, it exhibits low selectivity and interferents will often produce ions with similar K_0 values to known threats. The Army's existing experimental data for IMS is the result of years of repeated testing to develop "detection windows" for these threats and can be leveraged to train DNNs to improve these shortcomings and enhance Soldier lethality. Some past efforts have already been made to develop ML models and make predictions from IMS data. In one study, a NN was trained to predict the functional groups of analytes based on IMS spectra alone.[3,4] Another NN was trained with tandem ion mobility-mass spectrometry (IMMS) measurements to predict the IMS drift times of peptides and assist in protein identification.[5] These two studies demonstrate that IMS combined with ML can be used to predict chemical structures or improve chemical identification. However, there are many different IMS-based systems used in chemical detection with different operation specifications. These previously mentioned trained NNs are not generalizable to other IMS systems because they were not developed with a cross-platform capability in mind. To develop a DNN as a universal architecture would further increase a DNN's capability and advantages while broadly improving the greater arsenal of IMS-based detectors.

This type of cross-platform capability was recently demonstrated for optical coherence tomography (OCT) in a study from DeepMind Technologies (London, United Kingdom) that utilized an artificial intelligence (AI) framework to make referrals to retinal disease patients based on OCT input data.[6] The generalization of the framework to other OCT input data from a second platform was done by training two networks: 1) a segmentation network, and 2) a classification network. The segmentation network produced a device-independent tissue segmentation image map, and the classification network labeled this image for diagnosis and referral decisions. When retraining the network for images from the additional device, only the segmentation network had to be trained. This reduced the number of training cycles when adding new input data from the second detection device. Since previous NNs for IMS could not be generalized to other detectors, this demonstrates a potential solution.

Similar to creating two networks in the DeepMind Technologies study, it was believed that a DNN for this study could utilize instrumental parameters and molecular properties as two separate networks, and therefore the DNN could be generalized to other IMS detectors with less re-training. However, unlike in the DeepMind Technologies study, both instrumental parameters and molecular properties play a role in determining the resulting IMS spectrum. As such utilizing two separate networks would not be effective in both generalization and accurate predictions. Therefore, the proposed DNN framework in this study considered both instrument parameters and molecular properties as two hidden layers, to simulate the chemistry of a detection technology for which it is trained and predict the experimental result.

2. METHODS

2.1 Data selection

ML algorithms provide optimal results when the data covers a comprehensive range of feature permutations. A feature-to-data ratio of 1:10 is most effective for engineering and model prediction. The biggest challenges in ML are bias, variance, and determining the tradeoff between them. As such, the quality of data is of foremost importance for this DNN to operate effectively. Data generated by various IMS sensors comes in different formats, sizes, and quality. Commercial sensors have their own proprietary data structure to archive the information, whereas other sensors have non-structured data archiving processes. One key factor in the success of the DeepMind Technologies study was that the initial training set used high quality "gold standard" OCT image input data before the architecture was applied to the second platform. This "gold standard" data set contained OCT scans that were identified based on the accurate referral decisions of clinical experts. Training the architecture using this "gold standard" data set allowed the architecture to more accurately analyze lower quality and ambiguous OCT scans during the testing phase.[6] There are many available IMS-based systems from which data can be gathered and used for ML training, such as the M4A1

Joint Chemical Agent Detector (JCAD). These systems will produce clean experimental mobility spectra; however, the instrumental parameters associated with the data that are used to calculate K_0 values are inaccurate and vary between units under the same experimental conditions. Because of this, the K_0 values reported by a JCAD are not calculated *ab initio* from equation (1) but rather are corrected based on each unit's response to a chemical calibrant. However, the K_0 value referenced for the calibrant is itself inaccurate as it's an estimation based on repeated *ab initio* measurements across multiple platforms and instrumental conditions.

The appropriate high quality "gold standard" in IMS instrumentation is the accurate ion mobility instrument (AIMI). An AIMI system at ECBC is used to improve the calibration of inaccurate IMS-based systems, such as the JCAD, by supplying a library of accurate calibrant K_0 values across multiple instrumental conditions. This instrument is capable of measuring K_0 values an order of magnitude more accurately (± 0.1 %) than previous systems.[7] This is a result of accurately measuring and precisely controlling, to NIST traceable standards, the individual variables that affect an ion's K_0 value and calculating these K_0 values *ab initio* from equation (1). Further advantages of the AIMI system are—it is coupled to a time-of-flight mass spectrometer (tofMS) that produces a 2D IMMS spectra, is able to change drift gases, and can control and measure the water vapor content (wvc) of that drift gas. What results is a large "gold standard" data set that is accurate to 0.1 % of the measured K_0 value and is accurately and precisely characterized as a function of both instrumental parameters and molecular properties for multiple compounds. This "gold standard" data set is suitable for use in DNN training because the effects of molecular properties on the K_0 values of ions, as well as the relationship between those effects and the instrumental parameters, are inherently intertwined, complex, and non-linear.[8,9] Therefore, highly accurate IMS measurements will allow for the determination of instrumental parameters and molecular properties that do not directly correlate. This is analogous to the DeepMind Technologies study in which the "gold standard" (AIMI) data set is used to train the DNN architecture, which is then applied to a second platform (JCAD) of lower quality to improve the analysis of that lower quality data.

The selected data are large matrices of IMS-MS spectra, but a variety of instrument parameters and molecular properties determine the resulting spectra. Specifically, ion-neutral interactions that affect the t_d of the ion were considered. The t_d of the ion is a measurement dependent on the instrumental parameters of L, V, T, and P and may also be dependent on the ion source used and whether positive or negative ions are detected. Other than instrumental parameters, the ion-neutral interactions occurring within the drift tube determine the ccs of the ion and result from the molecular properties present. However, multiple molecular properties that determine ion-neutral interactions are not accounted for in equation (1) and must be considered as raw inputs in feature engineering. These include, but are not necessarily limited to, the drift gas used, the reduced mass of the ion-molecule pair, the polarizability of the drift gas, what dopants or drift gas modifiers are used if any, what analyte is being measured, and whether that analyte forms both monomer and dimer species. These molecular properties contribute to the overall ccs of the ion-neutral pair. These raw inputs were assigned as either instrument parameters or molecular properties when designing the raw feature inputs.

2.2 Data processing

This approach used Keras with Tensorflow libraries to model the data. The model was built with the activation function rectified linear unit (ReLU) and checked with the loss function of mean absolute error. Training and modelling of data was done on an HP® laptop running 64-bit Ubuntu 18.10 with a quad-core i5-3210M CPU with integrated Intel® HD Graphics 4000 and 16 GB of DDR3L 1600 MHz RAM. Miniconda was installed to create isolated environments for computation purposes to try different libraries for modeling and training of the data. Python scripts were written using NumPy and pandas to transform data in a more structured manner for features and case visualization of the data.

Table 1. Full AIMI data set for training with calculated total cases or points.

Compound	Days	Spectra	Rows	Features	Matrix	Cases
DMMP	9	230	13201	1500	19801500	3036230
DPM	16	192	13201	1500	19801500	2534592
TEPO	14	178	13201	1500	19801500	2349778
DtBP	10	168	13201	1500	19801500	2217768

Four different data sets were generated by AIMI in the lab, as shown in Table 1, and DMMP data was initially used for training and testing. Figure 1 shows the data file naming scheme that is used to generate raw data inputs. Background spectra were also included to teach the DNN the appropriate response in the absence of sample. Spectra

for DMMP data collected in the positive mode were selected where the mass was > 15 and ≤ 400 for training. Before this data could be used in training the DNN, cleaning was done to transform incomplete, missing, duplicate, irrelevant and non-structured data. Missing values were replaced with median values determined from the dataset. This step ultimately determines the prototype features and cases for hypothesis evaluation.

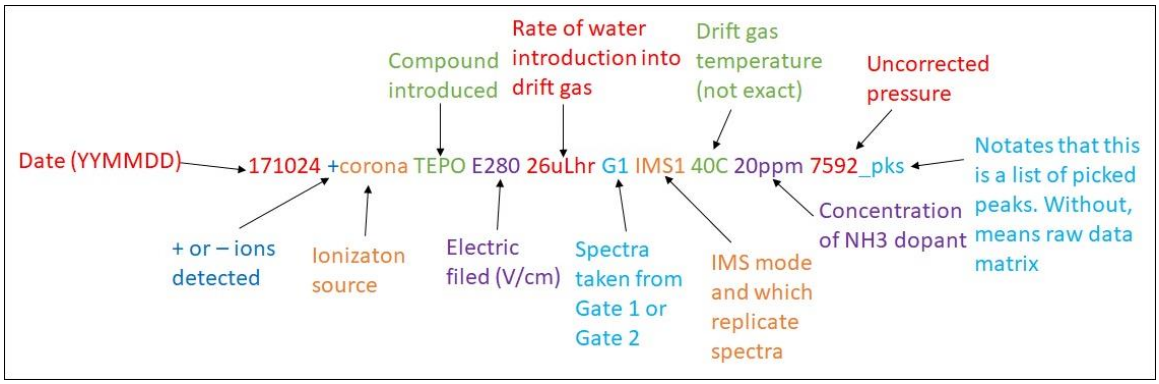

Figure 1. Raw data input. Example of raw data features imbedded in filename that were extracted for visualization.

Utilizing these raw inputs, a variety of visualizations are generated to direct feature engineering for training. Figure 2 shows an example of one of these visualizations—depicting a histogram of DMMP that was generated during this process. Histograms such as this highlight unexpected trends, potential outliers, measurement errors, and features that should be binary. After features are engineered, data was inputted into the model and a gradient descent generated to visualize model performance.

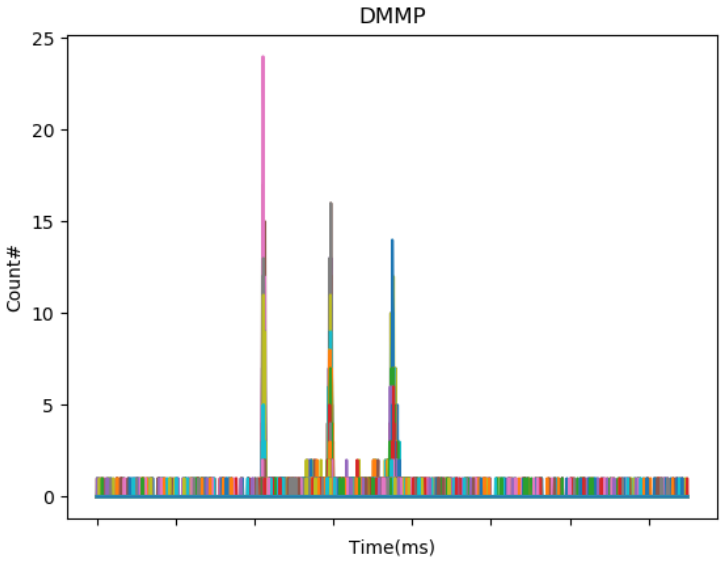

Figure 2. DMMP Drift Time Counts. Example of data visualization showing number of responses to DMMP at varying drift times.

3. RESULTS

This work proposed a DNN that could predict the mass spectrum of a molecule if it was provided the IMS drift time and molecular structure. Due to the time constraints of this project, a gradient descent was performed on only a portion of the data set to assess the training performance. The result lead to an unstable gradient and it was decided to revisit the assumptions on the treatment of the data and redesign the theoretical DNN framework. The three important factors that required changes were; the treatment of positive versus negative mode spectra, the inherent time series composition of IMS data, and overlapping molecular properties and instrumental parameters.

3.1 Treatment of ion mobility spectrometry modes

When training a DNN, it is important that the data provided is both robust and complete. When wanting to predict the spectra of an unknown molecule for IMS, a point must be made to consider whether the resulting ions are active in the positive, negative, or both modes of the IMS. To train for both positive and negative mode, parameters of each need to be inputted, including spectra representing each mode. This meant several key inputs would be duplicated and had to be annotated in a way to ensure results for each mode did not mix. Unfortunately, for some compounds in the data set, a negative mode spectrum was never obtained because it is well known that the compound is not active in that mode. When designing alarm algorithms for detection, a research scientist considers this information before inputting the results. A DNN cannot consider this piece of information unless it is explicitly trained to recognize that no product ions are produced in the negative mode. This proved to be a large challenge and a potential solution to this was to treat each mode as a separate detector. This provides several benefits in reducing the initial data size and reducing training time for each mode.

3.2 Processing of time-data series

IMS is designed to continuously acquire spectra and is inherently a time-sequence of data. A challenge associated with incorporating additional detection devices into the NN would be considering the background when an analyte of interest appears. This causes a variety of changes in the resulting spectra as detectors will respond differently, depending on the analyte concentration and environmental conditions. Long-short term memory (LSTM) is a type of recurrent neural network (RNN) that considers a previous state, X_{t-1}, as compared to the current state, X_t. Many IMS variables are constant over an experimental time, but when variables such as analyte concentration, temperature, or humidity change, the physical spectra can as well. Utilizing LSTM allows for consideration of these previous states before interrupting the results of a new state.

3.3 Overlapping factors in inputs

The original proposed DNN was designed to use a rectified linear unit (ReLU) activation function to pass properties from hidden layer 1 and 2. Initially, only raw input features were examined, and the intent was to weigh instrument parameters to always pass from hidden layer 1 to 2. In hidden layer 2, the dimensions could be reduced into the already reduced dimensions of the molecular properties. This decision was based on the knowledge that the properties of the molecule need to be accounted for, before being able to understand how an instrument parameter may affect its behavior. As inputs were assigned to properties and parameters, it was found that some inputs were neither solely an instrument parameter nor molecular property.

Rather, some inputs could be classified as either, due to the degree they affected inputs in the other class. It was decided that several features can be reduced into more complex features by calculating known molecular properties such as ccs. This more efficiently captures the effects of the raw input features on the resulting spectra. Figure 3 shows input assignments for either molecular properties, instrument parameters, or interrelated.

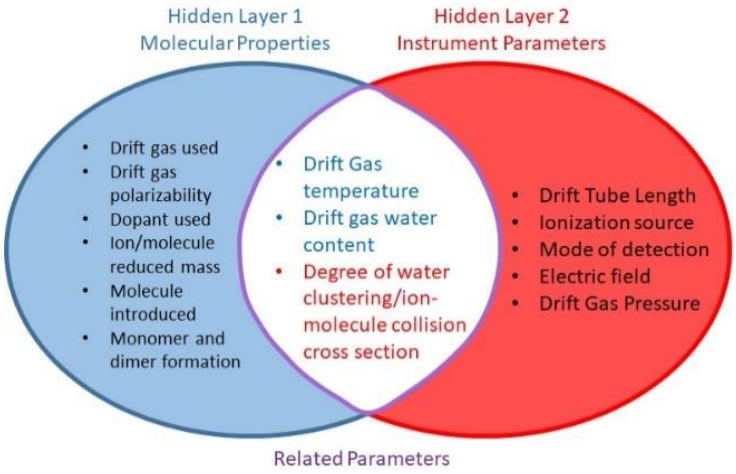

Figure 3. Interrelated inputs. Venn diagram showing distribution of instrumental parameters and molecular properties.

These assignments in Figure 3 are based on known ion-neutral interactions. Different drift gases—such as helium, carbon dioxide, or ambient air—have varying sizes that affect the overall ccs and reduced mass of the ion-neutral pair. The polarizability of the drift gas determines whether momentary electrostatic attraction and increased interaction occurs between the ion and neutral. If excess amounts of water vapor or any drift gas dopants, such as ammonia, are present within the drift gas, the ion chemistry may change to produce different product ions from non-doped conditions, and the dopant or water vapor neutrals can cluster around the ion, changing the overall ccs. Different ions will have different ccs's, but some analytes will produce multiple ions and may be active in only the positive or negative ion detection mode, or in both simultaneously. Many of these ions may also form dimers, thereby increasing their collision cross-section similar to clustering with water vapor. If stable dimers, or even trimmers, are formed, additional mobility peaks will be seen in the spectrum. These molecular properties are not included in equation (1) but can be affected by the variables therein. For example, a change in T at identical drift gas wvc levels will cause a change in the degree of water clustering around the ion. These changes will affect the calculated K_0 values of different ions to varying degrees and are important to consider for feature selection.

3.4 Finalized DNN framework

Figure 4 shows the new theoretical DNN framework when taking the above-mentioned considerations into account.

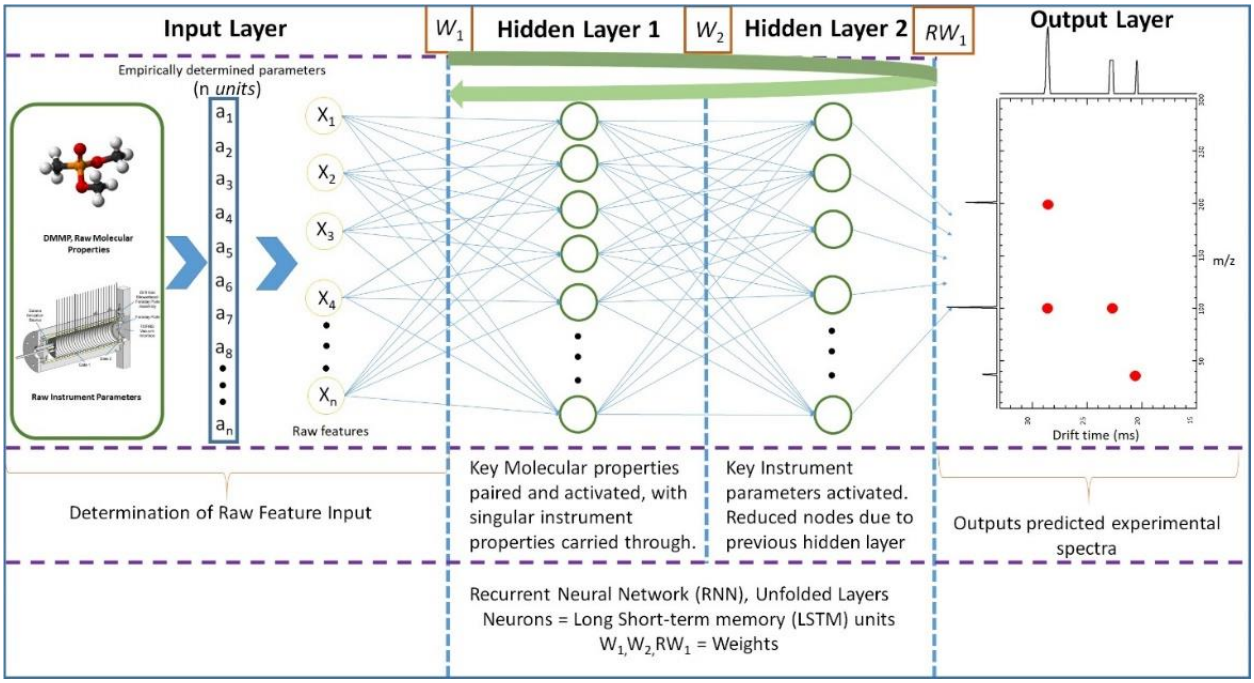

Figure 4. LSTM DNN Framework. DNN framework that uses two hidden layers and LSTM for predicting experimental IMS spectrum.

This framework takes a series of raw inputs, a_n, that are per-spectrum dependent, and processes these values into an input layer of vectors representing features X_n. A library of mathematical functions is performed on raw data inputs to determine values such as ccs and density. A variety of input vectors, X, are weighted by W_n, and processed through hidden layers 1 and 2 using LSTM. Configuration of the hidden layer is important as it establishes a nonlinear relationship into the nodes of the network that enables generalization. Currently, the true number of nodes and node-to-node connections are unknown, because the number of nodes in the hidden layers are increased with each iteration based on prediction results. It is accepted that a model's learning capabilities will increase when more nodes are added into the hidden layer, which enables the hidden layer to be flexible. Final output is a 2D spectrum of IMS-MS data and, when predicting, the DNN will predict the missing data points.

4. CONCLUSIONS

The originally engineered features and proposed DNN proved insufficient based on a partial gradient descent. A partial gradient descent was initially performed because the large data set proved too expansive to process given the timeframe. The partial gradient descent made clear the data had to be revisited to improve feature engineering and redesign the proposed DNN framework. This led to a more robust proposed DNN framework and a better plan for developing features that reduce the dimensions of the raw inputs before training occurs. Future work seeks to finish feature engineering and train the DNN to predict the spectra without saturating the gradient descent.

ACKNOWLEDGMENTS

Funding was provided by the Director, Edgewood Chemical Biological Center under the authorities and provisions of Section 2363 of the FY 2018 NDAA to develop new technologies, engineer innovations, and introduce game-changing capabilities. The authors would like to acknowledge Dr. Augustus W. Fountain, III for providing technical guidance.

REFERENCES

[1] Wei, J.N.; Duvenaud, D.; Aspuru-Guzik, A. Neural Networks for the Prediction of Organic Chemistry Reactions. *ACS Cent. Sci.* **2016,** *2* (10), pp 725–732.

[2] Gastegger, M.; Behler, J.; Marquetand, P. Machine learning molecular dynamics for the simulation of infrared spectra. *Chem. Sci.* **2017,** *8* (10), pp 6924–6935.

[3] Bell, S.; Nazarov, E.; Wang, Y.F.; Eiceman, G.A. Classification of ion mobility spectra by functional groups using neural networks. *Anal. Chim. Acta.* **1999,** *394* (2–3), pp 121–133.

[4] Bell, S.; Nazarov, E.; Wang, Y.F.; Rodriguez, J.E.; Eiceman, G.A. Neural network recognition of chemical class information in mobility spectra obtained at high temperatures. *Anal. Chem.* **2000,** *72* (6), pp 1192–1198.

[5] Wang, B.; Valentine, S.; Plasencia, M.; Raghuraman, S.; Zhang, X. Artificial neural networks for the prediction of peptide drift time in ion mobility mass spectrometry. *BMC Bioinf.* **2010,** *11* (1), p 182.

[6] De Fauw, J.; Ledsam, J.R.; Romera-Paredes, B.; Nikolov, S.; Tomasev, N.; Blackwell, S.; Askham, H.; Glorot, X.; O'Donoghue, B.; Visentin, D.; van den Driessche, G.; Lakshminarayanan, B.; Meyer, C.; Mackinder, F.; Bouton, S.; Ayoub, K.; Chopra, R.; King, D.; Karthikesalingam, A.; Hughes, C.O.; Raine, R.; Hughes, J.; Sim, D.A.; Egan, C.; Tufail, A.; Montgomery, H.; Hassabis, D.; Rees, G.; Back, T.; Khaw, P.T.; Suleyman, M.; Cornebise, J.; Keane, P.A.; Ronneberger, O. Clinically applicable deep learning for diagnosis and referral in retinal disease. *Nat. Med.* **2018,** *24* (9), pp 1342–1350.

[7] Hauck, B.C.; Siems, W.F.; Harden, C.S.; McHugh, V.M.; Hill, H.H. Construction and evaluation of a hermetically sealed accurate ion mobility instrument. *Int. J. Ion Mobility Spectrom.* **2017,** *20* (3–4), pp 57–66.

[8] Hauck, B.C.; Siems, W.F.; Harden, C.S.; McHugh, V.M.; Hill, H.H., Jr. Determination of E/N Influence on K0 Values within the Low Field Region of Ion Mobility Spectrometry. *J. Phys. Chem. A.* **2017,** *121* (11), pp 2274–2281.

[9] Hauck, B.C.; Siems, W.F.; Harden, C.S.; McHugh, V.M.; Hill, H.H., Jr. High Accuracy Ion Mobility Spectrometry for Instrument Calibration. *Anal. Chem.* **2018,** *90* (7), pp 4578–4584.